Quantum Information across Spacetime: From Gravitational Waves to Spinning Black Holes

by

Matthew P. G. Robbins

A thesis
presented to the University of Waterloo
in fulfillment of the
thesis requirement for the degree of
Doctor of Philosophy
in
Physics

Waterloo, Ontario, Canada, 2021

Examining Committee Membership

The following served on the Examining Committee for this thesis. The decision of the Examining Committee is by majority vote.

External Examiner:	Ralf Schützhold Professor, Helmholtz-Zentrum Dresden-Rossendorf Professor, Institut für Theoretische Physik, Technische Universität Dresden
Supervisors:	Robert Mann Professor, Dept. of Physics and and Astronomy, University of Waterloo Niayesh Afshordi Associate Professor, Dept. of Physics and Astronomy, University of Waterloo Associate Faculty, Perimeter Institute for Theoretical Physics
Internal Member:	Roger Melko Professor, Dept. of Physics and Astronomy, University of Waterloo Associate Faculty, Perimeter Institute for Theoretical Physics
Internal-External Member:	Eduardo Martin-Martinez Associate Professor, Dept. of Applied Mathematics, University of Waterloo
Other Member(s):	Rafael Sorkin Researcher Emeritus, Perimeter Institute for Theoretical Physics

Author's Declaration

This thesis consists of material all of which I authored or co-authored: see Statement of Contributions included in the thesis. This is a true copy of the thesis, including any required final revisions, as accepted by my examiners.

I understand that my thesis may be made electronically available to the public.

Statement of Contributions

This thesis is based on the following published and forthcoming articles:

- Chapter 3:
  - **M. P. G. Robbins**, N. Afshordi, and R. B. Mann, "Bose-Einstein Condensates as Gravitational Wave Detectors," *Journal of Cosmology and Astroparticle Physics.* **2019**, 7 (2019).
- Chapter 4:
  - **M. P. G. Robbins**, N. Afshordi, A. O. Jamison, and R. B. Mann, "Detection of Gravitational Waves using Parametric Resonance in Bose-Einstein Condensates," Submitted to *Journal of Cosmology and Astroparticle Physics*. arXiv:2101.03691 [gr-qc]. (2021).
- Chapter 6:
  - **M. P. G. Robbins** and R. B. Mann, "The Anti-Hawking Effect for Rotating BTZ Black Holes." Submitted to *Physical Review D*. arXiv:2107.01648 [gr-qc]. (2021).
- Chapter 7:
  - **M. P. G. Robbins**, L. J. Henderson, and R. B. Mann, "Entanglement Amplification from Rotating Black Holes," Accepted to *Classical and Quantum Gravity*. arXiv: 2010.14517 [hep-th]. (2020).

Abstract

This thesis is split into two parts. In the first part, we investigate Bose-Einstein condensates (BECs) as a means to detect gravitational waves. For the detection of continuous gravitational waves, we study its sensitivity with initially-squeezed phonons by optimizing the properties of the condensate and the measurement duration. We show that this method of detecting gravitational waves in the kilohertz regime is limited by current experimental techniques in squeezing BEC phonons. Without focusing on a specific detector setup, our study shows that substantive future improvements in technology (e.g., increasing the squeezing of BEC states or their physical size) will be necessary for such a detector to be competitive in measuring gravitational waves of astrophysical and/or cosmological origin. We then consider a modulating speed of sound of the BEC trap, whose frequency matches that of an incoming continuous gravitational wave. The trap modulation induces parametric resonance in the BEC, which in turn enhances sensitivity of the BEC to gravitational waves. We find that such a BEC detector could potentially be used to detect gravitational waves across several orders of magnitude in frequency, with the sensitivity depending on the speed of sound, size of the condensate, and frequency of the phonons. We estimate the sensitivity such an experiment would have to gravitational waves and discuss the current technological limitations. We also comment on the potential noise sources as well as what is necessary for such a detector to become feasible.

In the second part of this thesis, we turn our attention to Unruh-DeWitt detectors (a two-level quantum system) and rotating Bañados-Teitelboim-Zanelli (BTZ) black holes. In both flat and curved spacetimes, there are weak and strong versions of the anti-Unruh/anti-Hawking effects, relating the detector response, Kubo-Martin-Schwinger (KMS) temperature of the background scalar field, and the temperature given by the Excitation to De-excitation Ratio (EDR) of the detector. We first investigate the effect of rotation on the weak and strong anti-Hawking effects for an Unruh-DeWitt detector orbiting a BTZ black hole in the co-rotating frame. We will show that rotation amplifies the strength of the weak anti-Hawking effect while simultaneously being boundary condition dependent for whether it amplifies or reduces the strength of the strong anti-Hawking effect. There is also a non-monotonic relationship for the strong anti-Hawking effect between the EDR temperature and the angular momentum of the black hole. In addition, we note that the weak anti-Hawking effect is independent of a changing anti-de Sitter (AdS) length, while a longer AdS length increases the temperature range of the strong anti-Hawking effect. We then consider two detectors orbiting a BTZ black hole and show that such correlations – vacuum entanglement – in the environment of near-extremal black holes is significantly amplified (up to 10-fold) relative to their slowly rotating counterparts. We demonstrate this effect by calculating the entanglement between the detectors through the concurrence extracted from the vacuum. The effect is manifest at intermediate distances from the horizon, and is most pronounced for near-extremal small mass black holes. The effect is also robust, holding for all boundary conditions of the field and at large spacelike detector separations. Smaller amplification occurs near the horizon, where we find that the entanglement shadow – a region near the black hole from which entanglement cannot be extracted – is diminished in size as the black hole's angular momentum increases.

Acknowledgements

Thank you to my supervisors, Robert Mann and Niayesh Afshordi. I had a lot of fun working with you and you were always very supportive and encouraging. I also want to thank Alan Jamison for answering my many, many questions as I tried to better understand the experimental aspect of Bose-Einstein condensates and atomic physics. I'd also like to thank Laura, Erickson, and Robie for all the useful help and guidance they've provided over the past four years. And thank you to Aditya, Soham, Alice, Sam, Laura, Erickson, Robie, and everyone else in Robb's and Niayesh's groups for their useful questions/comments as I prepared for my thesis defence.

And thank you to Aditya and Soham for all the pool and foosball games and the great conversations we've had. Since, we haven't been able to hang out in-person for a while, I think this means that we have a bunch of pool/foosball to play once the pandemic is all over!

I'd also like to thank Nancy and David, Femmy and Grant, Ben, and Vinodh for your friendship in Waterloo. And thank you, Femmy and Grant, for all the home-made cookies that you have given me during the past year and a half. You definitely know how much I love cookies! If there is ever a world cookie shortage, we both know that it will probably be partially my fault.

And finally, thank you to my parents for all your support and encouragement over the past ten years in my undergrad, Masters, and PhD.

Table of Contents

List of Figures x

1 Introduction 1

1.1 Relativistic Quantum Information . . . 1

1.1.1 Gravitational Waves . . . 2

1.1.2 Spinning Black Holes . . . 3

I Detecting Gravitational Waves with Bose-Einstein Condensates 6

2 Introduction to using Bose-Einstein Condensates to Detect Gravitational Waves 7

2.1 Gravitational Waves . . . 7

2.1.1 Derivation in a Flat Background . . . 7

2.1.2 Sources and Detection of Gravitational Waves . . . 9

2.1.3 Direct Detection of Gravitational Waves . . . 12

2.2 Quantum Field Theory in Curved Spacetime . . . 15

2.2.1 Quantum Fisher Information . . . 18

2.2.2 Squeezing . . . 20

2.3 Bose-Einstein Condensates . . . 21

2.3.1 Ideal Gas . . . 21

2.3.2 Weakly Interacting Particles . . . 23

3 Detecting Gravitational Waves with Squeezing 25

3.1 Introduction . . . 25

3.2 Bose-Einstein condensates in a curved background . . . 26

3.2.1 Calculation of Bogoliubov Coefficients . . . 29

3.3 Gravitational wave detection via quantum metrology . . . 30

3.4 Sensitivity for specific experimental parameters . . . 34

3.4.1 Non-interacting modes . . . 34
3.4.2 Decoherence (damping) from interacting modes . . . 37
3.5 Conclusion . . . 38

4 Detecting Gravitational Waves with Parametric Resonance 41
4.1 Introduction . . . 41
4.2 Bose-Einstein condensates in curved spacetimes . . . 42
4.2.1 Equation of Motion . . . 42
4.3 Estimating the sensitivity to gravitational waves . . . 48
4.4 Damping . . . 52
4.4.1 Squeezing . . . 54
4.5 Implementation . . . 55
4.5.1 Observable Sources . . . 55
4.5.2 Experimental Design . . . 56
4.5.3 Experimental Challenges . . . 57
4.6 Conclusion and Future Prospects . . . 61

II Entanglement, Temperature, and Rotating BTZ Black Holes 63

5 Unruh-DeWitt detectors around rotating BTZ black holes 64
5.1 Unruh-DeWitt Detectors . . . 64
5.2 Transition Probability (one detector) . . . 65
5.3 Entanglement Harvesting Protocol (two detectors) . . . 66
5.3.1 Concurrence . . . 67
5.4 Rotating BTZ black holes . . . 67

6 Anti-Hawking Effect for Rotating BTZ Black Holes 71
6.1 Introduction . . . 71
6.2 Anti-Hawking effect . . . 72
6.3 Weak Anti-Hawking Effect for Rotating BTZ Black Holes . . . 74
6.4 Strong Anti-Hawking Effect for Rotating BTZ Black Holes . . . 78
6.5 Conclusion . . . 81

7 Entanglement Amplification from Rotating Black Holes 82
7.1 Introduction . . . 82
7.2 Entanglement Harvesting around a Rotating BTZ Black Hole . . . 83
7.3 Conclusion . . . 89

8 Conclusion **91**

8.1 Summary . . . 91

8.1.1 Part I . . . 91

8.1.2 Part II . . . 92

8.2 Where do we go from here? . . . 92

8.2.1 Gravitational Wave Detectors . . . 92

8.2.2 Spinning Black Holes . . . 93

8.3 Final Thoughts . . . 94

References **95**

APPENDICES **110**

A Derivation and Solution to Equation (4.12) **111**

B Calculation of Squeezing Expectation Values **113**

C Calculating the Matrix Elements of Equation (5.11) **115**

C.1 Detector Transition Probability . . . 115

C.2 Detector Non-localities . . . 117

C.3 Total Correlations . . . 119

List of Figures

1.1 Lightcone of detector A. As detector B is within the lightcone of detector A, we say that detector B can influence detector A. This is known as timelike separation. In contrast, detector C is outside of detector A's lightcone, so we say that A and C are spacelike separated. Physically, this means that detector C cannot normally influence detector A because signals from C would need to travel at superluminal speed to reach detector A. 4

2.1 The effect of on a multiparticle system by a gravitational wave, with the first line showing plus polarization and the second line showing cross polarization. 10

2.2 Different sources of gravitational waves and different gravitational wave detectors in operation (black), or planned/under construction (blue). We see that much effort has been exerted in designing detectors to investigate gravitational wave sources below 1000 Hz. The plot was produced using the online applet, www.gwplotter.com [159]. 11

2.3 A simplified diagram of the Laser Interferometer Gravitational-Wave Observatory (LIGO). We see that the setup is similar in nature of a Michelson interferometer. In inset (a), the detector locations are shown. In inset (b), we see an overlap of the strain sensitivities of the Hanford detector (H1) and the Livingston detector (L1). Image is reproduced from [2], available under the terms of the Creative Commons Attribution 3.0 License. 13

2.4 Three of the major sources of noise in LIGO. In black, we show the observed noise. For simplicity, we do not include subdominant noises, such as the noise from the residual gases in the interferometric arms. Data was obtained from the authors of [149]. 14

2.5 Number of particles in an excited state compared to the number of particles in the BEC. 22

3.1 Theoretical strain sensitivities $\left(\frac{\sqrt{\langle(\Delta\epsilon)^2\rangle}}{\sqrt{f}}\right)$ of a BEC gravitational wave detector (top curve) using current experimental capabilities, where f is the frequency of the gravitational wave. With $L = 10^{-3}$ m, $t_{obs} = 10^6$ s, $\tau = 10^{-3}$ s, $\phi = \pi/2$, and $r = 0.83$, a BEC is unable to detect kHz gravitational waves. The thick purple line is the general trend corresponding to the maximum design sensitivity of Advanced LIGO (extrapolated to 10^4 Hz). Note that phonons of frequency $\frac{f}{2}$ are necessary to detect gravitational waves of frequency f. 35

3.2 Theoretical strain sensitivity $\left(\frac{\sqrt{\langle(\Delta\epsilon)^2\rangle}}{\sqrt{f}}\right)$ to kHz gravitational waves for a futuristic BEC with $c_s = 1.2 \times 10^{-2}$ m/s, $t_{obs} = 10^6$ s, $\phi = \pi/2$, and $\tau = 10^{-3}$ s. In (a), $L = 10^{-3}$ m, while $L = 1$ m in (b). The thick purple line is the general trend of the design sensitivity of Advanced LIGO (extrapolated to 10^4 Hz). 36

3.3 The theoretical strain sensitivity $\left(\frac{\sqrt{\langle(\Delta\epsilon)^2\rangle}}{\sqrt{f}}\right)$ of a BEC to gravitational waves of frequency f, with τ optimized and r_0 maximized within the validity of the model (solid black and purple lines), including decoherence due to interacting modes. Over this frequency range, the measurement duration corresponds to $\tau \sim \frac{1}{\omega}$. We have set $t_{obs} = 10^6$ s, $m = 10^{-25}$ kg, $n = 7 \times 10^{20}$ m^{-3}, $\mu_0 = \mu_\infty = 1$, $c_s = 1.2 \times 10^{-2}$ m/s, and $\phi = \pi/2$. To facilitate comparison, we have also considered $r = 10$ for two different condensate lengths, assuming damping to be negligible (dashed blue and orange lines), where we have $\tau = 10^{-3}$ s in both cases. The overall trend of the design sensitivity of Advanced LIGO is indicated by the thick blue line (extrapolated to 10^4 Hz). 39

4.1 Resonances of the Mathieu equation. 46

4.2 Dependence of the number of cycles N needed to reach non-linearity, on $q = \frac{f_{\rm phonon}}{f_{\rm GW}}$ and the frequency (assuming $f_{\rm GW} = f_B$) for an undamped condensate. We see that, in general, the condensate is sensitive to a greater number of oscillations when considering a smaller frequency and larger condensates. We take the number density to be 10^{20} m^{-3} of ^{39}K atoms. The time to non-linearity is simply $N/f_{\rm GW}$. 47

4.3 Observation time for a gravitational wave interacting with a BEC with $q = 0.501245$. Lower frequencies correspond to longer observational times. We note that this neglects the effects of 3-body recombination, which limits the condensate lifetime. We discuss this effect further in Section 4.5). For smaller values of q (i.e. closer to the resonance peak), the maximum observational time of the condensate decreases. . . . 48

4.4 Frequency regime of a BEC gravitational wave detector for ^{39}K atoms. Note that the larger condensates can probe lower-frequency gravitational waves, whereas those with faster speeds of sound can probe higher-frequency gravitational waves. 51

4.5 The amplitude sensitivity $\left(\sqrt{\langle(\Delta\epsilon)^2\rangle}\right)$ of an undamped BEC gravitational wave when on resonance with an oscillating speed of sound. In each case, the condensate is observed for the maximum number of oscillations $N(q)$. We conduct the hypothetical experiment over the course of a year. We take the number density to be 10^{20} m^{-3} of ^{39}K atoms). The dashed lines represent different values of q, while the different colours are different values of c_s. Purple is the sensitive corresponding to LIGO. . . 52

4.6 Contour plot of the amplitude sensitivity $\left(\sqrt{\langle(\Delta\epsilon)^2\rangle}\right)$ of an undamped BEC to gravitational waves. The condensate is observed for the maximum number of oscillations $N(q)$. We run the experiment over the course of a year and see that undamped condensate could be sensitive to gravitational waves across the frequency spectrum. Changing the speed of sound and length of the condensate will affect the minimum and maximum gravitational wave frequency that can be observed. We take the number density to be 10^{20} m^{-3} of ^{39}K atoms). 53

4.7 The strain sensitivity of a damped BEC gravitational wave detector for various values of q (=ratio of phonon to GW frequency). We consider $c_s = 5$ cm/s and $L = 500$ μm. In each case, the condensate is observed for the maximum number of oscillations $N(q)$, before non-linearities become important. The different colours represent different values of q while the different line styles represent damped/undamped. The purple curve represents LIGO's sensitivity. 54

4.8 Speeds of sound and length of the condensate necessary to observe gravitational waves with a smaller amplitude. The green triangles represent the upper bounds the strain of various pulsar sources [3] while the red stars correspond to axion clouds based on several scenarios proposed in [258]. The error bars for the axion clouds assume a distance of 1kPc - 50 kPc. 56

4.9 A simple illustration of the effect of fluctuation on power on the condensate length. The orange solid line represents the chemical potential. The blue solid line represents the Gaussian potential energy in the absence of noise. For illustrative purposes, we take the chemical potential to have half the maximum potential energy. (In reality, the chemical potential is much less than the maximum potential energy). The ends of the trap are where the chemical potential equals the potential energy. Left: As laser power fluctuates (assuming that the power at each beamsplitter is fixed), the maximum potential energy will increase and decrease (dashed lines). The effect is to increase/decrease the length of the trap. Right: As the power at each beamsplitter fluctuates (assuming that the total power is fixed), the length of the trap will increase on one side, while decreasing on the other side. As a result, the total length of the trap will remain fixed, but the trap itself will move back and forth. 58

4.10 The amplitude sensitivity $\left(\sqrt{\langle(\Delta\epsilon)^2\rangle}\right)$ of a BEC ($a = 0.005$) to gravitational waves, assuming that the BEC has side lengths of 100 μm, the speed of sound is 1 cm/s, the lifetime of the BEC is limited to 3 s (without using a BEC machine), and the incoming gravitational wave has a frequency of 1000 Hz. We see that the greatest sensitivity to gravitational waves is achieved slightly off the centre of resonance and that moving outside the resonance band destroys the sensitivity to gravitational waves. 59

5.1 Contour to integrate over the τ_B variable when calculating L_{AB}. 70

6.1 Response functions for a black hole of mass $M = 1/10$ for Dirichlet, transparent, and Neumann boundary conditions (for the field at spatial infinity) and an energy gap of $\Omega\ell = 1/10$. The inset plots correspond to $M = 100$. As expected, the rotation of the black hole has a smaller effect for larger masses. As the mass of the black hole increases, the weak anti-Hawking effect goes away for $\zeta = 1$ and $\zeta = 0$. Note that for $\zeta = -1$, the weak anti-Hawking effect is still present even for large mass black holes. 75

6.2 Response of a rotating BTZ black hole with mass $M = 1/1000$ and Dirichlet boundary conditions ($\zeta = 1$). We note that for transparent and Neumann boundary conditions, qualitatively similar results are obtained. 76

6.3 Derivative of the response with respect to the KMS temperature of a rotating BTZ black hole with mass $M = 1/1000$ and Dirichlet boundary conditions ($\zeta = 1$). We note that for transparent and Neumann boundary conditions, qualitatively similar results are obtained. 77

6.4 EDR temperature for a black hole of mass $M = 1/1000$ and detector energy gap of $\Omega\sigma = 1$. We plot KMS temperature down to $T_{KMS}\ell = 10^{-5}$. The insets show the relation between the EDR temperature and KMS temperature for larger values of T_{KMS}. 78

6.5 EDR temperature for a black hole of mass $M = 1/1000$ and detector energy gap of $\Omega\sigma = 1/10$. The results are similar for $\Omega\sigma = 1/100$. The insets show the EDR temperature for our first three values of the angular momentum, plotted on a linear scale (rather than a log scale, as is the case for the main plots). 79

6.6 Changing AdS lengths for the strong anti-Hawking effect for a black hole of mass $M = 1/1000$, Dirichlet boundary conditions. We plot KMS temperature down to $T_{KMS}\ell = 10^{-5}$. The insets show the effect of changing AdS length on the EDR temperature for larger values of T_{KMS}. 80

7.1 Concurrence of two UDW detectors separated by a distance $d(R_A, R_B) = 1$ orbiting a black hole of mass $M = 1$ for various angular momenta. We have set $\zeta = 1$ and $\ell/\sigma = 10$. Note that all curves lie on top of one another. 83

7.2 Concurrence of two UDW detectors separated by a distance $d(R_A, R_B) = 1$ orbiting a black hole of mass $M = 10^{-3}$ for various angular momenta. We have set $\zeta = 1$ and $\ell/\sigma = 10$. 84

7.3 Concurrence as a function of $d(r_+, R_A)/\sigma$ for various co-rotating detector separations $d(R_A, R_B)$, for $M = 10^{-3}$, $\zeta = 1$, $\ell/\sigma = 10$, $\Omega\sigma = 1$, and $J/M\ell = 0.9999$. 86

7.4 Investigating the signalling estimator for various proper separations for a black hole of mass $M = 10^{-3}$, AdS length of $\ell/\sigma = 10$, and Dirichlet boundary conditions. . . . 86

7.5 The effect of changing the AdS length on the harvested entanglement. We see that smaller AdS lengths correspond to significantly greater amplification. We have set $\Omega\sigma = 1/100$, $J/M\ell = 0.999999$, $\zeta = 1$, and $M = 10^{-3}$. 87

7.6 Partial image sums of P_A, $|X|$, and concurrence for Unruh-DeWitt detectors orbiting a rotating BTZ black hole of angular momentum $J/M\ell = 0.9999$. In each plot, the detectors have a proper separation of $d(R_A, R_B) = 1$, the energy gap is $\Omega\sigma = 1$, the black hole, has a mass of $M = 10^{-3}$, $\zeta = 1$ and $\ell/\sigma = 10$. 88

7.7 Transition probabilities and non-locality for Unruh-DeWitt detectors orbiting a rotating BTZ black hole. In each plot, the detectors have a proper separation of $d(R_A, R_B) = 1$, the energy gap is $\Omega\sigma = 1$, the black hole, has a mass of $M = 10^{-3}$, $\zeta = 1$ and $\ell/\sigma = 10$. 89

7.8 Mutual information corresponding for a rotating black hole of mass $M = 10^{-3}$, Dirichlet boundary conditions, and $\ell/\sigma = 10$. The energy gap of the detectors is $\Omega\sigma = 1$. For smaller energy gaps, the figures look qualitatively similar. 90

Chapter 1

Introduction

1.1 Relativistic Quantum Information

Quantum mechanics and general relativity form the bedrock of modern physics. They are among the most-well tested theories and are critical to the functioning of today's society. There has also been recent interest in using quantum sensors to study fundamental physics, such as the gravitational constant, the equivalence principle, dark matter, dark energy, and gravitational waves [35]. When quantum mechanics is applied to relativistic phenomena, surprising new results can appear, such as the Unruh effect [61], Hawking radiation [173], and gravitational wave echoes [7]. However, it is well known that combining quantum mechanics with general relativity into a single theory is a highly non-trivial problem. Much research over the past several decades has been devoted to attempting to solve this problem and formulate a theory of quantum gravity.

There have been many proposals for a theory of quantum gravity as well as many suggested extensions of general relativity [16, 47]. Unfortunately, there exists no data to guide physicists towards understanding how to describe gravity as a fundamentally quantum mechanical phenomenon. Moreover, it is not even known if gravity is even quantum mechanical, or if it is actually classical [11, 49]. At best, physicists have only been able to use observations of relativistic phenomena to constrain the various theories of quantum gravity and extensions to general relativity [106, 136, 182].

In recent years, however, the situation has begun to change. In order to detect gravitational waves, we needed to construct experiments highly sensitive to fluctuations in spacetime. This raises the question of if these experiments are sensitive enough to hold the key to detecting signatures of quantum gravity and finally providing physicists with the knowledge necessary to determine whether gravity is fundamentally quantum mechanical or classical. There have been a flurry of investigations to further constrain models of quantum gravity and extended gravity through gravitational wave observations as well as understand how quantum gravity effects could be directly observed or how the gravitational wave experiments themselves may be directly affected [9, 33, 36, 45, 46, 128, 150, 174–177, 210]. For instance, the signal from the merger of two neutron stars (GW170817) can be used to investigate/constrain the number of spacetime dimensions [174]. In addition, [150] has also argued that the discretization of the area of a black hole could be imprinted within the gravitational wave signal. In terms of the detectors themselves, has argued gravitons may introduce a fundamental level of noise within gravitational wave detectors [175–177].

Another way to shed light on the interaction between classical gravitational systems and quantum mechanical phenomenon is through the use of quantum information. In particular, by analyzing

how two-level quantum systems interact with a background quantum field, techniques of quantum information can be applied to gain knowledge about the structure of spacetime, its properties, and the interaction between quantum mechanics and general relativity [72, 147, 220, 225]. The study of this relationship between special/general relativity and quantum information is a new field, known as relativistic quantum information.

Techniques in quantum information have been applied to a variety of spacetimes and dimensions, such as Minkowski [147], Rindler [201], de Sitter [116], Anti-de Sitter [99], Schwarzschild [122], Kerr [129], gravitational wave spacetimes [255], and 2+1-dimensional black holes [98, 103]. In this thesis, we want to use quantum information to study the opposite ends of the curvature spectrum. In the first part, we will consider gravitational waves and investigate how techniques in quantum information can be used to achieve the necessary sensitivity for gravitational wave detection. In the second part of this thesis, we will consider rotating Bañados-Teitelboim-Zanelli (BTZ) black holes and investigate the effect of a rotation upon two-level quantum detectors by discussing the temperature of a single detector and the amount of entanglement between two detectors.

1.1.1 Gravitational Waves

The recent direct detection of gravitational waves is revolutionizing our understanding of the Universe. Though our current observations have only detected black holes and neutron stars with the Laser Interferometer Gravitational-Wave Observatory (LIGO) and Virgo [133], it is expected that future gravitational wave detectors may also see phenomena such as supernovae, extreme-mass inspirals, and a stochastic gravitational wave background [14, 55, 224].

One of the challenges of gravitational wave astronomy is that current detectors are sensitive to only a small range of frequencies. Constructing a wide variety of detectors (both terrestrial and in space) is thus required to cover the entire gravitational wave spectrum [25, 156]. Much effort has been devoted to designing detectors for sub-kHz sources, such as the Laser Interferometer Space Antenna (LISA) (0.1 mHz - 1 Hz) [15], the Einstein Telescope ($1 - 10,000$ Hz) [140, 202] and pulsar timing arrays like the North American Nanohertz Observatory for Gravitational Wave and European Pulsar Timing Array ($\sim$nHz) [101, 124]. Atom interferometers have also been proposed to detect gravitational waves in the millihertz to decahertz regimes [56, 82, 88]. Though the Einstein Telescope is proposed to be sensitive up to 10 kHz, its optimal sensitivity will occur around the same frequency range as LIGO. Additional gravitational wave detector technologies have also been proposed, including a superfluid detector for continuous gravitational waves extending into the kilohertz regime [217,241] and a satellite-based cold atom interferometer for mid-frequency gravitational waves (30 mHz-10 Hz) [93].

In the frequency regime probed by LIGO, Virgo, and the recently operational Kamioka Gravitational Wave Detector (KAGRA) (above 100 Hz and below 1 kHz), the most common sources are binary black holes, binary neutron stars, and black hole-neutron star mergers [6]. In the kHz regime, it is predicted that transient (gravitational waves only detectable for a short time) sources include lower-mass black holes and neutron star mergers occur at frequencies outside the range that LIGO can currently observe (up to several kHz) [17, 18, 139]. Depending on the model, there could potentially even be primordial black holes in the kHz domain [84]. In the continuous regime, there may be magnetars (0.5-2 kHz) [226], neutron stars/pulsars (tens to hundreds of Hz) [3, 59], and potentially boson clouds (extending into the kHz regime) [195].

Unfortunately, detecting these high-frequency sources will require a new experimental design. One previously suggested method has been to use a Bose-Einstein condensate (BEC), which is

a gas of atoms all in the same lowest-energy quantum state, with a temperature near absolute zero [199]. Ref. [199] argued that when a gravitational wave passed by, it will produce density fluctuations (known as phonons) within the condensate. Therefore, by comparing the state of the phonon modes before and after interaction with the gravitational wave, it may be possible to determine the amplitude of the incoming wave. By also squeezing the phonon modes, the requisite sensitivity for detecting gravitational waves could be achieved. For simplicity, this first study considered a zero-temperature BEC. Later work considered more realistic temperatures and determined that the sensitivity of a BEC to an incoming gravitational wave was not strongly affected by the temperature [200].

In Chapter 2, we introduce the physics of gravitational waves, quantum field theory in curved spacetime, and Bose-Einstein condensates. Then, in Chapter 3, we consider detecting high-frequency continuous gravitational waves by initially squeezing phonons. We will show that such detection may be possible in principle, though significant advancements in phonon squeezing will be required for such an experiment to be implemented. In addition, decoherence effects will also significantly reduce sensitivity to high-frequency gravitational waves. In Chapter 4, we investigate continuous gravitational waves by considering a BEC with an oscillating speed of sound. We demonstrate that such an effect will amplify the sensitivity of the BEC to continuous gravitational waves. However, the experimental noise (namely that from vibrations and the laser photon noise) present in the currently viable setups will dominate over the gravitational wave signal, so future technological advancements will be required prior to a successful gravitational wave detection. We also consider three-body loss and show that it will have significant adverse effects on the sensitivity of these detectors. In both of these chapters, our goal will be to maximize the quantum information gained from measuring phonons as that will maximize the sensitivity to gravitational waves.

1.1.2 Spinning Black Holes

One of the hallmarks of quantum mechanics is the notion of entanglement, in which particles are correlated, regardless of whether they are spacelike or timelike separated (Figure 1.1). This phenomenon has been studied in a variety of research areas, such as investigating the presence of quantum effects in gravitational interactions [160], imaging quantum systems [125], metrology [187], and quantum information [127, 181]. Interestingly, the quantum vacuum itself is naturally entangled [230, 231]. This vacuum entanglement is central to several areas of physics, such as black hole entropy [41, 221], the AdS/CFT correspondence [198], the black hole information paradox and solutions [13, 39, 141, 151, 185], as well as quantum energy teleportation [108, 109].

Understanding how spacetime affects entanglement is a key area of research in relativistic quantum information. One way to make progress on this is to couple the vacuum field to particle detectors. This allows us the operational ability to better understand the nature of the quantum vacuum. A common theoretical method of doing this is by modelling the field-detector coupling as the light-matter interaction. This model, known as the Unruh-DeWitt detector model [66, 240], consists of a pair of two-level quantum systems interacting with a background scalar field [193, 194].

With a single detector interacting with the vacuum scalar field, several different phenomena can be investigated such as the the thermality of a field in various spacetimes [104, 137] and the effect of interactions with multiple scalar fields [54]. It is also possible to investigate the relationship between detector accelerations and the temperature of the detector. Normally, an accelerating detector in flat spacetime will heat up in a process known as the Unruh effect [62, 79, 240]. However, there

are some situations in which an accelerating detector will correspond to a decreasing temperature, which is known as the *anti*-Unruh effect. There exists a weak version of this effect, which says that particle detectors click less often as the field temperature increases, whereas the strong version says that the temperature measured by the detector decreases as the field temperature increases [40, 83]. In the case of black holes, the analogue of the Unruh effect is the Hawking effect. Similarly, an accelerating detector in a black hole spacetime can undergo an *anti*-Hawking effect, with the weak and strong versions defined similarly. [63, 64, 100].

With two detectors, new effects arise. Through the interaction with the scalar field, the vacuum entanglement can actually be transferred from the background to the two detectors themselves, in a process called entanglement harvesting [201]. By exploiting this new feature, it is possible to study phenomena inaccessible to a single detector, such as the thermal nature of de Sitter spacetime [116, 225] and the topology of spacetime [147]. Recently, entanglement harvesting has been used to probe the physics of black hole spacetimes, such as Schwarzschild [234] and static BTZ spacetimes, which are 2+1 dimensional black holes [98, 100].

The second part of this thesis seeks to understand how rotation affects the temperature of an Unruh-DeWitt detector as well as entanglement harvested from the quantum vacuum by a pair of Unruh-DeWitt detectors. This is the first time that rotation has been investigated in this context. In Chapter 5, we introduce the basic protocol of understanding how one and two Unruh-DeWitt detectors interact with the quantum vacuum. Then, in Chapter 6, we consider one detector and discuss the anti-Hawking effect for a rotating BTZ black hole. We show that rotation amplifies

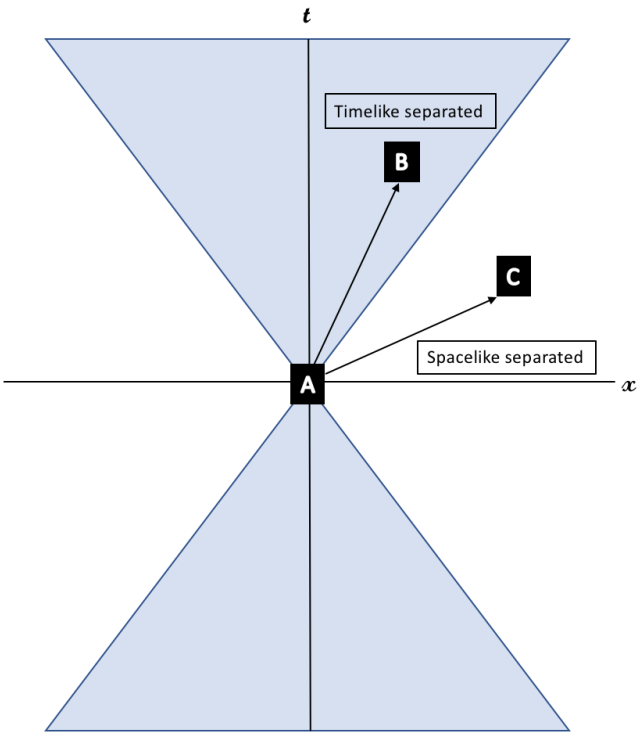

Figure 1.1: Lightcone of detector A. As detector B is within the lightcone of detector A, we say that detector B can influence detector A. This is known as timelike separation. In contrast, detector C is outside of detector A's lightcone, so we say that A and C are spacelike separated. Physically, this means that detector C cannot normally influence detector A because signals from C would need to travel at superluminal speed to reach detector A.

the weak anti-Hawking effect. In the case of the strong anti-Hawking effect, the effect of rotation is strongly dependent on the boundary conditions. In Chapter 7, we investigate entanglement harvesting with two detectors in the presence of a rotating BTZ black hole. We demonstrate that for small-mass, near-extremal black holes, the amount of entanglement transferred from the vacuum is amplified at intermediate distances from the black hole.

Part I

Detecting Gravitational Waves with Bose-Einstein Condensates

Chapter 2

Introduction to using Bose-Einstein Condensates to Detect Gravitational Waves

In this Chapter we shall first introduce the physics of gravitational waves in Section 2.1 by showing how they arise in a flat background as well as some of their key properties. We will also discuss the various gravitational wave sources as well as methods of detection. Next, in Section 2.2, we will turn our attention to quantum field theory in curved spacetime and Bogoliubov coefficients. We will also introduce the quantum Fisher information and the notion of squeezed states. Finally, in Section 2.3, we will present Bose-Einstein condensates in the context of both an ideal gas and a weakly-interacting gas of bosons.

2.1 Gravitational Waves

2.1.1 Derivation in a Flat Background

In a flat background, the line element is $ds^2 = \eta_{\mu\nu}dx^\mu dx^\nu = c^2dt^2 - dx^2 - dy^2 - dz^2$, where $\eta_{\mu\nu} = diag(c^2, -1, -1, -1)$ is the Minkowski metric and dx^μ are infinitesimal displacements of the coordinates. We are using the notation where Greek indices $\mu, \nu, ... = 0, 1, 2, 3$ represent both the spatial and temporal components of the spacetime, while Latin indices $i, j, ... = 1, 2, 3$ represent only the spatial parts. In this thesis, we will also use a $(+, -, -, -)$ signature. In the case of a curved background, the Minkowski background is generalized to the metric tensor $g_{\mu\nu}$, such that line element becomes $ds^2 = g_{\mu\nu}dx^\mu dx^\nu$. Using this form of the line element, gravitational physics can be described by Einstein's field equations

$$R_{\mu\nu} - \frac{1}{2}g_{\mu\nu}R = -\kappa T_{\mu\nu}, \tag{2.1}$$

where $R = g^{\mu\nu}R_{\mu\nu}$ is the Ricci scalar, $g_{\mu\nu}$ is the metric, $\kappa = \frac{8\pi G}{c^4}$, G is Newton's constant, c is the speed of light, $T_{\mu\nu}$ is the energy momentum tensor, and the Ricci tensor is $R_{\mu\nu} = R^\rho{}_{\mu\nu\rho}$, with the Riemann tensor given by

$$R^\rho{}_{\mu\nu\sigma} = \partial_\nu\Gamma^\rho{}_{\mu\sigma} - \partial_\sigma\Gamma^\rho{}_{\mu\nu} + \Gamma^\lambda{}_{\mu\sigma}\Gamma^\rho{}_{\lambda\nu} - \Gamma^\lambda{}_{\mu\nu}\Gamma^\rho{}_{\lambda\sigma} \tag{2.2}$$

and the Christoffel symbol,

$$\Gamma^{\rho}_{\ \mu\nu} = \frac{1}{2} g^{\rho\sigma} \left(\partial_\mu g_{\sigma\nu} + \partial_\nu g_{\mu\sigma} - \partial_\sigma g_{\mu\nu} \right) . \tag{2.3}$$

We are using condensed notation for the derivatives, such that $\partial_\mu \equiv \frac{\partial}{\partial x^\mu}$.

Using equations (2.1)-(2.3), we are in a position to investigate what happens when we consider perturbative effects on a flat background, such that $g_{\mu\nu} = \eta_{\mu\nu} + h_{\mu\nu}$, where $[h_{\mu\nu}] \ll [\eta_{\mu\nu}]$ is the perturbation. We shall outline the general procedure discussed in [102].

Substitution of this perturbation into Einstein's equations yields

$$\Gamma^{\sigma}_{\ \mu\nu} = \frac{1}{2} \left(\partial_\nu h^{\sigma}_{\ \mu} + \partial_\mu h^{\sigma}_{\ \nu} - \partial^\sigma h_{\mu\nu} \right) , \tag{2.4}$$

so that the Riemann tensor, Ricci tensor, and Ricci scalar respectively become

$$R^{\sigma}_{\ \mu\nu\rho} = \frac{1}{2} \left(\partial_\nu \partial_\mu h^{\sigma}_{\ \rho} + \partial_\rho \partial^\sigma h_{\mu\nu} - \partial_\nu \partial^\sigma h_{\mu\rho} - \partial_\rho \partial_\mu h^{\sigma}_{\ \nu} \right) , \tag{2.5}$$

$$R_{\mu\nu} = \frac{1}{2} \partial_\nu \partial_\mu h + \Box h_{\mu\nu} - \partial_\nu \partial_\rho h^{\rho}_{\ \mu} - \partial_\rho \partial_\mu h^{\rho}_{\ \nu} , \tag{2.6}$$

$$R = \Box h - \partial_\rho \partial_\mu h^{\mu\rho} , \tag{2.7}$$

where $\Box = \partial^\mu \partial_\mu$ is the d'Alembert operator and $h = h^\mu_\mu$ is the trace of $h_{\mu\nu}$. Therefore, Einstein field equations become

$$\partial_\nu \partial_\mu h + \Box h_{\mu\nu} - \partial_\nu \partial_\rho h^{\rho}_{\ \mu} - \partial_\rho \partial_\mu h^{\rho}_{\ \nu} - \eta_{\mu\nu} \left(\Box^2 h - \partial_\rho \partial_\sigma h^{\sigma\rho} \right) = -2\kappa T_{\mu\nu} , \tag{2.8}$$

To simplify this expression, define $\bar{h}_{\mu\nu} \equiv h_{\mu\nu} - \frac{1}{2} \eta_{\mu\nu} h$, so that

$$\Box \bar{h}_{\mu\nu} + \eta_{\mu\nu} \partial_\sigma \partial_\rho \bar{h}^{\rho\sigma} - \partial_\nu \partial_\rho \bar{h}^{\rho}_{\ \mu} - \partial_\rho \partial_\mu \bar{h}^{\rho}_{\ \nu} = -2\kappa T_{\mu\nu} . \tag{2.9}$$

This equation can be simplified further by noting that we can choose work in a particular gauge in order to reduce the degrees of freedom. Imposing the (Lorentz) gauge condition $\partial_\mu \bar{h}^{\mu\nu} = 0$, we see equation (2.9) reduces to

$$\Box \bar{h}^{\mu\nu} = -2\kappa T^{\mu\nu} . \tag{2.10}$$

We can reduce the number of components of $\bar{h}_{\mu\nu}$ by also working in the transverse-traceless gauge, such that $\bar{h}^{0i} = 0$ and $\bar{h}^{i}_{\ i} = 0$. Applying the Lorentz gauge and noting $\bar{h}_{\mu\nu} = h_{\mu\nu}$, for a gravitational wave propagating in the x^3-direction, this gauge simplifies $h_{\mu\nu}$ to

$$h_{\mu\nu} = \begin{pmatrix} 0 & 0 & 0 & 0 \\ 0 & h_+ & h_\times & 0 \\ 0 & h_\times & -h_+ & 0 \\ 0 & 0 & 0 & 0 \end{pmatrix} , \tag{2.11}$$

where $h_+ := h_{11} = -h_{22}$ and $h_\times := h_{12} = h_{21}$ represent the two remaining independent components. These components are the polarizations of the gravitational wave and describe how the particles are influenced by an incoming wave, which we discuss in the next section.

Properties of Gravitational Waves

We note that the linearized field equations are exactly the wave equation with a source term. Because we have the wave equation, and general solution can be written as a superposition of $\bar{h}^{\mu\nu} = A^{\mu\nu}e^{ik_\rho x^\rho}$, where k_ρ are the elements of the wavevector. Inserting this general expression for $\bar{h}^{\mu\nu}$ into the Lorentz gauge condition, we find that we can constrain the tensor coefficients by $A^{\mu\nu}k_\mu = 0$.

We are now in a position to understand how a gravitational wave affects test particles. Let us consider a multi-particle system. For two particles, we can represent their separation vector as $\vec{\zeta} = \zeta(\sin\theta\cos\phi\hat{e}_1 + \sin\theta\sin\phi\hat{e}_2 + \cos\theta\hat{e}_3)$, with their relative acceleration given by $a_i = -R_{0i0j}\zeta^j$. Upon computation of the Riemann tensor, we find [60]

$$\begin{aligned} a_1 &= \frac{1}{2}\ddot{h}_+\zeta\sin\theta\cos\phi + \frac{1}{2}\ddot{h}_\times\zeta\sin\theta\sin\phi\,, \\ a_2 &= -\frac{1}{2}\ddot{h}_+\zeta\sin\theta\sin\phi + \frac{1}{2}\ddot{h}_\times\zeta\sin\theta\cos\phi\,, \end{aligned} \tag{2.12}$$

and $a_3 = 0$. This is a general effect due to gravitational waves; there is no acceleration of particles in the direction of propagation. To understand the evolution of this separation vector, let us project the acceleration a_i along $\vec{\zeta}/\zeta$. In doing so, $\ddot{\zeta} \equiv \zeta^i a_i/\zeta = -\frac{1}{\zeta}R_{0i0j}\zeta^i\zeta^j$, such that integration yields [60]

$$\zeta(t) = \zeta(0)\left(1 + \frac{1}{2}h_+\sin^2\theta\cos 2\phi + \frac{1}{2}h_\times\sin^2\theta\sin 2\phi\right)\,. \tag{2.13}$$

This demonstrates that the a gravitational wave causes the separation between two particles to oscillate.

By using the relative acceleration of the particles in (2.12) and integrating twice, we can determine the motion of the individual particles in a multi-particle system. In Figure 2.1, we illustrate the effect of a gravitational wave polarization for two cases

(a) Plus-polarized gravitational waves: $h_+ = \epsilon\cos\omega t$, $h_\times = 0$

(b) Cross-polarized gravitational waves: $h_+ = 0$, $h_\times = \epsilon\cos\omega t$

For illustrative purposes, we consider unit frequency and set $\epsilon = 1$. In reality, the amplitude of gravitational waves correspond to $\epsilon \ll 1$ and their effect is to distort the distances between objects.[1]

2.1.2 Sources and Detection of Gravitational Waves

We have derived the linearized field equations and investigated some of the physical properties of gravitational waves. Let us now consider what produces gravitational waves.

As equation (2.10) is the wave equation, the general solution is

$$\bar{h}^{\mu\nu} = -\frac{4G}{c^4}\int\frac{T^{\mu\nu}(ct - |\vec{x} - \vec{x}'|, \vec{x}')}{|\vec{x} - \vec{x}'|}d^3\vec{x}' \tag{2.14}$$

[1] We also note that working with $\epsilon = 1$ violates linear perturbation theory, though the expansion and contraction features in Figure 2.1 will also be present in the $\epsilon \ll 1$, though on a greatly reduced (and therefore, more accurate) scale.

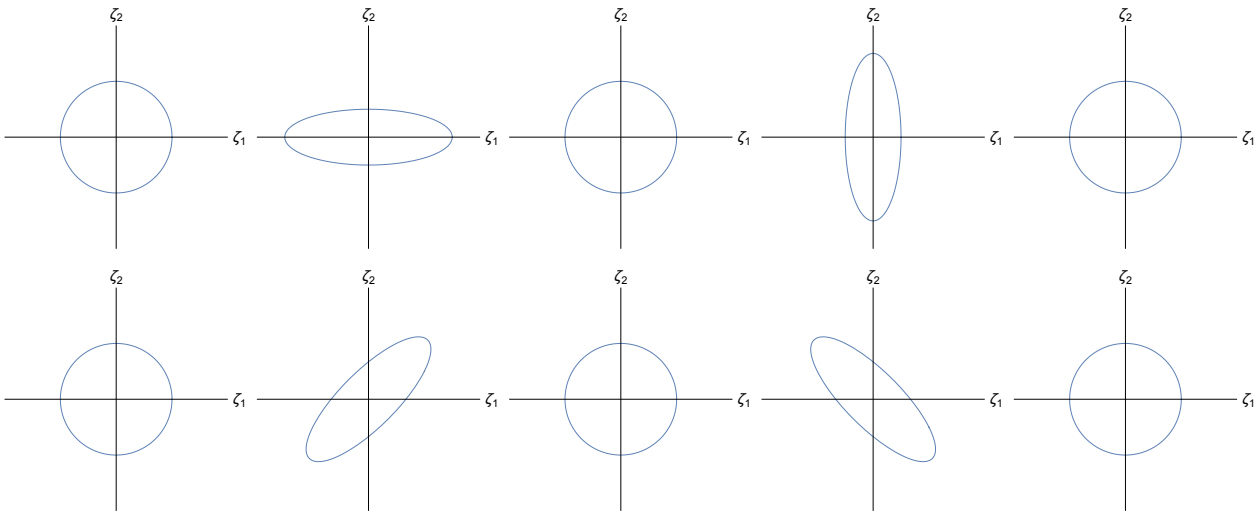

(a) $T = 0$ (b) $T = \pi/2$ (c) $T = \pi$ (d) $T = 3\pi/2$ (e) $T = 2\pi$

Figure 2.1: The effect of on a multiparticle system by a gravitational wave, with the first line showing plus polarization and the second line showing cross polarization.

Let us assume that the size of the source is much smaller than the distance to Earth, so that $|\vec{x} - \vec{x}'| \approx r$ is approximately a constant. By using identities of the stress-energy tensor, applying Gauss' theorem and assuming that the stress-energy tensor vanishes at the boundary, we find [60]

$$\bar{h}^{ij}(ct, \vec{x}) = -\frac{2G}{c^6 r}\left[\frac{d^2 I^{ij}(ct')}{dt'^2}\right]_{t'=t-r/c} \tag{2.15}$$

where

$$I^{ij} = \int T^{00}(ct, \vec{y}) y^i y^j d^3\vec{y} \tag{2.16}$$

is the quadrupole tensor. Therefore, for gravitational waves to be produced by non-relativistic compact sources, we require the second derivative of this tensor to be non-vanishing.

For a binary system, general relativity predicts that gravitational waves dissipate energy of the system, such that the orbital period changes at the rate [60]

$$\frac{dP}{dt} = -\frac{192\pi}{5}\frac{m_1 m_2}{(m_1+m_2)^2}\left(\frac{2\pi G(m_1+m_2)}{c^3 P}\right)^{5/3}\left(\frac{1+\frac{72}{24}e^2+\frac{39}{96}e^4}{(1-e^2)^{7/2}}\right), \tag{2.17}$$

where P is the period, m_i are the masses of the objects, and e is the eccentricity of the orbit. Observations of the binary pulsar PSR B1913+16 over several years noted that the period decayed with this relation, thereby providing the first indirect evidence demonstrating the existence of gravitational waves [251, 252].

The direct detection of gravitational waves requires different approaches that depend on the frequency regime of interest. There are many different sources which could be observed. In the following subsections, we briefly discuss some of the main sources that might be observed in various frequency regimes.

We emphasize that the frequencies of the emitted gravitational waves are highly-dependent on the motion, mass and type of source. For instance, in the case of a circular orbit of inspiralling

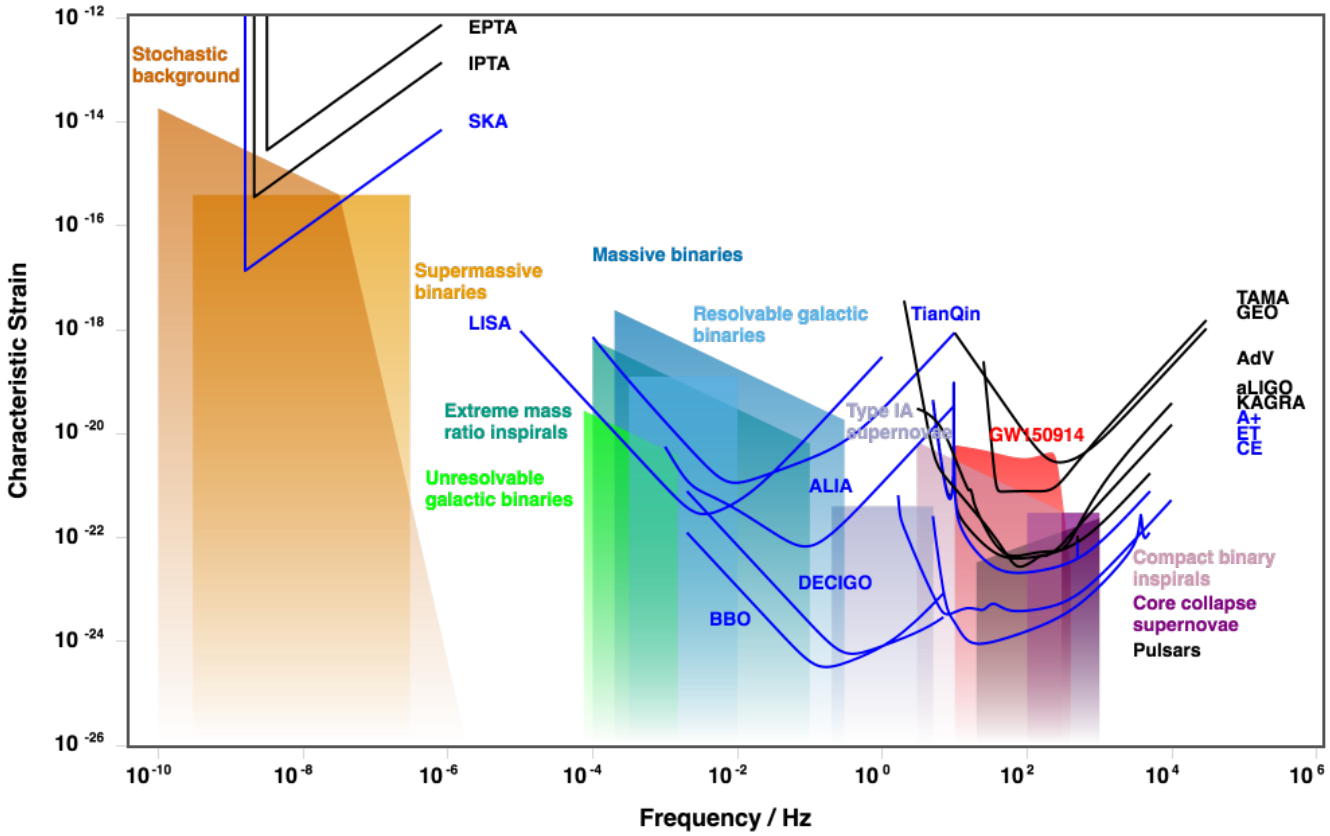

Figure 2.2: Different sources of gravitational waves and different gravitational wave detectors in operation (black), or planned/under construction (blue). We see that much effort has been exerted in designing detectors to investigate gravitational wave sources below 1000 Hz. The plot was produced using the online applet, www.gwplotter.com [159].

compact binaries [139],

$$f_{GW} = \frac{1}{\pi}\left(\frac{5}{256}\frac{1}{\tau}\right)^{3/8}\left(\frac{GM_c}{c^3}\right)^{3/8} = 134\text{ Hz}\left(\frac{1.21M_\odot}{M_c}\right)^{5/8}\left(\frac{1\text{ s}}{\tau}\right)^{3/8}, \tag{2.18}$$

where τ is the time to coalescence, and

$$M_c = \frac{(m_1 m_2)^{3/5}}{(m_1+m_2)^{1/5}} \tag{2.19}$$

is known as the chirp mass, with $m_{1,2}$ being the individual masses of the inspiralling objects. We see that for larger masses, the gravitational wave frequency is smaller. If we had two stellar mass black holes of mass $M_\odot$ and $\tau = 1$ s, this corresponds to a gravitational wave frequency of ~ 164 Hz. However, if the black holes were both $10^9 M_\odot$ with the same τ, the gravitational wave frequency would be ~ 0.4 mHz. As see in Figure 2.2, these frequencies are approximately what would be expected for gravitational wave emission from compact binary inspirals and massive binaries.

Nanohertz-microhertz gravitational waves

At the lower end of this frequency range, it may be possible to observe a stochastic background of gravitational waves due to supermassive black hole binaries. At slightly higher frequencies, such

binaries could be resolved as there would be fewer in each individual frequency bin [158].

Microhertz-Hertz gravitational waves

In the microhertz frequency range, even more sources may be observed, such as extreme-mass inspirals, in which a stellar-mass object merges with a supermassive black hole. In theory, this can occur for a black hole of any mass, so in principle, could be observed over a wide range of frequencies. It is also possible to observe binary inspirals of massive black holes ($10^4 M_\odot - 10^7 M_\odot$), with frequencies of $3 \times 10^{-4} - 3 \times 10^{-1}$ Hz [158]. Another possible source in the millihertz regime is the presence of white dwarf binaries [134, 162].

Hertz-kilohertz gravitational waves

In this frequency regime, we can see stellar-mass binary black hole mergers [2], binary neutron star mergers [4], and black hole-neutron star mergers [5]. Such mergers have frequencies on the order of hundreds of Hertz, though could extend into the kilohertz regime for sufficiently small objects [17, 18]. Core collapse supernovae would be able to produce frequencies between 100 Hz and 1000 Hz. Gravitational waves could also be produced by axially asymmetric rotating neutron stars. Such sources are also on the order of hundreds of Hertz, but could similarly extend into the kilohertz regime [158].

Gravitational waves with frequencies greater than a kilohertz

Above a kHz, it may be possible to observe creation of magnetars (frequencies of 500-2000 Hz) [226]. It may also be possible to detect primordial black holes [84], axion clouds around black holes [258], and signatures of inflation [60]. However, we note that for these sources, the frequency regime is model-dependent, so such sources may also be present at lower frequencies.

2.1.3 Direct Detection of Gravitational Waves

As we saw in equation (2.13), the distance between two particles oscillates in the presence of a gravitational wave. Suppose that an interferometer has arms of length ℓ_0 and a gravitational wave causes the arms to change by a length $\delta\ell$. To detect gravitational waves, we are required to resolve the fractional change $\frac{\delta\ell}{\ell_0}$ on the order of the amplitude of the gravitational wave. In practice, if we have a kilometer-sized interferometer, it is necessary to be sensitivity to changes in length on the order of the size of proton. Such a sensitivity can be achieved by using a Michelson interferometer (or more specifically, a Fabry-Perot interferometer). By using such a construction, the Laser Interferometer Gravitational-Wave Observatory (LIGO) was able to detect gravitational waves in 2015 by following these rough steps [2]:

1. Light is emitted from a laser source and travels towards a beam splitter
2. At the beam splitter, the laser is split into two beams and travels 4km down each of the interferometer arms

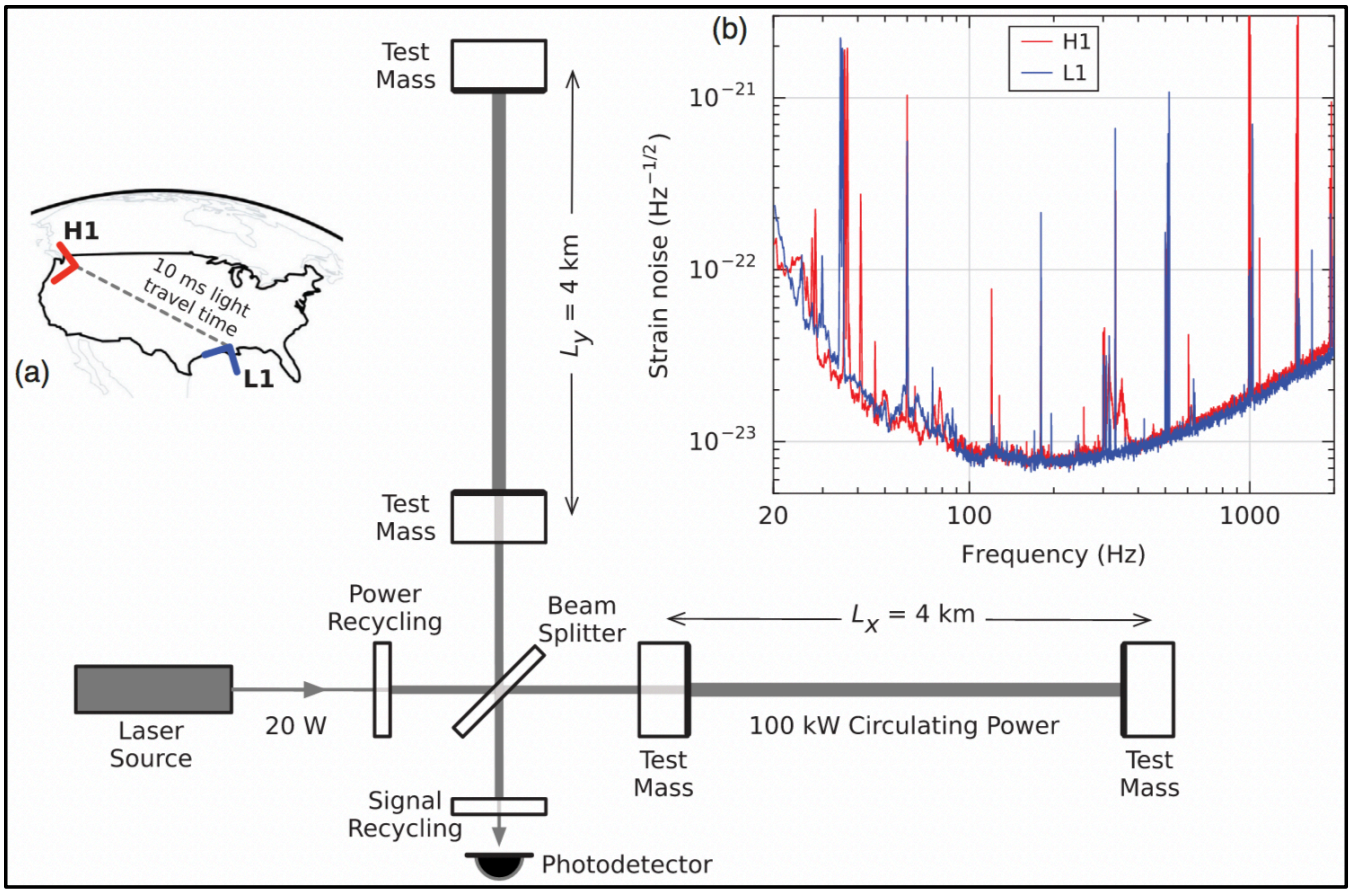

Figure 2.3: A simplified diagram of the Laser Interferometer Gravitational-Wave Observatory (LIGO). We see that the setup is similar in nature of a Michelson interferometer. In inset (a), the detector locations are shown. In inset (b), we see an overlap of the strain sensitivities of the Hanford detector (H1) and the Livingston detector (L1). Image is reproduced from [2], available under the terms of the Creative Commons Attribution 3.0 License.

3. Each test mass is a giant mirror. The laser beams bounce off the mirrors at the end of the arms and, instead of recombining at the beam splitters, bounce off a second set of mirrors to travel back towards the end of the arms.

4. The laser beams each travel approximately 1120 km in total before recombining at the beam splitter

5. The signal from the laser is then measured at the photodetector.

LIGO is constructed in a way so that if there is no gravitational wave present, upon recombination at the beam splitter, there will be destructive interference at the photodetector so that no signal is measured. If there is a gravitational wave present, the length of the arms will slightly change so that an overall phase shift in the beams will be detected at the photodetector, thereby indicating the presence of gravitational waves. In reality, there are several noise sources that causes LIGO to be most sensitive to gravitational waves between approximately 100-300 Hz, including: [57, 149]

- Seismic noise from ground vibrations such as earthquakes or the movements of vehicles
- Newtonian noise, such as the fluctuations in the gravitational field

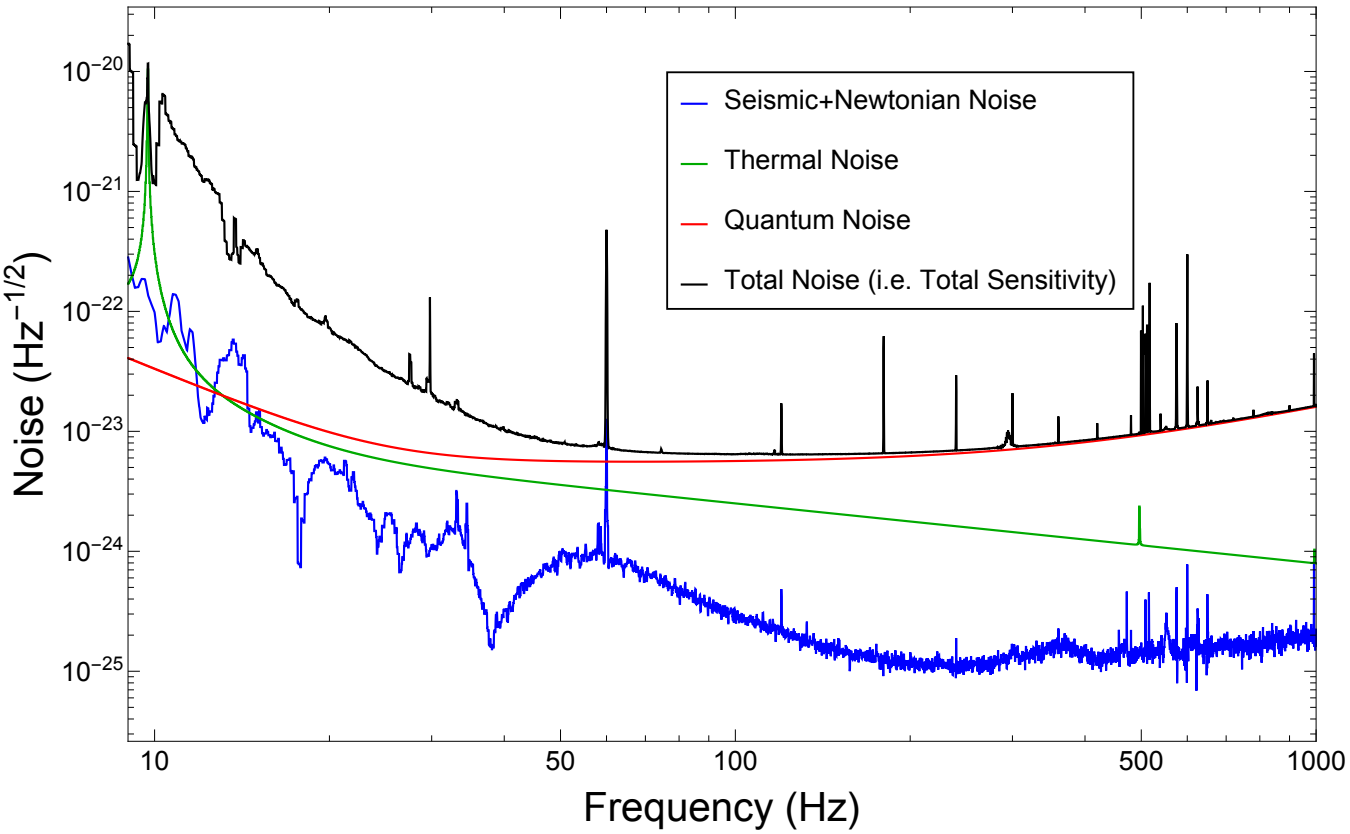

Figure 2.4: Three of the major sources of noise in LIGO. In black, we show the observed noise. For simplicity, we do not include subdominant noises, such as the noise from the residual gases in the interferometric arms. Data was obtained from the authors of [149].

- Thermal noise in the mirrors
- Thermal noise in the suspension system holding the mirrors in place
- Quantum noise from fluctuations in photon counts at the photodetector (shot noise) and radiation pressure from the photons on the mirrors

In Figure 2.4, we show the effects of each source of noise as well as the overall sensitivity of LIGO. We see that thermal noise from the suspension system, seismic noise, and Newtonian noise (such as gravitational gradients) limits sensitivity at lower frequencies, while sensitivity at higher frequencies is dominated by the quantum noise (radiation pressure and shot noise).

Returning to Figure 2.2, we also show several current and proposed gravitational wave experiments. The black curves indicate experiments currently in operation, while the blue curves represent experiments either under construction or proposed. We note that even for terrestrial interferometers which could detect gravitational waves into the kHz regime, their sensitivities are still optimized at roughly the same frequency as LIGO (see Figure 2.2). This raises the question of if and how one can design a gravitational wave detector whose sensitivity is optimized in the kHz frequency range. One way to do this may be by using a gas of cold atoms called a Bose-Einstein Condensate (BEC), which we shall discuss in Chapters 3 and 4.

LIGO has been an extraordinary achievement of technological development and implementation, which took decades to achieve. However, LIGO is only sensitive to a small part of the gravitational

wave frequency spectrum, seeing gravitational waves above its detector noise limit. One proposed gravitational wave detector that could push down this limit is the Einstein Telescope, which is designed to be composed of three 10 km long arms in a triangle, and will be most sensitive to gravitational waves of frequencies between 1 Hz up to 10 kHz [140]. Another proposed detector, Cosmic Explorer, is designed to probe a similar frequency range as Einstein Telescope, with sensitivities between 5 Hz and 4 kHz. Similar to LIGO, Cosmic Explorer will also be L-shaped, like LIGO, though the arms will be ten times longer [192]. Einstein Telescope and Cosmic Explorer will thus be able to see similar sources as LIGO, but may also be able to observe (or exclude) more exotic sources, such as dark matter, primordial black hole mergers, and the nature of dark energy [140, 192].

To detect nanohertz gravitational waves, pulsar timing arrays are being used (such as the European Pulsar Timing Array, which is part of the broader International Pulsar Timing array consortium, and the proposed Square Kilometer Array). Millisecond pulsars are some of the most precise clocks in the universe and tick with a regular frequency. If a gravitational wave passes by, the frequency will be affected. [60, 158]. Recently, the North American Nanohertz Observatory for Gravitational Wave (NANOgrav) has detected a signal that may be indicative of a low-frequency gravitational wave, though more work is required to ascertain whether this signal is from an astrophysical gravitational wave background [21].

In the next couple of decades, space-based interferometers are due to be launched, most notably the Laser Interferometer Space Antenna (LISA). Consisting of three spacecraft each separated by 2.5 million km in the shape of a triangle, LISA will be sensitive to gravitational waves between 3 mHz and 500 mHz originating from sources that could later be observed by LIGO (the early evolution of inspiralling black holes and neutron stars), as well as sources invisible to terrestrial gravitational wave detectors, such as extreme mass ratio inspirals [15].

Beyond pulsar timing arrays, space-based interferometers, and terrestrial interferometers, other forms of gravitational wave detectors have been proposed (and in some cases, constructed), such as resonant mass antennas [8], atom interferometers [88], superfluid helium [217, 241], and Bose-Einstein Condensates [196, 199].

2.2 Quantum Field Theory in Curved Spacetime

To detect gravitational waves with Bose-Einstein condensates, we need to make use of techniques of quantum field theory in curved spacetime. In this section, we will follow the treatment and discussion in [34] to demonstrate how to obtain Bogoliubov coefficients. These coefficients describe how to convert between different mode expansions in curved spacetime.

Let us first consider the flat spacetime case. The equations of motion of a scalar field can be derived from the Lagrangian, $\mathcal{L} = \frac{1}{2}\left(\eta^{\mu\nu}\partial_\mu\phi\partial_\nu\phi - m^2\phi^2\right)$, giving

$$\left[\Box + m^2\right]\phi = 0 \ , \tag{2.20}$$

where $\Box = \partial^\mu\partial_\mu = \frac{\partial^2}{\partial t^2} - \nabla^2$ is the d'Alembert operator. The solutions to this equation can be expanded in a set of modes $\{u_{\vec{k}}\}$ of the form

$$u_{\vec{k}} \propto e^{i\vec{k}\cdot\vec{x} - i\omega t} \ , \tag{2.21}$$

with $\vec{k}$ the wavevector and $\omega = \sqrt{k^2 + m^2}$. With the scalar product,

$$(\phi_1, \phi_2) = -i \int_t \{\phi_1 \partial_t \phi_2^* - \phi_2^* \partial_t \phi_1\} \, d^3\vec{x} \,, \tag{2.22}$$

where we evaluate on a spacelike hyperplane and at an instant t, we see that the modes obey orthonormality: $(u_{\vec{k}}, u_{\vec{k}'}) = \delta_{\vec{k}\vec{k}'}$.

Let us now quantize this system, so that ϕ obeys the commutation relations,

$$[\phi(t, \vec{x}), \phi(t, \vec{x}')] = 0 \,, \tag{2.23}$$
$$[\pi(t, \vec{x}), \pi(t, \vec{x}')] = 0 \,, \tag{2.24}$$
$$[\phi(t, \vec{x}), \pi(t, \vec{x}')] = i\delta^3(\vec{x} - \vec{x}') \,, \tag{2.25}$$

where we also use the conjugate momentum, π, defined as

$$\pi = \frac{\partial \mathcal{L}}{\partial(\partial_t \phi)} \,. \tag{2.26}$$

As a field, ϕ can be expressed as a sum of our modes $\{u_{\vec{k}}\}$ as well as creation ($a_{\vec{k}}$) and annihilation operators ($a^\dagger_{\vec{k}}$),

$$\phi = \sum_{\vec{k}} \left[\hat{a}_{\vec{k}} u_{\vec{k}} + \hat{a}^\dagger_{\vec{k}} u^*_{\vec{k}} \right] \,. \tag{2.27}$$

Therefore, the annihilation and creation operators obey the commutation relations,

$$[\hat{a}_{\vec{k}}, \hat{a}_{\vec{k}'}] = 0 \,, \tag{2.28}$$
$$[\hat{a}^\dagger_{\vec{k}}, \hat{a}^\dagger_{\vec{k}'}] = 0 \,, \tag{2.29}$$
$$[\hat{a}_{\vec{k}}, \hat{a}^\dagger_{\vec{k}'}] = \delta_{\vec{k}\vec{k}'} \,, \tag{2.30}$$

To understand the effect of these operators, construct a Fock space of normalized basis vectors by first defining the vacuum state, $|0\rangle$, such that $\hat{a}_{\vec{k}} |0\rangle = 0$ for all $\vec{k}$. Operating on the vacuum state with the creation operator then yields $\hat{a}^\dagger_{\vec{k}} |0\rangle = |1_{\vec{k}}\rangle$, which describes a state with a single particle. Successive operations of the creation operator can then yield states with n particles of wavevector $\vec{k}$, $|n_{\vec{k}}\rangle$. By imposing the conditions $\langle n_{\vec{k}} | m_{\vec{k}'} \rangle = \delta_{n_{\vec{k}} m_{\vec{k}'}}$, we find that, in general,

$$\hat{a}^\dagger_{\vec{k}} |n_{\vec{k}}\rangle = \sqrt{n+1} \, |(n+1)_{\vec{k}}\rangle \,, \tag{2.31}$$
$$\hat{a}_{\vec{k}} |n_{\vec{k}}\rangle = \sqrt{n} \, |(n-1)_{\vec{k}}\rangle \,, \tag{2.32}$$

where $\hat{a}^\dagger_{\vec{k}} \hat{a}_{\vec{k}} |n_{\vec{k}}\rangle = n_{\vec{k}} |n_{\vec{k}}\rangle$ defines the number operator, with the number of particles in state $|n_{\vec{k}}\rangle$ as the eigenvalue.

From the Lagrangian, we can also calculate the Hamiltonian in terms of creation/annihilation operators by using the stress-energy tensor,

$$T_{\mu\nu} = \frac{2}{\sqrt{-g}} \frac{\delta S}{\delta g^{\mu\nu}} \tag{2.33}$$
$$= \partial_\mu \phi \partial_\nu \phi - \frac{1}{2} \eta_{\mu\nu} \partial^\alpha \phi \partial_\alpha \phi + \frac{1}{2} m^2 \phi^2 \eta_{\mu\nu} \,, \tag{2.34}$$

where the action $S = \int d^4x\sqrt{-g}\mathcal{L}$ and we have taken the metric tensor $g_{\mu\nu}$ to be the Minkowski tensor in flat spacetime. The energy density corresponds to T_{00}, so

$$T_{00} = \frac{1}{2}\left[\dot{\phi}^2 - \partial^i\phi\partial_i\phi + m^2\phi^2\right] . \tag{2.35}$$

By writing the field in terms of creation/annihilation operators, we can integrate T_{00} over a spatial hypersurface to find the Hamiltonian,

$$H = \frac{1}{2}\sum_{\vec{k}}\left(\hat{a}^\dagger_{\vec{k}}\hat{a}_{\vec{k}} + \hat{a}_{\vec{k}}\hat{a}^\dagger_{\vec{k}}\right)\omega\,. \tag{2.36}$$

In curved spacetime, the Lagrangian density takes the form

$$\mathcal{L} = \frac{1}{2}\sqrt{-g}\left[g^{\mu\nu}\partial_\mu\phi\partial_\nu\phi - m^2\phi^2\right] \ , \tag{2.37}$$

where we are assuming a minimally coupled scalar field The Euler-Lagrange equations similarly become

$$\left[\Box + m^2\right]\phi = 0\,, \tag{2.38}$$

though now $\Box = \nabla^\mu\nabla_\mu = \frac{1}{\sqrt{-g}}\partial_\mu\left[\sqrt{-g}g^{\mu\nu}\partial_\nu\right]$. Similar to flat spacetime, we can expand the field ϕ in terms of modes $\{u_{\vec{k}}\}$, such that

$$\phi = \sum_{\vec{k}}\left[\hat{a}_{\vec{k}}u_{\vec{k}} + \hat{a}^\dagger_{\vec{k}}u^*_{\vec{k}}\right] \tag{2.39}$$

with the same commutation relations of the creation/annihilation operators as for flat spacetime.

In Minkowski spacetime, there was a natural mode decomposition because there exists a timelike Killing vector $\frac{\partial}{\partial t}$, and the modes were eigenfunctions of the Killing vector, which then defined which modes have a positive frequency. There also existed a natural separation of spatial modes because Minkowski spacetime is invariant under the Poincaré group. When considering an arbitrary curved spacetime, the situation becomes much more complicated because such symmetries do not generally exist. As a result, unlike in Minkowski spacetime, there does not exist a preferred set of spatial modes that decouple, nor will it be possible to identify those with frequencies which are positive compared to those which are negative.

Therefore, as there exists no preferred set of modes, let us then expand the field in terms of a second set of modes, $\{\bar{u}_{\vec{k}}\}$, such that

$$\phi = \sum_{\vec{k}}\left[\hat{\bar{a}}_{\vec{k}}\bar{u}_{\vec{k}} + \hat{\bar{a}}^\dagger_{\vec{k}}\bar{u}^*_{\vec{k}}\right] . \tag{2.40}$$

where $\hat{\bar{a}}_{\vec{k}}, \hat{\bar{a}}^\dagger_{\vec{k}}$ are still annihilation/creation operators with the same relations as flat space, though operating on a different Fock space (denoted by a bar), such that $\hat{\bar{a}}_{\vec{k}}\left|\bar{0}\right\rangle = 0$. By generalizing the Klein-Gordon inner product to curved spacetime,

$$(\phi_1, \phi_2) = -i\int_\Sigma\left\{\phi_1\partial_\mu\phi_2^* - \phi_2^*\partial_\mu\phi_1\right\}\sqrt{-g}d\Sigma^\mu\,, \tag{2.41}$$

where $d\Sigma^\mu = \eta^\mu d\Sigma$ and η^μ is a future-directed unit vector that is orthogonal to the spacelike hypersurface Σ, we can find the relation between the modes $u_{\vec{k}}$ and $\bar{u}_{\vec{k}}$ with

$$\bar{u}_{\vec{k}} = \sum_{\vec{k}'} \left(\alpha_{\vec{k}\vec{k}'} u_{\vec{k}'} + \beta_{\vec{k}\vec{k}'} u^*_{\vec{k}'}\right) , \tag{2.42}$$

$$u_{\vec{k}} = \sum_{\vec{k}'} \left(\alpha^*_{\vec{k}\vec{k}'} \bar{u}_{\vec{k}} + \beta^*_{\vec{k}\vec{k}'} \bar{u}^*_{\vec{k}}\right) . \tag{2.43}$$

We can also relate the creation and annihilation operators as

$$\hat{a}_{\vec{k}'} = \sum_{\vec{k}} \left(\alpha_{\vec{k}\vec{k}'} \hat{\bar{a}}_{\vec{k}} + \beta^*_{\vec{k}\vec{k}'} \hat{\bar{a}}^\dagger_{\vec{k}}\right) , \tag{2.44}$$

$$\hat{\bar{a}}_{\vec{k}} = \sum_{\vec{k}'} \left(\alpha^*_{\vec{k}\vec{k}'} \hat{a}_{\vec{k}'} - \beta^*_{\vec{k}\vec{k}'} \hat{a}^\dagger_{\vec{k}}\right) . \tag{2.45}$$

Here, $\alpha_{\vec{k}\vec{k}'} = (\bar{u}_{\vec{k}}, u'_{\vec{k}})$, $\beta_{\vec{k}\vec{k}'} = -(\bar{u}_{\vec{k}}, u^*_{\vec{k}'})$ are called Bogoliubov coefficients and have the properties

$$\sum_{\vec{k}''} (\alpha_{\vec{k}\vec{k}''} \alpha^*_{\vec{k}'\vec{k}''} - \beta_{\vec{k}\vec{k}''} \beta^*_{\vec{k}'\vec{k}''}) = \delta_{\vec{k}\vec{k}'} \tag{2.46}$$

$$\sum_{\vec{k}''} (\alpha_{\vec{k}\vec{k}''} \beta^*_{\vec{k}'\vec{k}''} - \beta_{\vec{k}\vec{k}''} \alpha_{\vec{k}'\vec{k}''}) = 0 \tag{2.47}$$

We see that $\hat{a}_{\vec{k}} |\bar{0}\rangle = \sum_{\vec{k}'} \beta^*_{\vec{k}'\vec{k}} |\bar{1}_{\vec{k}}\rangle \neq 0$. We also note that $\langle\bar{0}| \hat{a}^\dagger_{\vec{k}} \hat{a}_{\vec{k}} |\bar{0}\rangle = \sum_{\vec{k}'} |\beta_{\vec{k}'\vec{k}}|^2$. Therefore, we can interpret the sum as the number of particles in the vacuum of the barred modes.

2.2.1 Quantum Fisher Information

A key question in gravitational wave detection is how to characterize how well various parameters associated with a gravitational wave signal can be measured. To do this, we can use a quantity known as the Fisher information [38]:

$$\mathcal{I}_\theta = \int d\lambda p(\lambda|\theta) \left(\frac{d \ln p(\lambda|\theta)}{d\theta}\right)^2 , \tag{2.48}$$

where θ is an unknown parameter that needs to be estimated from observations $\{\lambda\}$. The Cramer-Rao bound then gives the minimum variance of that parameter as [38] $\langle(\Delta\theta)^2\rangle \geq \frac{1}{M\mathcal{I}_\theta}$, where M is the number of measurements of θ.

Now let us suppose that θ is a parameter of a quantum system, but cannot be represented as an operator. In this case, we can still calculate the classical Fisher information: [38]

$$\mathcal{I}_\theta = \int d\lambda \frac{[Tr(\hat{E}(\lambda)\frac{d\hat{\rho}(\theta)}{d\theta}]^2}{Tr[\hat{E}(\lambda)\hat{\rho}(\theta)]} , \tag{2.49}$$

where $\hat{E}$ is a Hermitian operator describing a measurement with result λ, such that $\int d\lambda \hat{E}(\lambda) = I$ and $\hat{\rho}$ is the density operator that depends on the parameter of interest, θ, with the probability

density of observation λ given parameter θ being $p(\lambda|\theta) = Tr\left[\hat{E}(\lambda)\hat{\rho}(\theta)\right]$. To obtain the *quantum* Fisher information, optimize over all possible measurements $\{\hat{E}(\lambda)\}$, so that [38]

$$H_\theta = \max_{\{\hat{E}(\lambda)\}} \mathcal{I}_\theta \tag{2.50}$$

Physically, the quantum Fisher information describes the amount of information that can be obtained about θ for a single measurement of the system. For M measurements, [10, 38]

$$\langle(\Delta\theta)^2\rangle \geq \frac{1}{M\mathcal{I}_\theta} \geq \frac{1}{MH_\theta}\,. \tag{2.51}$$

The quantum Fisher information can also be expressed as [10]

$$H_\theta = \frac{8(1-\sqrt{F(\rho_\theta, \rho_{\theta+d\theta})})}{d\theta^2}\,, \tag{2.52}$$

where $F(\rho_1, \rho_2) = (Tr\sqrt{\sqrt{\rho_1}\rho_2\sqrt{\rho_1}})^2$ is the fidelity, which describes the overlap between states ρ_1 and ρ_2 and is symmetric between ρ_1 and ρ_2 [168].

For Gaussian states, it can be easier to use covariance matrices, rather than density matrices. In general, for a system of bosons with n modes, we can use the results of the previous section to define the conjugate position $\hat{q}_k$ and conjugate momentum $\hat{p}_k$ with the creation/annihilation operators:

$$\hat{q}_k = \frac{1}{\sqrt{2}}\left(\hat{a}_k + \hat{a}_k^\dagger\right)\,, \tag{2.53}$$

$$\hat{p}_k = \frac{1}{\sqrt{2}i}\left(\hat{a}_k - \hat{a}_k^\dagger\right)\,, \tag{2.54}$$

with the commutation relation $[\hat{q}_j, \hat{p}_k] = \frac{i}{2}\delta_{jk}$ and $j, k = 1, \cdots, n$. Let us define a vector $R = (\hat{q}_1, \hat{p}_1, \cdots, \hat{q}_n, \hat{p}_n)^T$. Therefore, the bosonic commutation relation become [75]

$$[R_j, R_k] = i\Omega_{jk}\,, \tag{2.55}$$

where

$$\Omega = \bigoplus_{k=1}^{n} \begin{pmatrix} 0 & 1 \\ -1 & 0 \end{pmatrix}\,. \tag{2.56}$$

Let $\{A, B\}$ be the anti-commutator between operators A and B and let $\langle A\rangle = Tr(\rho A)$ be the expectation value of A for the density matrix ρ. We can then define a covariance matrix with elements

$$\sigma_{kl} = \langle\{R_k, R_l\}\rangle - 2\langle R_k\rangle\langle R_l\rangle\,, \tag{2.57}$$

where we are using the normalization condition[2] of [10]. For simplicity, we will consider $n = 1$ and let us assume that the first moments of the Gaussian states are zero (i.e. $\langle q\rangle = 0$). Therefore, the

[2] Ref. [143] uses an alternative definition for a covariance matrix, which is labelled as $\mathcal{V}$, with matrix elements (see also [75])

$$\mathcal{V}_{jk} = \frac{1}{2}\langle\{S_j, S_k\}\rangle - \langle S_l\rangle\langle S_k\rangle\,,$$

where $S = (\hat{q}_1, \cdots, \hat{q}_n, \hat{p}_1, \cdots, \hat{p}_n)^T$

fidelity of a single-mode quantum system is [10, 143]

$$F(\sigma_A, \sigma_B) = \frac{1}{\sqrt{\Lambda + \Delta} - \sqrt{\Lambda}}\,, \tag{2.58}$$

where

$$\Delta = \frac{1}{4}\det[\sigma_A + \sigma_B]\,, \tag{2.59a}$$

$$\Lambda = \frac{1}{4}\det\left[\sigma_A + \frac{i}{2}\Omega\right]\det\left[\sigma_B + \frac{i}{2}\Omega\right]\,, \tag{2.59b}$$

and $\sigma_{A,B}$ are covariance matrices. We will show later in this thesis that the key to determining the sensitivity in detecting gravitational waves with Bose-Einstein condensates is using the quantum Fisher information.

2.2.2 Squeezing

Key to LIGO and potentially crucial to using Bose-Einstein condensates to detect gravitational waves is using squeezed states. For two Hermitian operators $\hat{X}_1$ and $\hat{X}_2$ obeying the commutation relation $[\hat{X}_1, \hat{X}_2] = i\hat{C}$, where $\hat{C}$ is (in general) an operator, we know that they obey the uncertainty relation $(\Delta\hat{X}_1)^2(\Delta\hat{X}_2)^2 \geq \frac{1}{4}|\langle\hat{C}\rangle|^2$. However, in an experiment, sometimes only the uncertainties in one of the operators $\hat{X}_1$ or $\hat{X}_2$ might matter. In that case, it is beneficial to decrease the uncertainty in one of the operators, while increasing the uncertainty in the other operator. This process is known as squeezing [89].

Let us assume $\hat{C} = 1/2$ and suppose that we write our operators $\hat{X}_1$ and $\hat{X}_2$ in terms of a pair of creation/annihilation operators, such that such that $\hat{a} = \frac{\hat{X}_1 + i\hat{X}_2}{2}$ and $\hat{a}^\dagger = \frac{\hat{X}_1 - i\hat{X}_2}{2}$. We can generate a squeezed quantum state by considering the squeezing operator, [89]

$$\hat{S}(r) = e^{\zeta^*\hat{a}^2 - \zeta\hat{a}^{\dagger 2}}\,, \tag{2.60}$$

where $\zeta = re^{i\phi}$, r describes the amount of squeezing and ϕ is a phase. A squeezed vacuum state can be generated by calculating $\hat{S}(r)|0\rangle$. Applied to creation/annihilation operators, we see [89]

$$\hat{S}^\dagger\hat{a}\hat{S} = a\cosh r - \hat{a}^\dagger e^{i\phi}\sinh r \tag{2.61}$$

$$\hat{S}^\dagger\hat{a}^\dagger\hat{S} = \hat{a}^\dagger\cosh r - \hat{a}e^{-i\phi}\sinh r\,. \tag{2.62}$$

Therefore [89],

$$(\Delta\hat{X}_1)^2 = \frac{1}{4}\left[\cosh^2 r + \sinh^2 r - 2\sinh r\cosh r\cos\phi\right]\,, \tag{2.63}$$

$$(\Delta\hat{X}_2)^2 = \frac{1}{4}\left[\cosh^2 r + \sinh^2 r + 2\sinh r\cosh r\cos\phi\right]\,, \tag{2.64}$$

By varying ϕ, we can choose whether we want to squeeze $\hat{X}_1$ or $\hat{X}_2$.

In terms of covariance matrices, we will outline the treatment of [75]. A density operator is squeezed with $\hat{\rho}_{squeezed} = S\hat{\rho}S^\dagger$. Therefore, we can represent a squeezed state of a single mode

as $\sigma(r)_{squeezed} = \Sigma_\zeta \sigma(0) \Sigma_\zeta^T$, where $\sigma(r)$ is the squeezed covariance matrix, $\sigma(0)$ is the unsqueezed matrix, and

$$\Sigma_\zeta = \begin{pmatrix} \cosh r + \cos\phi \sinh r & \sin\phi \sinh r \\ \sin\phi \sinh r & \cosh r - \cos\phi \sinh r \end{pmatrix} . \tag{2.65}$$

Let us consider a single-mode vacuum state of bosons in thermal equilibrium, whose density matrix is

$$\hat{\rho} = \frac{e^{-\beta \hat{H}}}{Tr(e^{-\beta \hat{H}})} = \frac{e^{-\beta \hat{a}_k^\dagger \hat{a}_k}}{Tr(e^{-\beta \hat{a}_k^\dagger \hat{a}_k})} = \frac{1}{1+N} \sum_{m=0}^{\infty} \left(\frac{N}{1+N} \right)^m |m\rangle \langle m| , \tag{2.66}$$

where $N = \frac{1}{e^\beta - 1}$ is the average number number of particles in the mode. The covariance matrix corresponding to this state is

$$\sigma(0) = \frac{1}{2} \begin{pmatrix} 2N+1 & 0 \\ 0 & 2N+1 \end{pmatrix} . \tag{2.67}$$

Squeezing this covariance matrix (assuming that the displacement is zero), we obtain

$$\sigma = \frac{2N+1}{2} \begin{pmatrix} \cosh(2r) + \cos(\phi) \sinh(2r) & -\sin(\phi) \sinh(2r) \\ -\sin(\phi) \sinh(2r) & \cosh(2r) - \cos(\phi) \sinh(2r) \end{pmatrix} . \tag{2.68}$$

By squeezing the light in LIGO, the photon shot noise can be reduced, thereby improving its sensitivity to the gravitational wave strain. [1,237]. As we will show in this thesis, by using squeezed states (of phonons), the sensitivity of a Bose-Einstein condensate to gravitational waves might also conceivably be increased.

2.3 Bose-Einstein Condensates

2.3.1 Ideal Gas

Let us consider a thermal state of an ideal gas of non-interacting bosons, each with energy ϵ_i. Then, the total number of particles is given by a Bose-Einstein distribution [85],

$$N = \sum_i \frac{1}{e^{(\epsilon_i - \mu)/(k_B T)} - 1} , \tag{2.69}$$

where k_B is Boltzmann's constant, T is the temperature, and μ is the chemical potential, which describes the amount of energy necessary to add an additional particle to the system.

For simplicity, suppose that this gas is confined to a box with side length L. We will show that below a critical temperature, all the bosons in this box collapse condense into a single state by outlining the treatment in [85, 204]. The density of states of this gas is then given by $g(\epsilon) = \frac{2\pi L^3 (2m)^{3/2} \sqrt{\epsilon}}{h^3}$, where h is Planck's constant. In the case that we can treat the ideal gas as having a continuum of states, then the number of particles in the box is

$$N = \int_{\epsilon_0}^{\infty} \frac{g(\epsilon)}{e^{(\epsilon - \mu)/k_B T}} d\epsilon , \tag{2.70}$$

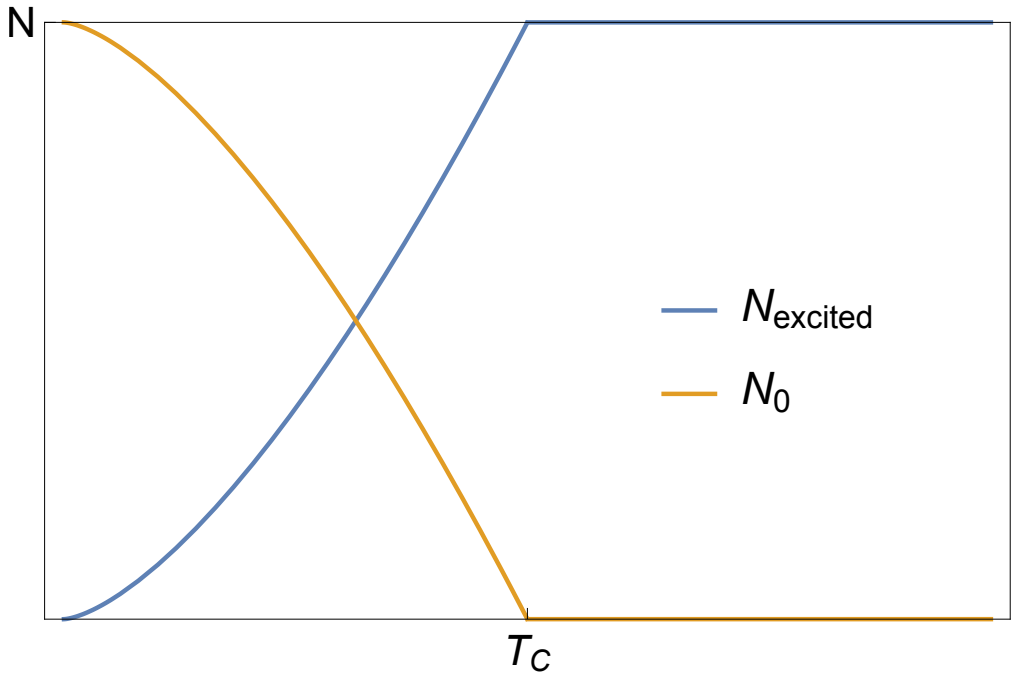

Figure 2.5: Number of particles in an excited state compared to the number of particles in the BEC.

where $\mu < \epsilon_0$. For an ideal gas in a box, this corresponds to $\epsilon_0 = 0$. When $\mu \to \epsilon_0$, an interesting phenomenon occurs. Upon carrying out the integral, we obtain

$$N = \zeta\left(\frac{3}{2}\right)\left(\frac{2\pi m k_B T}{\hbar^2}\right)^{3/2} L^3 \,, \tag{2.71}$$

where $\zeta(s)$ is the Riemann zeta function. Solving for T, there exists a critical temperature,

$$T_C = \left(\frac{N}{L^3\zeta(3/2)}\right)^{2/3} \frac{\hbar^2}{2\pi m k_B} \,, \tag{2.72}$$

in which above this temperature, all bosons are in a thermal cloud. At this temperature and below, the bosons all begin condensing into the ground state, such that the number of bosons in an excited state is given by (2.71). Noting that we can write

$$N_{excited} = \left(\frac{T}{T_C}\right)^{3/2} N \tag{2.73}$$

for temperatures $T < T_C$, we see that when $T = 0$, all particles will be in the ground state, with the number of particles in the ground state given by $N_0 = N - N_{excited}$ (Figure 2.5). This condensation of particles into the ground state is called a Bose-Einstein condensate.

We emphasize that the standard results above are for an ideal gas of bosons in a box. If the particles are in a non-zero potential, then Bose-Einstein condensation can still occur, though the critical temperature and density of states will change [85].

2.3.2 Weakly Interacting Particles

Let us now consider a gas of interacting ultracold bosons by considering the treatment in [95]. The Schrodinger equation takes the form

$$i\hbar\frac{\partial\Phi(\vec{r},t)}{\partial t} = \left[-\frac{\hbar^2\nabla^2}{2m} + V_{trap}(\vec{r}) + V_H(\vec{r},t)\right]\Phi(\vec{r},t) \tag{2.74}$$

where $\Phi(\vec{r},t)$ is the wavefunction of the condensate, V_{trap} is the trapping potential, and $V_H = g|\Phi|^2$ describes the interaction between the bosons, with g the interaction strength. We are implicitly assuming that the atoms are at $T = 0$, so all atoms are part of the condensate. For non-zero temperatures, the Schrodinger equation becomes

$$-\hbar\frac{\partial\hat{\psi}(\vec{r},t)}{\partial t} = \left[-\frac{\hbar^2\nabla^2}{2m} + V_{trap}(\vec{r})\right]\hat{\psi}(\vec{r},t) + g\left\langle\tilde{\psi}^\dagger(\vec{r},t)\tilde{\psi}(\vec{r},t)\tilde{\psi}(\vec{r},t)\right\rangle \tag{2.75}$$

where $\hat{\psi}(\vec{r},t) = \Phi(\vec{r},t)+\tilde{\psi}(\vec{r},t)$ is the sum of the condensate component $\Phi = \langle\hat{\psi}\rangle$ and non-condensate component is $\tilde{\psi}$, assuming that $\langle\tilde{\psi}\rangle = 0$. Therefore, (2.74) is generalized to

$$\begin{aligned} i\hbar\frac{\partial\Phi(\vec{r},t)}{\partial t} = &\left[-\frac{\hbar^2\nabla^2}{2m} + V_{trap}(\vec{r}) + gn_c(\vec{r},t) + 2g\tilde{n}(\vec{r},t)\right]\Phi(\vec{r},t) + g\tilde{m}(\vec{r},t)\Phi^* \\ &+ g\left\langle\tilde{\psi}^\dagger(\vec{r},t)\tilde{\psi}(\vec{r},t)\tilde{\psi}(\vec{r},t)\right\rangle\ , \end{aligned} \tag{2.76}$$

where $n_c(\vec{r},t) = |\Phi|^2$ is the density of the condensate, $\tilde{n} = \langle\tilde{\psi}^\dagger\tilde{\psi}\rangle$ is the density of the atoms outside of the condensate (called the normal density), and $\tilde{m} = \langle\tilde{\psi}\tilde{\psi}\rangle$ (called the anomalous density).

We will restrict ourselves to $T = 0$. We can then solve (2.74) using $\Phi = \Phi_0(\vec{r})e^{-i\mu t/\hbar}$, where $\Phi_0(\vec{r}) = \sqrt{n_c(\vec{r},t)}$. If we introduce a perturbation, such that $\Phi = [\Phi_0(\vec{r}) + \delta\Phi(\vec{r},t)]\,e^{-i\mu t/\hbar}$, with $\Phi_0(\vec{r}) \gg \delta\Phi(\vec{r},t)$, substitution into (2.74) yields the first-order equations of

$$\begin{aligned} i\hbar\frac{\partial\delta\Phi}{\partial t} &= \left[-\frac{\hbar^2\nabla^2}{2m} + V_{trap}(\vec{r}) + 2g|\Phi_0|^2 - \mu\right]\delta\Phi(\vec{r},t) + g\Phi_0^2\delta\Phi^*\,. \\ -i\hbar\frac{\partial\delta\Phi^*}{\partial t} &= \left[-\frac{\hbar^2\nabla^2}{2m} + V_{trap}(\vec{r}) + 2g|\Phi_0|^2 - \mu\right]\delta\Phi(\vec{r},t)^* + g\Phi_0^2\delta\Phi \end{aligned} \tag{2.77}$$

Restricting ourselves to periodic solutions in time, we can use the ansatz [183]

$$\delta\Phi = u(\vec{r})e^{-i\omega t} - v(\vec{r})e^{i\omega t} \tag{2.78}$$

to solve (2.77), where ω represents the frequency of the perturbation. For simplicity, assume that we have a uniform Bose gas, such that $V = 0$ and the density is constant. This corresponds to choosing $u(r) = ue^{i\vec{k}\cdot\vec{r}}$ and $v(r) = ve^{i\vec{k}\cdot\vec{r}}$ to be plane waves, where $\vec{k}$ is the wavevector. Substituting the ansatz into equation (2.77), then squaring and subtracting the results, we find [95]

$$(\hbar\omega)^2 = \left(\frac{\hbar^2k^2}{2m} - \mu + 2gn_c\right)^2 - g^2n_c^2\,, \tag{2.79}$$

which describes the energies of these fluctuations. We can simplify the energy by noting that $\mu = gn_c$ [85], so

$$\hbar\omega = \sqrt{\frac{\hbar^2k^2}{2m}\left(\frac{\hbar^2k^2}{2m} + 2\mu\right)}\,. \tag{2.80}$$

In the limit of small k, we call these fluctuations phonons, such that $\hbar\omega \sim \sqrt{\frac{\mu}{m}}k$. We can relate μ to the speed of the phonons by noting that $dE = -VdP + \mu dN$, where P is the pressure, N is the number of particles, E is the energy, and we are assuming the temperature is zero. Assuming E is constant, we find that $\mu = V\frac{dP}{dN} = m\frac{dP}{d\rho}$, where $\rho = \frac{mN}{V}$ is the mass density. Noting that $\frac{dP}{d\rho} = c_s^2$ is the speed of sound, we see that $\mu = mc_s^2$.

Even though we are working in the $T = 0$ limit, there will still be dissipative effects within our Bose-Einstein condensate. At these temperatures, phononic excitations are able to decay into new phonons. Physically, this occurs when an excited atom (i.e. an atom with a phononic excitation) interacts with an atom in its ground state (i.e. an atom in the condensate). These two atoms then share energy and momentum, which causes the second atom to also leave the condensate [190]. This process is known as Beliaev damping and has a damping rate of [90, 110],

$$\gamma_B = \frac{3\hbar\omega^5}{640\pi mnc_s^5}\,. \tag{2.81}$$

and n is the number density. We see that for sufficiently large phonon wavenumbers k, the damping rate will be extremely large. As we will see, it is this feature that provides one of the limitations to detecting gravitational waves with a Bose-Einstein condensate.

Chapter 3

Detecting Gravitational Waves with Squeezing

3.1 Introduction

As we discussed in Chapter 2, at the present time, gravitational wave detection is primarily done with interferometers. A drawback is that they are sensitive to only a small range of frequencies, with LIGO being most sensitive around 100-300 Hz, allowing it to detect stellar-mass inspiralling black holes and neutron stars [57]. However, interferometers involving cold atoms have previously been suggested as a means to detect kHz frequency gravitational waves [68, 105]. Recently, a novel suggestion [199] making use of a Bose-Einstein condensate (BEC) as a high frequency gravitational wave detector has been proposed. A zero temperature quasi (1+1)-dimensional BEC with fluctuating boundaries was considered in the presence of a continuous gravitational wave with plus polarization (in the BEC frame), $h_+ = \epsilon \sin \Omega t$, where ϵ is the amplitude of the gravitational wave and Ω is its frequency. By calculating the fidelity (overlap) between phonon states, it was possible to determine the quantum Fisher information H_ϵ of the phonon state of the BEC, which characterizes the amount of information contained in the amplitude of the gravitational wave [38, 199]:

$$M \langle (\Delta\epsilon)^2 \rangle \geq \frac{1}{H_\epsilon} , \tag{3.1}$$

where M is the number of independent measurements of the system and $\langle (\Delta\epsilon)^2 \rangle$ is the mean-square-error in the amplitude of the gravitational wave. Assuming that the phonons were in squeezed two-mode states, it was claimed that, with a suitable number of measurements of the fidelity between phonons interacting with a gravitational wave of amplitude ϵ and a gravitational wave of amplitude $\epsilon + d\epsilon$, the strain sensitivity $\sqrt{\langle \Delta\epsilon^2 \rangle}$ was able to exceed that of LIGO at frequencies in the kilohertz regime.

As a toy model, the condensate of Ref. [199] was assumed to be in a square well potential, such that the density was constant (i.e. the BEC was uniform). However, we note that this proposal has faced critique [206], in which it was argued that a gravitational wave will not directly create new phonons within the condensate, but only affects existing phonons or indirectly generates phonons. Therefore, it was suggested that using non-uniform condensates might be necessary in order to detect gravitational waves. The sensitivity of a BEC to gravitational waves also questioned. To detect gravitational waves, a detector needs to be sensitive to amplitudes on the order of $\mathcal{O}(10^{-19})$

and below. LIGO can achieve these sensitivities through a combination of factors, such as the length of the arms and number of photons within the interferometer. Ref. [206] noted that it was unclear how the parameters of a BEC could conspire to achieve such a sensitivity, as a BEC has length scales on the order tens-hundreds of microns and significantly fewer particles within the condensate, as compared to the number of photons within LIGO. Significant technological advancements would be required. See [113, 207] for a further discussion of these arguments.

In a later work, [190] investigated decoherence effects in a Bose-Einstein condensate arising from three-body loss (a third atom taking energy and momentum away from two atoms). This effect will be present even at low-temperatures and energies, so it is necessary to consider when using a Bose-Einstein condensate as a gravitational wave detector (or any other type of quantum sensor). The effect of such loss is to reduce the ability of a BEC to sense various physical effects.

As indicated by [206] and [190], gravitational wave detection with Bose-Einstein condensates will be extremely difficult. However, given that phonons might be able to be produced by gravitational waves indicates that a BEC could potentially be made into a future gravitational wave detector, provided that a BEC can be constructed to provide a long-enough measurement time, enough measurements of the gravitational waves can be done, and the phonons themselves can be squeezed enough [199]. In addition, recent work has suggested using specialized types of interferometers to amplify the gravitational wave sensitivity [111, 112]. Though new and advanced experimental techniques will almost certainly be required for a BEC to function as a gravitational wave detector, it seems that given sufficient effort, such a detector may be able to be put into practice. We caution, however, as we will discuss in Chapter 4, that the noise in the BEC will be a major obstacle to the experimental implementation of such a proposal.

In this chapter, we will consider zero-temperature (3+1)-dimensional BECs as a means to detect continuous gravitational waves interacting with a detector, modelled as $h_+ = \epsilon e^{-t^2/\tau^2}\sin(\Omega t)$, where Ω is the frequency of the incoming wave and τ captures the duration of a single measurement of the BEC. We treat the phonons as being initially in a single-mode squeezed states and examine whether current techniques of squeezing phonons and producing BECs are sufficient in order to use the condensate as a gravitational wave detector.

In Section 3.2, we introduce BECs in a curved spacetime and derive the Euler-Lagrange equation for the phonons being influenced by the gravitational waves. Then, in Section 3.3, we apply techniques in quantum metrology to estimate the sensitivity for the detection of gravitational waves. In Section 3.4, we consider whether or not current experimental techniques can be used to achieve the necessary sensitivity. We show that if the phonons are restricted to obey a linear dispersion relation, then the amount of phonon squeezing is the dominant limiting factor. We also address the damping present in the condensate at $T = 0$ and comment on how to increase the sensitivity of the condensate to gravitational waves. Section 3.5 presents our conclusions.

3.2 Bose-Einstein condensates in a curved background

We will now derive the equation of motion for the phonons as well as its Bogoliubov coefficients, with related derivations can be found in [74, 167, 199].

The Lagrangian for a BEC in a curved background is

$$\mathcal{L} = g^{\mu\nu}\partial_\mu\phi\partial_\nu\phi^\dagger - m^2|\phi|^2 - U(|\phi|^2) \tag{3.2}$$

where m is the mass of the atoms of the BEC, ϕ is the field, $U(|\phi|^2) = \lambda|\phi|^4 > 0$ describes the interaction of the BEC.[1] Let us write $\phi = \hat{\phi}e^{i\chi}$ (with real $\hat{\phi}$ and χ) and assume that the BEC is homogeneous. We want to determine the $\hat{\phi}$ that extremizes $\mathcal{L}$. Differentiating with respect to $\hat{\phi}$, we find that the extremum occurs at

$$\hat{\phi}^2 = \frac{1}{2\lambda}\left[\partial^\mu\chi\partial_\mu\chi - m^2\right] \ . \tag{3.3}$$

Inserting (3.3) into (3.2) and writing $\chi = \kappa t + \pi$ (where $\pi \in \Re$ is the Goldstone boson, describing the BEC acoustic perturbations or phonons), the action becomes

$$\begin{aligned} S &= \int \frac{d^4x}{4\lambda}\sqrt{-g}\left\{(\kappa\delta_0^\nu + \partial^\nu\pi)(\kappa\delta_0^\mu + \partial^\mu\pi)g_{\mu\nu} - m^2\right\}^2 \ , \\ &= \int \frac{d^4x}{4\lambda}\sqrt{-g}\left[\kappa^2 g_{00} + 2\kappa\dot{\pi}g_{00} + \kappa\partial^i\pi g_{0i} + |\dot{\pi}|^2 g_{00} + \partial^i\pi\partial^j\pi g_{ij} + 2\partial^i\pi\dot{\pi}g_{i0} - m^2\right]^2 \ . \end{aligned} \tag{3.4}$$

We are interested in low frequencies, using an effective field theory framework for χ, where "heavy" fields are "integrated out". As a result, $\partial_\mu\hat{\phi}$ terms are higher order and are therefore suppressed [222]. Take $g_{\mu\nu} = \eta_{\mu\nu} + h_{\mu\nu}$ and let us work in the traceless-transverse gauge, such that

$$h_{\mu\nu} = \begin{pmatrix} 0 & 0 & 0 & 0 \\ 0 & h_+(t) & h_\times(t) & 0 \\ 0 & h_\times(t) & -h_+(t) & 0 \\ 0 & 0 & 0 & 0 \end{pmatrix} \ , \tag{3.5}$$

describes a gravitational wave propagating in the z-direction and h_+ and $h_\times$ are the two polarizations of the gravitational wave.[2] Using $\sqrt{-g} \sim 1 + \mathcal{O}(h_{\mu\nu}h^{\mu\nu})$ and a $(+,-,-,-)$ signature, we can expand in terms of π to find

$$S = \int \frac{d^4x}{4\lambda}\left[\kappa^2 + 2\kappa\dot{\pi} + |\dot{\pi}|^2 + \partial^i\pi\partial^j\pi g_{ij} - m^2\right]^2 \ , \tag{3.6}$$

$$\approx \int \frac{d^4x}{4\lambda}\left[|\dot{\pi}|^2(6\kappa^2 - 2m^2) + (2\kappa^2 - 2m^2)(\eta_{ij} + h_{ij})\partial^i\pi\partial^j\pi\right] \ , \tag{3.7}$$

where the first-order terms can be written as a total derivative that integrates to zero on the boundary and we assume that the higher-order terms can be neglected.

Let us now determine the dispersion relation of our phonons in order to simplify the Lagrangian in equation (3.7). Inserting

$$\phi = \sqrt{\frac{\kappa^2 - m^2}{2\lambda}}\exp\left[i(\kappa t + \pi) + \sigma\right], \tag{3.8}$$

(with real σ and π) into equation (3.2), we find the Lagrangian to be

$$\mathcal{L} = \frac{(\kappa^2 - m^2)}{2\lambda}e^{2\sigma}\left[\partial_\mu\sigma\partial^\mu\sigma - (\nabla\pi)^2 + (\dot{\pi} + \kappa)^2\right] - \frac{m^2(\kappa^2 - m^2)e^{2\sigma}}{2\lambda} - \frac{(\kappa^2 - m^2)^2 e^{4\sigma}}{4\lambda} \ , \tag{3.9}$$

[1] As this describes the generalization of a BEC in curved spacetime, we note that it will only be accurate for $na^3 \ll 1$ as this is the regime of validity for the Gross-Pitaevskii equation, where n is the number density, a is the s-wave scattering wavelength, and c_s is the speed of sound defined below in equation (3.15) [130].

[2] We assume that the boundaries of the BEC move on geodesics. Therefore, starting at rest, they will not see the gravitational waves to linear order.

where

$$2\sigma = \ln\left[\frac{(\kappa+\dot{\pi})^2 - (\nabla\pi)^2 - m^2}{\kappa^2 - m^2}\right] . \tag{3.10}$$

Writing σ and π in terms of their inverse Fourier transforms,

$$\sigma \sim \int \hat{\sigma}(\omega,\vec{k}) e^{i(k\cdot x - \omega t)} d\omega d^3k \ , \tag{3.11}$$

$$\pi \sim \int \hat{\pi}(\omega,\vec{k}) e^{i(k\cdot x - \omega t)} d\omega d^3k \ , \tag{3.12}$$

we find

$$\frac{2\lambda}{\kappa^2 - m^2}\mathcal{L}_2 = \begin{pmatrix}\hat{\pi}^* & \hat{\sigma}^*\end{pmatrix}\begin{pmatrix}\omega^2 - k^2 + 2(m^2-\kappa^2) & -2i\kappa\omega \\ 2i\kappa\omega & \omega^2 - k^2\end{pmatrix}\begin{pmatrix}\hat{\pi}\\ \hat{\sigma}\end{pmatrix} \tag{3.13}$$

for the quadratic term in the Lagrangian.

Setting the determinant of this matrix equal to zero and solving for ω gives the dispersion relation,

$$\omega^2 = k^2 - m^2 + 3\kappa^2 \pm \sqrt{m^4 + 4k^2\kappa^2 - 6m^2\kappa^2 + 9\kappa^4} \ . \tag{3.14}$$

From equation 3.7, we know that the speed of sound can be written as

$$c_s^2 \equiv \frac{\kappa^2 - m^2}{3\kappa^2 - m^2} \ , \tag{3.15}$$

Solving this equation for κ,

$$\kappa = \frac{\sqrt{1-c_s^2}}{\sqrt{1-3c_s^2}} m \ . \tag{3.16}$$

and $k \ll m$ and $c_s \ll 1$, equation (3.14) (for the minus sign, associated with the low-frequency Goldstone mode) can be expanded in k and c_s to find

$$\omega^2 = c_s^2 k^2 + \mathcal{O}\left(\frac{k^4}{m^2}\right) . \tag{3.17}$$

Therefore, we obtain $\omega \approx c_s k$, as long as $\omega \ll \mu \equiv mc_s^2 = \kappa - m$, i.e. frequency is much smaller than the chemical potential μ. This was expected as we are working in a nearly flat spacetime, therefore our results should align with those of Section 2.3. Hence, the Euler-Lagrange equation is

$$\ddot{\pi} + c_s^2(\eta_{ij} + h_{ij})\partial^i\partial^j\pi + c_s^2(\partial^j h_{ij})\partial^i\pi = 0 \ , \tag{3.18}$$

For simplicity, we will assume that $h_\times = 0$. We model the plus polarization as $h_+ = \epsilon e^{-t^2/\tau^2}\sin\Omega t$ (ignoring its spatial dependence[3]), where ϵ is the amplitude of the gravitational wave, τ describes the duration of a single measurement of the gravitational wave, and Ω is the frequency of the wave.

[3]This is justified when the speed of sound is much smaller than that of gravitational waves, $c_s \ll 1$.

There are two interpretations of this waveform. One treats h_+ as approximating a transient gravitational wave. An alternate interpretation is to consider a continuous gravitational wave, $\epsilon \sin \Omega t$, interacting with a detector modelled as e^{-t^2/τ^2}. The Gaussian can be understood as a switching function that tells the detector how to turn on and off. In this Chapter, we will use this second interpretation of having a continuous gravitational wave interacting with a detector.

Noting that $(\partial_i h^{ij}) = 0$ in the traceless-transverse gauge and using the ansatz $\pi \propto e^{ik\cdot x}\psi(t)$, we find

$$\ddot{\psi} + c_s^2(\eta_{ij} + h_{ij})k^i k^j \psi = 0 \tag{3.19}$$

up to a normalization of ψ. Thus, with $k^1 = k_x$, $k^2 = k_y$, and $k^3 = k_z$,

$$\ddot{\psi} + c_s^2|k|^2\left[1 + \tilde{\epsilon} e^{-t^2/\tau^2}\sin(\Omega t)\right]\psi = 0 \ . \tag{3.20}$$

where $\tilde{\epsilon} = \frac{(k_x^2 - k_y^2)}{|k|^2}\epsilon$.

Let us briefly comment on the validity of equation (3.20), which was determined by neglecting higher-order terms in equation (3.6). The third-order terms in the Lagrangian are

$$\mathcal{L}_3 = \frac{\kappa}{\lambda}\left[|\dot{\pi}|^3 + \dot{\pi} g_{ij}\partial^i\pi\partial^j\pi\right] \ . \tag{3.21}$$

For $\kappa \approx m$, we have $c_s^2 \approx \frac{2(\kappa^2 - m^2)}{2m^2} \ll 1$, so $4m^2|\dot{\pi}|^2 \approx 2m^2 c_s^2|\nabla\pi|^2$ on average (because of the Virial Theorem). With $2m^2c_s^2 = 2\kappa^2 - 2m^2$, we can apply equation (3.7) to get

$$S = \frac{1}{4\lambda}\int d^4x\left[4m^2|\dot{\pi}|^2 - 2mc_s^2|\nabla\pi|^2\right] = 0 \tag{3.22}$$

Now, comparing equations (3.7) and (3.21), we see that linear theory is only valid when

$$c_s^{-1}|\dot{\pi}| \sim |\nabla\pi| \ll mc_s \ . \tag{3.23}$$

3.2.1 Calculation of Bogoliubov Coefficients

Solving (3.20) perturbatively by writing $\psi = \psi^{(0)} + \tilde{\epsilon}\psi^{(1)}$ yields

$$\ddot{\psi}^{(0)} + \omega^2\psi^{(0)} = 0 \ , \tag{3.24}$$

$$\ddot{\psi}^{(1)} + \omega^2\psi^{(1)} = -\omega^2 e^{-t^2/\tau^2}\sin(\Omega t)\psi^{(0)} \ , \tag{3.25}$$

which has the solutions

$$\psi^{(0)}(t) = C_1^{(0)}e^{i\omega t} + C_2^{(0)}e^{-i\omega t} \ , \tag{3.26}$$

$$\psi^{(1)}(t) = C_1^{(1)}e^{i\omega t} + C_2^{(1)}e^{-i\omega t} - \int_{-\infty}^{\infty} dt_1\omega^2 e^{-t_1^2/\tau^2}\sin(\Omega t_1)G(t,t_1)\psi^{(0)}(t_1) \ , \tag{3.27}$$

where [43]

$$G(t,t_1) = \frac{\sin[\omega(t-t_1)]}{\omega}\Theta(t-t_1) \ , \tag{3.28}$$

is the Green's function of a harmonic oscillator, while Θ represents the Heaviside function. Initially, assume we only have $\psi(t) \sim e^{i\omega t}$, so the initial conditions implies $C_2^{(0)} = C_1^{(1)} = C_2^{(1)} = 0$. In the $t \to \infty$ limit (i.e. after the measurement is finished), we can drop the Heaviside step function, such that combining our ansatz of $\pi \propto e^{ik\cdot x}\psi(t)$ with equations (3.26) and (3.27), yields

$$\pi(x,t) \propto e^{ikx}\left[e^{-i\omega t} + \frac{\sqrt{\pi}\tilde{\epsilon}\omega\tau}{4} e^{-\frac{1}{4}(\Omega+2\omega)^2\tau^2}\left(e^{2\omega\Omega\tau^2} - 1\right) e^{i\omega t}\right] . \tag{3.29}$$

As we are working in curved spacetime with a single mode, we can write $\pi(x,t) \propto e^{ikx}\left[\alpha e^{-i\omega t} + \beta e^{i\omega t}\right]$, where α and β are Bogoliubov coefficients. This immediately yields

$$\alpha = 1 , \tag{3.30}$$

$$\beta = \frac{\tilde{\epsilon}\sqrt{\pi}\omega}{4}\tau e^{-(\Omega+2\omega)^2\tau^2/4}\left(e^{2\omega\Omega\tau^2} - 1\right) . \tag{3.31}$$

Let us briefly comment on the large and small τ limits. We note that $\beta \to 0$ as $\tau \to 0$. Intuitively, this makes sense because a vanishing measurement duration implies that no information about the gravitational wave would be obtained. We further discuss the information that can be acquired in Section 3.3. For $\tau \to \infty$ we recover (as expected [199]) $\beta \to 0$. We note that for non-geodesic boundaries [199], we would have non-zero Bogoliubov coefficients α_{nm} and β_{nm} result for modes $n \neq m$. However, in our case coefficients with $n \neq m$ are zero since we assume non-interacting modes. [4]

In this special case, we find $\alpha = 1$. If, for example, we had instead considered an even function $h_+ = \epsilon e^{-t^2/\tau^2}\cos(\Omega t)$, then α would include a non-zero imaginary $\mathcal{O}(\epsilon)$ term. Such effects are necessary to consider if a BEC gravitational wave detector were constructed; we shall neglect this additional effect henceforth in order to keep the discussion as simple as possible.

3.3 Gravitational wave detection via quantum metrology

Quantum metrology is the study of making precision measurements by exploiting quantum mechanical properties, rather than solely relying on classical measurements of a system. This can be used, for example, to overcome shot noise in a detector [65, 91, 92]. Another advantage is that quantum metrology can be used to estimate a parameter θ that is not an operator observable of a system. This is done by determining how an infinitesimal change of the parameter affects the statistical distance between two quantum states, thereby defining their distinguishability (fidelity) and quantum Fisher information.

As we saw in Section 2.2, an estimate in the error in the measurement of θ is obtained from the quantum Fisher information [10],

$$H_\theta = \frac{8\left(1 - \sqrt{F(\rho_\theta, \rho_{\theta+d\theta})}\right)}{d\theta^2} , \tag{3.32}$$

with the fidelity

$$F(\rho', \rho'') = \left[\mathrm{Tr}\sqrt{\rho'\sqrt{\rho''}\rho'}\right]^2 , \tag{3.33}$$

[4] As there is no x dependence at quadratic order in the action, the modes will not mix and can instead be separated.

When both ρ' and ρ'' correspond to Gaussian states, it is often easier to use covariance matrices. In this case, the covariance matrix for a Gaussian state is $\sigma_{mn} = \frac{1}{2}\langle X_m X_n + X_n X_m\rangle - \langle X_m\rangle\langle X_n\rangle$, where $X_{2n-1} = \frac{1}{\sqrt{2}}(a_n + a_n^\dagger)$, $X_{2n} = \frac{1}{\sqrt{2}i}(a_n - a_n^\dagger)$, and $a_n, a_n^\dagger$ are the annihilation and creation operators. Note that this normalization convention is different from what was used in [10, 199]. Suppose that M independent measurements are done to determine θ. Then,

$$\langle(\Delta\theta)^2\rangle \geq \frac{1}{MH_\theta} \tag{3.34}$$

is the minimum error in measuring θ [38, 199].

We will now use the quantum Fisher information to estimate the minimum error in the amplitude of the gravitational wave. We will restrict ourselves to the case in which $\langle X_i\rangle = 0$. First, consider two Gaussian states described by the covariance matrices σ_A, σ_B. The fidelity between the two covariance matrices of two single-mode states is given by (2.58) [143],

$$F(\sigma_A, \sigma_B) = \frac{1}{\sqrt{\Delta + \Lambda} - \sqrt{\Lambda}}\ . \tag{3.35}$$

where Δ and Λ are given by equations (2.59a) and (2.59b), respectively.

Consider preparing the phonons in the BEC in a squeezed Gaussian single-mode state, described by an initial covariance matrix $\sigma(0)$ (at zero-temperature) in [75]:

$$\sigma(0) = \frac{1}{2}\begin{pmatrix} \cosh(2r) + \cos(\phi)\sinh(2r) & -\sin(\phi)\sinh(2r) \\ -\sin(\phi)\sinh(2r) & \cosh(2r) - \cos(\phi)\sinh(2r)\end{pmatrix}\ , \tag{3.36}$$

where r is the squeezing parameter and ϕ is the squeezing angle. When a gravitational wave passes by the BEC, it affects the phonons by transforming its covariance matrix to $\sigma_\ell(\tilde{\epsilon})$ where [10]

$$\sigma_\ell(\tilde{\epsilon}) = \mathcal{M}_{\ell\ell}(\tilde{\epsilon})\sigma(0)\mathcal{M}_{\ell\ell}(\tilde{\epsilon}) + \sum_{j\neq\ell}\mathcal{M}_{\ell j}(\tilde{\epsilon})\mathcal{M}_{\ell j}^T(\tilde{\epsilon})\ , \tag{3.37}$$

with ℓ the mode number of the phonon and

$$\mathcal{M}_{mn}(\tilde{\epsilon}) = \begin{pmatrix} \Re[\alpha_{mn} - \beta_{mn}] & \Im[\alpha_{mn} + \beta_{mn}] \\ -\Im[\alpha_{mn} - \beta_{mn}] & \Re[\alpha_{mn} + \beta_{mn}]\end{pmatrix}\ . \tag{3.38}$$

Our Bogloliubov coefficients in equations (3.30) and (3.31) do not couple different modes, so we note that $\alpha_{mn} = \alpha\delta_{mn}$ and $\beta_{mn} = \beta\delta_{mn}$.

As shown in [10], equation (3.32) can be written as

$$H_\epsilon = 4(\mathcal{E} + \mathcal{C})\,, \tag{3.39}$$

where $\mathcal{E}$ is proportional to the displacement of the squeezed state and

$$4\mathcal{C} = 2\left(\sigma_{11}^{(0)}\sigma_{22}^{(2)} + \sigma_{11}^{(2)}\sigma_{22}^{(0)} - 2\sigma_{12}^{(0)}\sigma_{12}^{(2)}\right) + \frac{1}{2}\left(\sigma_{11}^{(1)}\sigma_{22}^{(1)} - 2\sigma_{12}^{(1)}\sigma_{12}^{(1)}\right)\ , \tag{3.40}$$

where

$$\sigma_{ij}(\epsilon) = \sigma_{ij}^{(0)} + \sigma_{ij}^{(1)}\epsilon + \sigma_{ij}^{(2)}\epsilon^2 + \mathcal{O}(\epsilon^3) \tag{3.41}$$

and $\sigma_{ij}^{(n)}$ is the ij matrix element in an expansion of the covariance matrix in powers of ϵ. Assuming that the displacement of the squeezed state is zero, we then have

$$H_\epsilon = 4\mathcal{C} \ . \tag{3.42}$$

Combining equations (3.30), (3.31), and (3.36)-(3.42), we calculate

$$H_\epsilon = \frac{1}{64}\pi\tau^2\omega^2 e^{-\frac{1}{2}\tau^2(2\omega+\Omega)^2}\left(e^{2\tau^2\omega\Omega}-1\right)^2 R \tag{3.43}$$

where

$$R \equiv \sinh^2(2r)(6\sin^2\phi - 2) + \cosh(4r) + 1 \ . \tag{3.44}$$

Therefore, from equation (3.34), we can estimate the sensitivity to gravitational waves for a single mode:

$$\frac{1}{M\left\langle(\Delta\tilde{\epsilon})^2\right\rangle} \leq \frac{\pi\omega^2\tau^2}{64} R \left(e^{-\frac{(\Omega-2\omega)^2\tau^2}{4}} - e^{-\frac{(\Omega+2\omega)^2\tau^2}{4}}\right)^2 . \tag{3.45}$$

We can exploit all modes of the BEC to improve the sensitivity. From $\tilde{\epsilon} = \frac{k_x^2-k_y^2}{k^2}\epsilon$, we have $\langle(\Delta\tilde{\epsilon}_{\vec{k}})^2\rangle = \left(\frac{k_x^2-k_y^2}{k^2}\right)^2\langle(\Delta\epsilon_{\vec{k}})^2\rangle$, where $\langle(\Delta\epsilon_{\vec{k}})^2\rangle$ is the error in ϵ for mode $\vec{k}$. Noting that $k_x = k\sin\theta\cos\phi$ and $k_y = k\sin\theta\sin\phi$, we can then average over the solid angle, such that

$$\frac{1}{4\pi}\int d\theta d\varphi \left\langle(\Delta\tilde{\epsilon}_{\vec{k}})^2\right\rangle \sin\theta = \frac{4}{15}\left\langle(\Delta\epsilon_{\vec{k}})^2\right\rangle \ .$$

Substituting this average into $\langle(\Delta\tilde{\epsilon}_{\vec{k}})^2\rangle$, we find

$$\frac{1}{\left\langle(\Delta\epsilon)^2\right\rangle_{tot}} = \sum_{\vec{k}}\left\langle\left(\frac{k_x^2-k_y^2}{k^2}\right)^2\right\rangle\frac{1}{\left\langle(\Delta\tilde{\epsilon}_{\vec{k}})^2\right\rangle} = \frac{4}{15}\sum_{\vec{k}}\frac{1}{\left\langle(\Delta\tilde{\epsilon}_{\vec{k}})^2\right\rangle} \ , \tag{3.46}$$

where $\left\langle(\Delta\epsilon)^2\right\rangle_{tot}$ is the total error in the measurement of the amplitude of the gravitational wave. For a large number of single-mode states and assuming that the modes are non-interacting, we can convert equation (3.46) into an integral. With $\omega = c_s k$, assuming the BEC has a volume of L^3, $k = \sqrt{\left(\frac{n_x\pi}{L}\right)^2 + \left(\frac{n_y\pi}{L}\right)^2 + \left(\frac{n_z\pi}{L}\right)^2}$, using spherical coordinates (with the both the altitudinal and azimuthal integrals between 0 and $\frac{\pi}{2}$), and letting $n^2 = n_x^2 + n_y^2 + n_z^2$, we can combine (3.45) and (3.46) so that,

$$\frac{1}{\left\langle(\Delta\epsilon)^2\right\rangle_{tot}} \lesssim \frac{\pi^4 M c_s^2 R\tau^2}{480L^2}\int_0^\infty n^4 e^{-\frac{(2\pi c_s n+L\Omega)^2\tau^2}{2L^2}}\left(e^{\frac{2\pi c_s n\Omega\tau^2}{L}}-1\right)^2 dn \, , \tag{3.47}$$

where we are assuming that the Gaussian is centred at $n \gg 1$. Expansion of the exponential term in the integrand yields

$$\begin{aligned} e^{-\frac{(2\pi c_s n+L\Omega)^2\tau^2}{2L^2}}\left(e^{\frac{2\pi c_s n\Omega\tau^2}{L}}-1\right)^2 = {} & e^{-\frac{2\pi^2c_s^2n^2\tau^2}{L^2}-\frac{2\pi c_s n\tau^2\Omega}{L}-\frac{1}{2}\tau^2\Omega^2} + e^{\frac{2\pi^2c_s^2n^2\tau^2}{L^2}+\frac{2\pi c_s n\tau^2\Omega}{L}-\frac{1}{2}\tau^2\Omega^2} \\ & - 2e^{-\frac{2\pi^2c_s^2n^2\tau^2}{L^2}-\frac{1}{2}\tau^2\Omega^2} \end{aligned} \tag{3.48}$$

We can complete the square of each term to find that the first-term is centred at $n = -\frac{L\Omega}{2\pi c_s}$, the second-term is centred at $n = \frac{L\Omega}{2\pi c_s}$, and the third-term is centred at $n = 0$. As we are integrating

over the region $n \geq 0$, we note that only the second term is dominant in the integrand, so we require $\frac{L\Omega}{2\pi c_s} \gg 1$.

We note that we can rewrite $e^{-\frac{(2\pi c_s n + L\Omega)^2 \tau^2}{2L^2}} \left(e^{\frac{2\pi c_s n \Omega \tau^2}{L}} - 1\right)^2 = 4e^{-\tau^2\left(\frac{2{c_s}^2 n^2 \pi^2}{L^2} + \frac{\Omega^2}{2}\right)} \sinh\left(\frac{c_s n \pi \tau^2 \Omega}{L}\right)^2$. Therefore,

$$\frac{1}{\langle(\Delta\epsilon)^2\rangle_{tot}} = \frac{ML^3 e^{-\frac{1}{2}\tau^2\Omega^2} R \left(e^{\frac{\tau^2\Omega^2}{2}} \left(\tau^4\Omega^4 + 6\tau^2\Omega^2 + 3\right) - 3\right)}{7680\sqrt{2\pi} c_s^3 \tau^3} , \tag{3.49}$$

where we have neglected $\mathcal{O}(\epsilon^2)$.

Now, for a total observation time of t_{obs}, we can approximately run $M \sim t_{obs}/\tau$ separate measurements of the BEC state. Therefore,

$$\langle(\Delta\epsilon)^2\rangle_{tot} \geq \frac{7680\sqrt{2\pi} c_s^3 \tau^4 e^{\frac{\tau^2\Omega^2}{2}}}{L^3 t_{obs} R \left(e^{\frac{\tau^2\Omega^2}{2}} \left(\tau^4\Omega^4 + 6\tau^2\Omega^2 + 3\right) - 3\right)} . \tag{3.50}$$

Note that R is maximized at $\phi = \pi/2$, such that $R_{\max} = 3\cosh(4r) - 1$. We point out that squeezing at specific angles is physical and has previously been done [52, 120].

Fixing Ω and assuming $\Omega\tau \ll 1$, we find

$$\langle(\Delta\epsilon)^2\rangle_{tot} \geq \frac{1024\sqrt{2\pi} c_s^3 \tau^2}{L^3 t_{obs} \Omega^2 R} + \mathcal{O}(\Omega^4\tau^4) , \tag{3.51}$$

indicating that shorter (individual) measurement times, τ, for a fixed total observation time t_{obs}, will maximize the sensitivity of the BEC to an incoming gravitational wave. However, τ cannot be made arbitrarily short; we shall briefly discuss this in Section 3.4.

Let us now investigate the maximum squeezing of the system. From equation (3.7), for $4|\dot{\pi}|^2 \approx 3c_s^2|\nabla\pi|^2$, which is true on average, the Hamiltonian is

$$H = \frac{7m^2}{4\lambda} \int d^3x |\nabla\pi|^2 \sim \frac{7m^2}{4\lambda} L^3 |\nabla\pi|^2 , \tag{3.52}$$

where L^3 is the volume of the condensate. In the ground state of the system, we would be able to write the Hamiltonian as

$$H = L^3 \int \frac{d^3k}{(2\pi)^2} \frac{1}{2}\omega \sim \frac{L^3}{32\pi^2} k^4 c_s , \tag{3.53}$$

where k is the maximum effective wavenumber obeying the linearity condition (3.23): $\langle|\nabla\pi|^2\rangle \ll m^2c_s^2$. Comparing equations (3.52) and (3.53), we find $|\nabla\pi|^2 \sim \frac{\lambda k^4 c_s}{56m^2\pi^2}$. If we squeeze the ground state, then we require $\frac{\lambda k^4 c_s}{56m^2\pi^2} e^{2r} \ll m^2c_s^2$. Therefore, after re-inserting $\hbar$ and c, we have

$$e^{2r} \ll \frac{56\pi^2}{\lambda} \left(\frac{mc}{\hbar k}\right)^4 \left(\frac{c_s}{c}\right) . \tag{3.54}$$

To calculate λ, we need only to consider the background, such that $\pi = 0$. With

$$T_{\mu\nu} = \frac{2}{\sqrt{-g}} \frac{\delta S}{\delta g^{\mu\nu}} , \tag{3.55}$$

and

$$S = \int d^4x\sqrt{-g}\mathcal{L} \ , \tag{3.56}$$

where $\mathcal{L} = \frac{1}{4\lambda}\left[g^{\mu\nu}\partial_\mu\chi\partial_\nu\chi - m^2\right]^2$, we find

$$T_{\mu\nu} = g_{\mu\nu}\mathcal{L} + 4\left[g^{\mu'\nu'}\partial_{\mu'}\chi\partial_{\nu'}\chi - m^2\right]\partial_\mu\chi\partial_\nu\chi \ . \tag{3.57}$$

Let $\rho = T_{00}$ be the energy density. Then, with $\dot{\pi} = 0$, $\nabla\pi \sim \dot{\pi}$, and $2m^2c_s^2 \approx \kappa^2 - m^2$, we see (again re-inserting $\hbar$ and c),

$$\rho \approx \frac{1}{\lambda}\frac{m^4c_s^2c^3}{\hbar^3} \ . \tag{3.58}$$

Therefore, after solving for λ and noting that $\omega = c_sk$, equation (3.54) becomes

$$e^{2r} \ll \frac{56\pi^2c_s^3\rho}{\omega^4\hbar} \ , \tag{3.59}$$

For a BEC with number density 7×10^{20} m^{-3} containing atoms of mass 10^{-25} kg and in the case of phonons of frequency $\frac{\omega}{2\pi} = 10^4$ Hz and speed $c_s = 1.2$ cm/s, we have $r \lesssim 27$.

3.4 Sensitivity for specific experimental parameters

3.4.1 Non-interacting modes

Let us now analyze the experimental feasibility of using a BEC to detect gravitational waves. We will consider condensates with non-interacting modes, which corresponds to the model described in Sections 3.2 and 3.3. In reality, this is an oversimplification, and we discuss how our model will be affected by damping effects in Section 3.4.2.

Numerical simulations involving optomechanics and trichromatic lasers have been able to squeeze phonons by at least 7.2 dB [96], corresponding to a squeezing parameter of $r = 0.83$.[5] Phonons have been squeezed using second-order Raman scattering [86, 115], in which phonons though this was in the presence of a crystal lattice. It may be possible to exploit this feature, though it will most likely depend on the specific experimental setup used to construct a BEC gravitational wave detector.

The key concept in this Chapter is initially squeezing the phonons. As discussed in [190], squeezing increases the sensitivity of distinguishing between two different states. The current limitation on squeezing phonons arguably represents one of the greatest challenges for using a BEC as a gravitational wave detector. With $r = 0.83$ and $\phi = \pi/2$, we see that $R \approx 41$. If phonons were squeezed 20 dB, corresponding to $r = 2.3$, then $R \approx 1.5 \times 10^4$. An increase in the amount of squeezing would exponentially increase the sensitivity to the gravitational wave [107], though we note that this will be extremely difficult to achieve. For simplicity, we have assumed that the BEC is cubic in shape

[5] Note that position squeezing s is reported in decibels and can be converted to the squeezing parameter r with $s = -10\log_{10}\left(e^{-2r}\right)$ [138].

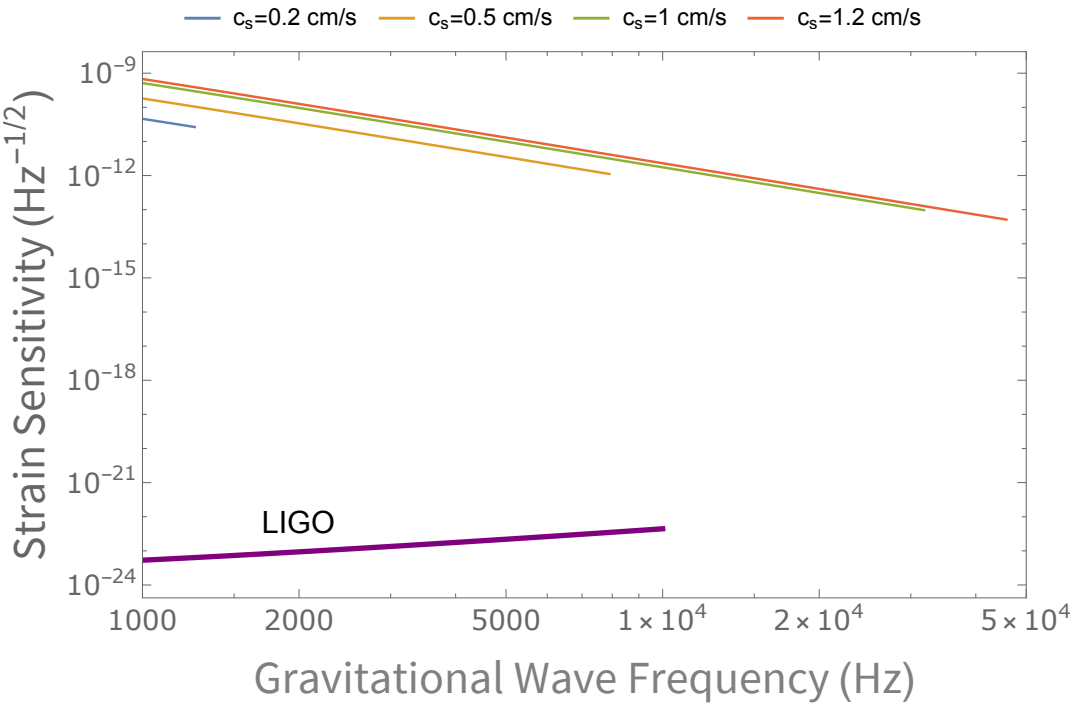

Figure 3.1: Theoretical strain sensitivities $\left(\frac{\sqrt{\langle(\Delta\epsilon)^2\rangle}}{\sqrt{f}}\right)$ of a BEC gravitational wave detector (top curve) using current experimental capabilities, where f is the frequency of the gravitational wave. With $L = 10^{-3}$ m, $t_{obs} = 10^6$ s, $\tau = 10^{-3}$ s, $\phi = \pi/2$, and $r = 0.83$, a BEC is unable to detect kHz gravitational waves. The thick purple line is the general trend corresponding to the maximum design sensitivity of Advanced LIGO (extrapolated to 10^4 Hz). Note that phonons of frequency $\frac{f}{2}$ are necessary to detect gravitational waves of frequency f.

with no external potential, but realistically, we note that certain trap geometries and trapping potentials may lend themselves to large (number) squeezing [120].

Let us now consider the ratio $\frac{c_s^3}{L^3 t_{obs}}$. Experiments have been done to create condensates with lengths on the order of tens of microns to mm [28, 94, 245]. However, these lengths are only in a single direction, with the other length (in the case of quasi-two-dimensional BECs) much smaller. As shown in [19, 20], speeds of sound in BECs were analyzed as a function of the density, with a speed of approximately 1.2 cm/s being obtained at a number density of 7×10^{20} m^{-3}.

For a gravitational wave of period T, sensitivity is optimized for $T \lesssim \tau \lesssim t_d$, where t_d is the decoherence time of the phonons, which we discuss in more detail in Section 3.4.2. For gravitational waves in the kHz frequency range, the minimum time required is $\tau \gtrsim 10^{-3}$ s. One proposal in [199] is to use quantum dots to make measurements on the BEC in which they suggested using 1500 dots to make 10^6 measurements per second. It was suggested that each quantum dot could interact with the condensate, such that 10^{16} continuous measurements could be made by over the course of a year.

In Figure 3.1, we assume that a BEC can be constructed with the best experimental/numerical parameters that have been achieved: modes are squeezed by 7.2 dB ($r = 0.83$) [96], the BEC has a length of $L = 10^{-3}$ m [28, 94, 245], the speed of sound of $c_s = 1.2 \times 10^{-2}$ m/s [19, 20], the quadrature angle is $\phi = \pi/2$, and there is a total observational time of 10^6 s. For simplicity, we

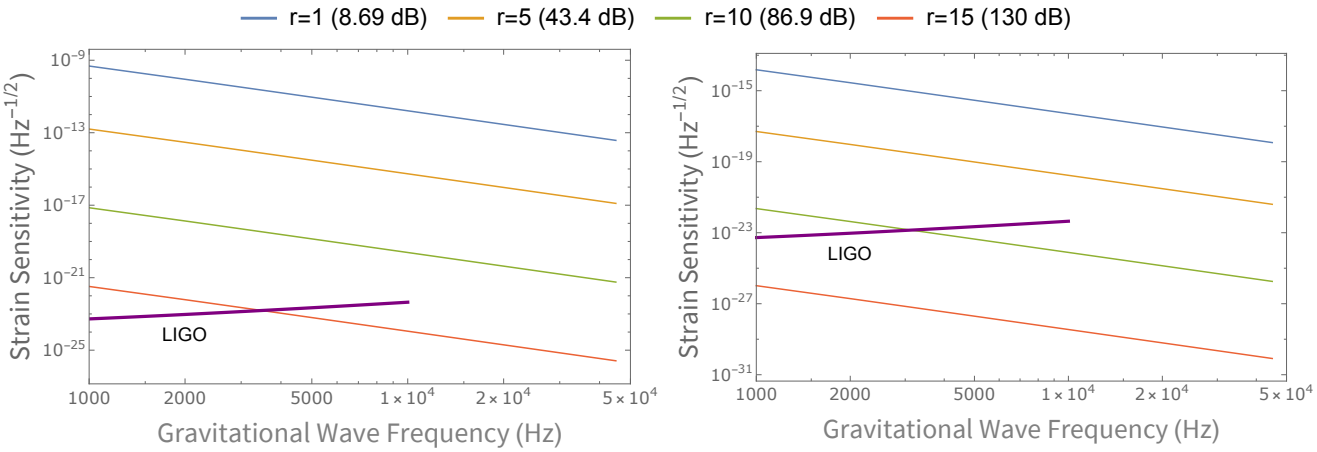

Figure 3.2: Theoretical strain sensitivity $\left(\frac{\sqrt{\langle(\Delta\epsilon)^2\rangle}}{\sqrt{f}}\right)$ to kHz gravitational waves for a futuristic BEC with $c_s = 1.2 \times 10^{-2}$ m/s, $t_{obs} = 10^6$ s, $\phi = \pi/2$, and $\tau = 10^{-3}$ s. In (a), $L = 10^{-3}$ m, while $L = 1$ m in (b). The thick purple line is the general trend of the design sensitivity of Advanced LIGO (extrapolated to 10^4 Hz).

will also assume that millimetre length scales in all three dimensions can be made feasible. We see that the maximum sensitivity for a gravitational wave in the kHz regime is approximately $\mathcal{O}(10^{-12})$ Hz$^{-1/2}$. From equation (3.50), though smaller speeds of sound will increase the sensitivity at lower frequencies, the available frequency range will also decrease because the chemical potential $\mu = mc_s^2$ becomes smaller. To detect a gravitational wave of 1 kHz using atoms of $m = 10^{-25}$ kg, the maximum sensitivity of 4×10^{-11} Hz$^{-1/2}$ occurs when $\mu = 500$ Hz ($c_s \approx 1.8$ mm/s). In Figure 3.2a, we illustrate how increased squeezing can affect the BEC's sensitivity to gravitational waves. We assume that a BEC in the future can be constructed with similar properties as those in figure 3.1, but with r in excess of 0.83. It is necessary to squeeze phonons above $r = 15$ in order to rival LIGO-level sensitivities. In an alternate scenario shown in Figure 3.2b, we suppose that metre-long BECs can be constructed. For this case, we can exceed a LIGO-level sensitivity at $r \approx 10$. We acknowledge that several difficulties exist in constructing large-scale BECs, such as how to cool to sufficiently low temperatures. This is a major experimental challenge for the future that we will not further consider here. Indeed, attaining values $r \geq 1$ is currently unfeasible, and would require advances in squeezing techniques.[6]

The average number of particles in a squeezed vacuum state is $\langle n \rangle = \sinh^2(r)$, with its energy expectation value being $\sinh^2(r)\hbar\omega$ [27]. It should be mentioned that, even though Figures 3.2a and 3.2b demonstrate that the desired sensitivity can be achieved for $r \approx 10$ and $r \approx 15$, depending on the size of the condensate, we note that this results in $\langle n \rangle \approx 10^8$ and $\langle n \rangle \approx 2 \times 10^{12}$, respectively. In fact, for $r \approx 27$, which is the maximum squeezing possible before our model breaks down, we have $\langle n \rangle \approx 7 \times 10^{22}$. Using current techniques, these expectation values exceed the number of particles that can be confined in rubidium BECs, which is on the order of 2×10^7 [229], though 10^9 particles were confined in a hydrogen BEC [94]. If such values of squeezing were achieved without also increasing the number of particles present in a condensate, additional effects may manifest

[6]For instance, the width of the semi-major axis of a squeezed state is $\frac{1}{2}e^{2r}$, while the width of the semi-minor axis is $\frac{1}{2}e^{-2r}$. Therefore, with $r = 27$, the ratio of the widths would be $\sim 8 \times 10^{46}$.

themselves that might act to decrease the sensitivity to gravitational waves. However, in the case of Figure 3.2b, an increase in the length of the condensate will probably also correspond to an increase in the number of particles present in the BEC, thereby negating this problem.

3.4.2 Decoherence (damping) from interacting modes

Let us now look at the maximum value of τ. We have assumed that the system has been free from dissipation. When accounting for this effect, the covariance matrices evolve as $\sigma(t) = e^{-\gamma t}\sigma(0) + \sigma_\infty(1 - e^{-\gamma t})$, where γ is the damping rate and σ_∞ is the covariance matrix as $t \to \infty$. Noting that the purity of the quantum state is given by $\mu(t) = \frac{1}{2\sqrt{\det \sigma(t)}}$, we can normalize equation (3.36) by a factor of $\frac{1}{\mu}$, and calculate the purity to be

$$\mu(t) = \mu_0 \left(e^{-2\gamma t} + \frac{\mu_0^2}{\mu_\infty^2}\left(1 - e^{-\gamma t}\right)^2 + 2\frac{\mu_0}{\mu_\infty} e^{-\gamma t}\left(1 - e^{-\gamma t}\right)\cosh(2r_0)\right)^{-1/2}, \tag{3.60}$$

where μ_0 is the initial purity, μ_∞ is the purity as $t \to \infty$, r_0 is the initial squeezing (which will decay over time). Differentiating with respect to time (assuming that $r_0 > \max[\mu_0/\mu_\infty, \mu_\infty/\mu_0]$) and setting equal to zero, we can approximate the decoherence time as [211]

$$t_d = \frac{1}{\gamma} \ln\left(\frac{\frac{\mu_0}{\mu_\infty} + \frac{\mu_\infty}{\mu_0} - 2\cosh(2r_0)}{\frac{\mu_0}{\mu_\infty} - \cosh(2r_0)} \right), \tag{3.61}$$

As discussed in Section 2.3, for low temperatures, Beliaev damping is dominant and at zero-temperature is given by [90]

$$\gamma_B \approx \frac{3}{640\pi} \frac{\hbar \omega_{\vec{k}}^5}{mnc_s^5}, \tag{3.62}$$

where $\omega_{\vec{k}}$ is the frequency of the single phonon mode $\vec{k}$, m is the mass of the atoms making up the BEC, and n is the number density. For simplicity, consider the case in which r_0 is large enough such that $\ln\left(\frac{\frac{\mu_0}{\mu_\infty} + \frac{\mu_\infty}{\mu_0} - 2\cosh(2r_0)}{\frac{\mu_0}{\mu_\infty} - \cosh(2r_0)} \right) \sim \mathcal{O}(1)$. From equation (3.49), note that phonons with a frequency $\omega_{\vec{k}} \approx \frac{\Omega}{2}$ are most important for the gravitational wave detection. In this case, sensitivity to gravitational waves is maximized when our measurement duration is in the range $\frac{2\pi}{\Omega} \leq \tau \lesssim \frac{1}{\gamma_B}$. Taking our BEC to have $c_s = 1.2 \times 10^{-2}$ m/s, $n = 7 \times 10^{20}$ m^{-3}, $m = 10^{-25}$ kg, our sensitivity to gravitational waves is optimal when $\frac{2\pi}{\Omega} \leq \tau \lesssim (3.6 \times 10^2 \text{sec}) \left(\frac{f}{2\pi \cdot 10^3 \text{ Hz}}\right)^{-5}$. For a 10 kHz gravitational wave, we find $t_d \approx 3.62$ s, which is greater than the period of the gravitational wave.

We can analyze decoherence effects more rigorously by noting that the squeezing parameter evolves in time as [211]

$$\cosh[2r(t)] = \mu(t)\left(e^{-\gamma_B t}\frac{\cosh(2r_0)}{\mu_0} + \frac{1 - e^{-\gamma_B t}}{\mu_\infty} \right). \tag{3.63}$$

is the purity. We will now determine the measurement time of $\tau = t$ in order to maximize the sensitivity to gravitational waves. Taking $e^r, e^{r_0} \gg 1$ and $\mu_0 = \mu_\infty = 1$, we note that equation (3.63) behaves as

$$e^{2r} \sim \frac{e^{-\gamma_B \tau} e^{2r_0} + 1 - e^{-\gamma_B \tau}}{\sqrt{e^{-2\gamma_B \tau} + \left(1 - e^{-\gamma_B \tau}\right)^2 + 2e^{-\gamma_B \tau}\left(1 - e^{-\gamma_B \tau}\right) e^{2r_0}}}. \tag{3.64}$$

We see that the squeezing decays from $e^{2r_0} \to e^{r_0}$ on a time-scale of

$$\tau \sim \frac{\log\left(\frac{\sqrt{e^{2r_0}-e^{4r_0}-e^{6r_0}+e^{8r_0}}+2e^{2r_0}-e^{4r_0}-1}{e^{2r_0}-1}\right)}{\gamma_B} \tag{3.65}$$

Expanding in terms of e^{r_0}, we find

$$\tau \sim \frac{-\log 2 + \log 3}{\gamma_B} + \mathcal{O}\left(\frac{1}{e^{r_0}}\right) \sim \frac{2}{5\gamma_B}, \tag{3.66}$$

which provides an estimate for the decoherence time Consider phonons at a frequency of $\frac{\Omega}{2}$. For $\tau \approx \frac{2}{5\gamma_B}$ and large e^r, e^{r_0}, we can use equations (3.64) and (3.45) to find that the sensitivity at decoherence time is

$$\frac{1}{\langle(\Delta\tilde{\epsilon})^2\rangle} \sim \frac{\Omega^2 e^{4r_0}\left(1-e^{-\frac{4\Omega^2}{25\gamma_B^2}}\right)^2}{25\gamma_B^2}. \tag{3.67}$$

Let us now consider more formally how decoherence could affect the sensitivity to gravitational waves. We can incorporate decoherence into (3.45) with equation (3.63) by letting $r \to r(t)$ and following the same steps that were used to arrive at equation (3.50). We also note from [110, 170] that the purity divides the covariance matrix, equation (3.36), so $\mu(t)$ also multiplies equation (3.45). By integrating over all the modes, we can then determine an equation analogous to (3.50), such that $\langle\Delta\epsilon^2\rangle_{tot}$ now includes effects arising from decoherence. We note that this is only an approximation; decoherence should, strictly speaking, be introduced prior to solving equation (3.20), such as what was done in [110].

In Figure 3.3, we consider the maximum value of the squeezing parameter from equation (3.59) and the optimal measurement duration to maximize the sensitivity to gravitational waves in the kHz range. As we are considering all modes, in this regime $\tau \approx \frac{1}{\omega}$ (verified numerically). We see that, because of decoherence, the sensitivity decreases for higher frequencies.

It will be necessary to constantly regenerate the BEC [229, 232] in order to repeatedly perform measurements over the $t_{obs} = 10^6$ s. With such a BEC machine, it will be easier to generate and trap BECs, which could mean that it would be easier to create multiple BECs simultaneously. In equation (3.50), we assumed that the number of measurements was $M \sim t_{obs}/\tau$. For N BECs, the sensitivity to gravitational waves will improve by $1/\sqrt{N}$. To obtain a sensitivity $\frac{\sqrt{\langle\Delta\epsilon^2\rangle}}{\sqrt{f}} \approx 10^{-23}$ $\text{Hz}^{-1/2}$ to a gravitational wave of frequency $f = 10^4$ Hz using the parameters in Figure 3.1, we would therefore require $\mathcal{O}(10^{22})$ BECs, which is impractical. This number is commensurate with other work [207], though an alternative detection scheme has been argued to be possible [113]. Improved techniques of increasing the squeezing of the phonons and increasing the volume of the condensate will be necessary for a BEC kHz gravitational wave detector to be achievable.

3.5 Conclusion

We have investigated the feasibility of using a BEC as a gravitational wave detector by modelling the wave-detector interaction as $h_+ = e^{-t^2/\tau^2}\sin(\Omega t)$, where the Gaussian prefactor is included to

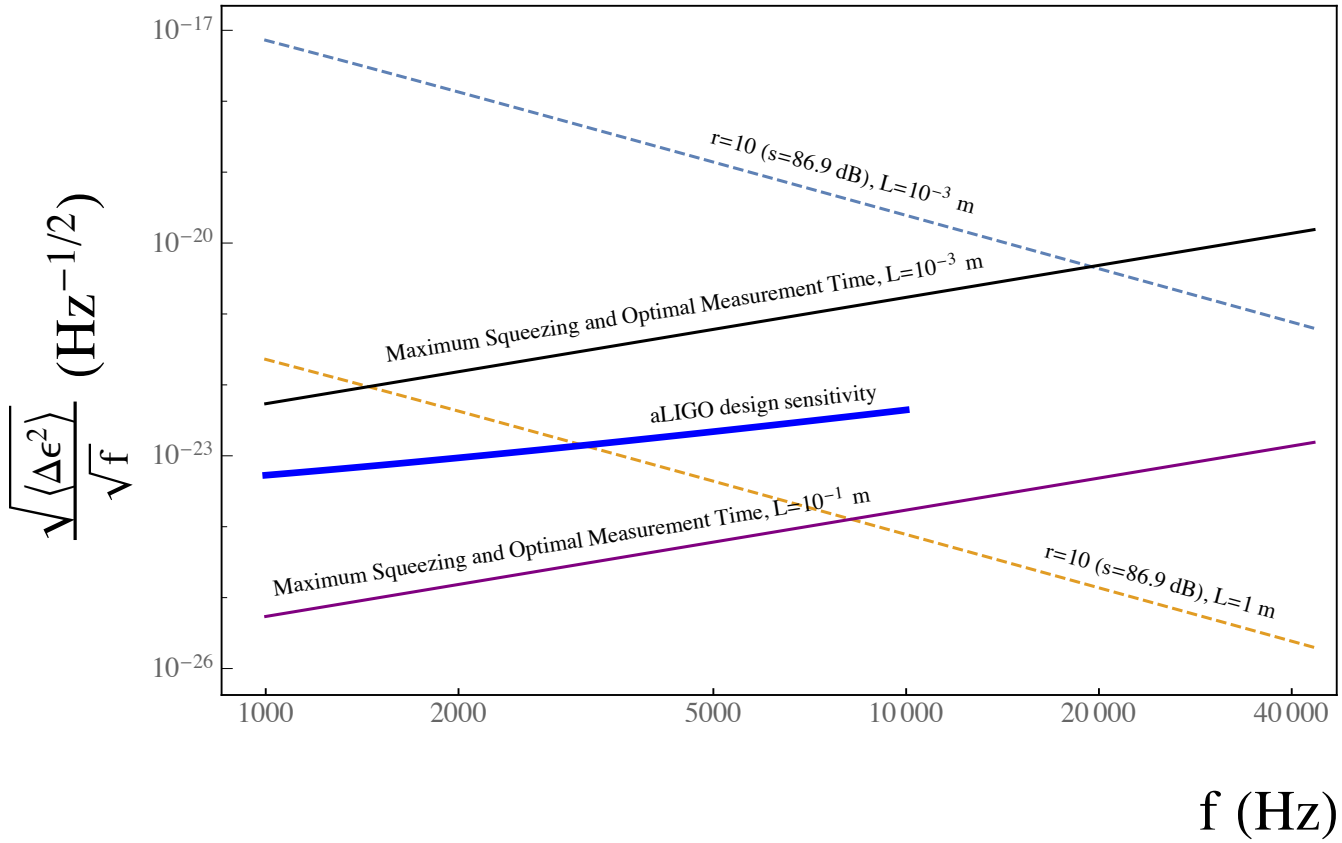

Figure 3.3: The theoretical strain sensitivity $\left(\frac{\sqrt{\langle(\Delta\epsilon)^2\rangle}}{\sqrt{f}}\right)$ of a BEC to gravitational waves of frequency f, with τ optimized and r_0 maximized within the validity of the model (solid black and purple lines), including decoherence due to interacting modes. Over this frequency range, the measurement duration corresponds to $\tau \sim \frac{1}{\omega}$. We have set $t_{obs} = 10^6$ s, $m = 10^{-25}$ kg, $n = 7 \times 10^{20}$ m^{-3}, $\mu_0 = \mu_\infty = 1$, $c_s = 1.2 \times 10^{-2}$ m/s, and $\phi = \pi/2$. To facilitate comparison, we have also considered $r = 10$ for two different condensate lengths, assuming damping to be negligible (dashed blue and orange lines), where we have $\tau = 10^{-3}$ s in both cases. The overall trend of the design sensitivity of Advanced LIGO is indicated by the thick blue line (extrapolated to 10^4 Hz).

model the measurement duration. We have derived an analytic expression in equation (3.49) for the mean-square error in the amplitude of the gravitational wave, which depends on the squeezing of the phonons in the BEC, volume of the BEC, speed of sound, and frequency of the gravitational wave. Turning to a consideration of currently available techniques to improve sensitivity within the linear dispersion regime, we find that a BEC constructed using the best possible parameters to maximize the sensitivity will be unable to detect gravitational waves in the kHz range, in contrast to the work of [199].

Though a BEC as a gravitational wave detector using initially squeezed phonon modes is currently not feasible for observing kHz gravitational waves, it could be a promising method for observing waves at this frequency once it is understood how to increase phonon squeezing as well as the volumes of BECs. In the meantime, it will be productive to analyze how properties of the BEC can be optimized to improve sensitivity to gravitational waves by investigating different trap geometries and understanding the effects of vortices and inhomogeneities on the sensitivity. Furthermore,

different trapping and optical potentials should be examined as this could have ramifications for the amount of squeezing that can be done and the speed of the phonons. The introduction of additional effects into the BEC may result in a way of using a BEC to detect gravitational waves without resorting to such large values of the squeezing parameter.

While here we focused on BECs at zero temperature, finite temperature effects can further affect the metrology and decoherence (through Landau damping), and will be studied in future work. Furthermore, we have considered a homogeneous BEC. Recent work [206] has emphasized the importance of using inhomogeneous BEC condensates, since they scale with the number of condensate atoms instead of the number of phonons as in the homogeneous case. It would be of interest to extend our work to the inhomogeneous case to see how to better optimize detection. It is only once these questions are answered that it will be possible to rival the sensitivities of LIGO (and its successors) for kHz gravitational waves.

Chapter 4

Detecting Gravitational Waves with Parametric Resonance

4.1 Introduction

In the previous chapter, we realized that, while a BEC could in principle be used to detect gravitational waves, it is necessary to squeeze the initial state of the BEC phonons well beyond current experimental capabilities. Furthermore, the natural decay of the BEC by Beliaev damping limits the sensitivity, especially at the higher frequencies of interest. A somewhat stronger critique [206] argued that non-uniform condensates are required, as otherwise the phonons produced are not within the realm of detectability, though it should be noted that the critique assumed a condensate without any boundary conditions, whereas the original proposal [199] considered a hard-wall condensate.

In the frequency regime probed by LIGO, Virgo, and KAGRA (above 100 Hz and below 1 kHz), the most common sources are binary black holes, binary neutron stars, and black hole-neutron star mergers [6]. As we discussed earlier, in the kHz regime, it is predicted that transient sources can include lower-mass black holes and neutron star mergers at frequencies outside the range that LIGO can currently observe (up to several kHz) [17, 18, 139] and magnetars (0.5-2 kHz) [226]. Depending on the model, there could potentially even be primordial black holes in the kHz domain [84]. In the continuous regime, there may be, neutron stars/pulsars (tens-hundreds of Hz) [3, 59], and boson clouds (extending into the kHz regime and above) [195].

We investigate here the possibility of improving the sensitivity of a BEC detector by modulating the speed of sound to induce a parametric resonance with the BEC phonons, which then boosts their sensitivity to gravitational waves. In contrast to previous studies [196, 199], we find that parametric resonance causes the BEC to be more sensitive to gravitational waves at lower frequencies than at higher frequencies, though detection of higher frequency gravitational waves may still be possible. The optimum sensitivity depends upon the parameters of the condensate such as its length, speed of sound and phonon frequency.

Noting that LIGO detects gravitational waves by exploiting ratios of large numbers in order to improve the sensitivity by 20 orders of magnitude [206], in our proposal close to 20 orders of magnitude can be obtained through the parametric amplification of phonons by modulations of the speed of sound. These modulations induce instabilities in the phononic modes, which we

then exploit. In addition, by repeatedly measuring the condensate over the course of a year, we exploit the ratio between the duration of a year and the period of the gravitational wave. It should be emphasized that, in contrast to [199] and [196], the initial squeezing of phonons is not a requirement of our proposal. Experimentally, this can be achieved through increased laser power, larger condensates, using a similar suspension system as LIGO to minimize vibrations in the optical setup, and squeezed light generating the trap.

The outline of the subsequent sections is as follows: In Section 4.2, we review the theory behind BECs in curved spacetime and solve the equations of motion of the phonons as well as the Bogoliubov coefficients. We also discuss the effect of parametric resonance and non-linearities in our model. In Section 4.3, we then show how quantum Fisher information is used to determine the sensitivity to gravitational waves. Next, in Section 4.4, we discuss how Beliaev damping will limit the sensitivity of the BEC to gravitational waves at high frequencies. In Section 4.5, we discuss the possible sources that a BEC could observe, consider the sensitivity of a BEC experiment to gravitational waves, comment on expected noise sources, and discuss what may be necessary to make this proposal a reality. Section 4.6 summarizes our conclusions and presents possible directions for future work.

4.2 Bose-Einstein condensates in curved spacetimes

4.2.1 Equation of Motion

Similar to Section 3.2, we first derive the equations of motion and Bogoliubov coefficients for BEC phonons in a curved spacetime. As we saw, we can rewrite the BEC Lagrangian of equation (3.2) as

$$\mathcal{L} = \frac{1}{2\lambda}\left[g^{\mu\nu}\partial_\mu\chi\partial_\nu\chi - m^2\right]^2 \ . \tag{4.1}$$

Let $\chi = \frac{mct}{\hbar} + f(t) + \pi(x^\mu)$, where $\pi(x^\mu) \in \Re$ is a pseudo-Goldstone boson representing the acoustic perturbation (phonon) field of the condensate. These phonons can be represented as fluctuations in the phase [205]. Inserting this ansatz into equation (4.1), we get

$$S = \int \frac{d^4x}{4\lambda}\sqrt{-g}\left\{(m\delta^\nu_0 + \dot{f}\delta^\nu_0 + \partial^\nu\pi)(m\delta^\mu_0 + \dot{f}\delta^\mu_0 + \partial^\mu\pi)g_{\mu\nu} - m^2\right\}^2 \ . \tag{4.2}$$

Let us take $g_{\mu\nu} = \eta_{\mu\nu} + h_{\mu\nu}$, where $[h_{\mu\nu}] \ll 1$ describes the distortion of spacetime due to a gravitational wave. As we showed in [196], the action can be written as

$$S \approx \int \frac{d^4x}{4\lambda}\left[|\dot{\pi}|^2(6\dot{f}^2 - 2m^2) + (2\dot{f}^2 - 2m^2)(\eta_{ij} + h_{ij})\partial^i\pi\partial^j\pi\right] \ , \tag{4.3}$$

where we are working in the $(+,-,-,-)$ convention and have expanded to second order in π, assuming that the higher-order terms in π can be neglected and the first-order term integrates to zero on the boundary. Therefore,

$$S \approx \int \frac{d^4x}{4\lambda}\left[|\dot{\pi}|^2 - \frac{\dot{f}(2m+\dot{f})}{2m^2 + 6m\dot{f} + 3\dot{f}^2}(\eta_{ij} + h_{ij})\partial^i\pi\partial^j\pi\right] \ . \tag{4.4}$$

We will now consider a BEC with its scattering length modulated using a Feshbach resonance,[1] such that it will have an oscillating speed of sound [78]. Let $\dot{f} = mc_s^2\,(1 + a\sin\Omega_B t)$, where c_s is the average speed of sound, Ω_B is the oscillation frequency of the applied magnetic field inducing the Feshbach resonance, and $a \ll 1$. Therefore, we find the equation of motion

$$\ddot{\psi} + c_s^2(1 + 2a\sin\Omega_B t)(\eta_{ij} + h_{ij})\partial^i\partial^j\pi = 0 \tag{4.6}$$

Let $\pi = e^{i\vec{k}\cdot\bar{x}}\psi(t)$ and assume a linear dispersion relation. We will also work in the TT-gauge and assume no cross-polarization for simplicity,

$$h_{\mu\nu} = \begin{pmatrix} 0 & 0 & 0 & 0 \\ 0 & h_+(t) & 0 & 0 \\ 0 & 0 & -h_+(t) & 0 \\ 0 & 0 & 0 & 0 \end{pmatrix} . \tag{4.7}$$

Taking $h_+(t) = \epsilon\sin\Omega t$, where ϵ is the amplitude of the continuous gravitational wave and Ω is its frequency, the equation of motion (4.6) becomes

$$\ddot{\psi} + \omega^2(1 + 2a\sin\Omega_B t)(1 + \tilde{\epsilon}\sin\Omega t)\psi = 0\ , \tag{4.8}$$

where $\omega^2 = c_s^2k^2$ and $\tilde{\epsilon} = \frac{(k_x^2 - k_y^2)}{|k|^2}\epsilon$, which we see can be interpreted as having a modulating speed of sound $\ddot{\psi} + k^2c_s(t)^2\psi = 0$. Part of the modulation arises from Feshbach resonance, with the other part of the modulation arising due to gravitational waves.

Let $\omega_1(t)^2 = \omega^2(1 + \tilde{\epsilon}\sin\Omega t + 2a\sin\Omega_B t + 2a\tilde{\epsilon}\sin\Omega t\sin\Omega_B t)$. As we want to consider the gravitational wave on resonance with the frequency of the modulations of the speed of sound, we will take $\Omega_B = \Omega$. We can expand to first-order in ϵ and second-order in a (neglecting the $\mathcal{O}(a\tilde{\epsilon})$ terms as $a\tilde{\epsilon} \ll a$). We will see that it is the presence of the $\mathcal{O}(a)$ terms that induce parametric resonance within the condensate.

To solve equation (4.8) in this approximation, let us assume that we can decompose the solutions as [37]

$$\pi = \alpha(t)\frac{e^{-i\int\omega_1(t')dt'}}{\sqrt{2\omega_1(t)}} + \beta(t)\frac{e^{i\int\omega_1(t')dt'}}{\sqrt{2\omega_1(t)}}\ , \tag{4.9}$$

$$\dot{\pi} = -i\alpha(t)\sqrt{\frac{\omega_1(t)}{2}}e^{-i\int\omega_1(t')dt'} + i\beta(t)\sqrt{\frac{\omega_1(t)}{2}}e^{i\int\omega_1(t')dt'}\ , \tag{4.10}$$

where $\alpha(t)$ and $\beta(t)$ are time-dependent Bogoliubov coefficients that satisfy the coupled differential equations

$$\dot{\alpha} = \frac{\dot{\omega}_1}{2\omega_1}e^{2i\int\omega_1(t')dt'}\beta(t) \qquad \dot{\beta} = \frac{\dot{\omega}_1}{2\omega_1}e^{-2i\int\omega_1(t')dt'}\alpha(t) \tag{4.11}$$

[1] When an atom has a Feshbach resonance, applying a magnetic field changes the scattering length, such that [85]

$$a_s = a_{bg}\left(1 - \frac{\Delta}{B - B_0}\right)\ , \tag{4.5}$$

where a_s is the scattering length, a_{bg} is the background scattering length, B is the magnetic field, B_0 is the strength of the magnetic field at resonance, and Δ is the width of the resonance. We see that by varying a magnetic field, this will induce a varying scattering length. As the speed of sound is $c_s \propto \sqrt{a}$, the speed of sound will also oscillate.

We will solve these coupled equations using the method outlined in [249]. Setting $\hat{\alpha} = e^{-i\bar{\omega}t}\alpha$ and $\hat{\beta} = e^{i\bar{\omega}t}\beta$, where $\bar{\omega} = \frac{1}{T}\int_0^T \omega_1(t)dt$, we derive in Appendix A to obtain

$$\frac{d}{dt}\begin{pmatrix}\hat{\alpha}\\ \hat{\beta}\end{pmatrix} = \begin{pmatrix} -i\bar{\omega} & \frac{\dot{\omega}_1}{2\omega_1}e^{2i\int\delta\omega(t')dt'} \\ \frac{\dot{\omega}_1}{2\omega_1}e^{-2i\int\delta\omega(t')dt'} & i\bar{\omega}\end{pmatrix}\begin{pmatrix}\hat{\alpha}\\ \hat{\beta}\end{pmatrix}\ , \tag{4.12}$$

where $\delta\omega(t) = \omega_1(t) - \bar{\omega}$. Let $\hat{\alpha} = \hat{\alpha}_0 + b\hat{\alpha}_1 + b^2\hat{\alpha}_2$ and $\hat{\beta} = \hat{\beta}_0 + b\hat{\beta}_1 + b^2\hat{\beta}_2$, where $b = 2a + \epsilon \ll 1$. Note that, up to second order in b, $\bar{\omega} = \omega\left(1 - \frac{b^2}{16}\right)$.

Substitution into equation (4.12), solving order-by-order, and restricting ourselves to solving the system after each period, we can define:

$$\begin{pmatrix}\hat{\alpha}(T)\\ \hat{\beta}(T)\end{pmatrix} = M\begin{pmatrix}\hat{\alpha}(0)\\ \hat{\beta}(0)\end{pmatrix} = \begin{pmatrix}M_{11} & M_{12}\\ M_{12}^* & M_{22}\end{pmatrix}\begin{pmatrix}\hat{\alpha}(0)\\ \hat{\beta}(0)\end{pmatrix}\ , \tag{4.13}$$

where after a a period $T = 2\pi/\Omega$, we have

$$M_{11} = \frac{e^{-2i\pi q}\left(4 + q^2\left(b^2\left(-\left(-8i\pi q^3 + 2i\pi q + e^{4i\pi q} - 1\right)\right) + 64q^2 - 32\right)\right)}{4\left(1 - 4q^2\right)^2}\ , \tag{4.14}$$

$$M_{12} = \frac{bq\left(-3ibq + 4q^2 - 4\right)\sin(2\pi q)}{4\left(4q^4 - 5q^2 + 1\right)}\ , \tag{4.15}$$

$$M_{22} = \frac{e^{-2i\pi q}\left(-b^2q^2 + e^{4i\pi q}\left(4 + q^2\left(b^2\left(-8i\pi q^3 + 2i\pi q + 1\right) + 64q^2 - 32\right)\right)\right)}{4\left(1 - 4q^2\right)^2}\ . \tag{4.16}$$

We have assumed that $\hat{\alpha}_1(0) = \hat{\beta}_1(0) = \hat{\alpha}_2(0) = \hat{\beta}_2(0) = 0$. We see that the 1st order resonance occurs when $q \approx \frac{1}{2}$.

After N periods of the gravitational wave oscillations (or equivalently after N periods of the trap modulation), we have

$$\begin{pmatrix}\hat{\alpha}(NT)\\ \hat{\beta}(NT)\end{pmatrix} = \begin{pmatrix}e^{-2\pi iqN}\alpha(NT)\\ e^{2\pi iqN}\beta(NT)\end{pmatrix} = M^N\begin{pmatrix}\hat{\alpha}(0)\\ \hat{\beta}(0)\end{pmatrix}\ . \tag{4.17}$$

Diagonalizing M and writing $\begin{pmatrix}\hat{\alpha}(0)\\ \hat{\beta}(0)\end{pmatrix} = k_1\lambda_1\vec{x}_1 + k_2\lambda_2\vec{x}_2$, where $\lambda_i, \vec{x}_i$ are the eigenvalues/eigenvectors of M and k_i are coefficients related to the eigenvalues, we see

$$\begin{pmatrix}\hat{\alpha}(NT)\\ \hat{\beta}(NT)\end{pmatrix} = k_1\lambda_1^N\vec{x}_1 + k_2\lambda_2^N\vec{x}_2\ . \tag{4.18}$$

Let λ_2 correspond to the eigenvalue whose magnitude is less than one around resonance. We can neglect this term because it will become negligible after many periods. Therefore, the only relevant quantities are

$$k_1 = -\frac{b\left(128\zeta^3 - 64i\zeta^2 + 3\zeta + i\right) + 128\zeta^2 - 2}{4\left(1 - 64\zeta^2\right)^{3/2}} \tag{4.19}$$

$$\lambda_1 = \pi b^2\left(\frac{5\sqrt{1 - 64\zeta^2}\zeta}{512\zeta^2 - 8} + \pi\left(2\zeta^2 - \frac{1}{32}\right)\right) - \frac{1}{4}\pi b\sqrt{1 - 64\zeta^2} - 1 \tag{4.20}$$

where $\zeta \equiv (q - \frac{1}{2})/b$, and

$$\vec{x}_1 = \begin{pmatrix} x_0 + bx_1 + b^2 x_2 \\ 1 \end{pmatrix} \tag{4.21}$$

with

$$x_0 = \sqrt{1 - 64\zeta^2} - 8i\zeta \tag{4.22}$$

$$x_1 = 8i\zeta^2 + \frac{\zeta(3 + 64\zeta(2\zeta - i)) + i}{2\sqrt{1 - 64\zeta^2}} + 4\zeta + \frac{3i}{16} \tag{4.23}$$

$$x_2 = -16i\zeta^3 + \frac{28\zeta^2}{3} - \frac{1}{12}i\pi^2\zeta + \frac{37i\zeta}{16} - \frac{3}{32} \tag{4.24}$$

$$+ \frac{-219 + 128\zeta\left(4\zeta\left(2\pi^2\left(64\zeta^2 - 1\right) + 16\zeta(4\zeta(-63 + 32\zeta(12\zeta + 7i)) - 43i) + 75\right) + 29i\right)}{1536\left(1 - 64\zeta^2\right)^{3/2}} \tag{4.25}$$

Let us further define $\alpha_{2a+\tilde{\epsilon}} = \alpha_{2a} + \tilde{\epsilon}\alpha_{\tilde{\epsilon}}$ and $\beta_{2a+\tilde{\epsilon}} = \beta_{2a} + \tilde{\epsilon}\beta_{\tilde{\epsilon}}$. The goal is to calculate the Bogoliubov coefficients $\alpha_{\tilde{\epsilon}}$ and $\beta_{\tilde{\epsilon}}$, which correspond to the effect solely due to the of the gravitational wave interacting with the speed of sound modulation. Using the definition of the Bogoliubov coefficients, we can write $\hat{a}_0 = \alpha_{2a+\tilde{\epsilon}}\hat{a}_{2a+\tilde{\epsilon}} + \beta^*_{2a+\tilde{\epsilon}}\hat{a}^\dagger_{2a+\tilde{\epsilon}}$, where $\hat{a}_0$ is the the annihilation operator in the mode decomposition with no gravitational wave or modulation and $\hat{a}_{2a+\tilde{\epsilon}}$ is the annihilation operator in the mode decomposition containing both a gravitational wave and modulation. Thus $\hat{a}_{2a+\tilde{\epsilon}} = \alpha^*_{2a+\tilde{\epsilon}}\hat{a}_0 - \beta^*_{2a+\tilde{\epsilon}}\hat{a}^\dagger_0$. We can also write $\hat{a}_{2a+\tilde{\epsilon}} = \alpha_{rel}\hat{a}_{2a} - \beta^*_{rel}\hat{a}^\dagger_{2a}$. Therefore,

$$\hat{a}_{2a+\tilde{\epsilon}} = \alpha^*_{2a+\tilde{\epsilon}}\left(\alpha_{2a}\hat{a}_{2a} + \beta^*_{2a}\hat{a}^\dagger_{2a}\right) - \beta^*_{2a+\tilde{\epsilon}}\left(\alpha^*_{2a}\hat{a}^\dagger_{2a} + \beta_{2a}\hat{a}_{2a}\right) \tag{4.26}$$

$$= \left(\alpha^*_{2a+\tilde{\epsilon}}\alpha_{2a} - \beta^*_{2a+\tilde{\epsilon}}\beta_{2a}\right)\hat{a}_{2a} + \left(\alpha^*_{2a+\tilde{\epsilon}}\beta^*_{2a} - \beta^*_{2a+\tilde{\epsilon}}\alpha^*_{2a}\right)\hat{a}^\dagger_{2a} \ . \tag{4.27}$$

With $\alpha_{2a+\tilde{\epsilon}} = \alpha_{2a} + \tilde{\epsilon}\alpha_{\tilde{\epsilon}}$ and $\beta_{2a+\tilde{\epsilon}} = \beta_{2a} + \tilde{\epsilon}\beta_{\tilde{\epsilon}}$, we see

$$\alpha^*_{rel} = 1 + \tilde{\epsilon}\left(\alpha^*_{\tilde{\epsilon}}\alpha_{2a} - \beta^*_{\tilde{\epsilon}}\beta_{2a}\right) \ , \tag{4.28}$$

$$\beta^*_{rel} = -\tilde{\epsilon}\left(\alpha^*_{\tilde{\epsilon}}\beta^*_{2a} - \beta^*_{\tilde{\epsilon}}\alpha^*_{2a}\right) \ . \tag{4.29}$$

Resonance

Equation (4.8) is a perturbed form of the Mathieu differential equation (as $a\tilde{\epsilon}$ is a sub-dominant term), which implies that our system includes parametric resonance effects [70, 161].

In Figure 4.1a, we show the locations of the first four resonances of the system, where the shading illustrates the instability bands associated with each individual resonance in the Mathieu equation (Figure 4.1a) [188]. For a system lying within these bands (indicated by the shaded regions), evolution is unstable and will become non-perturbative after a certain amount of time, with the amount of time before non-perturbative effects occurs depending on the precise location within these regions. In Figure 4.1b, we see that if $q = \frac{\omega}{\Omega}$ is too far off the resonance, the instability band is exited, which limits production of particles and nonlinearities.

By considering phonons with frequencies that that are within the instability bands (locations of parametric resonance) for a time t, we can enhance the sensitivity of the BEC to gravitational waves. In Section 4.2.1, we address the maximum time that we can lie within the regions of instability before the system becomes non-perturbative in a.

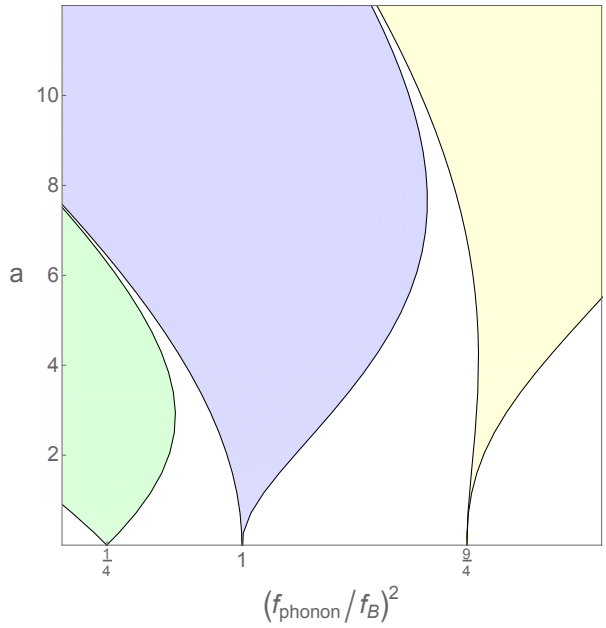

(a) Shaded areas show the locations of instability bands in $(a, f_{phonon}/f_B)$ plane, associated with resonances between the speed of sound oscillations and the gravitational wave of equation (4.8), such that $f_B = f_{GW}$. By lying within these regions for a time t, it is possible to improve the sensitivity to gravitational waves. Note that maximum value of the phonon frequency will be constrained by the chemical potential of the condensate.

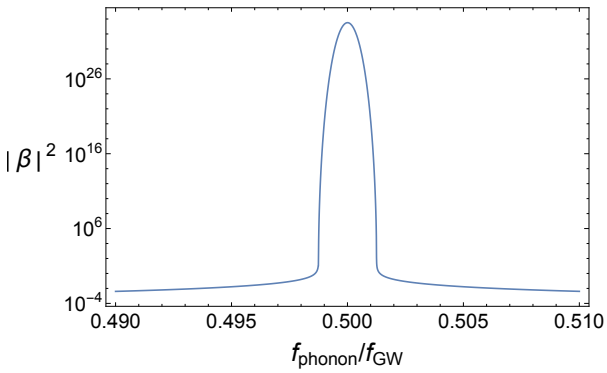

(b) The first resonance of our undamped system, where for illustrative purposes, we set $N = 5 \times 10^3$ and $a = 0.005$ Note that $|\beta|^2$ is maximized around $q \approx \frac{1}{2}$, before there is a sharp cutoff around $q = 0.499$ and $q = 0.501$. This corresponds to moving outside the instability band.

Figure 4.1: Resonances of the Mathieu equation.

Our focus has been on parametric resonance, though additional effects could also be considered, such as direct driving and mode coupling [189]. However, we note that mode-mode coupling can be neglected as it will not couple the Bogoliubov coefficients of our phonons. We also note that direct driving will be a higher order effect that can also be neglected.

Non-linearities

Similar to [196], we have the constraint of $\dot{\pi} \ll \mu = mc_s^2$. By squaring both sides (as $\langle \dot{\pi} \rangle = 0$) and writing $\dot{\pi}$ as a sum of creation and annihilation operators, we find that this is equivalent to $\sum_{\vec{k}} |\beta_{2a,\vec{k}}|^2 \hbar\omega_{\vec{k}} \ll nmc_s^2 L^3$, where L^3 is the volume of the condensate (taking the BEC to be cubic with sides of length L), n is the number density, m is the mass of the atoms, and $|\beta_{2a,\vec{k}}|^2$ is the number of phonons present in each mode $\vec{k}$ [2].

Rewriting $|\beta_{2a,\vec{k}}|^2$ in terms of $q = \frac{\omega}{\Omega}$ and assuming that the BEC is constructed such that only a single phonon mode dominates the resonance instability (i.e., the most unstable mode), we note that at each value of q, there is a maximum number of trap oscillations $N(q)$ satisfying $\frac{|\beta_{2a,q}|^2 \hbar\omega_q}{\rho L^3} \lessapprox 0.05$, where we relabel $|\beta_{2a,\vec{k}}|^2$ as $|\beta_{2a,q}|^2$ to explicitly indicate the dependence on q.

[2] Accounting for the effect of the gravitational wave on this energy condition is negligible.

Physically, $N(q)$ describes the maximum time that a gravitational wave could be observed by the condensate before the condensate becomes non-linear (because, by assumption, we take the frequency of the speed of sound oscillation to be the same as the period of the gravitational wave). Noting that $|\beta_{2a,q}|^2 = |k_1|^2|\lambda_1|^{2N}$, we see that

$$N \leq \frac{\log\left[\frac{0.05mnc_S^2L^3}{\pi\hbar q f_{GW}|k_1|^2}\right]}{2\log[|\lambda_1|]} \,. \tag{4.30}$$

In Figure 4.2, we demonstrate the dependence of N on q, the size of the condensate, and the frequency of the trap modulation. We consider a cross-section of this plot in Figure 4.3. Throughout

Maximum number of gravitational wave periods detectable by a BEC.

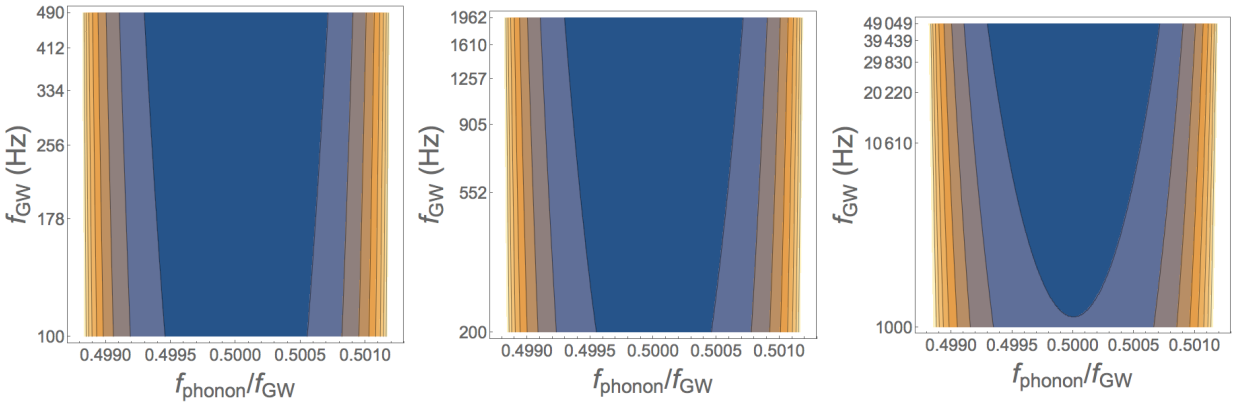

(a) $c_s = 0.5$ cm/s, $L = 100$ μm (b) $c_s = 1$ cm/s, $L = 100$ μm (c) $c_s = 5$ cm/s, $L = 100$ μm

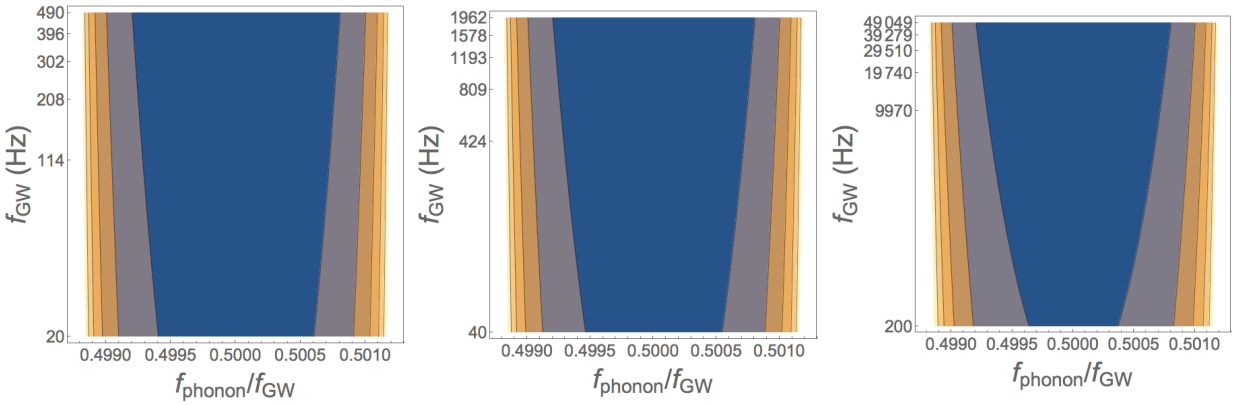

(d) $c_s = 0.5$ cm/s, $L = 500$ μm (e) $c_s = 1$ cm/s, $L = 500$ μm (f) $c_s = 5$ cm/s, $L = 500$ μm

Figure 4.2: Dependence of the number of cycles N needed to reach non-linearity, on $q = \frac{f_{\text{phonon}}}{f_{\text{GW}}}$ and the frequency (assuming $f_{\text{GW}} = f_B$) for an undamped condensate. We see that, in general, the condensate is sensitive to a greater number of oscillations when considering a smaller frequency and larger condensates. We take the number density to be 10^{20} m^{-3} of ^{39}K atoms. The time to non-linearity is simply N/f_{GW}.

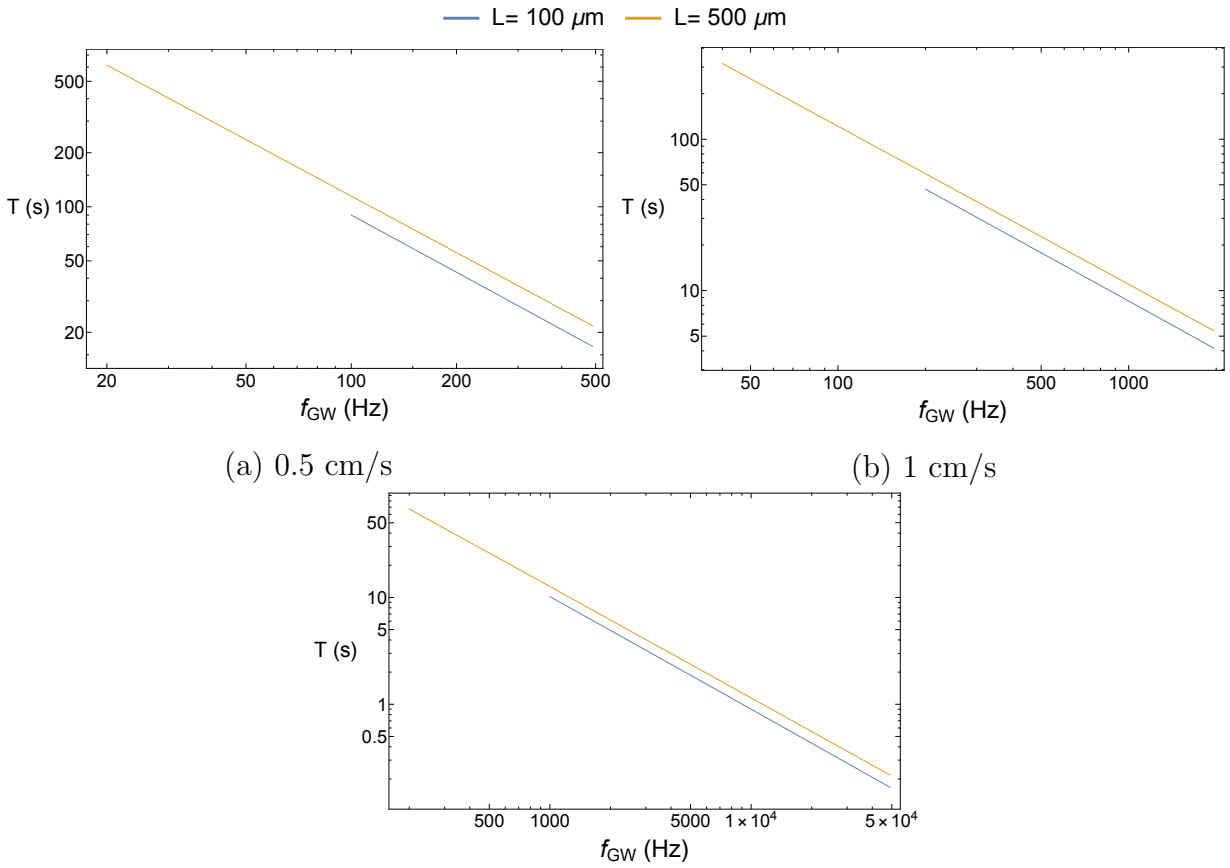

(a) 0.5 cm/s

(b) 1 cm/s

(c) 5 cm/s

Figure 4.3: Observation time for a gravitational wave interacting with a BEC with $q = 0.501245$. Lower frequencies correspond to longer observational times. We note that this neglects the effects of 3-body recombination, which limits the condensate lifetime. We discuss this effect further in Section 4.5). For smaller values of q (i.e. closer to the resonance peak), the maximum observational time of the condensate decreases.

the remainder of this paper, all calculations and discussions will assume that this non-linearity condition is saturated.

4.3 Estimating the sensitivity to gravitational waves

As phonons are affected by the gravitational wave, the gravitational wave's amplitude is imprinted on the phonon's density matrix. The question then becomes how to extract the gravitational wave amplitude from the density matrix. This can be done by exploiting techniques in quantum metrology, which allows measurements to be done on quantities in quantum systems that are not operator observables [65, 91, 92, 199]. In this Section, we will be determine the sensitivity of an undamped condensate at zero-temperature with no extra sources of noise in the system. In Section 4.4, we will consider the more realistic case by investigating the sensitivity of a damped BEC.

As we discussed in Chapters 1 and 3, Given a parameter $\tilde{\epsilon}$ in a quantum system, the quantum

Cramer-Rao bound is [38]

$$\langle(\Delta\epsilon)^2\rangle \geq \frac{1}{MH_\epsilon} \ , \tag{4.31}$$

where $\langle(\Delta\epsilon)^2\rangle$ is the expectation value of the uncertainty in ϵ, M is the number of measurements of the system, and H_ϵ is the Fisher information [10, 38]

$$H_\epsilon = \frac{8\left(1-\sqrt{F(\rho_\epsilon,\rho_{\epsilon+d\epsilon})}\right)}{d\epsilon^2} \ , \tag{4.32}$$

with $F(\rho_\epsilon,\rho_{\epsilon+d\epsilon}) = \left[\mathrm{Tr}\sqrt{\sqrt{\rho_\epsilon}\rho_{\epsilon+\mathrm{d}\epsilon}\sqrt{\rho_\epsilon}}\right]^2$ quantifying the overlap (fidelity) between the states ρ_ϵ and $\rho_{\epsilon+d\epsilon}$ [121, 239]. Note that we can recast equations (4.28) and (4.29) as $\alpha_{rel} = e^{-i\theta_\alpha}\cosh r_{rel}$ and $\beta_{rel} = e^{-i\theta_\beta}\cosh r_{rel}$, where r_{rel} is the squeezing that results from the gravitational wave and $e^{-i\theta_\alpha}, e^{-i\theta_\beta}$ are phase factors.[3]

Let us suppose that before a gravitational wave interacts with the condensate, our phonons are in a squeezed state, with squeezing parameter r_0 and quadrature angle ϕ_0, where the state of the phonons is $|\zeta_0\rangle = S_0\,|0\rangle = \exp\left[\frac{1}{2}(\zeta_0^*\hat{a}^2 - \zeta_0\hat{a}^{\dagger 2})\right]|0\rangle$, S_0 is the squeezing operator, and $\zeta_0 = r_0 e^{i\phi_0}$.

Let $\epsilon_1 = \tilde{\epsilon}$ and $\epsilon_2 = \tilde{\epsilon} + d\epsilon$. In a pure state, $\rho_\epsilon = |\epsilon\rangle\langle\epsilon|$, so the fidelity is

$$F(\rho_{\epsilon_1,\epsilon_2}) = Tr\left[\sqrt{|\epsilon_1\rangle\langle\epsilon_1|\epsilon_2\rangle\langle\epsilon_2|\epsilon_1\rangle\langle\epsilon_1|}\right] = |\langle\epsilon_1|\epsilon_2\rangle| \, . \tag{4.33}$$

Therefore, the quantum Fisher information is $H_\epsilon = \frac{8(1-|\langle\epsilon_1|\epsilon_2\rangle|)}{(\epsilon_1-\epsilon_2)^2}$. The state after interaction with a gravitational wave is $|\epsilon_i\rangle = S_{\epsilon_i}S_0\,|0\rangle$, where S_{ϵ_i} encodes the gravitational wave's influence. Then, $S_{rel} := S_{\epsilon_1}^\dagger S_{\epsilon_2}$, we have

$$\langle\epsilon_1|\epsilon_2\rangle = \langle 0|S_0^\dagger S_{rel} S_0|0\rangle \tag{4.34}$$

$$= \langle 0|S_0^\dagger \exp\left[\frac{1}{2}(\zeta_{rel}^*\hat{a}^2 - \zeta_{rel}\hat{a}^{\dagger 2})\right] S_0|0\rangle \tag{4.35}$$

where $\zeta_{rel} = r_{rel}e^{i\phi_{rel}}$. Noting that $r_{rel} \propto \epsilon_1 - \epsilon_2$, we have

$$\langle\epsilon_1|\epsilon_2\rangle \sim 1 + \frac{1}{2}\langle 0|S_0^\dagger\left(\zeta_{rel}^*\hat{a}^2 - \zeta_{rel}\hat{a}^{\dagger 2}\right)S_0|0\rangle + \frac{1}{8}\langle 0|S_0^\dagger\left(\zeta_{rel}^*\hat{a}^2 - \zeta_{rel}\hat{a}^{\dagger 2}\right)^2 S_0|0\rangle \tag{4.36}$$

Let $Q = \zeta_{rel}^*\hat{a}^2 - \zeta_{rel}\hat{a}^{\dagger 2}$. Then,

$$\langle\epsilon_1|\epsilon_2\rangle\langle\epsilon_1|\epsilon_2\rangle^* = \left(1 + \frac{1}{2}\langle 0|S_0^\dagger Q S_0|0\rangle + \frac{1}{8}\langle 0|S_0^\dagger Q^2 S_0|0\rangle\right)\left(1 + \frac{1}{2}\langle 0|S_0^\dagger Q^\dagger S_0|0\rangle + \frac{1}{8}\langle 0|S_0^\dagger Q^{\dagger 2} S_0|0\rangle\right) \tag{4.37}$$

Noting that $\langle 0|S_0^\dagger Q S_0 + S_0^\dagger Q^\dagger S_0|0\rangle = 0$, we see that to second-order in $\epsilon_1 - \epsilon_2$, we have

$$|\langle\epsilon_1|\epsilon_2\rangle|^2 = 1 + \frac{1}{8}\langle 0|S_0^\dagger Q^2 S_0|0\rangle + \frac{1}{8}\langle 0|S_0^\dagger Q^{\dagger 2} S_0|0\rangle + \frac{1}{4}\langle 0|S_0^\dagger Q S_0|0\rangle\langle 0|S_0^\dagger Q^\dagger S_0|0\rangle \ , \tag{4.38}$$

[3] We note that Bogoliubov coefficients obey the relation $|\alpha|^2 - |\beta|^2 = 1$, which is reminiscent of the hyperbolic trigonometric relation, $\cosh(x)^2 - \sinh(x)^2 = 1$.

where we note that the first-order terms in ϵ vanish because of antisymmetry. As we show in Appendix B, we can use $S_0^\dagger a S_0 = a\cosh r_0 - a^\dagger e^{i\phi_0}\sinh r_0$ and $S_0^\dagger a^\dagger S_0 = a^\dagger \cosh r_0 - a e^{-i\phi_0}\sinh r_0$ to find

$$\langle 0|S_0^\dagger a^{\dagger 2} S_0|0\rangle = -e^{-i\phi_0}\cosh r_0 \sinh r_0 \tag{4.39}$$
$$\langle 0|S_0^\dagger a^2 S_0|0\rangle = -e^{i\phi_0}\cosh r_0 \sinh r_0 \tag{4.40}$$
$$\langle 0|S_0^\dagger a^{\dagger 4} S_0|0\rangle = 3e^{-2i\phi_0}\cosh^2 r_0 \sinh^2 r_0 \tag{4.41}$$
$$\langle 0|S_0^\dagger a^4 S_0|0\rangle = 3e^{2i\phi_0}\cosh^2 r_0 \sinh^2 r_0 \tag{4.42}$$
$$\langle 0|S_0^\dagger a^2 a^{\dagger 2} S_0|0\rangle = 2\cosh^4 r_0 + \cosh^2 r_0 \sinh^2 r_0 \tag{4.43}$$
$$\langle 0|S_0^\dagger a^{\dagger 2} a^2 S_0|0\rangle = 2\sinh^4 r_0 + \cosh^2 r_0 \sinh^2 r_0 \,. \tag{4.44}$$

We then calculate

$$|\,\langle 0|S_0^\dagger Q S_0|0\rangle\,|^2 = 4r_{rel}^2 \sinh^2(r_0)\cosh^2(r_0)\sin^2(\phi_0 - \phi_{rel}) \tag{4.45}$$

and

$$\begin{aligned}\langle 0|S_0^\dagger Q^2 S_0|0\rangle &= \zeta_{rel}^{*2}\langle 0|S_0^\dagger a^{\dagger 4} S_0|0\rangle + \zeta_{rel}^2\langle 0|S_0^\dagger a^4 S_0|0\rangle - |\zeta_{rel}|^2\langle 0|S_0^\dagger a^{\dagger 2}a^2 S_0 + S_0^\dagger a^2 a^{\dagger 2} S_0|0\rangle \\ &= -2r_{rel}^2\left(\sinh^2(r)\cosh^2(r)(1-3\cos(2(\phi+\phi_{rel}))) + \sinh^4(r) + \cosh^4(r)\right)\,,\end{aligned} \tag{4.46}$$

where we note $\langle 0|S_0^\dagger Q^2 S_0|0\rangle = \langle 0|S_0^\dagger Q^{\dagger 2} S_0|0\rangle$.

Therefore, after averaging over angles and using $H_\epsilon = \frac{8\left(1-|\langle\epsilon_1|\epsilon_2\rangle|\right)}{d\epsilon^2}$, we get

$$(\epsilon_1 - \epsilon_2)^2 H_\epsilon = \frac{1}{4} r_{rel}^2\left(\cosh^4 r_0 + \sinh^4 r_0\right)\,. \tag{4.47}$$

Recalling from above that $|\alpha_{rel}| = \cosh r_{rel}$ and $|\beta_{rel}| = \sinh r_{rel}$, we see that $|\alpha_{rel}| + |\beta_{rel}| = \exp r_{rel}$. We also note that $|\zeta_{rel}| = r_{rel}$, so we see that

$$|\zeta_{rel}| = \ln\left[|\alpha_{rel}| + |\beta_{rel}|\right]\,. \tag{4.48}$$

Applying equations (4.28)-(4.29), we find $r_{rel} \sim \left(\Re\left[\alpha_{rel}^{(1)}\right] + |\beta_{rel}|\right)^2 \tilde{\epsilon}^2$, where $\alpha_{rel} = 1 + \tilde{\epsilon}\alpha_{rel}^{(1)}$ Therefore, with equations (4.31) and (4.47), the sensitivity to gravitational waves is given by

$$\langle(\Delta\tilde{\epsilon})^2\rangle = \frac{4}{M\left(\Re\left[\alpha_{rel}^{(1)}\right] + |\beta_{rel}|\right)^2(\cosh 4r_0 + 3)}\,. \tag{4.49}$$

In this and all subsequent considerations, we take $M = 1$. This corresponds to a gravitational wave interacting with a M BECs for N periods. We also assume that the BEC can continuously be regenerated over the course of a year [229, 232], similar to the BEC machine idea suggested by [199] such that observations can be continuously made of a gravitational wave, whose frequency remains approximately constant over the total time of observation. In this case, we find

$$\sqrt{\langle(\Delta\tilde{\epsilon})^2\rangle} = \sqrt{\frac{1}{N_{tot}}}\frac{2}{\left(\Re\left[\alpha_{rel}^{(1)}\right] + |\beta_{rel}|\right)\sqrt{\cosh 4r_0 + 3}}\,, \tag{4.50}$$

where N_{tot} is the total number of regenerations of the condensates. For simplicity, we consider a year of continuous observation, so $N_{tot} \approx \frac{1\text{yr}}{N/f}$.

We note that, in practice, it would be quite difficult to reconstruct the BEC with exactly the same properties. Extra source noise would be introduced into the system, and so such a BEC machine would be beneficial only if the noise resulting from an inexact replication is smaller than the gain in sensitivity resulting from multiple BEC experiments.

We also note that, in equation (4.50), we are calculating the sensitivity of the scaled gravitational wave amplitude $\tilde{\epsilon}$, rather than ϵ itself. To obtain $\langle(\Delta\epsilon)^2\rangle$ from $\langle(\Delta\tilde{\epsilon})^2\rangle$, one can either average or maximize over the components $k_{x,y}$ of the wavevector. As both methods scale the estimation of the gravitational wave amplitude by $\mathcal{O}(1)$, we will not include this effect in our subsequent calculations and Figures.

As the BEC has a finite size, we note that the minimum gravitational wave frequency that can be observed is $f \approx \frac{2c_s}{L}$ (where we use the relation that resonance between the gravitational wave and phonon occurs at $q = \frac{\omega}{\Omega} \approx \frac{1}{2}$ and c_s is the speed of the phonons). The maximum frequency observed is derived from the chemical potential $\mu = mc_s^2$, which sets the upper bound on the frequency of phonons created: $f \ll \mu$. Again using $q \approx \frac{1}{2}$, we see that the maximum gravitational wave frequency is $f \approx \frac{2mc_s^2}{2\pi\hbar\times 10}$, where the 10 comes from the inequality. We show in Figure 4.4 how the frequency bands of our gravitational wave detector are dependent on the speed of sound and length of the condensate. For lower-frequency gravitational wave detection, a larger condensate is required while high-frequency gravitational wave detection requires a faster speed of sound.

To illustrate the sensitivity to gravitational waves, we take the number density to be 10^{20} m^{-3} and a mass of the atoms to be 10^{-25} kg. In Figures 4.5 and 4.6, we consider the sensitivity of an (undamped) BEC and illustrate the effect of q, length of the condensate, and frequency of incoming

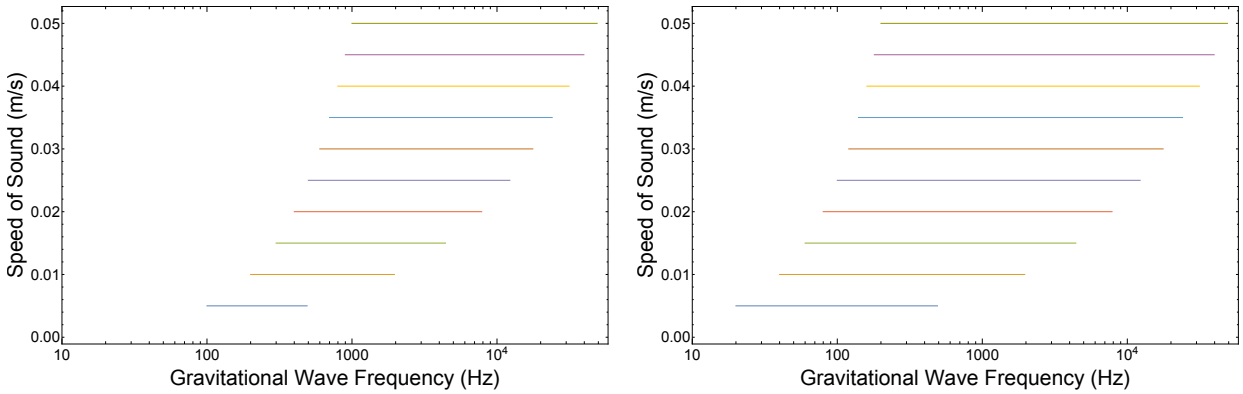

(a) $L = 100$ μm (b) $L = 500$ μm

Figure 4.4: Frequency regime of a BEC gravitational wave detector for ^{39}K atoms. Note that the larger condensates can probe lower-frequency gravitational waves, whereas those with faster speeds of sound can probe higher-frequency gravitational waves.

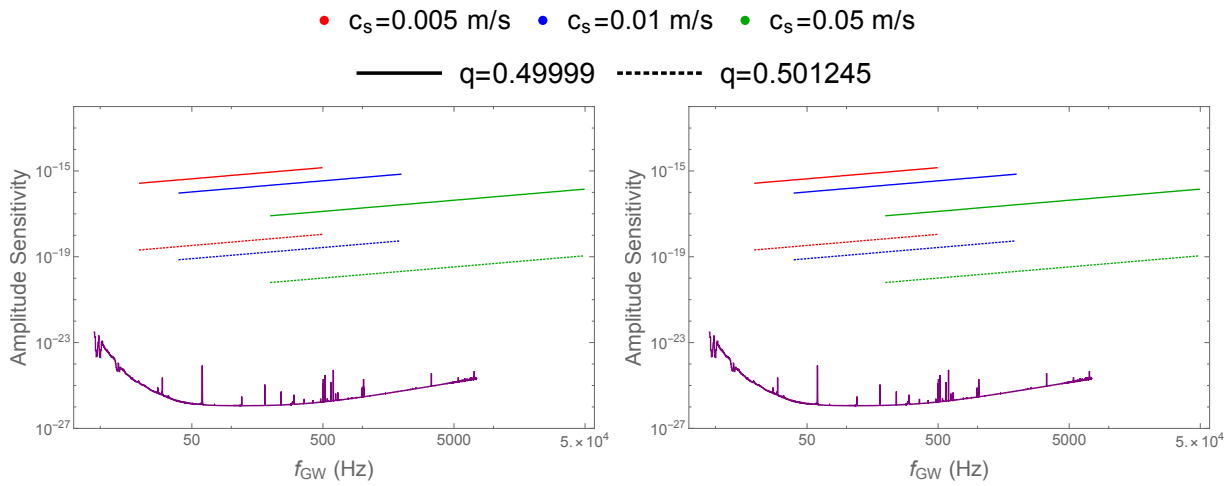

(a) $L = 100$ μm (b) $L = 500$ μm

Figure 4.5: The amplitude sensitivity $\left(\sqrt{\langle(\Delta\epsilon)^2\rangle}\right)$ of an undamped BEC gravitational wave when on resonance with an oscillating speed of sound. In each case, the condensate is observed for the maximum number of oscillations $N(q)$. We conduct the hypothetical experiment over the course of a year. We take the number density to be 10^{20} m^{-3} of ^{39}K atoms). The dashed lines represent different values of q, while the different colours are different values of c_s. Purple is the sensitive corresponding to LIGO.

gravitational waves on strain sensitivity. We note that a BEC in a speed of sound-modulated trap is most sensitive to lower frequency gravitational waves, in contrast to [199] and [196]. In Section 4.4, we consider a more realistic situation by modelling Beliaev damping of the phonons within the condensate [95].

This effect of having greater sensitivity away from resonance must be highlighted. When the system is away from $\frac{\omega}{\Omega} = \frac{1}{2} \pm \delta$, where $\delta \ll 1$, we saw that the sensitivity to gravitational waves is actually increased. In these off-resonance cases, the population of phonons grows more slowly, which corresponds to total energy growing more slowly. Hence we can observe gravitational waves for a longer time (a cross-section of this effect is illustrated in Figure 4.5).

4.4 Damping

In Section 4.3, we considered an undamped BEC with no additional sources of noise and demonstrated that, if such a system could be created, then a BEC could potentially be used to detect gravitational waves across several orders of magnitude in frequency, depending on the speed of the phonons and the length of the condensate. In reality, even at zero-temperature (which was implicitly considered), the phonons within the BEC will naturally undergo decoherence through Beliaev damping, where the damping rate is given by [90]

$$\gamma_B = \frac{3}{640\pi} \frac{\hbar\omega^5}{mnc_s^5} \tag{4.51}$$

for a cubic BEC with no speed of sound modulation, where any correction due to modulation of the speed of sound would manifest itself as a higher-order term.

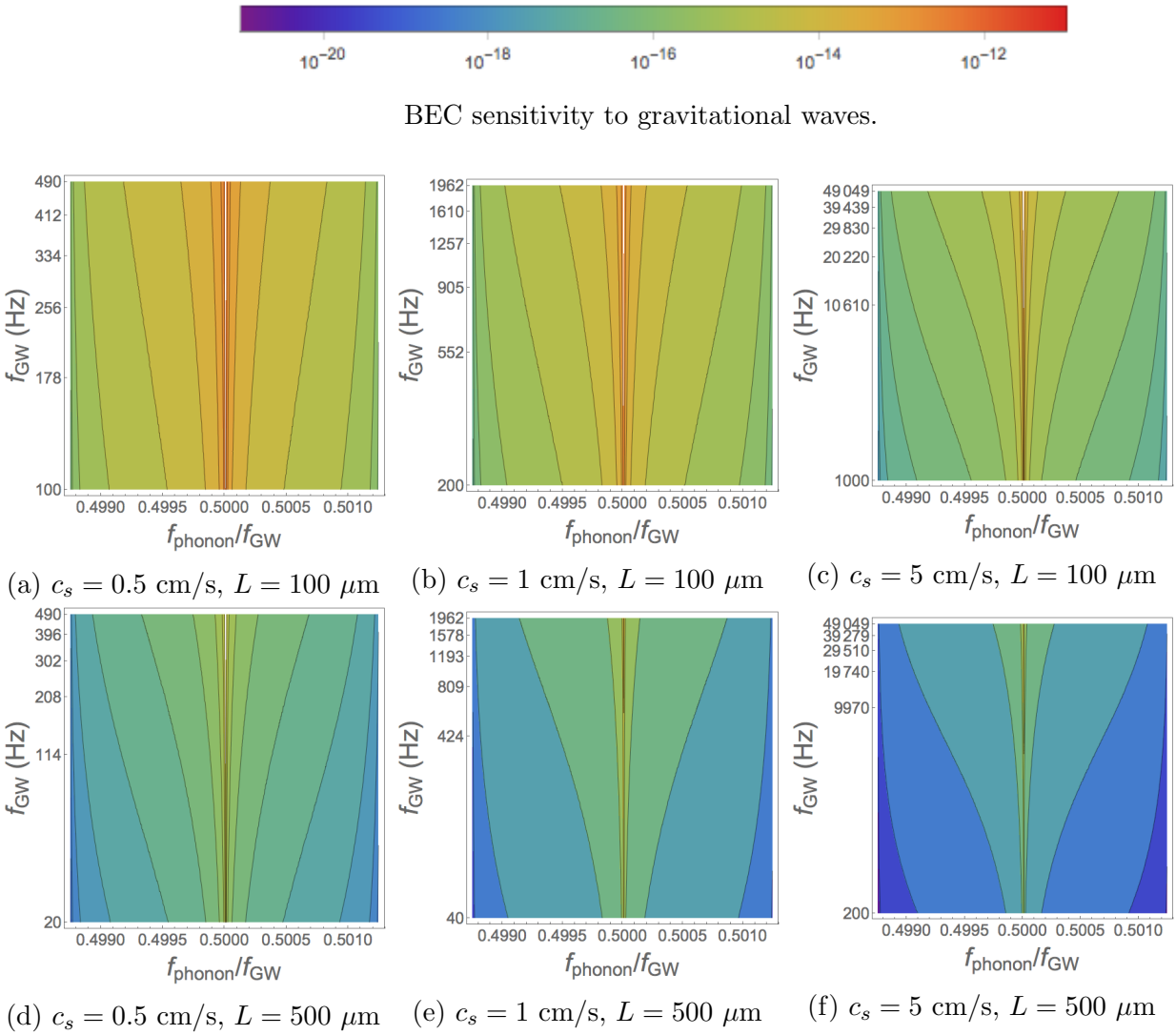

(a) $c_s = 0.5$ cm/s, $L = 100$ μm (b) $c_s = 1$ cm/s, $L = 100$ μm (c) $c_s = 5$ cm/s, $L = 100$ μm

(d) $c_s = 0.5$ cm/s, $L = 500$ μm (e) $c_s = 1$ cm/s, $L = 500$ μm (f) $c_s = 5$ cm/s, $L = 500$ μm

Figure 4.6: Contour plot of the amplitude sensitivity $\left(\sqrt{\langle(\Delta\epsilon)^2\rangle}\right)$ of an undamped BEC to gravitational waves. The condensate is observed for the maximum number of oscillations $N(q)$. We run the experiment over the course of a year and see that undamped condensate could be sensitive to gravitational waves across the frequency spectrum. Changing the speed of sound and length of the condensate will affect the minimum and maximum gravitational wave frequency that can be observed. We take the number density to be 10^{20} m^{-3} of ^{39}K atoms).

Since the corresponds to a Gaussian state, we can use a covariance matrix to compute the fidelity. As demonstrated in [110], the covariance matrix σ is damped as $\sigma = e^{-\gamma_B t}\sigma_0 + (1 - e^{-\gamma_B t})\sigma_\infty$, where σ_0 is the initial covariance matrix and σ_∞ is the $t \to \infty$ covariance matrix. For our purposes, we will neglect the second term as $\gamma_B t \gg 1$. From [10], the quantum Fisher information depends only the square of several combinations of elements of the covariance matrix. Hence, the quantum Fisher information is damped as $H_{\epsilon,\text{damped}} \sim e^{-2\gamma_B t} H_{\epsilon,\text{undamped}}$. Therefore,

$$\langle(\Delta\tilde{\epsilon})^2\rangle = \frac{1}{T_{tot}} \frac{4}{M\left(\Re\left[\alpha^{(1)}_{rel}\right] + |\beta_{rel}|\right)^2 (\cosh 4r_0 + 3)} e^{2\gamma_B t} \tag{4.52}$$

where $t = N_{max}T$ is the maximum time of observation of the condensate, N_{max} is the maximum

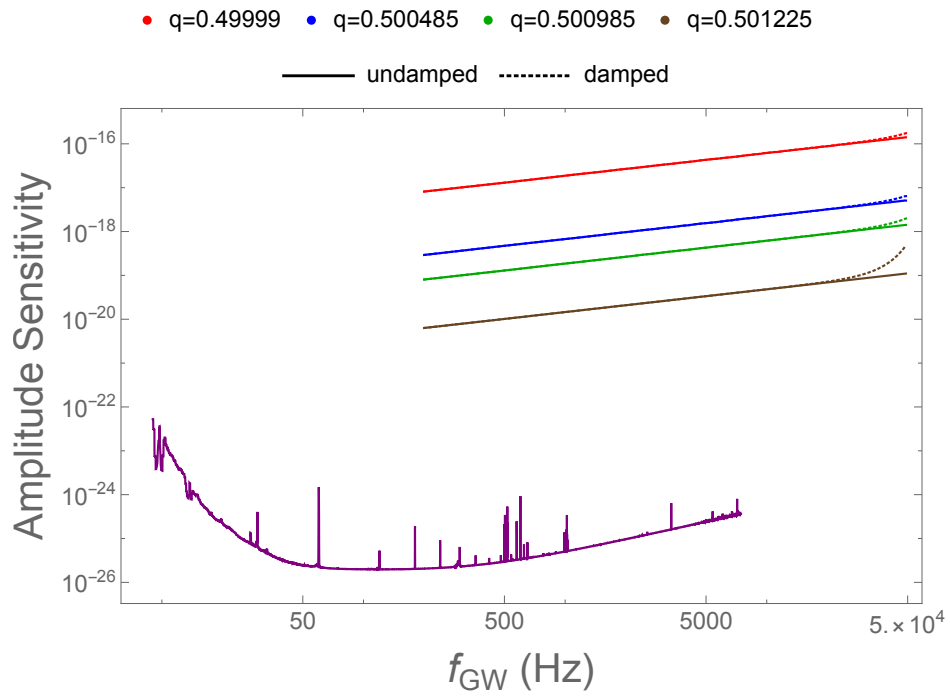

Figure 4.7: The strain sensitivity of a damped BEC gravitational wave detector for various values of q (=ratio of phonon to GW frequency). We consider $c_s = 5$ cm/s and $L = 500$ μm. In each case, the condensate is observed for the maximum number of oscillations $N(q)$, before non-linearities become important. The different colours represent different values of q while the different line styles represent damped/undamped. The purple curve represents LIGO's sensitivity.

number of oscillations of the speed of sound, and $T = \frac{2\pi}{\Omega}$ is the period of the gravitational wave. We note that $N_{max}T < \frac{1}{\gamma_B}$, where $\frac{1}{\gamma_B}$ is approximately the decoherence time [110].

In Figure 4.7, we consider how the strain sensitivity is affected when damping is considered for various gravitational wave frequencies and values of q. We see that larger condensates and faster speeds of the phonons give rise to greater sensitivity. However, we note that the sensitivity of a BEC to gravitational waves is optimal at lower frequencies, in contrast to the results of [199] and [196]. In Figure 4.7, when fixing q, we see that the the strain sensitivity becomes worse further away from the resonance peak of $q = \frac{1}{2}$.

4.4.1 Squeezing

In the previous Chapter, we noted that the initial squeezing of the phonon states seemed to be a necessary feature for a BEC to detect gravitational waves. A similar conclusion was implied by the figures in [199]: to exceed the sensitivity of LIGO, the phonons needed to be squeezed by much more than the capabilities of current experimental designs (7.2 dB), though it was noted that there might be a means [212] of exceeding current limitations.

Though initially squeezing[4] phonons improves the sensitivity to gravitational waves in our current work by a factor of

$$\sqrt{3 + \cosh 4r_0}\,,$$

[4]Parametric resonance also provides a mechanism for squeezing [115, 131], though we have assumed earlier in this Chapter that our system is originally in an unsqueezed state, in contrast to Chapter 3.

we note that this feature is no longer an essential element of our proposal. For $r = 0.83$ (potentially achievable with current technology [96]), this improves sensitivity by only a factor of 2.05. Improvements in squeezing may increase the sensitivity to gravitational waves, though we note that squeezed states would contribute to the energy density of the condensate, and therefore cause the condensate to become unstable quicker (Section 4.2.1). Furthermore, the squeezing parameter would also decay, as discussed in [110].

At the present time using current techniques (which we discuss in more detail in the next section), it would be difficult to detect gravitational waves using a BEC, though the results of this Chapter indicate that this could potentially be achieved in the future. When this occurs, then Beliaev damping and the effects of squeezing may need to be considered in more detail. However, in the case of observing a continuous gravitational wave by using parametric resonance, initially squeezing the system and Beliaev damping are not the primary limiting factors. Rather it is 3-body recombination, which we comment on in the following section.

4.5 Implementation

4.5.1 Observable Sources

In Figure 4.7, we demonstrated that with a speed of sound of $c_s = 5$ cm/s and a cubic condensate with side lengths of $L = 500$ μm, gravitational waves of amplitude $\mathcal{O}(10^{-20})$ could be detected at frequencies around 500 Hz. In Figure 4.5, lower frequency gravitational waves could be detected if their amplitude was $\mathcal{O}(10^{-21})$ and higher. However, as was noted in [195], the amplitude of continuous gravitational waves tends to be weaker than that of transient gravitational waves.

For this reason, it is unlikely that a BEC could detect gravitational waves without going to larger sizes or faster speeds of sound. In Figure 4.8, we illustrate the speeds of sound and condensate lengths necessary to detect gravitational waves with a smaller amplitude, where we also account for Beliaev damping. Currently, it is not possible to create condensates that large, nor is it possible for the condensates to have a long enough lifetime; as we discuss in the next section, larger speeds of sound increase the three-body recombination rate, which in turn decreases the lifetime of the condensate.

A Bose-Einstein condensate is an advantageous gravitational wave detector as it is capable, in principle, of observing gravitational wave sources across several orders of magnitude in frequency, depending on the condensate's length and speed of sound. At gravitational wave frequencies in the tens or hundreds of Hertz, continuous signals from rotating neutron stars or pulsars could be detected [3, 59]. The amplitude of such waves may be $\mathcal{O}(10^{-24})$.

Around black holes, it has been theorized that a boson cloud could form through superradiance, and then emit continuous gravitational waves during annihilation processes. [258] The frequency of the emitted waves will be dependent on the mass of the bosons and distance from Earth, though could potentially be in the kilohertz regime (smaller boson masses will have frequencies in the tens or hundreds of Hertz). The amplitudes of such waves could be as large as $\mathcal{O}(10^{-22})$ [258]. One candidate for boson clouds is axions. In addition to annihilations, axions can undergo energy level transitions, which will also emit gravitational waves. These tend to be in the low-frequency regime (< 200 Hz) and have amplitudes $\mathcal{O}(10^{-24})$ and below, though one energy level transitions could be $\mathcal{O}(10^{-22})$ (frequency of gravitational wave ~ 40 Hz). At higher frequencies, there may be additional

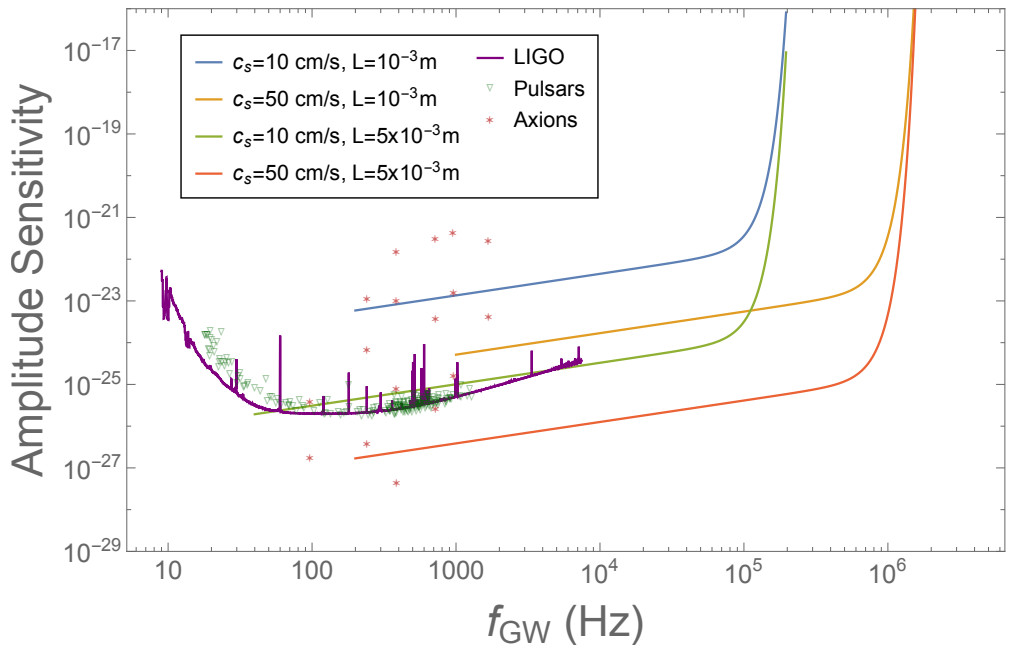

Figure 4.8: Speeds of sound and length of the condensate necessary to observe gravitational waves with a smaller amplitude. The green triangles represent the upper bounds the strain of various pulsar sources [3] while the red stars correspond to axion clouds based on several scenarios proposed in [258]. The error bars for the axion clouds assume a distance of 1kPc - 50 kPc.

cosmological sources, such as cosmic strings or inflationary signatures. However, we note that the signals from such sources may be too weak to be detected by our proposed setup [30]. Though the preceding will also hold true for other suggested methods of detecting gravitational waves with a Bose-Einstein condensate, we will now provide a discussion of the expected universal noise terms, which have not yet been extensively considered by past proposals from an experimental standpoint.

In Figure 4.8, we also illustrate the amplitude and frequency regimes of such signals. We find that, though it may be necessary to go to larger length scales and speeds of sound to observe most of the continuous gravitational wave sources, it may still be possible to detect gravitational waves using condensates of lengths $L \sim 5 \times 10^{-4}$ m and speeds of sound $c_s \sim 5 \times 10^{-2}$ m/s.

4.5.2 Experimental Design

In the previous sections, we considered the theoretical sensitivity for a BEC to detect continuous gravitational waves. We assumed the ideal case of zero temperature initially without damping. When (Beliaev) damping was incorporated, we saw that sensitivity to higher-frequency gravitational waves was reduced. At smaller frequencies, Beliaev damping is irrelevant, though at non-zero temperatures, Landau damping will play a more prominent role [90]. Let us now consider additional limitations to the detector setup by investigating possible sources of noise based upon current technologies. However, we note that the exact nature of the noise sources will be highly dependent on the specific experimental setup. While this is true for all previously suggested techniques to detect gravitational waves with a BEC, we believe this is the first discussion of these universal noise terms in the context of an experimental design.

In our analysis, we assumed that the BEC was in a cubical box trap for simplicity. However,

our findings extend beyond the specific geometry considered. We first note that optical traps have confined BECs to cylindrical boxes [87, 154]. Such a trap can be constructed so that the phonon resonance is available at a desired frequency. In [87], a BEC was created in such a potential with a radius of 15 ± 1 μm and length of 63 ± 2 μm. The "flatness" of the potential could be modelled as $\propto r^{13\pm2}$. A similar design will be used for the experiment we envision.

In the preceding sections, we considered a a modulating speed of sound as a means to induce parametric resonance within the trap. It is simpler to instead induce these fluctuations in the trap by modulating the power of the trapping laser. However, we note that the potential generated will have edges of a high-order polynomial, rather than perfectly sharp, where such a method was used by [178]. In that case, a Fermi gas was trapped in a box and the sound waves were excited.

To create the trap, we need the optical setup to be insensitive to vibrations. We propose doing this using the same technique that LIGO uses to suspend their mirrors [149]. To estimate the effect of such vibrational noise on the BEC, let us assume that the BEC's noise has a similar spectrum as that of LIGO. As a note, we also need to cancel out the effects of Earth's gravity, which can be achieved by applying an additional magnetic field gradient to the trap [87].

4.5.3 Experimental Challenges

There are many experimental challenges that will be faced by any BEC wanting to use phonons to detect gravitational waves as there will be a number of effects that will hinder the sensitivity of the BEC. In this section, we provide a first discussion about some of the noise sources and their effect on the parametric resonance technique discussed earlier in the chapter.

The length of the trap is approximately the distance between the two points where the chemical potential is equal to the trapping potential.[5] We can trap the BEC by using lasers to generate light sheets. The potential energy of the light sheet can be modelled as a Gaussian $U = U_0 e^{-2(z/w_0)^2}$, where U_0 is the peak potential for a blue-detuned light sheet (i.e. the laser is repulsive), w_0 is the Gaussian beam waist, and z is the distance between the peak intensity and the edge of the trap. As the length of the trap is given by $\mu - U = 0$ [85] and assuming a constant chemical potential and beam waist, we have $dz/dU_0 = w_0^2/(4zU_0)$. Then, as the power P of the light sheet is proportional to U_0, we see that for a small change in distance dz, resulting from a small change in power dP,

$$dz = \frac{w_0^2}{4z}\frac{\delta P}{P}. \tag{4.56}$$

[5] This is in the Thomas-Fermi approximation, which takes the kinetic term of the non-relativistic Gross-Pitaevskii equation [85],

$$-\frac{\hbar^2}{2m}\frac{d^2}{dx^2}\phi(x) + V(x)\phi(x) + g|\phi(x)|^2\phi(x) = \mu\phi(x)\,, \tag{4.53}$$

to be negligible, such that

$$V(x)\phi(x) + g|\phi(x)|^2\phi(x) = \mu\phi(x)\,. \tag{4.54}$$

The solution for the wavefunction $\phi(x)$ is then

$$\phi(x) = \sqrt{\frac{\mu - V(x)}{g}} \tag{4.55}$$

for $\mu > V(x)$ and $\phi(x) = 0$ for $\mu < V(x)$ [85].

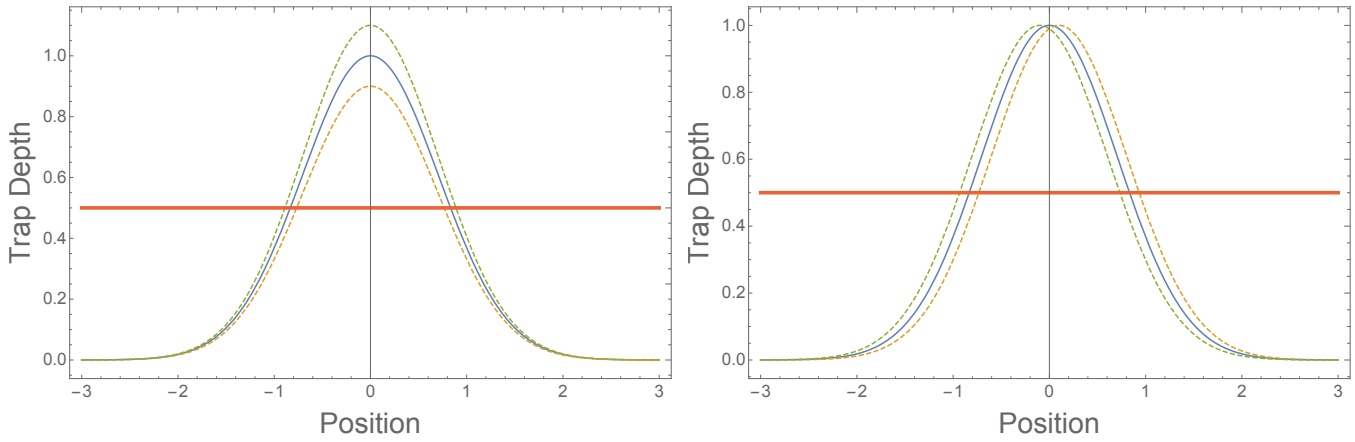

Figure 4.9: A simple illustration of the effect of fluctuation on power on the condensate length. The orange solid line represents the chemical potential. The blue solid line represents the Gaussian potential energy in the absence of noise. For illustrative purposes, we take the chemical potential to have half the maximum potential energy. (In reality, the chemical potential is much less than the maximum potential energy). The ends of the trap are where the chemical potential equals the potential energy. Left: As laser power fluctuates (assuming that the power at each beamsplitter is fixed), the maximum potential energy will increase and decrease (dashed lines). The effect is to increase/decrease the length of the trap. Right: As the power at each beamsplitter fluctuates (assuming that the total power is fixed), the length of the trap will increase on one side, while decreasing on the other side. As a result, the total length of the trap will remain fixed, but the trap itself will move back and forth.

From $\mu - U = 0$, we can solve for z and using currently available laser powers and focal parameters, this corresponds to $z = w_0\sqrt{\ln \frac{U_0}{\mu}} \approx 2w_0$. Supposing that the BEC is in a cubic trap of length L, setting the Rayleigh range (distance along a beam between w_0 and $\sqrt{2}w_0$, so that $z_R = \pi w_0^2/\lambda$ [155]) equal to the length gives the waist, $w_0 = \sqrt{\lambda L \pi}$, so that $\delta z = \sqrt{L\lambda\pi}/(8) \cdot \delta P/P$.

Two effects can introduce noise into the intensity of the light sheets: the power going towards the beamsplitter can fluctuate or the ratio of power of the beams after the beamsplitter can fluctuate. In the first case, if we assume no fluctuations in the splitting power, the peak of the potential energy increases or decreases (for a fixed chemical potential). The result is to change the length of the trap. In the second case, the potential energy from one sheet increases while the potential energy for the second sheet decreases. This will cause the length of the trap to remain constant, though the trap will vibrate back and forth (Figure 4.9) Let us assume that the laser power fluctuations for the sheet are correlated, while the fluctuations for the beamsplitting power are anticorrelated. As z describes the length of the condensate, we can immediately write,

$$\frac{\delta L}{L} = \sqrt{\frac{\lambda}{16\pi L}}\frac{\delta P}{P}. \tag{4.57}$$

In an experiment, let us use the same wavelength light as in [87] (532 nm) and take the trap length to be $L = 1$ mm. Thus, $\delta L/L \approx 0.003(\delta P/P)$. Now suppose that we used 50 W lasers and the duration of the experiment was 3 seconds. Assuming we are working at the shot noise limit, we

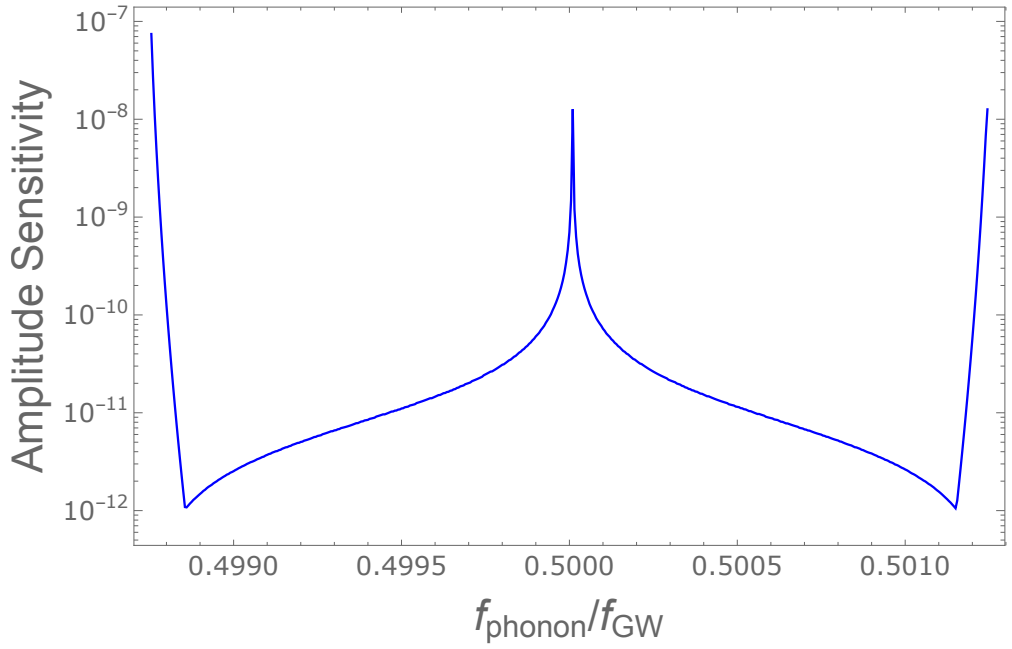

Figure 4.10: The amplitude sensitivity $\left(\sqrt{\langle(\Delta\epsilon)^2\rangle}\right)$ of a BEC ($a = 0.005$) to gravitational waves, assuming that the BEC has side lengths of 100 μm, the speed of sound is 1 cm/s, the lifetime of the BEC is limited to 3 s (without using a BEC machine), and the incoming gravitational wave has a frequency of 1000 Hz. We see that the greatest sensitivity to gravitational waves is achieved slightly off the centre of resonance and that moving outside the resonance band destroys the sensitivity to gravitational waves.

have that [139]

$$\delta P\Big|_{shot} = \sqrt{N_\gamma} P \sim \sqrt{P}\,, \tag{4.58}$$

where N_γ is the number of photons and $P = \frac{N_\gamma \hbar \omega_L}{T}$ is the average power of the laser, with T being the duration of the measurement and ω_L the frequency of the laser. Therefore, we find that the noise in the length of the trap is $\delta L/L \sim 10^{-13}$.

In Figure 4.10, we show the sensitivity curve of a BEC for a 1000 Hz gravitational wave, with the observation time the minimum of the non-linearity time and the lifetime of the BEC (3 seconds). We notice that there are two minima before the sensitivity dramatically worsens. These points correspond to the non-linearity times being exactly equal to the lifetime of the BEC. When the non-linearity time exceeds the lifetime of the BEC, parametric resonance is unable to fully amplify the sensitivity due to insufficient time.

Let us now consider how to improve the intrinsic noise of the BEC. We note that this could potentially be doing by squeezing the intensity noise of the laser because the laser's phase is not critical to our experimental proposal. At present, experiments have been able to achieve squeezing (i.e. reduce the noise) of up to 15 dB. [29, 243]. Even assuming that the squeezing can be doubled to 30 dB, this still produces a strain of $\delta L/L \sim 10^{-16}$, which is far worse than what LIGO is able to achieve.

An alternative method is to modify the geometry of the trap. Supposing that we had an asymmetric box trap and were only interested in phonons whose modes were along the longest

dimension of the trap, we can increase L will decreasing the beam waist. Supposing that the trap was 5 mm long and 100 nm wide, we could increase sensitivity by a factor of $\sqrt{5}$. Therefore, it may be possible to use a combination of techniques to push the strain sensitivity down to 10^{-17}.

We have focused on laser noise as being the primary limiting factor for such an experiment. To reduce the effect of mechanical vibrations of the optical components, we can do the experiment in an ultrahigh vacuum chamber, with the optics being built directly into a single piece of Zerodur glass [73]. We chose Zerodur glass because this material has a a very low coefficient of thermal expansion. In addition, the only types of excitations are from centre of mass oscillations (causing pendular motion) and high-frequency collective excitations (causing vibrations). With a size of 10-20 cm and a speed of sound of 6511 m/s [209], the fundamental mode of this setup is greater than 10-20 kHz.

Using this optical setup, we can then suspend this apparatus using similar methods as the LIGO mirror suspension system [149]. We note that with this suspension system, high-frequency vibrations are effectively damped, so the main physical limitation at high frequencies would be Beliaev damping. The level of vibrational noise present in this setup will be $\delta L_{vibration}/L$ (i.e. change in length induced by the vibrations of the system) multiplied a transfer function, which describes the ratio between the noise measured in the BEC compared to the noise available to couple to the BEC after travelling through the suspension system. In practice, this ratio will be much less than one. Hence, using current technologies, the amount of vibrational noise will be suppressed below the noise from laser intensity fluctuations.

One major challenge is that BECs have a short lifetime because of three-body recombination. In this effect, there is a collision between three atoms, which a molecular bound state of two of the atoms to form. This causes the binding energy of the molecule to be released as kinetic energy for both the molecule and third atom. As a result, the atom and molecule are energetic-enough to then be ejected from the trap.

In previous sections, we assumed that the lifetime was three seconds in length. For alkali atoms at the densities of interest, the lifetimes of a BEC tend to be 1-10 seconds. Three-body recombination (in the absence of additional effects giving loss) is described with [223, 257]

$$\dot{n} = -K_3 n^3 \,, \tag{4.59}$$

where K_3 is a coefficient depending on the specific parameters of the atom and condensate. Hence, we see that the number density n evolves as

$$n(t) = \frac{n_0}{\sqrt{n_0^2 K_3 t + 1}} \,, \tag{4.60}$$

where $n_0 = n(0)$.

As a result of three-body loss, the speed of sound will change. As a result, the phonon dispersion relation will change, which will affect the coupling between gravitational waves and phonons. As our idea is extremely sensitive to the number density of the condensate, speed of sound, and lifetime of the BEC, three-body recombination will have disastrous effects on the sensitivity to gravitational waves. For the timescales of interest (i.e. 1-10 seconds), one way to solve part of this problem is to continuous change the interaction strength g of the condensate. It is well-known that $c_s = \sqrt{gn/m}$ [153], so we can keep the averaged speed of sound c_s approximately constant by increasing g as n decreases. We note that this method will only work for short times and cannot be done arbitrarily long. In addition, we also have $K_3 \propto g^4$ [69], so if we want to hold gn fixed

while increasing g to compensate for a decreasing n, we see that $K_3 n^3$ in equation (4.59) will scale as $1/n$. As a result, 3-body recombination will still accelerate. It should also be noted that with decreasing number density, the maximum instability time will also decrease, thereby significantly reducing sensitivity to gravitational waves.

We have focused our discussion on three-body recombination, laser noise, and vibrational noise. We note that there exists other sources of noise that would need to be considered in a BEC experiment, such as the scattering of trap light as well as collisions of the condensate atoms with the residual background gas. In addition, the transfer function will not be constant over all frequencies and will become worse at higher frequencies where there is resonance between the modes noise and modes of the trap.

Even if the technical noise of the trap is mitigated, there will remain a few caveats. In Section 4.4, we noted that faster speeds of sound gave rise to greater sensitivity. This was because the damping rate was $\gamma_B \propto c_s^{-5}$. With faster speeds of sounds, a BEC will have a larger minimum observable gravitational wave frequency ($\propto c_s$), though a much larger maximum observable gravitational wave frequency ($\propto c_s^2$). However, at larger speeds of sound, we note that the maximum time of observation will no longer be given by the non-linearity condition of Section 4.2.1, but by three-body recombination, as we just discussed. Larger speeds of sound correspond to greater number densities, implying a greater decrease in the number atoms in the condensate [130, 153]. We also note quantum depletion, which describes the loss of atoms from the condensate because of interactions between the atoms and excitations, will contribute to additional noise in the condensate, where the number of atoms in an excited state (therefore, leaving the condensate) is given by [183]

$$\frac{n_{ex}}{N} = \frac{8}{3\sqrt{\pi}}(na^3)^{1/2} \tag{4.61}$$

where a is the scattering length and is valid for a zero-temperature uniform Bose gas.

4.6 Conclusion and Future Prospects

In this Chapter, we investigated how a BEC could potentially be used to detect a gravitational wave of the form $h_+ = \epsilon \sin \Omega t$. Using the parametric resonance induced within the system, we were able to amplify the sensitivity to gravitational waves, with the greatest sensitivity occurring at lower frequencies.

We also considered the experimental implementation of this proposal and realized that there are several formidable challenges that must be addressed for a BEC to detect continuous gravitational waves. Currently, the intrinsic noise present within the condensate and experimental setup with dominate over gravitational wave signals. Further, the lifetime of the BEC poses a hard limit on the duration of any experiment. If technology and experimental techniques sufficiently advance to addresses these challenges, then a BEC may a more feasible detector than previously believed [196, 206].

There are a few methods to address these formidable challenges. We noted that three-body recombination effectively reduces the number of atoms in our condensate, though three-body loss coefficients are similar for those atoms that undergo laser cooling. With fewer atoms, we have worse sensitivity to gravitational waves. Hydrogen may provide a way around this, which could then increase the lifetime of our condensate. As the triplet potential of H_2 supports no bound

states, there will be minimal three-body loss for spin-polarized hydrogen [186]. Instead, BECs with hydrogen in magnetic traps exhibit dipolar relaxation. [77]. In magnetic traps, the hydrogen is in the high-energy Zeeman sublevel. However, if we use optical traps, the hydrogen will be in the lowest-energy Zeeman sublevel, so dipolar relaxation will no longer be a factor (as there is no level to relax to). Hence, the BEC lifetime could be relatively long (with the lifetime limited by scattered trap light).

Alternatively, we could use CO_2 lasers in our BEC. Such lasers can currently produce greater than 10 kW of power [22]. Suppose that a 25 kW CO_2 laser producing light of 10.6 μm. Such a laser would further decrease the shot-noise limit (as compared to using a 50 W laser producing 532 nm light).

As an alternative method, once could use a set of BEC machines [229]. This setup could continuously produce BECs to simultaneously observe an incoming gravitational wave. However, we note that this would greatly increase the size and price of the experiment, thereby reducing its potential feasibility.

Though using a BEC to detect gravitational waves will be extremely difficult, it should be noted that LIGO was first conceptualized in the 1980s and only detected gravitational waves in 2015. BECs have a head start in knowing that gravitational waves *can* be directly detected and some of LIGO's technical innovations could potentially be adapted for use by a BEC GW detector. Though such an experiment may take years or decades to achieve, doing so will provide a new method to detecting gravitational waves across potentially several orders of magnitude in frequency.

Part II

Entanglement, Temperature, and Rotating BTZ Black Holes

Chapter 5

Unruh-DeWitt detectors around rotating BTZ black holes

As we discussed in Chapter 1, Unruh-DeWitt detectors are used to investigate how properties of the spacetime vacuum affect physical systems. In the second part of the thesis, we will investigate how a rotating Bañados-Teitelboim-Zanelli (BTZ) black hole affects the temperature of an orbiting Unruh-DeWitt detector and the amount of entanglement transferred from the quantum vacuum to a pair of Unruh-DeWitt detectors. This is the first investigation of how rotation affects the temperature and entanglement of Unruh-deWitt detectors. In this chapter, we will first discuss in Section 5.1 the Unruh-DeWitt detector model. We will then consider in Section 5.2 a single detector and derive its transition probability. Then, in Section 5.3, we will consider two detectors and show that a new effect, known as entanglement harvesting, arises, which is not present when analyzing a single detector. We will also discuss how this entanglement can be quantified. In these sections, we will follow the arguments of [147, 220]. Afterwards, in Section 5.4, we will specialize to the case of rotating BTZ black holes.

5.1 Unruh-DeWitt Detectors

Let us consider a two-level quantum system with energy levels $|0\rangle_D$, $|1\rangle_D$ and energy gap Ω_D. Suppose that the detector and the quantum vacuum interact in a manner similar to that of the light-matter interaction, such that the interaction Hamiltonian is[1]

$$H_D = \lambda \chi_D(\tau) \left(e^{i\Omega_D \tau} \sigma^+ + e^{-i\Omega_D \tau} \sigma^- \right) \otimes \phi[x_D(\tau)] \,, \tag{5.2}$$

[1] The interaction Hamiltonian of the light-matter interaction takes the form [184]

$$H = e^{i\Omega\tau} \left|1\right\rangle \left\langle 0\right|_D \otimes \int d\vec{x} \vec{F}(\vec{x}) \cdot \vec{E}(t, \vec{x}) + e^{-i\Omega\tau} \left|0\right\rangle \left\langle 1\right|_D \otimes \int d\vec{x} \vec{F}^*(\vec{x}) \cdot \vec{E}(t, \vec{x}) \,, \tag{5.1}$$

where $\vec{E}$ is the electric field and $\vec{F}$ is a smearing function that describes the spatial extent of the matter. To derive the Unruh-DeWitt detector Hamiltonian, we assume that the atoms are point-like and replace the electric field with the scalar field. We also introduce a function that turns the detector on and off (the switching function). We note that this model is a reasonable approximation when there is no angular momentum exchange [12, 146]. We also note that this model does not account for the non-isotropies of atomic orbitals nor does it account for the vector nature of the electromagnetic field (the background field is assumed to be a scalar) [184].

where λ is the coupling constant between the detector and the field (which we will take to be small), $0 \leq \chi_D(\tau) \leq 1$ is the switching function that governs when the detector turns on and off, $\sigma^+ = |1\rangle_D \langle 0|_D$, $\sigma^- = |0\rangle_D \langle 1|_D$ are ladder operators that raise and lower the energy levels, $x_D(\tau)$ is the trajectory of the detector and ϕ is the field of the quantum vacuum.

5.2 Transition Probability (one detector)

From the Hamiltonian in equation (5.2), we know that the unitary operator can be represented as

$$U = \mathcal{T} e^{-\frac{i}{\hbar}\int H d\tau} \quad = 1 - \frac{i}{\hbar}\int H_D d\tau - \frac{1}{2\hbar^2}\mathcal{T}\int H_D(\tau_1) H_D(\tau_2) d\tau_1 d\tau_2 + \cdots , \tag{5.3}$$

where $\mathcal{T}$ is the time-ordering operator defined as

$$\mathcal{T}(A(t_1)B(t_2)) = \begin{cases} A(t_1)B(t_2) & t_1 > t_2 \\ B(t_2)A(t_1) & t_2 > t_1 \end{cases} . \tag{5.4}$$

Let the initial state of the system be $|\Psi_i\rangle = |0\rangle_D |0\rangle$, so the final state of the system is $|\Psi_f\rangle = U|\Psi_f\rangle = U|0\rangle_D|0\rangle$, where $|0\rangle$ denotes the vacuum field. Therefore,

$$\begin{aligned} |\Psi_f\rangle \sim U|0\rangle_D|0\rangle = |0\rangle_D|0\rangle - \frac{i\lambda}{\hbar}\int d\tau \chi(\tau) e^{i\Omega_D \tau} |1\rangle_D \otimes \phi[x_D(\tau)]|0\rangle \\ - \frac{\lambda^2}{2\hbar^2}\mathcal{T}\Bigg[\int \chi(\tau_1)\chi(\tau_2)\left(e^{i\Omega_D\tau_1}\sigma^+ + e^{-i\Omega_D\tau_1}\sigma^-\right)\left(e^{i\Omega_D\tau_2}\sigma^+ + e^{-i\Omega_D\tau_2}\sigma^-\right) \\ \otimes \phi[x_D(\tau_1)]\phi[x_D(\tau_2)]\Bigg]|0\rangle + \mathcal{O}(\lambda^4) . \end{aligned} \tag{5.5}$$

To determine state of our detectors, we need to calculate the reduced density operator, $\rho_D = Tr_\phi[|\Psi_f\rangle\langle\Psi_f|]$. Upon calculating ρ_D, we see that only the λ^0 and λ^2 are relevant, meaning that the field only comes in at second order in λ. (In fact, if ρ_D were calculated to higher-order terms in λ, only the even powers of the field would appear in ρ_D). Specifically, we find

$$\rho_D = Tr_\phi[\rho] = \begin{pmatrix} 1 - P_D & 0 \\ 0 & P_D \end{pmatrix} + \mathcal{O}(\lambda^4) , \tag{5.6}$$

where

$$P_D = \lambda^2 \int d\tau_D d\tau'_D \chi_D(\tau_D)\chi_D(\tau'_D) e^{-i\Omega_D(\tau_D - \tau'_D)} W(x_D(\tau_D), x_D(\tau'_D)) . \tag{5.7}$$

Here, $W(x, x') = \langle 0|\phi(x)\phi(x')|0\rangle$ is the two-point correlation function (also called the Wightman function). Physically, P_D represents the probability of the detector transitioning from the ground state to the excited state.

5.3 Entanglement Harvesting Protocol (two detectors)

Let us now consider two detectors, whose interaction Hamiltonians are each given by (5.2). We can carry out the same steps as we did for a single detector, though now the unitary operator is

$$U = \mathcal{T} e^{-\frac{i}{\hbar}\int dt\left(H_A(\tau_A)\frac{d\tau_A}{dt}+H_B(\tau_B)\frac{d\tau_B}{dt}\right)} \tag{5.8}$$

We will again assume that the initial state of our detect-field system is a product state, so the final state is $|\Psi_f\rangle = U|0\rangle_A|0\rangle_B|0\rangle$. We can rewrite this relation as $|\Psi_f\rangle = \sum_{n=0}^{\infty} U^{(n)}|0\rangle_A|0\rangle_B|0\rangle$, where

$$U^{(n)} = \frac{(-i)^n}{n!\hbar^n}\mathcal{T}\int\left(H_A(\tau_A)\frac{d\tau_A}{dt_1}+H_B(\tau_B)\frac{d\tau_B}{dt_2}\right)\cdots\left(H_A(\tau_A)\frac{d\tau_A}{dt_n}+H_B(\tau_B)\frac{d\tau_B}{dt_n}\right)dt_1\cdots dt_n\,. \tag{5.9}$$

Therefore, the reduced state of our detectors is

$$\begin{aligned}\rho_{AB} &= Tr_\phi\left[|\Psi_f\rangle\langle\Psi_f|\right],\\ &= \sum_{n=0}^{\infty}\sum_{m=0}^{\infty} Tr_\phi\left[U^{(n)}|0\rangle_A|0\rangle_B|0\rangle\langle 0|\langle 0|_A\langle 0|_B U^{\dagger(m)}\right],\\ &= \sum_{n=0}^{\infty}\sum_{m=0}^{\infty}\int dx\,\langle x|\left|\left[U^{(n)}|0\rangle_A|0\rangle_B|0\rangle\langle 0|\langle 0|_A\langle 0|_B U^{\dagger(m)}\right]\right||x\rangle\,,\end{aligned} \tag{5.10}$$

where we have traced over the field states $|x\rangle$ in the last line. Let us now analyze each of the terms. If $n = m = 0$, we recover the identity matrix. If $n = 0, m = 1$ or $n = 1, m = 0$, the term will vanish, similar to the previous section. In fact, if n and m have opposite parity, these types of terms will not contribute to the trace. For the case of $n = 1, m = 1$, $n = 0, m = 2$, $m = 2, n = 0$, or $n = m = 1$ the terms in the density operator will be non-zero. In fact, only the terms that have even powers of ϕ will provide any contribution to the trace. Therefore, we find that the reduced density operator for our detectors is

$$\rho_{AB} = \begin{pmatrix} 1-P_A-P_B & 0 & 0 & X\\ 0 & P_B & L_{AB} & 0\\ 0 & L_{AB}^* & P_A & 0\\ X^* & 0 & 0 & 0\end{pmatrix} + \mathcal{O}(\lambda^4)\,, \tag{5.11}$$

where we are working in the in the $\{|0\rangle_A|0\rangle_B, |0\rangle_A|1\rangle_B, |1\rangle_A|0\rangle_B, |1\rangle_A|1\rangle_B\}$ basis. Here, P_A, P_B are the transition probabilities for detector $D = A, B$ and are given by equation (5.7). The non-local correlations in the system are described by

$$X = -\lambda^2\int d\tau_A d\tau_B \chi(\tau_A)\chi(\tau_B)e^{-i(\Omega_A\tau_A+\Omega_B\tau_B)}\left[\Theta[t'-t]W(x_A(t),x_B(t'))+\Theta[t-t']W(x_B(t'),x_A(t))\right] \tag{5.12}$$

and

$$L_{AB} = \lambda^2\int dt dt'\eta_B(t')\eta_A(t)e^{i[\Omega_B\tau_B(t')-\Omega_A\tau_A(t)]}W(x_A(t),x_B(t'))\,, \tag{5.13}$$

represents the total correlations between the two detectors. Here, $\eta_D(t) = \frac{d\tau_D}{dt}\chi(\tau_D)$. We note that tracing equation (5.11) over detectors A or B recovers the reduced density matrix (5.6).

In deriving the reduced density operator elements ρ_{ij}, we expanded to $\mathcal{O}(\lambda^2)$. We note that if we were to expand to $\mathcal{O}(\lambda^4)$, we would obtain an additional term $\rho_{44} = |X|^2 + |L_{AB}|^2 + P_A P_B$.

5.3.1 Concurrence

We are now in a position to discuss the entanglement transferred from the vacuum quantum field to the detector. One way to quantify this is through the concurrence.[2] The concurrence is given by [254]

$$\mathcal{C}(\rho_{AB}) = \max\left[0, w_1 - w_2 - w_3 - w_4\right] , \tag{5.16}$$

where w_i are the eigenvalues of $\rho_{AB}\left(\sigma_y \otimes \sigma_y\right)\rho^*_{AB}\left(\sigma_y \otimes \sigma_y\right)$, with σ_y the Pauli y matrix (and w_1 is the largest eigenvalue). These eigenvalues are

$$w_1 = \sqrt{\rho_{11}\rho_{44}} + |\rho_{14}| = \sqrt{|X|^2 + |L_{AB}|^2 + P_A P_B} + |X| \tag{5.17}$$

$$w_2 = \sqrt{\rho_{22}\rho_{33}} + |\rho_{23}| = \sqrt{P_A P_B} + |L_{AB}| \tag{5.18}$$

$$w_3 = \sqrt{\rho_{11}\rho_{44}} - |\rho_{14}| = \sqrt{|X|^2 + |L_{AB}|^2 + P_A P_B} - |X| \tag{5.19}$$

$$w_4 = \sqrt{\rho_{22}\rho_{33}} - |\rho_{23}| = \sqrt{P_A P_B} - |L_{AB}| , \tag{5.20}$$

where ρ_{ij} is the i, j element of equation (5.11). Therefore, we obtain

$$\mathcal{C}(\rho_{AB}) = 2\max\left[0, |X| - \sqrt{P_A P_B}\right] . \tag{5.21}$$

for the concurrence. If the concurrence is non-zero, then the entanglement between the two detectors is non-zero. As the detectors were initially in a product state with the field, this means that some of the vacuum entanglement has been transferred to the two detectors. Hence ρ_{AB} describes an entangled system, if $|X|^2 > P_A P_B$.

5.4 Rotating BTZ black holes

We can write the action of our system as $S = S_{EH} + S_\phi$, where

$$S_{EH} = \frac{1}{16\pi}\int R\sqrt{-g}d^3x \tag{5.22}$$

is the Einstein-Hilbert action (R is the Ricci scalar and g is the determinant of the metric tensor $g_{\mu\nu}$) and

$$S_\phi = -\int\left(\frac{1}{2}g^{\mu\nu}\partial_\mu\phi\partial_\nu\phi + \frac{1}{16}R\phi^2\right)\sqrt{-g}d^3x \tag{5.23}$$

[2] We note that there are additional ways, such as the negativity [147, 247],

$$\mathcal{N}(\rho_{AB}) = \max\left[0, \sqrt{|X|^2 + \left(\frac{P_A - P_B}{2}\right)^2} - \frac{P_A + P_B}{2}\right] + \mathcal{O}(\lambda^2) \tag{5.14}$$

or the entanglement of formation [254],

$$E_f(\rho_{AB}) = h\left(\frac{1 + \sqrt{1 - \mathcal{C}(\rho_{AB})^2}}{2}\right), \tag{5.15}$$

where $h(x) = -x\log x - (1-x)\log(1-x)$ and $\mathcal{C}(\rho_{AB})$ denotes the concurrence. In this part of the thesis, we will focus on the concurrence as we are considering a pair of qubits. If we were to consider other systems, then concurrence would no longer be applicable and it would be better to use negativity.

is the action for a conformally-coupled scalar field ϕ.

We are primarily interested in a rotating BTZ black hole, which is a 2+1 dimensional black hole that is asymptotically anti-de Sitter (AdS).[3] The line element of this black hole is [24]

$$ds^2 = -(N^\perp)^2 dt^2 + f^{-2} dr^2 + r^2 (d\phi + N^\phi dt)^2 \tag{5.24}$$

where, $N^\perp = f = \sqrt{-M + \frac{r^2}{\ell^2} + \frac{J^2}{4r^2}}$ and $N^\phi = -\frac{J}{2r^2}$ with $M = \frac{r_+^2 + r_-^2}{\ell^2}$ and $J = \frac{2 r_+ r_-}{\ell}$ the respective mass and angular momentum of the black hole, whose respective inner and outer horizon radii are r_- and r_+; ℓ is the Anti-deSitter (AdS) length. Note that $|J| \leq M\ell$, with equality yielding extremality ($r_+ = r_-$).

Throughout the calculations, we will assume that the detectors are co-rotating with the black hole, with transformations [103]

$$t_D = \frac{\ell r_+ \tau_D}{\sqrt{r^2 - r_+^2}\sqrt{r_+^2 - r_-^2}} \,, \tag{5.25}$$

$$\phi_D = \frac{r_- \tau_D}{\sqrt{r^2 - r_+^2}\sqrt{r_+^2 - r_-^2}} \,, \tag{5.26}$$

so the proper time τ_D for each detector is related to these coordinates via

$$\phi_D = \frac{r_-}{\ell r_+} t_D = \frac{r_- \tau_D}{\sqrt{R_D^2 - r_+^2}\sqrt{r_+^2 - r_-^2}} \,. \tag{5.27}$$

For a conformally coupled scalar field (in the Hartle-Hawking vacuum) the Wightman function is known analytically [50, 132], and can be written as the image sum,

$$W_{BTZ}(x, x') = \sum_{n=-\infty}^{\infty} \eta^n W_{AdS_3}(x, \Gamma^n x') \,, \tag{5.28}$$

over the vacuum Wightman functions for AdS_3, where $\Gamma x'$ takes $(t, r, \phi) \to (t, r, \phi + 2\pi)$ and $\eta = \pm 1$ describes the untwisted/twisted nature of the scalar field. With this identification, we have [103,219],

$$W_{BTZ} = \frac{1}{4\pi}\frac{1}{2\sqrt{\ell}} \sum_{n=-\infty}^{\infty} \eta^n \left(\frac{1}{\sqrt{\sigma_\epsilon(x, \Gamma^n x')}} - \frac{\zeta}{\sqrt{\sigma_\epsilon(x, \Gamma^n x') + 2}} \right) \,, \tag{5.29}$$

where

$$\begin{aligned} \sigma_\epsilon(x, \Gamma^n x') = &-1 + \sqrt{\alpha(r)\alpha(r')} \cosh\left[\frac{r_+}{\ell}(\Delta\phi - 2\pi n) - \frac{r_-}{\ell^2}(t - t') \right] \\ &- \sqrt{(\alpha(r) - 1)(\alpha(r') - 1)} \cosh\left[\frac{r_+}{\ell^2}(t - t') - \frac{r_-}{\ell}(\Delta\phi - 2\pi n) \right] \,, \end{aligned} \tag{5.30}$$

and

$$\alpha(r) = \frac{r^2 - r_-^2}{r_+^2 - r_-^2} \,, \qquad \Delta\phi = \phi - \phi' \,. \tag{5.31}$$

[3] We can think of AdS spacetime as being like a cavity. One of the interesting features of AdS spacetime is that it is necessary (unlike Minkowski spacetime) to specify boundary conditions on an underlying field in order to describe the field's evolution [23].

The boundary conditions (at spatial infinity) for the scalar field (Dirichlet, Neumann, transparent) are represented by $\zeta = 1, -1, 0$, respectively. In all subsequent calculations, we shall also assume an untwisted scalar field.

We are now in a position to calculate P_D, X, and L_{AB} in equation (5.11). We outline the calculations here and provide more details in Appendix C. Through straightforward manipulations, we find $P_D = \sum_{n=-\infty}^{\infty} \eta^n \{I_n^- - \zeta I_n^+\}$, where

$$I_n^{\pm} = K_P \int_{-\infty}^{\infty} dz \frac{e^{-a\left(z-\frac{2\pi n r_-}{\ell}\right)^2} e^{-i\beta\left(z-\frac{2\pi n r_-}{\ell}\right)}}{\sqrt{(\cosh(\alpha_n^{\pm}) - \cosh(z))}} \tag{5.32}$$

and

$$K_P = \frac{\lambda^2 \sigma_D}{4\sqrt{2\pi}} \tag{5.33}$$

$$a = \frac{R_D^2 - r_+^2}{r_+^2 - r_-^2} \frac{\ell^2}{4\sigma_D^2} \tag{5.34}$$

$$\beta = \Omega_D \ell \sqrt{\frac{R_D^2 - r_+^2}{r_+^2 - r_-^2}} \tag{5.35}$$

$$\cosh(\alpha_n^{\pm}) = \frac{1}{\alpha(R_D) - 1} \left[\pm 1 + \alpha(R_D) \cosh\left(2\pi n \frac{r_+}{\ell}\right)\right] \tag{5.36}$$

for $D = A, B$.

To calculate the non-local correlation term X, let

$$x_A(\tau_A) := \left\{ t = \frac{\ell r_+ \tau_A}{\sqrt{r^2 - r_+^2}\sqrt{r_+^2 - r_-^2}}, r = R_A, \phi_A = \frac{r_- \tau_A}{\sqrt{r^2 - r_+^2}\sqrt{r_+^2 - r_-^2}} \right\} \tag{5.37}$$

$$x_B(\tau_B) := \left\{ t' = \frac{\ell r_+ \tau_B}{\sqrt{r^2 - r_+^2}\sqrt{r_+^2 - r_-^2}}, r = R_B, \phi_B = \frac{r_- \tau_B}{\sqrt{r^2 - r_+^2}\sqrt{r_+^2 - r_-^2}} \right\} \tag{5.38}$$

Similar calculations show $X = \sum_{n=-\infty}^{\infty} \eta^n \left[\left(I_{AB,n}^- + I_{BA,-n}^-\right) - \zeta \left(I_{AB,n}^+ + I_{BA,-n}^+\right)\right]$ where

$$I_{AB,n}^{\pm} + I_{BA,-n}^{\pm} = \frac{K_X}{2} \int_0^{\infty} dz \left[\frac{e^{-a_X\left(z-\frac{2\pi n r_-}{\ell}\right)^2} e^{-i\beta_X\left(z-\frac{2\pi n r_-}{\ell}\right)} + e^{-a_X\left(z+\frac{2\pi n r_-}{\ell}\right)^2} e^{i\beta_X\left(z+\frac{2\pi n r_-}{\ell}\right)}}{\sqrt{\cosh(\alpha_{X,n}^{\pm}) - \cosh(z)}} \right] \tag{5.39}$$

with

$$K_X = -\frac{\lambda^2 \sigma_A \sigma_B \sqrt[4]{(R_A^2 - r_+^2)(R_B^2 - r_+^2)} \exp\left(-\frac{\sigma_A^2 \sigma_B^2 \left(\Omega_A \sqrt{R_A^2 - r_+^2} + \Omega_B \sqrt{R_B^2 - r_+^2}\right)^2}{2\left(\sigma_A^2 (R_B^2 - r_+^2) + \sigma_B^2 (R_A^2 - r_+^2)\right)}\right)}{2\sqrt{\pi}\sqrt{\sigma_A^2 (R_B^2 - r_+^2) + \sigma_B^2 (R_A^2 - r_+^2)}} \tag{5.40}$$

$$a_X = \frac{1}{2(\bar{\sigma}_A^2 + \bar{\sigma}_B^2)} \left(\frac{\ell^2 r_+}{r_+^2 - r_-^2}\right)^2 \tag{5.41}$$

$$\beta_X = \frac{(\bar{\sigma}_B^2 \bar{\Omega}_B - \bar{\sigma}_A^2 \bar{\Omega}_A)}{\bar{\sigma}_A^2 + \bar{\sigma}_B^2} \left(\frac{\ell^2 r_+}{r_+^2 - r_-^2}\right) \tag{5.42}$$

$$\cosh(\alpha_{X,n}^{\pm}) = \frac{1}{\sqrt{\alpha(R_A) - 1}\sqrt{\alpha(R_B) - 1}} \left[\pm 1 + \sqrt{\alpha(R_A)}\sqrt{\alpha(R_B)} \cosh\left(2\pi n \frac{r_+}{\ell}\right)\right]. \tag{5.43}$$

and

$$\begin{aligned}\bar{\sigma}_A &= \sigma_A/\gamma_A \\ \bar{\sigma}_B &= \sigma_B/\gamma_B \\ \bar{\Omega}_A &= \Omega_A\gamma_A \\ \bar{\Omega}_B &= \Omega_B\gamma_B\end{aligned} \tag{5.44}$$

and

$$\begin{aligned}\gamma_A &= \frac{\sqrt{R_A^2 - r_+^2}\sqrt{r_+^2 - r_-^2}}{\ell r_+} \\ \gamma_B &= \frac{\sqrt{R_B^2 - r_+^2}\sqrt{r_+^2 - r_-^2}}{\ell r_+}.\end{aligned} \tag{5.45}$$

Working in the co-rotating frame, we can write the total correlations as $L_{AB} = \sum_{n=-\infty}^{\infty}(I_n^- - \zeta I_n^+)$ where

$$I_n^{\pm} = K_L \int_{-\infty}^{\infty} dz \frac{e^{-a_X\left(z-\frac{2\pi n r_-}{\ell}\right)^2} e^{-i\beta_X\left(z-\frac{2\pi n r_-}{\ell}\right)}}{\sqrt{\cosh(\alpha_{X,n}^{\pm}) - \cosh(z)}} \tag{5.46}$$

with

$$K_L = \frac{1}{\sqrt{\sqrt{\alpha(R_A)-1}\sqrt{\alpha(R_B)-1}}} \frac{\lambda^2}{8\pi\sqrt{2}\ell} \gamma_B\gamma_A \left(\frac{2\sqrt{2\pi}\bar{\sigma}_A\bar{\sigma}_B}{\sqrt{\bar{\sigma}_A^2+\bar{\sigma}_B^2}}\right) e^{-\frac{\bar{\sigma}_A^2\bar{\sigma}_B^2(\bar{\Omega}_A-\bar{\Omega}_B)^2}{2(\bar{\sigma}_A^2+\bar{\sigma}_B^2)}} \frac{\ell^2 r_+}{r_+^2 - r_-^2}. \tag{5.47}$$

To calculate the total correlations numerically, equation (5.13) can be applied in conjunction with the methodology discussed in [234] to a precision of 10^{-4}. We approximate the integral as $-5s < \tau_A, \tau_B < 5s$ and integrate τ_B on the contour in Figure 5.1.

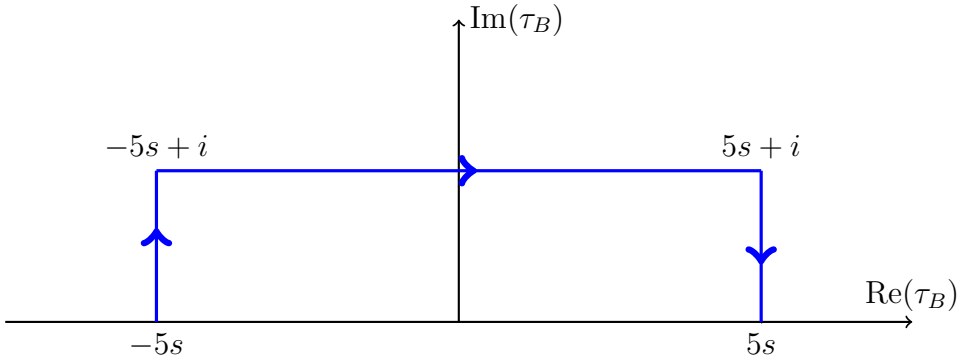

Figure 5.1: Contour to integrate over the τ_B variable when calculating L_{AB}.

Chapter 6

Anti-Hawking Effect for Rotating BTZ Black Holes

6.1 Introduction

Let us first consider a uniformly accelerating detector in Minkowski spacetime. It is well-known that the detector will increase in temperature, which will be proportional to the acceleration. This is known as the Unruh effect [62, 79, 240]. The Unruh affect appears because, as we saw in Chapter 2, the vacuum for one set of modes is different than the vacuum for another set. Therefore, the vacuum temperature of one set of modes is all different the the vacuum temperature of the other set.

We note that this is an idealized situation (for example, we are assuming the detector accelerates for eternity), though the Unruh effect has also been derived in a model-independent context in axiomatic quantum field theory [213]. The temperature of the field is given by the Kubo-Martin-Schwinger (KMS) condition, and this is exactly the temperature measured by the detector. It has also been shown that detectors experiencing other forms of acceleration (such as non-uniform or circular) also get hotter [31, 58, 71, 114, 171, 180, 248]. In these other situations, the temperature of the field and temperature of the detector are positively correlated, with the detector temperature monotonically increasing with the field temperature.

It has recently been shown that this positive correlation is not always true, and some situations actually exhibit the *anti*-Unruh effect. In this case, the field and detector temperatures are no longer positively correlated [40, 83]. The anti-Unruh effect can be split into the weak anti-Unruh effect (as the temperature of the field increases, the detector clicks less often) and the strong Anti-Unruh effect (the field temperature and detector temperature are inversely related) [83].

In the context of black holes, the Hawking effect is analogous to the Unruh effect [34]. Though it has been shown that, outside a black hole, the temperature of a detector tends to be positively correlated with the field temperature [103, 104, 163, 219], an anti-Hawking effect has recently been shown to exist, such that a static Unruh-DeWitt detector experiences both strong and weak versions of the anti-Hawking effect [100]. By considering $2+1$ dimensional static BTZ black holes, [100] showed that in some cases, there was an inverse relationship between the temperature of the detector and the temperature of the field, similar to the anti-Unruh effect.

Around rotating black holes, we note that the quantum vacuum differs significantly from non-rotating black holes [51, 172, 253]. To understand the quantum vacuum of a rotating BTZ black

hole, there have been many investigations into the scalar fields [42, 142, 152, 216] and the behaviour of Unruh-DeWitt detectors [103]. In a recent paper (and the subject of the next Chapter) [197], we demonstrated that rotation can significantly amplify the amount of entanglement harvested by Unruh-DeWitt detectors from the background at intermediate distances from near-extremal, small-mass black holes [197].

Motivated by this, here we study the implications of rotation for the anti-Hawking effect. In Section 6.2, we introduce the anti-Hawking effect and how to apply it for a rotating BTZ black hole. Then, in Section 6.3, we find that rotation increases the intensity of the weak anti-Hawking effect, but has a negligible influence on its threshold critical temperature. However for the strong anti-Hawking effect, which we discuss in Section 6.4 we find that there is a strong dependence on the angular momenta, with the effect becoming stronger or weaker depending on the boundary conditions. The influence of AdS length on the strong and weak versions of the effect is likewise distinct: the weak anti-Hawking effect is independent of AdS length whereas the strong version sees an increased temperature range. We provide our concluding remarks in Section 6.5.

6.2 Anti-Hawking effect

As we discussed in Chapter 5, we can use the light-matter interaction to model the detector-field interaction, where we take the detectors to be two-level quantum systems with ground state $|0\rangle_D$ and excited state $|1\rangle_D$, separated by an energy gap Ω_D, and having switching function $\chi_D(\tau)$. With the Unruh-DeWitt detector Hamiltonian of equation (5.2), the transition probability for our detector is given by equation (5.7). From the transition probability, we can then define the response function,

$$\mathcal{F} = \frac{P_D}{\lambda^2 \sigma}\,, \tag{6.1}$$

where σ describes the timescale of interaction between the field and the detector. In this paper, we shall focus on a Gaussian switching function, $\chi_D(\tau) = e^{-\frac{\tau^2}{2\sigma^2}}$.

We will consider fields whose Wightman functions that obey

$$W(\tau - i\beta, \tau') = W(\tau', \tau)\,, \tag{6.2}$$

which is known as the Kubo-Martin-Schwinger (KMS) condition[1] [97, 126, 144] and $T_{KMS} = 1/\beta$ is the temperature of the field. We see that this temperature is dependent only on the background spacetime and the quantum field. We are considering a Hartle-Hawking vacuum, so we note that the KMS condition will be affected if an alternative vacuum state was chosen.

We are now in a position to define a quantity known as the excitation to de-excitation ratio (EDR) temperature. Let the switching function by Gaussian of the form $\chi(\tau) = e^{-\tau^2/\sigma^2}$. Note that we can write the response function as [83]

$$\mathcal{F} = \frac{1}{2\pi}\int_{-\infty}^{\infty} d\omega |\tilde{\chi}(\omega)|^2 \tilde{W}(\Omega + \omega/\sigma)\,, \tag{6.3}$$

[1]Strictly speaking, this is only one part of the KMS condition. The pull-back of the Wightman function also requires holomorphicity and must be polynomially bounded [48, 76].

where ω is the Fourier transform variable, $\tilde{\chi}$ is the Fourier transform of the switching function and $\tilde{W}$ is the Fourier transform of the Wightman function. We have used the fact that we are considering fields obeying the KMS condition, which implies that the Wightman function obeys [83]

$$W(\tau, \tau') = W(\tau - \tau') \,. \tag{6.4}$$

We can also define the detector's excitation to de-excitation ratio [40, 83]:

$$\mathcal{R} = \frac{\mathcal{F}(\Omega)}{\mathcal{F}(-\Omega)} \,, \tag{6.5}$$

In the limit of infinite interaction time (i.e. $\sigma \to \infty$), we see that $\mathcal{F} \to \tilde{W}(\Omega)$. As we have $W(\tau - \tau' - i\beta) = W(\tau' - \tau)$, Fourier transforming both sides yields $\tilde{W}(-\omega) = e^{\beta\omega} W(\omega)$. Hence, we see that

$$\lim_{\sigma \to \infty} \mathcal{R} \to \frac{\tilde{W}(\Omega)}{\tilde{W}(-\Omega)} = e^{-\beta\Omega} \,. \tag{6.6}$$

We call the expression

$$\mathcal{R} = e^{-\Omega\beta}$$

the detailed balance condition. As β is the periodicity of the Wightman function, it can once again be assigned a temperature, which can be called the EDR temperature (T_{EDR}) [40, 83]. In the limit of infinite interaction time and flat spacetime, the EDR temperature is exactly equal to the KMS temperature. However, for finite interaction time, using $\mathcal{R} = e^{-\Omega/T_{EDR}}$ as a measure of temperature need not yield the same result as the KMS temperature [83].

This demonstrates that there are two methods of defining the temperature. One could define the temperature based on the response function or the temperature could be defined through the excitation to de-excitation ratio. However, for finite interaction time, T_{EDR} will be a complicated expression depending on T_{KMS} and Ω, though we emphasize that the dependence on Ω is relatively weak until Ω becomes too large. Because the detector approximately satisfies the detailed balance condition, it looks like the detector has thermalized, even though this has not yet occurred as the interaction is only finite in time [83].

Usually, an increase in the temperature of the black hole implies that the temperature measured by the Unruh-DeWitt detector also increases, so that T_{KMS} is proportional to T_{EDR}. However, this positive correlation does not always hold, and sometimes the anti-Hawking effect occurs [100]. Similar to the anti-Unruh effect , we can define the weak and strong versions of the phenomenon as [40, 83]:

$$\frac{d\mathcal{F}(\Omega)}{dT_{KMS}} < 0 \quad \text{weak} \,, \tag{6.7}$$

$$\frac{\partial T_{EDR}}{\partial T_{KMS}} < 0 \quad \text{strong} \,. \tag{6.8}$$

Physically, the weak effect says that a detector will click less often for larger field temperatures, while the strong effect says that the EDR detector temperature and KMS field temperature are inversely correlated.

We will be using the assumptions of Chapter 5.4 (i.e. Hartle-Hawking vacuum, co-rotating frame, Gaussian switching function, untwisted scalar field). Therefore, from the the Hawking temperature of a rotating BTZ black hole,

$$T_H = \frac{1}{2\pi\ell}\left(\frac{r_+^2 - r_-^2}{r_+}\right), \tag{6.9}$$

we can also write down its KMS temperature [242],

$$T_{KMS} = T_H/\gamma\,, \tag{6.10}$$

where

$$\gamma = \frac{\sqrt{r^2 - r_+^2}\sqrt{r_+^2 - r_-^2}}{r_+} \tag{6.11}$$

is the Lorentz factor in the co-rotating frame. Therefore, we can solve for the detector's coordinate position, R_D, in terms of T_{KMS}. As we showed in Section 5.4, we can write the detector's transition probability as $P_D = \sum_{n=-\infty}^{\infty}\eta^n\left\{I_n^- - \zeta I_n^+\right\}$, where

$$I_n^{\pm} = K_P\int_{-\infty}^{\infty} dz \frac{e^{-a\left(z-\frac{2\pi n r_-}{\ell}\right)^2} e^{-i\beta\left(z-\frac{2\pi n r_-}{\ell}\right)}}{\sqrt{(\cosh(\alpha_n^{\pm}) - \cosh(z))}}\,, \tag{6.12}$$

so that in terms of T_{KMS}, we have

$$K_P = \frac{\lambda^2\sigma_D}{4\sqrt{2\pi}}\,, \tag{6.13}$$

$$a = \frac{1}{(4\pi T_{KMS}\sigma_D)^2} \qquad \beta = \frac{\Omega_D}{2\pi T_{KMS}}\,, \tag{6.14}$$

$$\cosh(\alpha_n^{\pm}) = \pm 4\ell^2\pi^2 T_{KMS}^2 + (1 + 4\ell^2\pi^2 T_{KMS}^2)\cosh\frac{2\pi n r_+}{\ell}\,. \tag{6.15}$$

In the limit of an infinite interaction time (i.e. $\sigma \to \infty$), we note that we can write the $n = 0$ term (corresponding to AdS spacetime) analytically as

$$\lim_{\sigma\to\infty} P_{D,n=0} = \lim_{\sigma\to\infty} I_0 = \frac{\sqrt{\pi}}{4}\left[1 - \tanh\frac{\Omega_D}{2T_{KMS}}\right]\left[1 - \zeta P_{-1/2+i\beta}\left(\cosh\alpha_0^+\right)\right] \tag{6.16}$$

In subsequent sections, we are interested in the dependence of the response function and EDR temperature on the angular momentum and the AdS length.. We shall analyze the effects of varying the KMS temperature of the detectors, which is equivalent to varying the detector's coordinate position.

6.3 Weak Anti-Hawking Effect for Rotating BTZ Black Holes

Let us first consider the situation for black holes with large and intermediate masses. We will set the energy gap of the detector to be $\Omega_D\ell = 1/10$, though qualitatively similar results are obtained

for other energy gaps. In Figure 6.1, we consider the detector response as function of T_{KMS}. We see that for both $M = 100$ and $M = 1/10$, as well as all boundary conditions, the detector response decays to zero at small KMS temperatures. At larger KMS temperatures, the detector response asymptotes to a constant. In the case of the intermediate mass of $M = 1/10$, we see that rotation amplifies the detector's response at a given KMS temperature, with the greatest impact appearing at intermediate temperatures. We also see that that the boundary condition plays a large role as the weak anti-Hawking effect is absent for Dirichlet boundary conditions, yet present for the transparent and Neumann boundary conditions. We also see that the rate of change for the Neumann boundary condition case is greater than the rate of change for the transparent boundary condition case. This indicates that the weak effect is stronger for Neumann boundary conditions. In each of the insets, we consider $M = 100$ and find that the weak anti-Hawking effect vanishes for Dirichlet and transparent boundary conditions, yet is present for Neumann, confirming the results

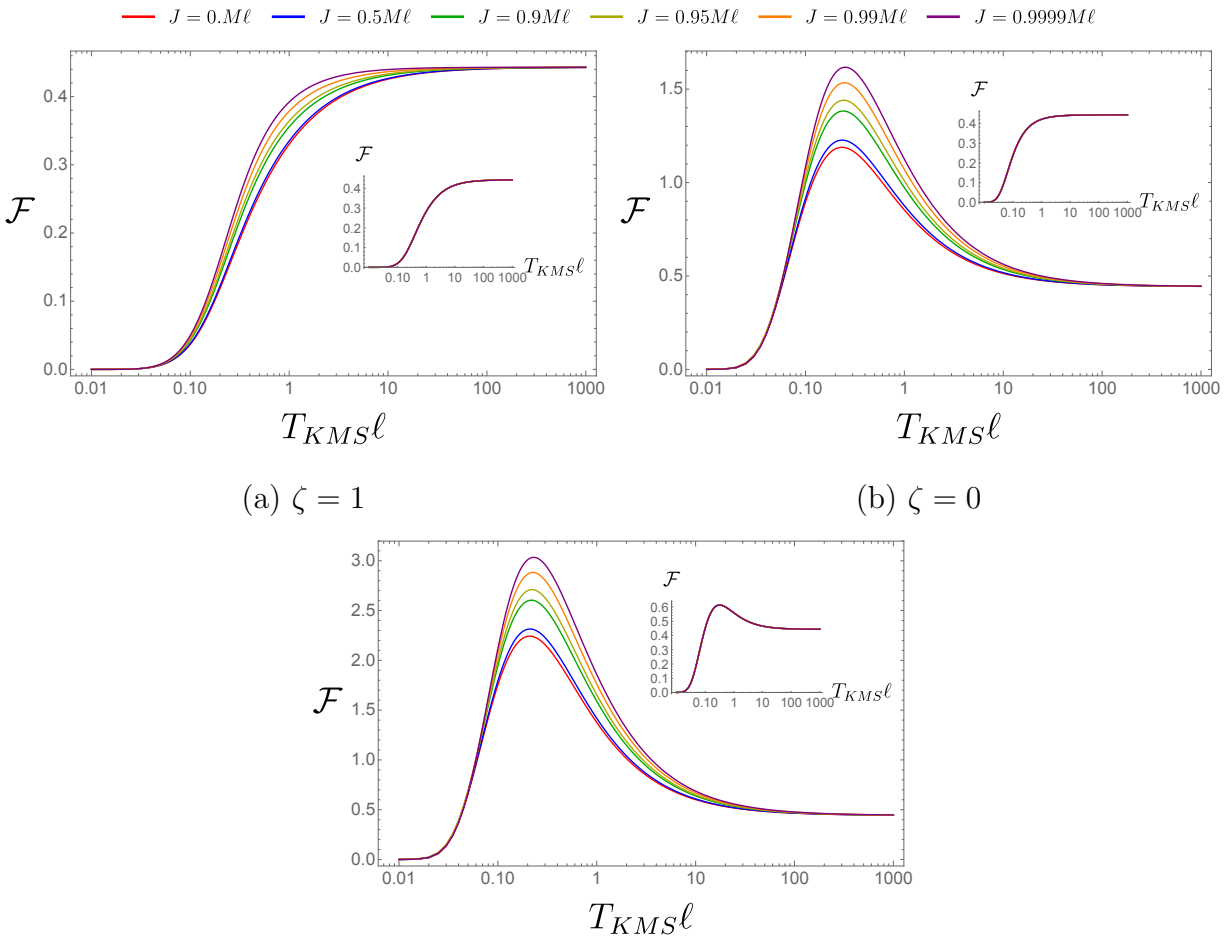

(a) $\zeta = 1$

(b) $\zeta = 0$

(c) $\zeta = -1$

Figure 6.1: Response functions for a black hole of mass $M = 1/10$ for Dirichlet, transparent, and Neumann boundary conditions (for the field at spatial infinity) and an energy gap of $\Omega\ell = 1/10$. The inset plots correspond to $M = 100$. As expected, the rotation of the black hole has a smaller effect for larger masses. As the mass of the black hole increases, the weak anti-Hawking effect goes away for $\zeta = 1$ and $\zeta = 0$. Note that for $\zeta = -1$, the weak anti-Hawking effect is still present even for large mass black holes.

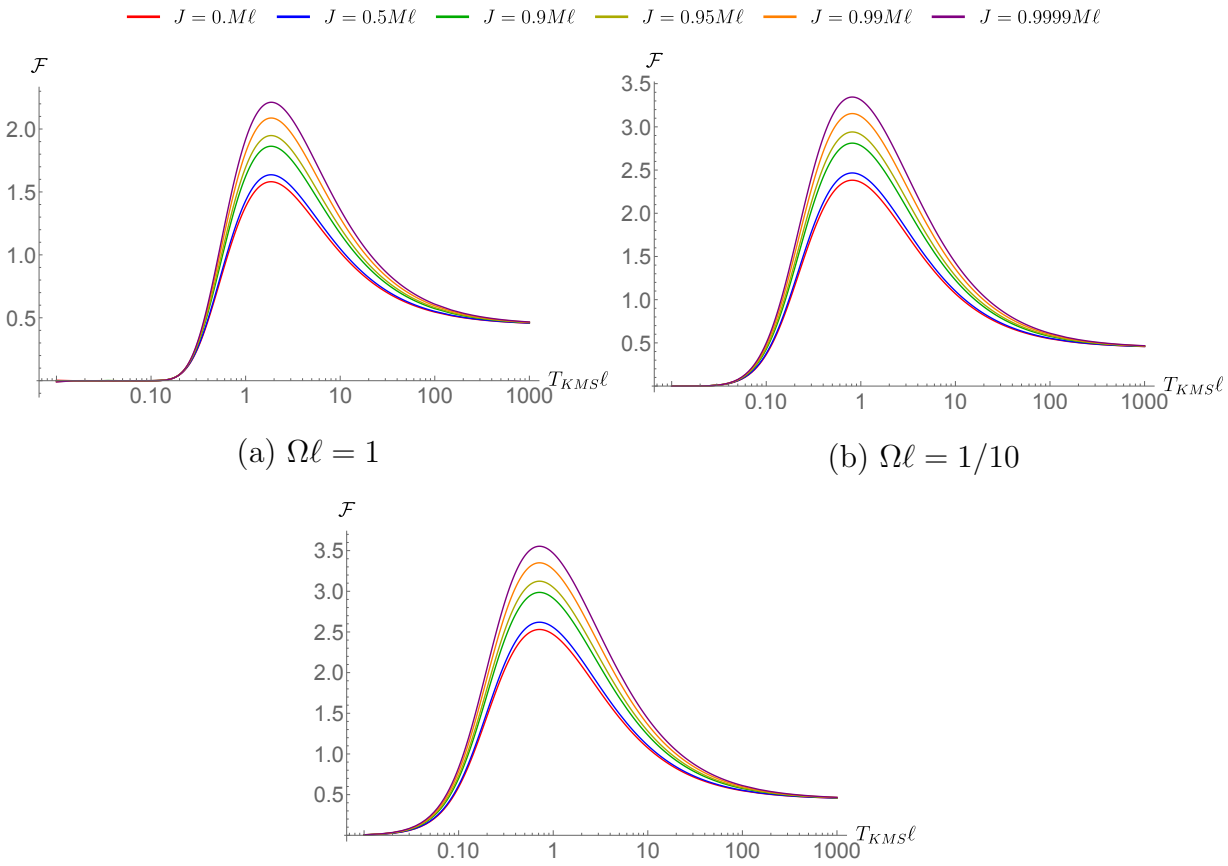

(a) $\Omega\ell = 1$

(b) $\Omega\ell = 1/10$

(c) $\Omega\ell = 1/100$

Figure 6.2: Response of a rotating BTZ black hole with mass $M = 1/1000$ and Dirichlet boundary conditions ($\zeta = 1$). We note that for transparent and Neumann boundary conditions, qualitatively similar results are obtained.

of [100] for large-mass black holes. We also note that angular momentum plays a negligible role in the case of large-mass black holes, regardless of KMS temperature.

As we have seen (and as found by [197]), rotation has a much greater influence for smaller mass black holes. In Figure 6.2, we consider a black hole of mass $M = 1/1000$ and plot the response function against KMS temperature. We see that, in this case, the weak anti-Hawking effect also appears for Dirichlet boundary conditions. In fact, the peak response function is seven times as large as the maximum of the response function for Dirichlet boundary conditions in Figure 6.1. Similarly, the other boundary conditions show an enhanced response function for the $M = 1/1000$ case, as compared to $M = 1/10$. Indeed, rotation continues to enhance the response function for all KMS temperatures. We also see that, regardless of the black hole's angular momentum or the detector's energy gap, the response function asymptotes to $P_D = \frac{\sqrt{\pi}}{4}$, as seen in equation (6.16), where we note that from equation (6.12) that $I_n \to 0$ for $n \neq 0$.

The strength of the weak effect is given by the magnitude of the slope after the peak, as seen in equation (6.7) We see that the magnitude of the slope increases with decreasing gap, showing that smaller gap enhances the weak anti-Hawking effect, which we illustrate for Dirichlet boundary conditions in Figure 6.3, with the slope peaking at $\frac{d\mathcal{F}}{dT_{KMS}\ell} \approx -0.15$ for the large energy gap and $\frac{d\mathcal{F}}{dT_{KMS}\ell} \approx -0.6$ for the small gap. We also see that the weak anti-Hawking effect is amplified for

increasing rotation, by as much as 50% as compared to the non-rotating case, depending on the energy gap.

We also find that the critical KMS temperature corresponding to the appearance of the weak effect depends on the energy gap of the detectors, yet does not depend on rotation, as we see in Figure 6.2. However, we also emphasize that this critical temperature does depend on the boundary condition.Though we have only illustrated results for Dirichlet boundary conditions $\zeta = 1$, we emphasize that this critical value depends on ζ, with the critical temperature becoming smaller as $\zeta \to 1$.

Finally, we note that changing the AdS length will not change the strength of the weak effect. Physically, this is because the AdS length is the only length scale present (as $\sigma \to \infty$), and everything is calibrated against this length.

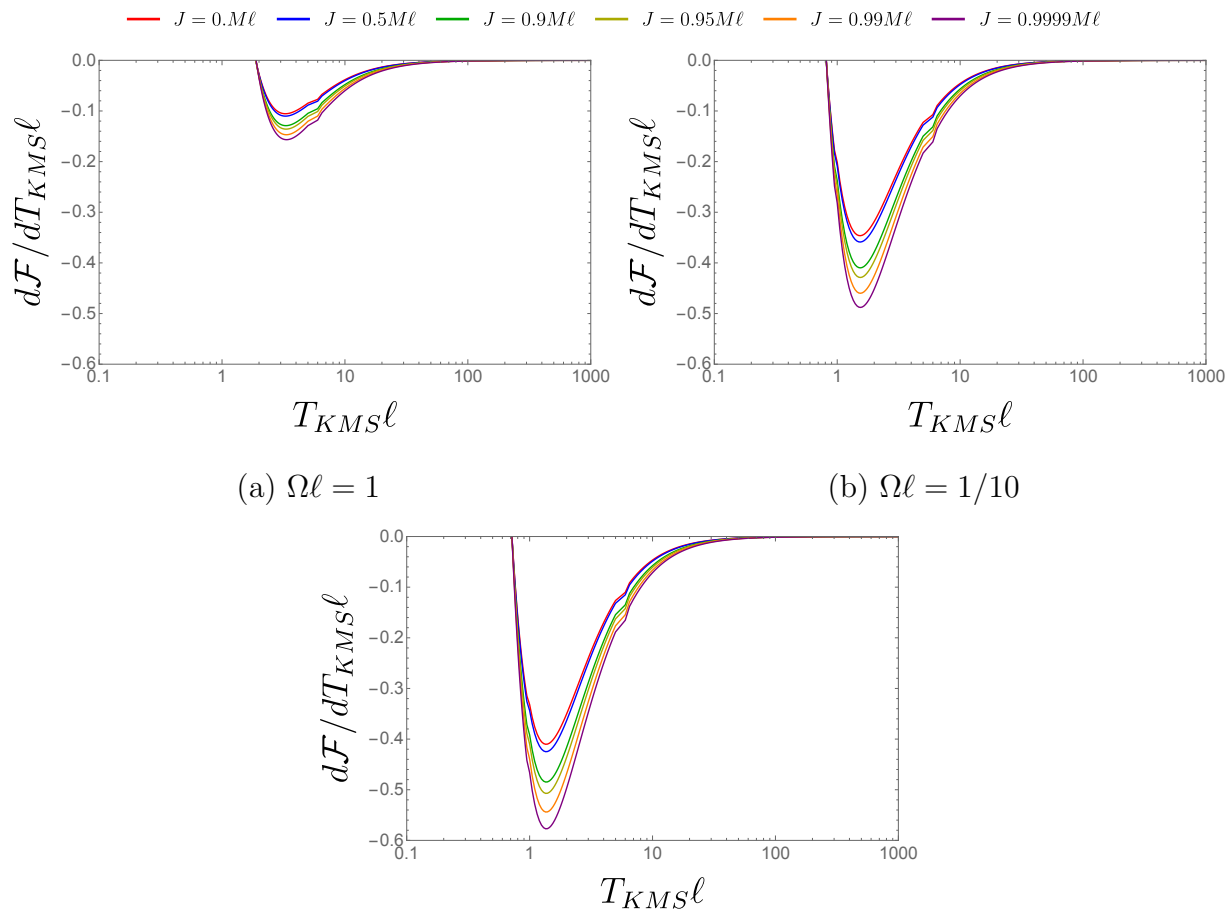

(a) $\Omega\ell = 1$

(b) $\Omega\ell = 1/10$

(c) $\Omega\ell = 1/100$

Figure 6.3: Derivative of the response with respect to the KMS temperature of a rotating BTZ black hole with mass $M = 1/1000$ and Dirichlet boundary conditions ($\zeta = 1$). We note that for transparent and Neumann boundary conditions, qualitatively similar results are obtained.

6.4 Strong Anti-Hawking Effect for Rotating BTZ Black Holes

We will now investigate the strong anti-Hawking effect. In Figures 6.4 and 6.5, we consider the relationship between the EDR and KMS temperatures. We set $M = 1/1000$ and analyze the dependence on rotation, boundary condition, and energy gap.

We first note that in Figure 6.4, the strong anti-Hawking is present for transparent on Neumann boundary conditions. For Dirichlet boundary conditions, we need to consider temperatures close to zero, as shown in Figure 6.5, though we see that the strong anti-Hawking effect will also be present. Let us first focus on Neumann and transparent boundary conditions. For small values of the KMS temperature, we see that an increase T_{KMS} corresponds to a decreasing T_{EDR}. As seen in the insets, a critical KMS temperature will eventually be reached so that the KMS and EDR temperatures then become positively correlated. At these larger temperatures exhibiting positive correlation, we see that there will be little dependence on angular momentum. In contrast to the weak anti-Hawking effect, an increasing angular momentum corresponds to a weaker strong anti-Hawking effect, with the strength of the effect given by equation (6.8). We see that as extremality is approached, the

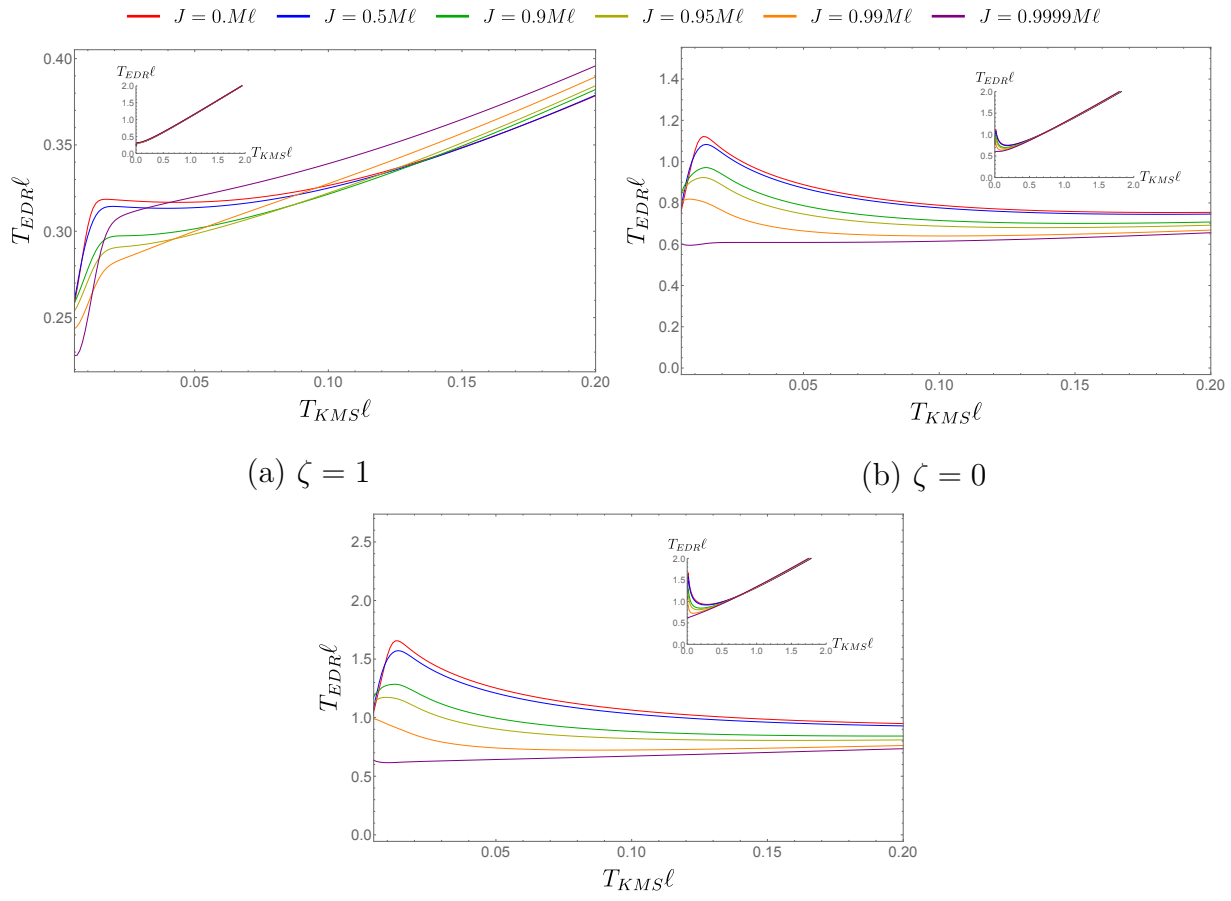

(a) $\zeta = 1$

(b) $\zeta = 0$

(c) $\zeta = -1$

Figure 6.4: EDR temperature for a black hole of mass $M = 1/1000$ and detector energy gap of $\Omega\sigma = 1$. We plot KMS temperature down to $T_{KMS}\ell = 10^{-5}$. The insets show the relation between the EDR temperature and KMS temperature for larger values of T_{KMS}.

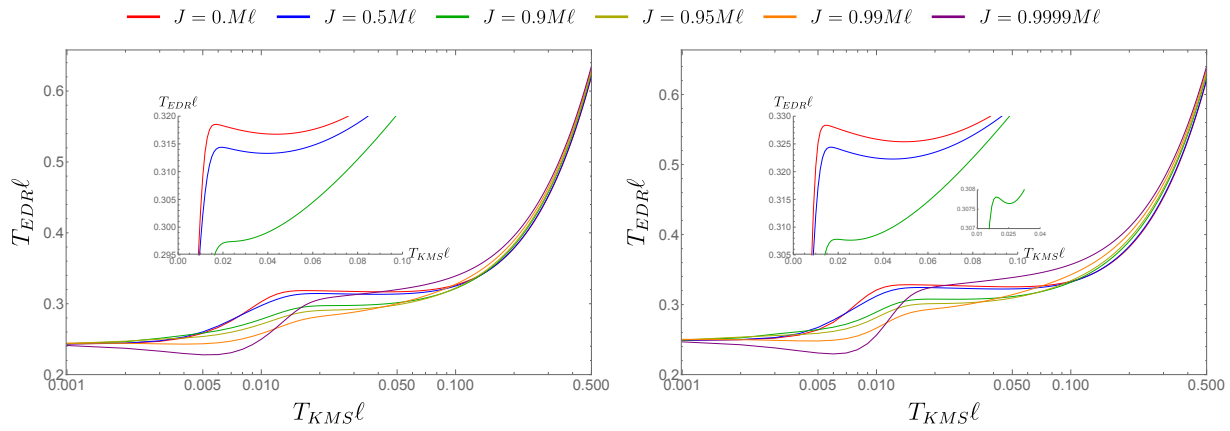

(a) $\Omega\sigma = 1$ (a) $\Omega\sigma = 1/100$

Figure 6.5: EDR temperature for a black hole of mass $M = 1/1000$ and detector energy gap of $\Omega\sigma = 1/10$. The results are similar for $\Omega\sigma = 1/100$. The insets show the EDR temperature for our first three values of the angular momentum, plotted on a linear scale (rather than a log scale, as is the case for the main plots).

strong anti-Hawking effect disappears.

Dirichlet boundary conditions shows a different trend than transparent or Neumann boundary conditions. In Figure 6.5, we plot the strong the EDR temperature for Dirichlet boundary conditions for $\Omega\sigma = 1$ and $\Omega\sigma = 1/100$. In the insets, we see that there is a small strong anti-Hawking effect for non-rotating black holes, similar to what was found in [100]. As the angular momentum increases, the critical KMS temperature at which this effect first appears decreases. We also qualitatively see that the magnitude of the slope becomes larger for larger angular momenta, indicating that the strong anti-Hawking effect becomes stronger. For smaller values of the energy gap, we see that strong anti-Hawking effect increases in strength, with the $\Omega\sigma = 1/10$ case being similar to $\Omega\sigma = 1/100$. This can be seen by noting that $J/M\ell = 0.9$ does not exhibit the strong anti-Hawking effect for $\Omega\sigma = 1$, but there is a small effect present at this value of the angular momentum for $\Omega\sigma = 1/100$. However, for near-extremality, the strength of the strong anti-Hawking effect appears to be approximately the same.

As ζ increases from -1 to 1 in Figure 6.4, We see that the temperature range of the strong anti-Hawking effect decreases, with the range being quite small for Dirichlet boundary conditions. As we see in Figure 6.5, the strong anti-Hawking effect only occurs for a relatively small range of KMS temperatures. As angular momentum increases, the range of KMS temperatures decreases for transparent and Neumann boundary conditions.

For Dirichlet boundary conditions and sufficiently small angular momentum, an increasing angular momentum also corresponds to a decreasing range of T_{KMS} temperatures, but beyond a critical value, increasing angular momenta corresponds to a greater range of T_{KMS} temperatures for which the effect is present. As a result, the anti-Hawking effect appears to nearly disappear for near-extremal black holes $J \geq 0.9999M\ell$ for transparent and Neumann boundary conditions, yet is still present for Dirichlet boundary conditions. In Figure 6.5, we see that there is a strong anti-Hawking effect for a non-rotating black hole, but the effect disappears (or almost disappears, depending on the energy gap) as the angular momentum increases to $J/M\ell = 0.9$. However, as we continue to approach extremality, the effect emerges at low KMS temperature and begins to grow

in the strength, as evidenced by the curve for $J/M\ell = 0.9999$. It is quite remarkable that there is such a strong dependence on boundary conditions.

In Figures 6.4 and 6.5, we also note that for Dirchlet boundary conditions, there appears to be a 'crossover' effect for small KMS temperatures. At the lowest KMS temperature, we see that smaller angular momenta correspond to larger EDR temperature. However, as the KMS temperature increases, we see that the rate of change of the EDR temperature with respect to the KMS temperature increases with increasing angular momentum. As a result, the curves corresponding to larger values of the angular momentum cross the lower angular momentum curves at a sufficiently large KMS temperature. At large KMS temperature, we see that $T_{EDR} \sim T_{KMS}$, such that now, at a fixed KMS temperature, the larger angular momentum corresponds to a larger EDR temperature, completely reversing the order of the curves for small KMS temperature. We have numerically verified that this also effect appears for Neumann and transparent boundary conditions.

We see that by comparing Figures 6.2-6.5, the ranges of the weak and strong anti-Hawking effects do not overlap. The weak anti-Hawking effect appears for $T_{KMS}\ell \gtrsim 1$, while the strong anti-Hawking effect appears for $T_{KMS}\ell \lesssim 0.1 - 0.5$ (with the exact temperature range dependent on the boundary conditions, energy gap, and in the case of the strong anti-Hawking effect, the angular momentum). In addition, the critical KMS temperature corresponding to the disappearance of the strong anti-Hawking effect decreases with increasing angular momentum. This is in contrast to what we saw earlier for the weak anti-Hawking effect – an increasing angular momentum has minimal effect on the critical KMS temperature. However, we emphasize that the value of the critical temperature for the strong anti-Hawking effect strongly depends on the boundary conditions.

Finally we consider the impact of changing the AdS length on the strong effect. Here the situation differs from the weak anti-Hawking effect as now there is a second length scale present (σ). In Figure 6.6, we consider the effect of changing the AdS length for a non-rotating BTZ black hole, compared to a near-extremal BTZ black hole. In the non-rotating case, an increased AdS length increases the KMS temperature range for the strong anti-Hawking effect. However, the marginal effect of increasing ℓ is reduced for larger and larger values of the AdS length. We also

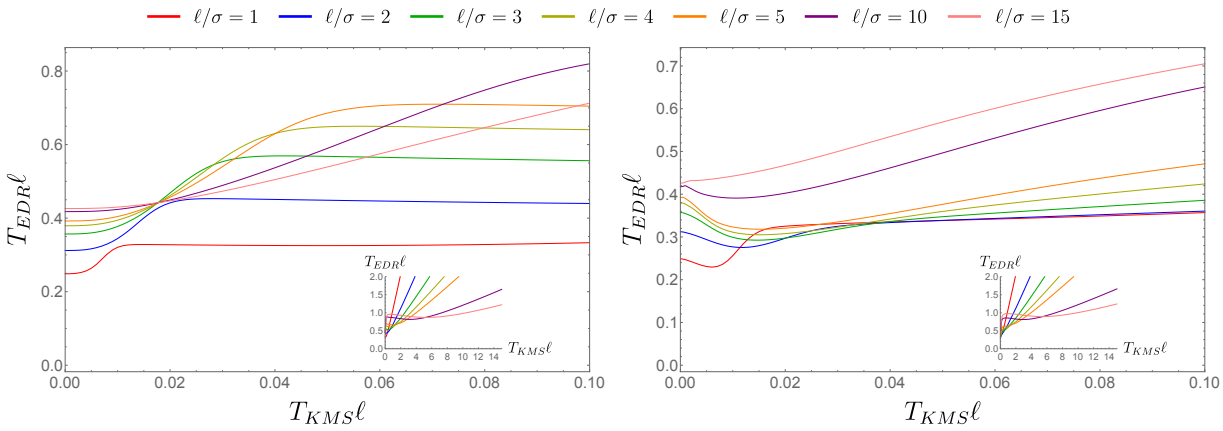

(a) $J/M\ell = 0$ (b) $J/M\ell = 0.9999$

Figure 6.6: Changing AdS lengths for the strong anti-Hawking effect for a black hole of mass $M = 1/1000$, Dirichlet boundary conditions. We plot KMS temperature down to $T_{KMS}\ell = 10^{-5}$. The insets show the effect of changing AdS length on the EDR temperature for larger values of T_{KMS}.

see that for small $T_{KMS}\ell$, a larger AdS length will broaden out the initial peak. In the case of a near-extremal black hole, the situation is similar. As we saw in Figure 6.5, there was a strong anti-Hawking effect present for near-extremal black holes. For larger AdS lengths, we similarly see that the temperature range of the strong anti-Hawking effect increases in size, though still remains relatively weak.

6.5 Conclusion

As we saw with entanglement harvesting, rotating can have a significant and non-trivial effect on Unruh-DeWitt detectors [197]. In the case of large-mass black holes with Dirichlet and transparent boundary conditions, we saw that the weak anti-Hawking effect disappeared, though it is still present for Neumann boundary conditions, as found by [100]. For large-mass black holes, rotation has a negligible effect, but begins to amplify the response function and the weak anti-Hawking effect as the mass of the black hole is decreased.

For the strong anti-Hawking effect, rotation weakens the effect in the case of Neumann and transparent boundary conditions. For Dirichlet boundary conditions, however, increasing angular momentum decreases the strength of the effect before increasing it again.

In addition, we also found that there is a 'crossover' phenomenon for the strong anti-Hawking effect for each boundary condition (and most noticeable for Dirichlet boundary conditions.). We found that for small $T_{KMS}\ell$, larger angular momentum corresponded to smaller $T_{EDR}\ell$. In contrast, for larger values of $T_{KMS}\ell$, we saw that larger angular momenta corresponded to a *larger* value of $T_{EDR}\ell$. More work is needed to better understand how this cross-over effect comes about and why it is only present for Dirichlet boundary conditions. It would also be interesting to consider whether $3+1$ dimension rotating black holes also exhibit these same findings as the rotating BTZ black hole.

We also showed that the weak anti-Hawking effect is independent of AdS length, while increasing the KMS temperature range of the strong anti-Hawking effect. However, as the AdS length increases, the marginal effect on the strong anti-Hawking effect is reduced.

It is surprising that there is such a strong dependence of the strong Anti-Hawking effect on the form of boundary conditions for a small-mass rotating black holes. Understanding the rationale behind this will require a further investigation. In particular, it would be interesting to determine if a similar effect can be seen in Kerr black hole spacetimes as the spacetime is asymptotically Minkowski, so there would not be a dependence on boundary conditions of the field).

Chapter 7

Entanglement Amplification from Rotating Black Holes

7.1 Introduction

As discussed in Chapter 1, there is large interest in understanding the nature of the quantum vacuum. In the previous Chapter, we considered a single Unruh-DeWitt detector orbiting a rotating BTZ black hole. With two detectors, we can now consider a phenomenon known as entanglement harvesting. As shown by [230, 231], the vacuum (taken to be a free field) in Minkowski spacetime is naturally entangled. In fact, it was later shown that when atoms interacts with the vacuum, part of the vacuum's entanglement could be transferred to atoms, even if the atoms were initially uncorrelated and spacelike or timelike separated [244]. It was also shown that this continues to hold true when specifically considering the Unruh-DeWitt detector model [193, 194]. This transfer of entanglement has been termed 'entanglement harvesting.'

With entanglement harvesting, it is possible to investigate a wide variety spacetimes, such as Minkowski [147], de Sitter [116, 225], and anti-de Sitter [99]. This allows us study effects like geometry and spacetime topology [147, 225], the thermal nature of de Sitter spacetime [116, 225], and new features of anti-de Sitter spacetime [99, 166]. However, little research into entanglement harvesting has been done for black hole spacetimes. This was only first done relatively recently for a $2+1$ dimensional spacetime, in which it was found that there are regions (called entanglement shadows) of such spacetimes in which harvesting entanglement is not possible [98]. However, it is believed that such phenomena may be universal to other black hole spacetimes [100]. A recent study of entanglement harvesting in Schwarzschild/Vaidya spacetimes is commensurate with this expectation [234].

In Section 7.2, we show that the harvested entanglement (as measured by the concurrence of two Unruh-DeWitt detectors) can be significantly amplified at intermediate distances away from a rotating BTZ black hole. This effect is most pronounced for near-extremal small-mass black holes and still occurs even for large spacelike detector separations. With increasing angular momentum of the black hole, we also find that there is still amplification near the horizon of the black hole as well as a smaller size of the entanglement shadow. These results indicate that the properties of the vacuum are more subtle than has been anticipated. We then provide our concluding remarks in Section 7.3.

7.2 Entanglement Harvesting around a Rotating BTZ Black Hole

We are interested in implementing the entanglement harvesting protocol near a rotating BTZ black hole using the Unruh-DeWitt detector model of equation (5.2). We will be using the same assumptions that we discussed in Chapter 5 (i.e. conformally-coupled field, Gaussian switching function, untwisted scalar field, co-rotating frame). We shall also consider detectors with equal energy gaps, $\Omega_A = \Omega_B = \Omega$, and switching functions, $\chi(\tau_A) = e^{-\tau_A^2/2\sigma_A^2}$ and $\chi(\tau_B) = e^{-\tau_B^2/2\sigma_B^2}$. For simplicity, we will focus on the case of $\sigma_A = \sigma_B = \sigma$ and we will only consider Dirichlet boundary conditions of $\zeta = 1$. However, we obtain qualitatively similar results for $\zeta = -1$ and 0.

In the co-rotating frame, we consider two detectors A and B, respectively located at R_A and R_B whose proper separation is,

$$d(R_A, R_B) = \ell \log\left(\frac{\sqrt{R_B^2 - r_-^2} + \sqrt{R_B^2 - r_+^2}}{\sqrt{R_A^2 - r_-^2} + \sqrt{R_A^2 - r_+^2}}\right), \tag{7.1}$$

at fixed (t, ϕ). We will keep $d(R_A, R_B)/\sigma$ fixed whilst computing the concurrence for as a function

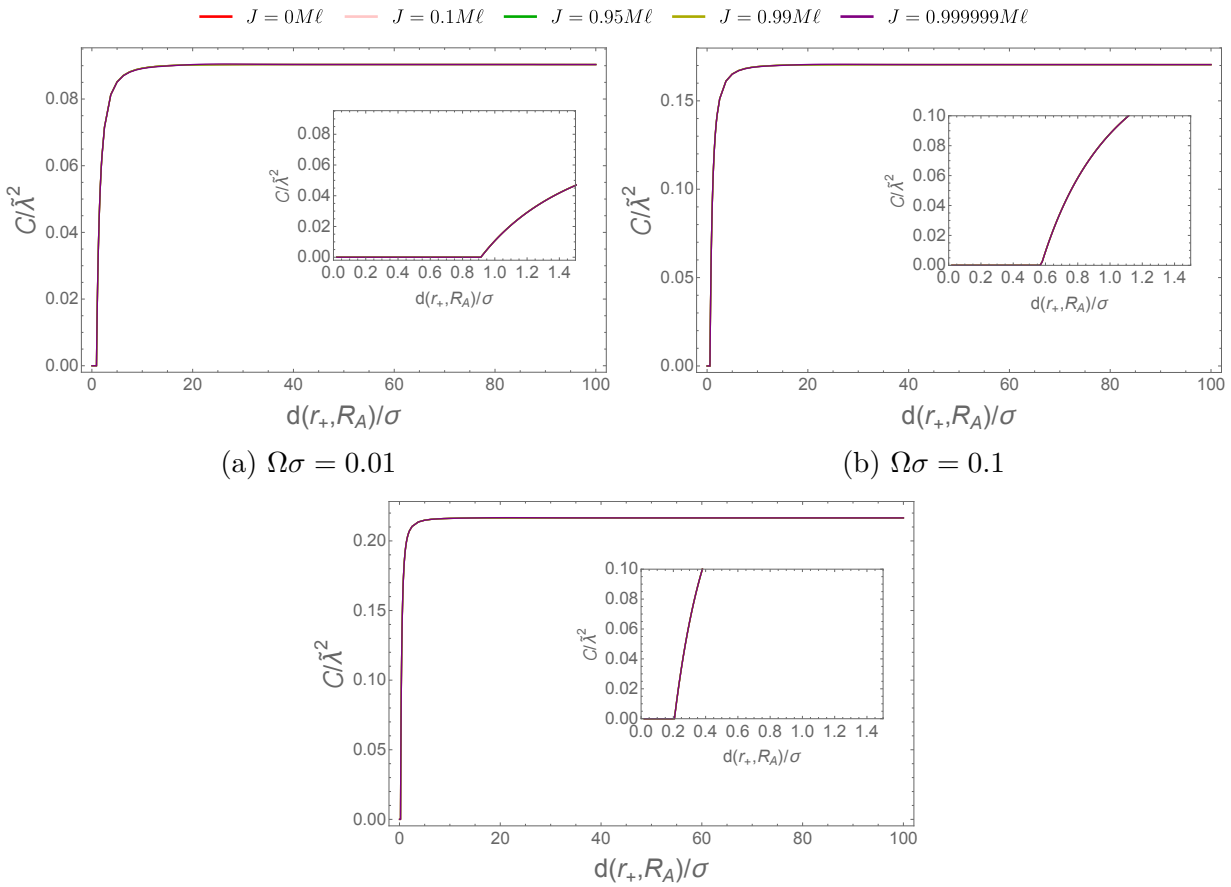

(a) $\Omega\sigma = 0.01$

(b) $\Omega\sigma = 0.1$

(c) $\Omega\sigma = 1$

Figure 7.1: Concurrence of two UDW detectors separated by a distance $d(R_A, R_B) = 1$ orbiting a black hole of mass $M = 1$ for various angular momenta. We have set $\zeta = 1$ and $\ell/\sigma = 10$. Note that all curves lie on top of one another.

of the proper distance $d(r_+, R_A)/\sigma$ between detector A and the outer horizon at $r = r_+$.

We will first discuss the case of a large-mass black hole, as considered by [98] (though, only for the non-rotating case), which we illustrate in Figure 7.1. We plot the concurrence for various values of angular momentum and see that all curves lie on top of each other, indicating that rotation has minimal effect on entanglement harvesting for large-mass black holes. There are a couple features of note that were realized by [98]. First, we see that there is a region of zero concurrence close to the black hole, which is called the entanglement shadow. As indicated by the insets, the size of this shadow decreases for larger energy gap. We also see that for larger energy gap, the maximum concurrence also increases, with it plateauing to a constant. Far away from the black hole, the spacetime is AdS. Close to the black hole, as realized by [98], there will be a larger Hawking temperature, which corresponds to an increased transition probability. In addition, the redshift will also decrease the non-local correlations. As the concurrence is $\mathcal{C} = 2\max\left[0, |X| - \sqrt{P_A P_B}\right]$, these two effects contribute to the appearance of an entanglement shadow in which the two detectors cannot become entangled. As was noted by [98], the size of the energy gap contributes to the relative importance of X and $P_{A,B}$, and thus, the size of the entanglement shadow.

At smaller masses, however, there is far more structure that can be seen. We show our main result in Figure 7.2. As we see, rotation (especially for the near-extremal case) has a significant

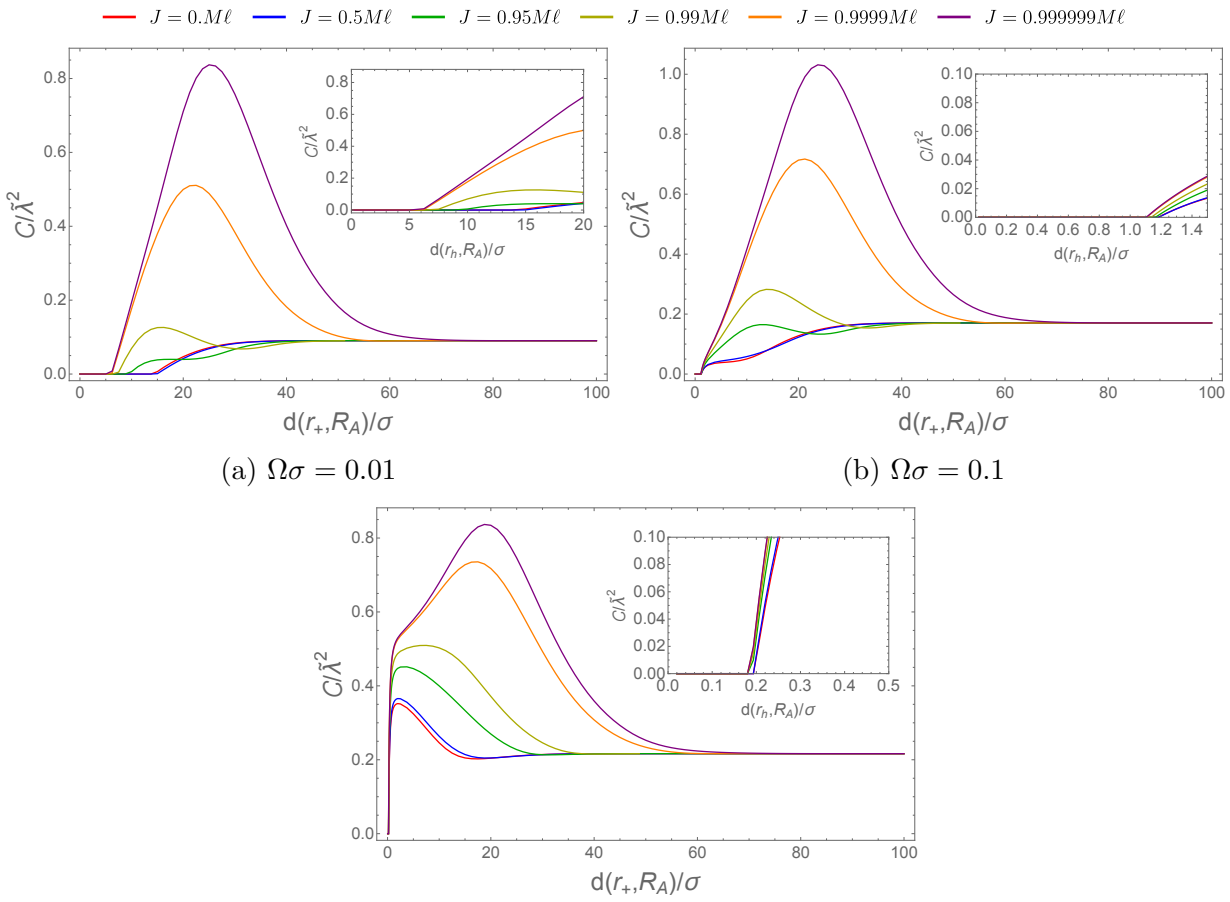

(a) $\Omega\sigma = 0.01$

(b) $\Omega\sigma = 0.1$

(c) $\Omega\sigma = 1$

Figure 7.2: Concurrence of two UDW detectors separated by a distance $d(R_A, R_B) = 1$ orbiting a black hole of mass $M = 10^{-3}$ for various angular momenta. We have set $\zeta = 1$ and $\ell/\sigma = 10$.

effect on the amount of concurrence that can be harvested. In the case of a small energy gap and small angular momentum, the concurrence montonically increases with increasing proper separation of detector A from the horizon. For large-enough proper distances, the concurrence will asymptote to its value in AdS spacetime. We have numerically verified that this value is independent of both the angular momentum and mass of the black hole, as expected.

For most values of the angular momentum, there is not a significant difference from the $J = 0$ case. Above $J/M\ell \geq 0.9$, we begin to see significant departures from the non-rotating case. Above this value, we see that the concurrence grows beyond the value predicted for the non-rotating black hole. Furthermore, the insets demonstrate the entanglement shadow will also decrease in size. Near extremality, the growth in the concurrence becomes quite rapid. As we see in the case of $\Omega\sigma = 0.01$, the peak in the concurrence is ~ 8 times larger than the non-rotating case, occurring relatively far from the horizon at $d(r_+, R_A) \sim 25\sigma \sim 100r_+$. We note that such a peak will occur at intermediate distance from the horizon, rather than near the boundary of the black hole. For this reason, we conjecture that the amplification is independent of the asymptotics of the black hole.

Let us now consider an increasing energy gap. As $\Omega\sigma$ grows, these trends that we have identified are exaggerated. The entanglement shadow will further shrink with the maximum value of the concurrence continuing to grow. In fact for $\Omega\sigma = 0.1$, the concurrence is peaked with a value ~ 10 times larger than the non-rotating case. We also see that the growth in the concurrence becomes more rapid and the shadow still decreases in size as $\Omega \to \sigma$, though we note that the maximum concurrence is slightly smaller than the $\Omega\sigma = 0.1$ case. As compared to the $J = 0$ maximum value of the concurrence, we see that the peak for the $\Omega\sigma = 1$ is only about 2 times as large. For large proper distances, the concurrence then decreases to its asymptotic value of AdS spacetime, independent of $J/M\ell$. Interestingly, for intermediate values of the angular momentum, both amplification and diminishment are exhibited in the concurrence before achieving the AdS value are large proper distances.

Let us now consider how amplification is affected by proper distance between the detectors. For increasing distances, the amplification effect still remains at intermediate distances (up to a maximum proper separation between the detectors. We demonstrate this finding in Figure 7.3 for $\Omega\sigma = 1$. One way to try and understand this effect is through the use of a signalling estimator (adapted from [145, 234], where we are using the Wightman function without derivative coupling),

$$\mathcal{E} = -\frac{\lambda^2}{2}\Im\left[\int d\tau_a d\tau_B \chi(\tau_A)\chi(\tau_B)W(x_A(\tau_A), x_B(\tau_B)\right] . \tag{7.2}$$

This estimator helps describe the ability of the two detectors to communicate with each other, and should be non-zero only where there is non-zero concurrence [234]. However, as shown in Figure 7.4a, this analysis is inconclusive as we see that the signalling estimator is non-zero even where the concurrence is zero. We believe that this is because the signalling estimator is picking up dependence on the part corresponding to $|X|^2 - \sqrt{P_A P_B} < 0$ (Figure 7.4b).

Therefore, to try and understand the amplification for large proper separations, let us. instead calculate the strength of the coupling (which we call the overlap) between one detector and the field when the maximum signal of the other detector reaches it. This will tell us how the signal from one detector has degraded when it reaches the light cone of the other detector. By fixing the AdS length, proper distance between detector A and the black hole, and the proper distance between detectors A and B, we can calculate the light travel distance between detectors A and B. This will then let us calculate the elapsed time on each detector's clock, thereby giving us calculate the

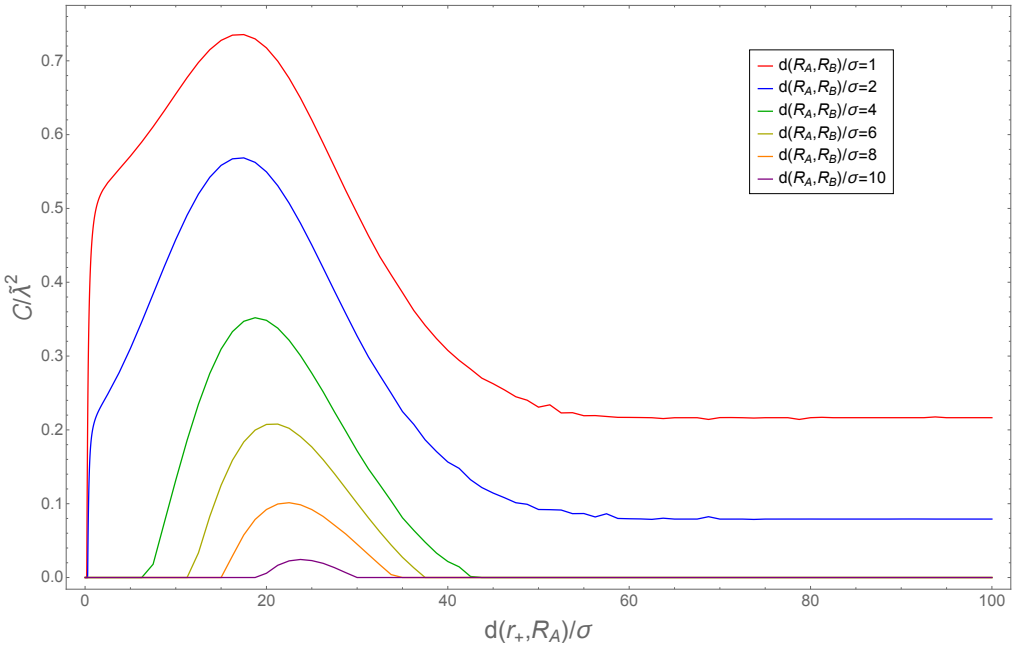

Figure 7.3: Concurrence as a function of $d(r_+, R_A)/\sigma$ for various co-rotating detector separations $d(R_A, R_B)$, for $M = 10^{-3}$, $\zeta = 1$, $\ell/\sigma = 10$, $\Omega\sigma = 1$, and $J/M\ell = 0.9999$.

value of the Gaussian switching function. When the overlap between the switching functions of the detectors is $\lesssim 10^{-8}$, they are effectively spacelike separated, yet still possess a non-zero concurrence. Further, at $d(R_A, R_B) = 10\sigma$, the overlap is $\lesssim 10^{-22}$. These estimates demonstrate that small-mass near-extremal black holes still permit entanglement harvesting even at large detector separations.

We note that our results are qualitatively similar for different AdS lengths. For larger ℓ/σ, the height of the peak decreases and broadens in width, with the maximum moving to larger proper distances. For smaller ℓ/σ, the peak increases in height, narrows, with the maximum moving closer to the horizon. In Figure 7.5, we show changing AdS lengths for a near-extremal case, where these distinctions are most significant.

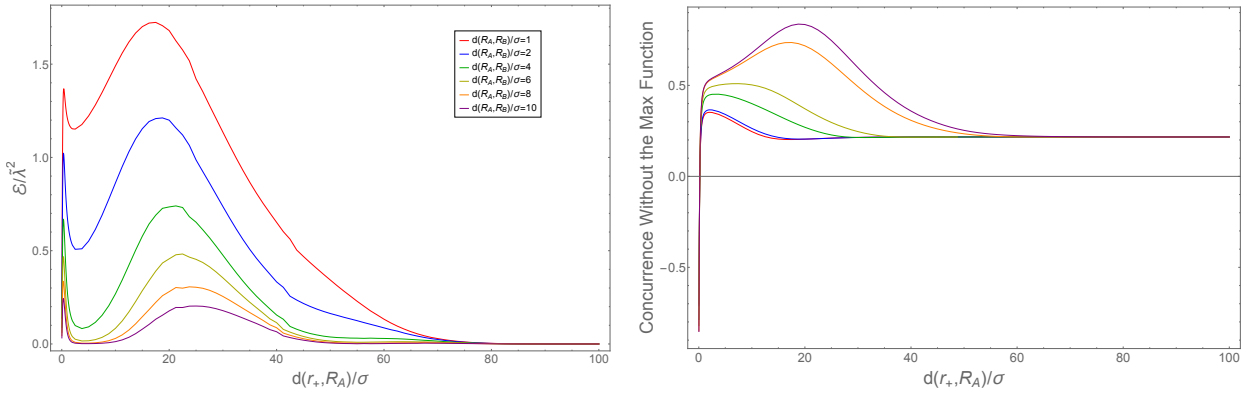

(a) Signalling Estimator for $\Omega\sigma = 1$, $J/M\ell = 0.9999$, and $d(R_A, R_B)/\sigma = 1$.

(b) $2\left(|X| - \sqrt{P_A P_B}\right)$ for $\Omega\sigma = 1$.

Figure 7.4: Investigating the signalling estimator for various proper separations for a black hole of mass $M = 10^{-3}$, AdS length of $\ell/\sigma = 10$, and Dirichlet boundary conditions.

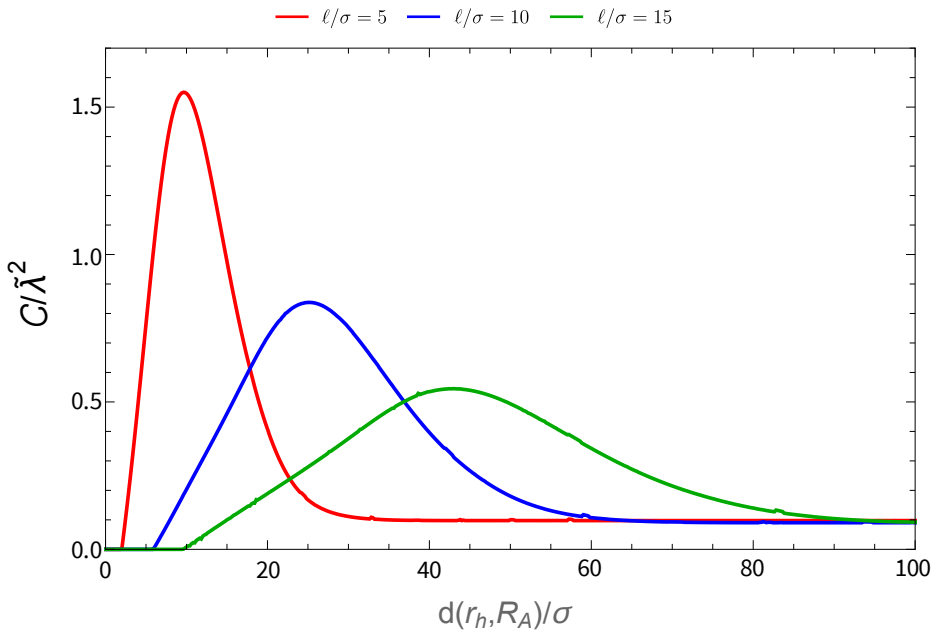

Figure 7.5: The effect of changing the AdS length on the harvested entanglement. We see that smaller AdS lengths correspond to significantly greater amplification. We have set $\Omega\sigma = 1/100$, $J/M\ell = 0.999999$, $\zeta = 1$, and $M = 10^{-3}$.

We will now attempt to understand the origin of this entanglement amplification for near-extremal black holes. From equation (5.21), we see that concurrence is depends on the relative sizes of $|X|$ and $\sqrt{P_A P_B}$. Therefore, the peak will arise because of the difference in the rates of growth/rate of these two quantities. We can investigate the coefficients of terms and see from equations (C.14) and (C.39) that there are no divergences in coefficients of the detector probabilities and non-locailities. In fact, both are independent of r_-, so are well-behaved as $r_+ \to r_-$. The partial image sums also demonstrate that this amplification effect is also not a kinematic effect, in contrast to what was found for AdS-Rindler spacetime [100,119]. In Figure 7.6, we plot the detector probabilities, non-locality, and concurrence for several different partial image sums. There is no entanglement amplification for the $n = 0$ term, which corresponds to the AdS-Rindler case [100]. Instead the concurrence only begins to show a definite peak for $|n| > 3$. This demonstrates that the amplification effect arises from the black hole itself. For an increasing number of terms in the image sum, the peak in $|X|$ broadens for increasing detector distance from the horizon. This is the result of the shift in the exponential part of the integrand of X by $\frac{2\pi n r_-}{\ell}$. In contrast, for an increasing number of terms in P_D, no such broadening will occur for large-enough values of J.

We note that the image sum appears to converge beyond $|n| > 30$ for all detector separations studied. In fact, comparing the image sums for $\sum_{n=-1}^{1}$ and $\sum_{n=-7}^{7}$demonstrates a greater difference than $\sum_{n=-7}^{7}$ and $\sum_{n=-100}^{100}$. In Figure 7.7, we also see that $|X|$ monotonically increases with increasing J for $\sim 20\sigma \lesssim d(r_+, R_A) \lesssim 40\sigma$. In contrast, P_A and P_B only increase with increasing J up to a maximum value of J before beginning to decrease. This illustrates that the non-local correlations between the detectors are enhanced for distances that are far, but not too far, from the horizon of near-extremal black holes.

We note that when fixing $J/M\ell$ that that the shift in the integrand of X is independent of ℓ. Instead, it seems like the reason that the peak broadens with increasing AdS length is because the exponential itself broadens (Figure 7.5).

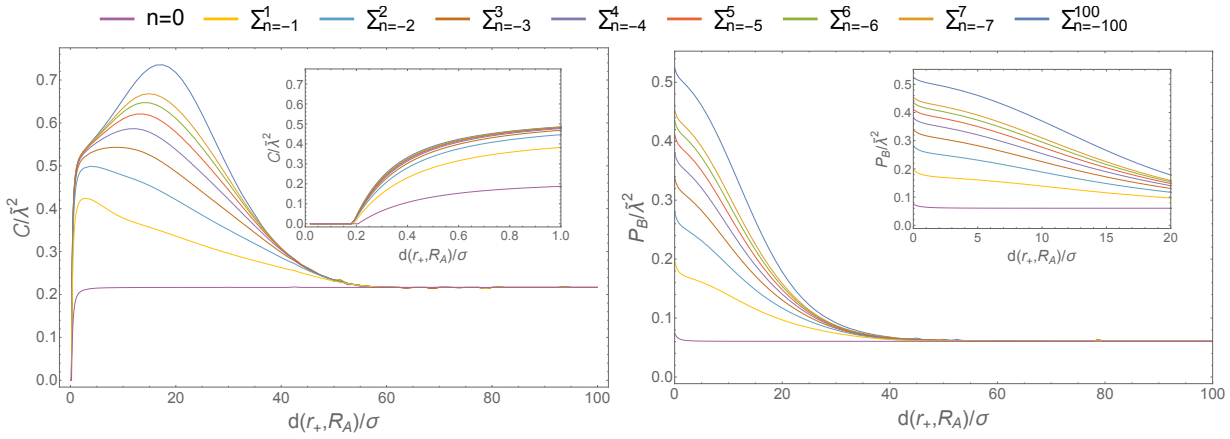

(a) P_A (b) P_B

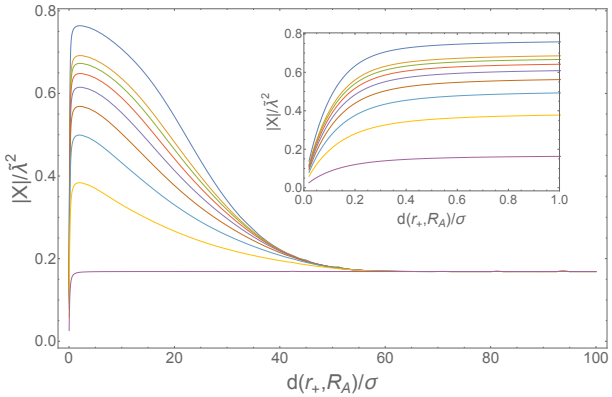

(c) $|X|$

Figure 7.6: Partial image sums of P_A, $|X|$, and concurrence for Unruh-DeWitt detectors orbiting a rotating BTZ black hole of angular momentum $J/M\ell = 0.9999$. In each plot, the detectors have a proper separation of $d(R_A, R_B) = 1$, the energy gap is $\Omega\sigma = 1$, the black hole, has a mass of $M = 10^{-3}$, $\zeta = 1$ and $\ell/\sigma = 10$.

It also appears that the ergosphere is not significant in entanglement harvesting. From equation (5.24), we have $-(N^{\perp})^2+r^2(N^{\phi})^2 = M-r^2/L^2 > 0$. Thus, the ergosphere extends out to $R = \sqrt{M}\ell$. We see in Figure 7.2 that the ergosphere lies entirely within the entanglement shadow for $\Omega\sigma = 0.01$ and $\Omega\sigma = 0.1$, yet extends beyond the entanglement shadow for $\Omega\sigma = 1$. As we see in Figure 7.7, as detector A approaches the horizon, its transition probability increases before a sharp decrease. This is exhibited for all angular momenta, and seems to be indicative of an anti-Hawking effect [100].

What of other vacuum correlations? An investigation of the mutual information [215]

$$I_{AB} = \mathcal{L}_+ \log \mathcal{L}_+ + \mathcal{L}_- \log \mathcal{L}_- - P_A \log P_A - P_B \log P_B \tag{7.3}$$

where $\mathcal{L}_\pm = \frac{1}{2}\left(P_A + P_B \pm \sqrt{(P_A - P_B)^2 + 4|L_{AB}|^2}\right)$ indicates that it peaks away from the black hole, albeit at smaller distances than the concurrence, and likewise undergoes significant amplification as extremality is approached (Figure 7.8). The nearer location of the peak occurs because P_A, P_B, and $|L_{AB}|$ are all sharply peaked relatively close to the horizon, whereas $|X|$ peaks at notably larger distances. Hence only the quantum correlations are enhanced in the intermediate regime.

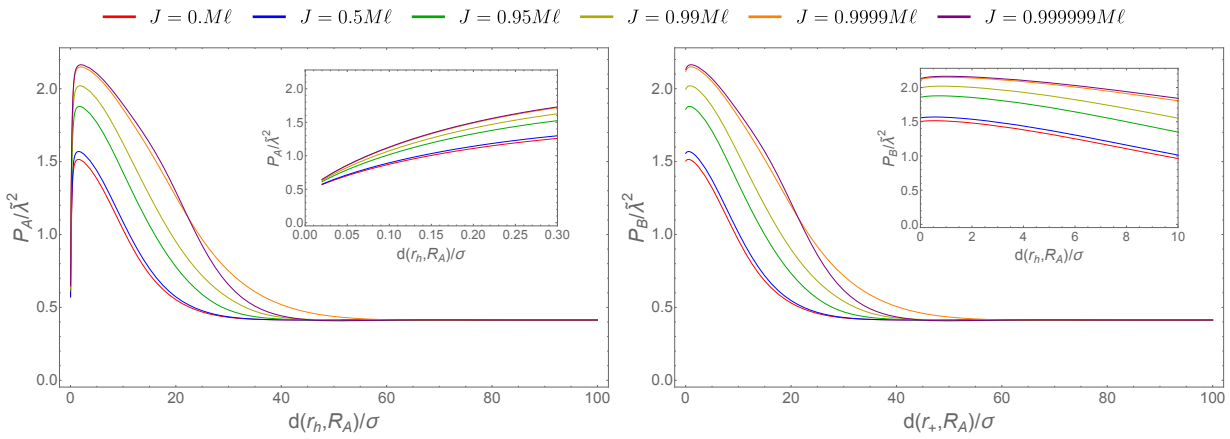

(a) P_A (b) P_B

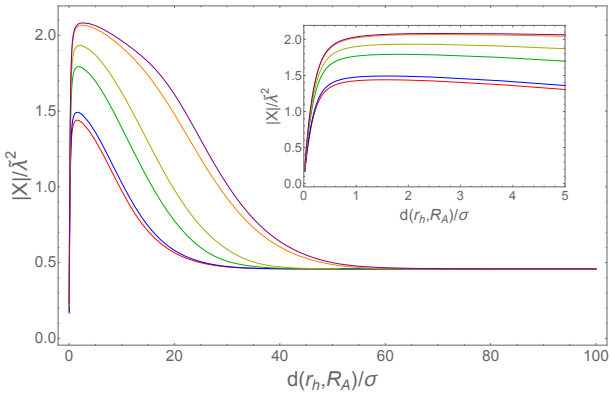

(c) $|X|$

Figure 7.7: Transition probabilities and non-locality for Unruh-DeWitt detectors orbiting a rotating BTZ black hole. In each plot, the detectors have a proper separation of $d(R_A, R_B) = 1$, the energy gap is $\Omega\sigma = 1$, the black hole, has a mass of $M = 10^{-3}$, $\zeta = 1$ and $\ell/\sigma = 10$.

7.3 Conclusion

We have demonstrated that for near-extremal values of the angular momentum, BTZ black holes significantly amplify the amount of entanglement that can be harvested from the quantum vacuum. Interestingly, this amplification occurs at intermediate distances from the black hole and the effect (dependent on the energy gap of the Unruh-DeWitt detectors) does not seem to appear for small values of the angular momentum. We note that this effect takes place for all boundary conditions, a large range of AdS lengths, and detector proper separations. This effect seems to be partly due to a decrease in the transition probabilities at intermediate distances, relative to the non-local correlations. Unlike the transition probabilities, the non-local correlations always increase for increasing angular momentum for a fixed distance of the detectors from the event horizon within this intermediate distance regime.

The width and height of the peaks are sensitive to the spacetime and detector parameters considered. By decreasing the mass, increasing the angular momentum, and by decreasing the AdS length, the height of the peak will increase. Increasing the AdS length will also broaden the width of the peak. In contrast, width and height of the peaks appear not to be as strongly affected by

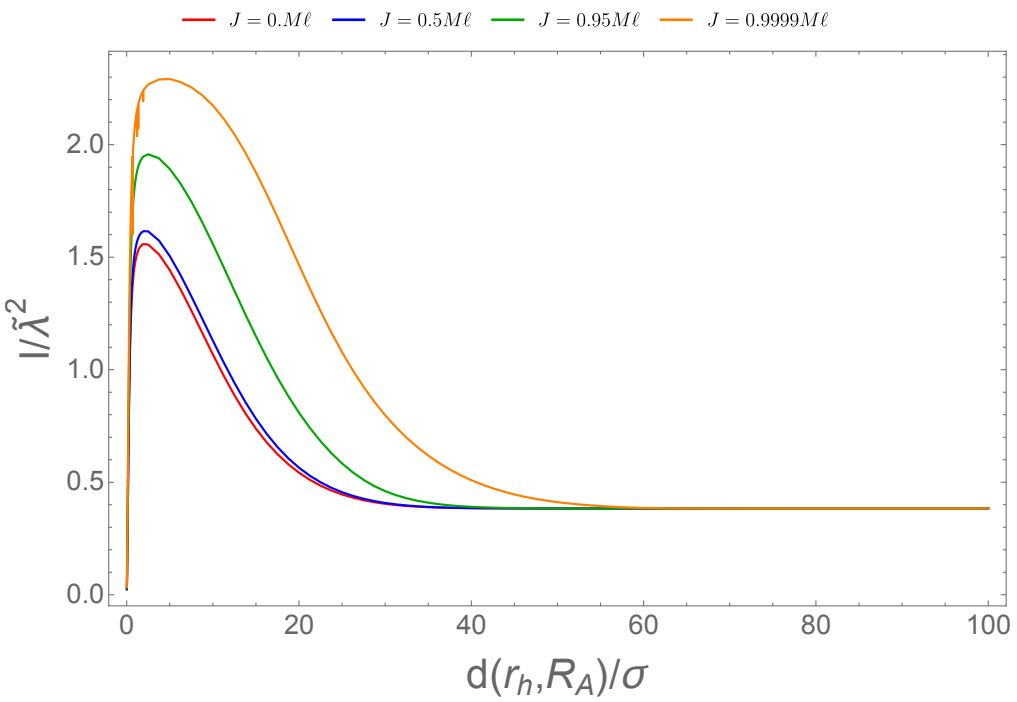

Figure 7.8: Mutual information corresponding for a rotating black hole of mass $M = 10^{-3}$, Dirichlet boundary conditions, and $\ell/\sigma = 10$. The energy gap of the detectors is $\Omega\sigma = 1$. For smaller energy gaps, the figures look qualitatively similar.

changing the energy gap.

We emphasize that these findings are most pronounced for black holes of small mass. As the mass increases, the transition probabilities, non-locality, and hence the concurrence become increasingly insensitive to the angular momentum, especially for $M > 1$. At these masses, the additional non-zero terms in the image sum of (5.29) become tiny, so that the image sum (and hence the physics) is dominated by the $n = 0$ term correspond to AdS spacetime [100].

In this chapter, we have assumed that the switching functions of detectors A and B are peaked at the same proper time, such that their temporal shift is $\Delta\tau_0 = 0$. In [99], a non-zero shift in the temporal peak was considered for AdS spacetime ($M = -1$). It was found that entanglement harvesting was dependent on this temporal shift, and resulted in asymmetries between the detectors. This was the result of the relative redshift between the detectors as compared to frame that the temporal shifts were measured in. A natural question is to ask how such a temporal shift will affect the results in this chapter. Similar to AdS spacetime, it is likely that asymmetries and other effects distorting the shape and location of the peaks will occur, though entanglement harvesting will not vanish. However, a more thorough study to understand how the results would change is required.

It is quite surprising that rotation is able to have such a dramatic effect on the vacuum correlations. It is expected that these findings will have implications in analogue gravity experiments as there has been recent interest in simulations of the quantum vacuum in the presents of (analogue) rotating black holes [179, 235]. It remains an open question for how this amplification effect is exhibited in other spacetimes and dimensions, which will remain a subject for a future study.

Chapter 8

Conclusion

8.1 Summary

Quantum information has the capacity to revolutionize our understanding of the universe. As we discussed in Chapter 1, quantum information has been applied to understand relativistic phenomena in a variety of different settings. Though we do not yet know whether gravity is a fundamentally classical or quantum, studying quantum information across spacetime may one day be able to answer this key question. At the very least, however, quantum information provides additional techniques that can be used to study classical phenomena in new ways and gain greater insights into the fundamental nature of spacetime.

With this in mind, we have studied two aspects of spacetime by using techniques of quantum information. We investigated gravitational wave detection with Bose-Einstein condensates as well how the rotation of a BTZ black hole affects orbiting Unruh-DeWitt detectors. In this chapter, we shall highlight our main results and comment on potential directions of future research.

8.1.1 Part I

In Chapter 3, we considered a detector-gravitational wave interaction of the form $h_+(t) = \epsilon \sin(\Omega t) e^{-t^2/\tau^2}$, where ϵ was the amplitude of the gravitational waves, Ω was the frequency of the gravitational waves and τ was the duration of the measurement. We showed that the quantum Fisher information contained in the phonons could, in principle, be used to estimate the amplitude of the gravitational wave. However, for such an experiment to achieve the requisite sensitivity for gravitational wave detection, the phonons would need to be squeezed far beyond current experimental capabilities. We also investigated Beliaev damping and concluded that higher frequency gravitational waves would not be able to be detected without first reducing the damping rate of the phonons.

In Chapter 4, we then turned our attention to continuous gravitational waves of the form $h_+(t) = \epsilon \sin \Omega t$. By modulating the speed of sound of the BEC, a transient instability could be induced into the condensate. When a continuous gravitational wave passes by, this instability can be used to amplify the sensitivity of the condensate to gravitational waves. However, advancements in experimental techniques will be required for such a setup to achieve the required sensitivity to detect gravitational waves. Using currently realizable parameters, a BEC would have the sensitivity

to detect only a handful of astrophysical sources (in the absence of experimental noise). However, once the experimental noise arising from the implementation of such an experiment is accounted for, we realized that it would dominate over the gravitational wave signal.

8.1.2 Part II

In Chapter 6, we considered a single Unruh-DeWitt detector to investigate how the weak and strong anti-Hawking effects were affected by the rotation of a BTZ black hole. We found that the critical temperature at which the weak effect appears was relatively insensitive to rotation, though rotation increased the response function. We also saw that a small mass enhanced the weak anti-Hawking effect and that the weak effect was independent of the AdS length. In terms of the strong anti-Hawking effect, we found that there was a strong dependence on boundary conditions. For transparent and Neumann boundary conditions, increased rotation caused a decrease in the anti-Hawking effect, with it nearly disappearing for near-extremal black holes. In contrast, for Dirichlet boundary conditions, increasing rotation caused a decrease in the strong effect, though after a critical angular momentum, the effect began to increase in strength again. Furthermore, we found a 'crossover' effect of the angular momenta curves in the strong anti-Hawking condition, where at lower KMS temperatures, smaller angular momenta corresponded to larger EDR temperatures, while for larger KMS temperatures, this trend completely reversed itself. We also saw that an increased AdS length caused the temperature range exhibiting the anti-Hawking effect to increase. In addition, we saw that a smaller energy gap tended to amplify both the weak and strong anti-Hawking effects.

In Chapter 7, we considered two Unruh-DeWitt detectors orbiting a rotating BTZ black hole and analyzed how rotation affected the amount of entanglement that could be harvested. We found that for small-mass and near-extremal black holes, there was a large amplification in the amount of concurrence present between the two detectors at intermediate distances from the black hole. This amplification effect was found to be universal to rotating BTZ black holes as it was present for a variety of energy gaps, detector separations, AdS lengths, and boundary conditions.

8.2 Where do we go from here?

8.2.1 Gravitational Wave Detectors

We considered Bose-Einstein condensates as [199] demonstrated that phonons could be produced within the condensates by an incoming gravitational wave. However, we emphasize that this does not mean that BECs are the best quantum system to use. As we briefly mentioned in Chapters 1 and 2, superfluid helium has been proposed as a method of detecting continuous gravitational waves [217, 241]. It is natural to ask if other systems exhibiting condensation can be used as better gravitational wave detectors, such as fermions [191], excitons [169], magnons [228], or even phonons themselves [157]. Low-temperature phenomena offer a large array of physical resources that might be able to be used to detect gravitational waves.

We noted that for the experimental setup we proposed, significant advances in experimental techniques would be required. As discussed in [206], inhomogeneous condensates might be necessary for sufficient sensitivity to be achieved. This warrants further investigation. For simplicity, we worked with a cubic condensate, but this begs the question of whether additional enhancement effects could be achieved by using a different potential.

Ultimately, if a Bose-Einstein condensate is to be used to detect gravitational waves, it will be necessary to start accounting for extraneous noise effects, such as temperature [200] and the metric of the Earth [123]. It will also be necessary to do a more detailed analysis of damping. We estimated how Beliaev damping would affect the quantum Fisher information of the phonons, though a more proper treatment would be required. In addition, for non-zero temperatures, Landau damping would also be present [95, 110].

Gravitational wave detection is extremely difficult, and it took LIGO decades for the necessary sensitivity to be achieved. Even after constructing the interferometer, additional technologies and overhauls were required before the first detection was able to occur. A similar situation may happen for a BEC. In general, larger BECs and faster speeds of sound correspond to greater sensitivities. However, this also corresponds to worse damping effects and 3-body losses. It is likely that when a BEC is constructed and the noise sources are all properly taken into account, additional new technologies and techniques will still be required for a BEC, such as what was considered by [111, 112], to start detecting gravitational waves.

8.2.2 Spinning Black Holes

Perhaps the most striking phenomenon of Chapter 6 was the dependence of the strong anti-Hawking effect on boundary conditions. This warrants a further investigation to understand why Dirichlet boundary conditions behave so differently than transparent or Neumann boundary conditions. To do so, we will need to conduct a more thorough analysis of the strong anti-Hawking effect, but now also considering the cases of when $\zeta \neq 0, \pm 1$.

We also found that there was a 'crossover' of the angular momenta curves for the strong anti-Hawking effect. We saw that at lower temperatures, larger angular momenta corresponded to a smaller EDR temperature. However, for a sufficiently large temperature, this trend reversed, so that smaller angular momenta had a smaller EDR temperature with larger angular momenta having a larger EDR temperature. Once again, boundary conditions played a strong role in how this effect was manifested, with 'crossover' being much more noticeable for Dirichlet boundary conditions than Neumann or transparent boundary conditions. To truly understand how rotation affects the strong anti-Hawking effect, it will be essential to understand the 'crossover.' It is posited that the rationale for why the 'crossover' behaves differently for Dirichlet boundary conditions is a related reason to why the strong anti-Hawking effect for Dirichlet boundary conditions exhibits a completely different trend compared to Neumann and transparent boundary conditions.

In terms of entanglement harvesting, there are several future avenues of research that can be considered. Most crucial is understanding the origin of this amplification effect:

- Why does amplification occur at intermediate distances from the black hole?
- Why does amplification only significantly occur for near-extremal values of the angular momenta?

To try and understand this question, the concurrence was decomposed into its transition probability and non-local terms. In addition, the image sums of the concurrence, transition probabilities of the detectors, and non-local terms were also decomposed to identify that what was observed was, in fact, a black hole effect. There are a few paths available to try and make greater progress in better understanding the amplification. For instance, concurrence is only one possible way of quantifying

the entanglement. Another common way is the negativity in equation (5.14). It is natural to ask whether considering the negativity will yield additional insights into the origin of this effect. It will also be necessary to consider additional values of the angular momentum. We noted that there is little change in the concurrence between $0 < J/M\ell < 0.5$, though additional structure in the curves begin to form between $0.5 < J/M\ell < 0.99$. By understanding why there is little change between $0 < J/M\ell < 0.5$ and how the structure begins to form between $0.5 < J/M\ell < 0.99$, then it may be possible to make conclusions about the concurrence for $J/M\ell > 0.99$.

It is important to note that the BTZ is a $2+1$ dimensional black hole. Will this entanglement amplification effect appear for Kerr black holes? This is an extremely interesting, though non-trivial question as a sum over modes will be required as it will not be possible to do an image sum any more [165].

It is also natural to wonder if a charged BTZ black hole will exhibit amplification effects. In this case, the metric of such a line element is [44, 148]

$$ds^2 = -f(r)dt^2 + \frac{dr^2}{f(r)} + r^2 d\theta^2 \,, \tag{8.1}$$

where

$$f(r) = -8GM + \frac{r^2}{\ell^2} - 8\pi G Q^2 \ln\left(\frac{r}{\ell}\right) \,, \tag{8.2}$$

and Q is the charge. Because of the presence of the $\ln\left(\frac{r}{\ell}\right)$, there is no guarantee that we will still obtain amplification, though it is extremely likely that we will find new effects on the entanglement, induced by the non-zero charge.

8.3 Final Thoughts

Techniques of quantum information are being used to analyze relativistic systems from a different standpoint and are making new and groundbreaking discoveries. Gravitational wave detection and rotating BTZ black holes are only one small part of using quantum information to study different spacetimes. In recent years, quantum techniques have been considered as a means to learn more about general relativity through techniques like analogue gravity [26, 117] and atom interferometry [67, 233, 238]

We know that quantum mechanics and general relativity is not the full story. However, by using quantum technologies to study the Universe, it seems like it's only a matter of time before we can definitively say whether gravity is an inherently classical or quantum as well discover new phenomena that we have never imagined. Applied across spacetime, the field of relativistic quantum information is providing a powerful tool to be able to do just that. However, we have really only scratched the surface of what relativistic quantum information can do for us. There are many more spacetimes that need to be considered and more phenomena that need to be probed. To paraphrase Calvin in the final comic strip of Calvin and Hobbes: "It's a magical universe, Hobbes, ol' buddy. Let's go exploring!" [250]

References

[1] J. Aasi et al. Enhanced sensitivity of the LIGO gravitational wave detector by using squeezed states of light. *Nature Photonics*, 7(8), 2013.

[2] B. P. Abbott et al. Observation of gravitational waves from a binary black hole merger. *Physical Review Letters*, 116(6), 2016.

[3] B. P. Abbott et al. First search for gravitational waves from known pulsars with Advanced LIGO. *The Astrophysical Journal*, 839(1), 2017.

[4] B. P. Abbott et al. Multi-messenger observations of a binary neutron star merger. *The Astrophysical Journal Letters*, 848(2), 2017.

[5] B. P. Abbott et al. Observation of gravitational waves from two neutron star–black hole coalescences. *The Astrophysical Journal Letters*, 915(1), 2021.

[6] B. Abbott et al. Prospects for observing and localizing gravitational-wave transients with Advanced LIGO, Advanced Virgo and KAGRA. *Living Reviews of Relativity*, 21(1), 2018.

[7] J. Abedi et al. Quantum black holes in the sky. *Universe*, 6(3), 2020.

[8] O. D. Aguiar. Past, present and future of the resonant-mass gravitational wave detectors. *Research in Astronomy and Astrophysics*, 11(1), 2011.

[9] I. Agullo et al. Potential gravitational wave signatures of quantum gravity. *Physical Review Letters*, 126(4), 2021.

[10] M. Ahmadi, D. E. Bruschi, and I. Fuentes. Quantum metrology for relativistic quantum fields. *Physical Review D*, 89(6), 2014.

[11] M. Albers, C. Kiefer, and M. Reginatto. Measurement analysis and quantum gravity. *Physical Review D*, 78(6), 2008.

[12] Á. M. Alhambra, A. Kempf, and E. Martín-Martínez. Casimir forces on atoms in optical cavities. *Physical Review A*, 89(3), 2014.

[13] A. Almheiri, D. Marolf, J. Polchinski, and J. Sully. Black holes: complementarity or firewalls? *Journal of High Energy Physics*, 02, 2013.

[14] P. Amaro-Seoane et al. Topical review: intermediate and extreme mass-ratio inspirals—astrophysics, science applications and detection using LISA. *Classical and Quantum Gravity*, 24(17), 2007.

[15] P. Amaro-Seoane et al. Laser interferometer space antenna. *arXiv:1702.00786*, 2017.

[16] G. Amelino-Camelia. Quantum-spacetime phenomenology. *Living Reviews in Relativity*, 16(1), 2013.

[17] N. Andersson et al. Gravitational waves from neutron stars: promises and challenges. *General Relativity and Gravitation*, 43(2), 2011.

[18] N. Andersson. Gravitational waves from instabilities in relativistic stars. *Classical and Quantum Gravity*, 20(7), 2003.

[19] M. R. Andrews et al. Propagation of sound in a Bose-Einstein condensate. *Physical Review Letters*, 79(4), 1997.

[20] M. R. Andrews et al. Erratum: Propagation of sound in a Bose-Einstein condensate. *Physical Review Letters*, 80(13), 1998.

[21] Z. Arzoumanian et al. The NANOGrav 12.5 yr data set: search for an isotropic stochastic gravitational-wave background. *The Astrophysical Journal Letters*, 905(2), 2020.

[22] A. Ashkin. *Optical Trapping And Manipulation Of Neutral Particles Using Lasers: A Reprint Volume With Commentaries*. World Scientific Publishing Company, 2006.

[23] S. J. Avis, C. J. Isham, and D. Storey. Quantum field theory in anti-de Sitter space-time. *Physical Review D*, 18(10), 1978.

[24] M. Bañados, C. Teitelboim, and J. Zanelli. Black hole in three-dimensional spacetime. *Physical Review Letters*, 69(13), 1992.

[25] S. Ballmer and V. Mandic. New technologies in gravitational-wave detection. *Annual Review of Nuclear and Particle Science*, 65(1), 2015.

[26] C. Barceló, S. Liberati, and M. Visser. Analogue gravity. *Living Reviews in Relativity*, 8(1), 2005.

[27] S. Barnett and P. Radmore. *Methods in Theoretical Quantum Optics*. Oxford Series in Optical and Imaging Sciences. Clarendon Press, 2002.

[28] I. Barr. *Investigating the dynamics of a Bose Einstein condensate on an atom chip*. PhD thesis, Imperial College London, 2015.

[29] L. Barsotti, J. Harms, and R. Schnabel. Squeezed vacuum states of light for gravitational wave detectors. *Reports on Progress in Physics*, 82(1), 2019.

[30] R. A. Battye, R. R. Caldwell, and E. P. S. Shellard. Gravitational waves from cosmic strings. In M. Signore and F. Melchiorri, editors, *Topological Defects in Cosmology*, 1998.

[31] J. S. Bell and J. M. Leinaas. The Unruh effect and quantum fluctuations of electrons in storage rings. *Nuclear Physics B*, 284, 1987.

[32] F. Benatti et al. Generation and detection of squeezed phonons in lattice dynamics by ultrafast optical excitations. *New Journal of Physics*, 19(2), 2017.

[33] S. Bhattacharyya, S. Gangopadhyay, and A. Saha. Generalized uncertainty principle in resonant detectors of gravitational waves. *Classical and Quantum Gravity*, 37(19), 2020.

[34] N. D. Birrell and P. C. W. Davies. *Quantum Fields in Curved Space*. Cambridge Monographs on Mathematical Physics. Cambridge University Press, 1982.

[35] K. Bongs et al. Taking atom interferometric quantum sensors from the laboratory to real-world applications. *Nature Reviews Physics*, 1(12), 2019.

[36] P. Bosso, S. Das, and R. B. Mann. Potential tests of the generalized uncertainty principle in the advanced LIGO experiment. *Physics Letters B*, 785, 2018.

[37] J. Braden, L. Kofman, and N. Barnaby. Reheating the universe after multi-field inflation. *Journal of Cosmology and Astroparticle Physics*, 2010(7), 2010.

[38] S. L. Braunstein and C. M. Caves. Statistical distance and the geometry of quantum states. *Physical Review Letters*, 72(22), 1994.

[39] S. L. Braunstein, S. Pirandola, and K. Zyczkowski. Better late than never: Information retrieval from black holes. *Physical Review Letters*, 110(10), 2013.

[40] W. Brenna, R. B. Mann, and E. Martín-Martínez. Anti-Unruh phenomena. *Physics Letters B*, 757, 2016.

[41] R. Brustein, M. B. Einhorn, and A. Yarom. Entanglement interpretation of black hole entropy in string theory. *Journal of High Energy Physics*, 01, 2006.

[42] F. Bussola et al. Ground state for a massive scalar field in the BTZ spacetime with Robin boundary conditions. *Physical Review D*, 96(10), 2017.

[43] F. Byron and R. Fuller. *Mathematics of Classical and Quantum Physics*. Dover Books on Physics. Dover Publications, 2012.

[44] M. Cadoni and M. R. Setare. Near-horizon limit of the charged BTZ black hole and AdS_2 quantum gravity. *Journal of High Energy Physics*, 2008(7), 2008.

[45] G. Calcagni et al. Gravitational-wave luminosity distance in quantum gravity. *Physics Letters B*, 798, 2019.

[46] G. Calcagni et al. Quantum gravity and gravitational-wave astronomy. *Journal of Cosmology and Astroparticle Physics*, 2019(10), 2019.

[47] S. Capozziello and M. de Laurentis. Extended theories of gravity. *Physics Reports*, 509(4), 2011.

[48] R. Carballo-Rubio et al. Unruh Effect without Thermality. *Physical Review Letters*, 123(4), 2019.

[49] S. Carlip. Is quantum gravity necessary? *Classical and Quantum Gravity*, 25(15), 2008.

[50] S. Carlip. *Quantum Gravity in 2+1 Dimensions*. Cambridge Monographs on Mathematical Physics. Cambridge University Press, 1998.

[51] M. Casals et al. Bulk emission of scalars by a rotating black hole. *Journal of High Energy Physics*, 2008(06), 2008.

[52] S. Chelkowski et al. Experimental characterization of frequency-dependent squeezed light. *Physical Review A*, 71(1), 2005.

[53] C. Chin et al. Feshbach resonances in ultracold gases. *Reviews of Modern Physics*, 82(2), 2010.

[54] C. Chowdhury, A. Das, and B. Ranjan Majhi. Unruh-DeWitt detector in presence of multiple scalar fields : A Toy Model. *arXiv e-prints*, 2017.

[55] N. Christensen. Stochastic gravitational wave backgrounds. *Reports on Progress in Physics*, 82(1), 2019.

[56] J. Coleman. MAGIS-100 at Fermilab. *arXiv e-prints*, 2018.

[57] L. S. Collaboration. Advanced LIGO. *Classical and Quantum Gravity*, 32(7), 2015.

[58] I. Costa. Separable coordinates and particle creation. 1. the klein-gordon equation. *Rev. Bras. Fis.*, 17, 1987.

[59] P. B. Covas and A. M. Sintes. First all-sky search for continuous gravitational-wave signals from unknown neutron stars in binary systems using advanced ligo data. *Physical Review Letters*, 124(19), 2020.

[60] J. D. E. Creighton and W. G. Anderson. *Gravitational-wave physics and astronomy: An introduction to theory, experiment and data analysis*. Wiley-VCH, 2011.

[61] L. C. B. Crispino, A. Higuchi, and G. E. A. Matsas. The unruh effect and its applications. *Reviews of Modern Physics*, 80(3), 2008.

[62] P. C. W. Davies. Scalar production in Schwarzschild and Rindler metrics. *Journal of Physics A Mathematical General*, 8(4), 1975.

[63] L. de Souza Campos and C. Dappiaggi. Comments on the anti-Hawking effect on a BTZ black hole spacetime. *arXiv e-prints*, 2020.

[64] L. de Souza Campos and C. Dappiaggi. The anti-Hawking effect on a BTZ black hole with Robin boundary conditions. *Physics Letters B*, 816, 2021.

[65] R. Demkowicz-Dobrzański, J. Kołodyński, and M. Guţă. The elusive Heisenberg limit in quantum-enhanced metrology. *Nature Communications*, 3, 2012.

[66] B. S. DeWitt. Quantum gravity: The new synthesis. In *General Relativity: An Einstein Centenary Surve*. Cambridge University Press, Cambridge, 1979.

[67] S. Dimopoulos et al. Testing general relativity with atom interferometry. *Physical Review Letters*, 98(11), 2007.

[68] S. Dimopoulos et al. Gravitational wave detection with atom interferometry. *Physics Letters B*, 678(1), 2009.

[69] J. P. D'Incao and B. D. Esry. Scattering length scaling laws for ultracold three-body collisions. *Physical Review Letters*, 94(21), 2005.

[70] *NIST Digital Library of Mathematical Functions*. http://dlmf.nist.gov/, Release 1.0.25 of 2019-12-15. F. W. J. Olver, A. B. Olde Daalhuis, D. W. Lozier, B. I. Schneider, R. F. Boisvert, C. W. Clark, B. R. Miller, B. V. Saunders, H. S. Cohl, and M. A. McClain, eds.

[71] J. Doukas et al. Unruh effect under non-equilibrium conditions: oscillatory motion of an unruh-dewitt detector. *Journal of High Energy Physics*, 2013(11), 2013.

[72] H. Du and R. B. Mann. Fisher information as a probe of spacetime structure: relativistic quantum metrology in (A)dS. *Journal of High Energy Physics*, 2021(5), 2021.

[73] H. Duncker et al. Ultrastable, zerodur-based optical benches for quantum gas experiments. *Appl. Opt.*, 53(20), 2014.

[74] S. Fagnocchi et al. Relativistic Bose-Einstein condensates: a new system for analogue models of gravity. *New Journal of Physics*, 12(9), 2010.

[75] A. Ferraro, S. Olivares, and M. G. A. Paris. Gaussian states in continuous variable quantum information. *arXiv:arXiv:quant-ph/0503237*, 2005.

[76] C. J. Fewster, B. A. Juárez-Aubry, and J. Louko. Waiting for Unruh. *Classical and Quantum Gravity*, 33(16), 2016.

[77] D. G. Fried et al. Bose-Einstein condensation of atomic hydrogen. *Physical Review Letters*, 81(18), 1998.

[78] H. Fu et al. Density waves and jet emission asymmetry in bose fireworks. *Physical Review Letters*, 121(24), 2018.

[79] S. A. Fulling. Nonuniqueness of Canonical Field Quantization in Riemannian Space-Time. *Physical Review D*, 7(10), 1973.

[80] N. Funai. *Investigations into quantum light-matter interactions, their approximations and applications*. PhD thesis, U. Waterloo (main), 2021.

[81] N. Funai, J. Louko, and E. Martín-Martínez. $\hat{\boldsymbol{p}} \cdot \hat{\boldsymbol{A}}$ vs $\hat{\boldsymbol{x}} \cdot \hat{\boldsymbol{E}}$: Gauge invariance in quantum optics and quantum field theory. *Physical Review D*, 99(6), 2019.

[82] D.-F. Gao, J. Wang, and M.-S. Zhan. Atomic interferometric gravitational-wave space observatory (AIGSO). *Communications in Theoretical Physics*, 69(1), 2018.

[83] L. J. Garay, E. Martín-Martínez, and J. de Ramón. Thermalization of particle detectors: The unruh effect and its reverse. *Physical Review D*, 94(10), 2016.

[84] J. García-Bellido. Massive primordial black holes as dark matter and their detection with gravitational waves. In *Journal of Physics Conference Series*, volume 840 of *Journal of Physics Conference Series*, 2017.

[85] W. C. Gardiner and P. Zoller. *The Quantum World Of Ultra-cold Atoms And Light, Book III: Ultra-cold Atoms*. Cold Atoms. World Scientific Publishing Company, 2017.

[86] G. A. Garrett et al. Vacuum squeezing of solids: Macroscopic quantum states driven by light pulses. *Science*, 275(5306), 1997.

[87] A. L. Gaunt et al. Bose-Einstein condensation of atoms in a uniform potential. *Physical Review Letters*, 110(20), 2013.

[88] R. Geiger. *Future Gravitational Wave Detectors Based on Atom Interferometry*. World Scientific, 2017.

[89] C. Gerry and P. Knight. *Introductory Quantum Optics*. Cambridge University Press, 2004.

[90] S. Giorgini. Damping in dilute Bose gases: A mean-field approach. *Physical Review A*, 57(4), 1998.

[91] V. Giovannetti, S. Lloyd, and L. Maccone. Quantum metrology. *Physical Review Letters*, 96(1), 2006.

[92] V. Giovannetti, S. Lloyd, and L. Maccone. Advances in quantum metrology. *Nature Photonics*, 5, 2011.

[93] P. W. Graham et al. Mid-band gravitational wave detection with precision atomic sensors. *arXiv e-prints*, 2017.

[94] T. Greytak et al. Bose-Einstein condensation in atomic hydrogen. *Physica B: Condensed Matter*, 280(1), 2000.

[95] A. Griffin, T. Nikuni, and E. Zaremba. *Bose-Condensed Gases at Finite Temperatures*. Cambridge University Press, 2009.

[96] W. Gu, G. Li, S. Wu, and Y. Yang. Generation of non-classical states of mirror motion in the single-photon strong-coupling regime. *Opt. Express*, 22(15), 2014.

[97] R. Haag, N. M. Hugenholtz, and M. Winnink. On the equilibrium states in quantum statistical mechanics. *Communications in Mathematical Physics*, 5(3), 1967.

[98] L. J. Henderson et al. Harvesting entanglement from the black hole vacuum. *Classical and Quantum Gravity*, 35(21), 2018.

[99] L. J. Henderson et al. Entangling detectors in anti-de sitter space. *Journal of High Energy Physics*, 2019(5), 2019.

[100] L. J. Henderson et al. Anti-Hawking phenomena. *Physics Letters B*, 809, 2020.

[101] G. Hobbs et al. The international pulsar timing array project: using pulsars as a gravitational wave detector. *Classical and Quantum Gravity*, 27(8), 2010.

[102] M. Hobson, G. Efstathiou, and A. Lasenby. *General Relativity: An Introduction for Physicists*. Cambridge University Press, 2006.

[103] L. Hodgkinson and J. Louko. Static, stationary, and inertial unruh-dewitt detectors on the BTZ black hole. *Physical Review D*, 86(6), 2012.

[104] L. Hodgkinson, J. Louko, and A. C. Ottewill. Static detectors and circular-geodesic detectors on the Schwarzschild black hole. *Physical Review D*, 89(10), 2014.

[105] J. M. Hogan et al. An Atomic Gravitational Wave Interferometric Sensor in Low Earth Orbit (AGIS-LEO). *Gen. Rel. Grav.*, 43, 2011.

[106] S. Hossenfelder. Experimental Search for Quantum Gravity. *arXiv e-prints*, 2010.

[107] O. Hosten, N. J. Engelsen, R. Krishnakumar, and M. A. Kasevich. Measurement noise 100 times lower than the quantum-projection limit using entangled atoms. *Nature*, 529, 2016.

[108] M. Hotta. Quantum energy teleportation in spin chain systems. *Journal of the Physical Society of Japan*, 78(3), 2009.

[109] M. Hotta. Quantum energy teleportation: an introductory review. *arXiv preprint arXiv:1101.3954*, 2011.

[110] R. Howl et al. Quantum decoherence of phonons in Bose-Einstein condensates. *Journal of Physics B: Atomic, Molecular and Optical Physics*, 51(1), 2018.

[111] R. Howl and I. Fuentes. Active Interferometry with Gaussian Channels. *arXiv e-prints*, 2019.

[112] R. Howl and I. Fuentes. Quantum frequency interferometry: with applications ranging from gravitational wave detection to dark matter searches. *arXiv e-prints*, 2021.

[113] R. Howl, D. Rätzel, and I. Fuentes. Comment on "Interaction of a Bose-Einstein condensate with a gravitational wave". *arXiv e-prints*, 2018.

[114] B. L. Hu, S.-Y. Lin, and J. Louko. Relativistic quantum information in detectors-field interactions. *Classical and Quantum Gravity*, 29, 2012.

[115] X. Hu and F. Nori. Phonon squeezed states generated by second-order Raman scattering. *Physical Review Letters*, 79(23), 1997.

[116] Z. Huang and Z. Tian. Dynamics of quantum entanglement in de Sitter spacetime and thermal Minkowski spacetime. *Nuclear Physics B*, 923, 2017.

[117] M. J. Jacquet, S. Weinfurtner, and F. König. The next generation of analogue gravity experiments. *Philosophical Transactions of the Royal Society of London Series A*, 378(2177), 2020.

[118] D. Jaksch et al. Cold bosonic atoms in optical lattices. *Physical Review Letters*, 81(15), 1998.

[119] D. Jennings. On the response of a particle detector in anti-de Sitter spacetime. *Classical and Quantum Gravity*, 27(20), 2010.

[120] M. T. Johnsson, G. R. Dennis, and J. J. Hope. Squeezing in Bose-Einstein condensates with large numbers of atoms. *New Journal of Physics*, 15(12), 2013.

[121] R. Jozsa. Fidelity for mixed quantum states. *Journal of Modern Optics*, 41(12), 1994.

[122] G. Kaplanek and C. P. Burgess. Qubits on the Horizon: Decoherence and Thermalization near Black Holes. *arXiv e-prints*, 2020.

[123] J. Kohlrus et al. Quantum communications and quantum metrology in the spacetime of a rotating planet. *arXiv e-prints*, 2015.

[124] M. Kramer and D. J. Champion. The European Pulsar Timing Array and the Large European Array for pulsars. *Classical and Quantum Gravity*, 30(22), 2013.

[125] T. Krisnanda et al. Observable quantum entanglement due to gravity. *npj Quantum Information*, 6(1), 2020.

[126] R. Kubo. Statistical-mechanical theory of irreversible processes. I. general theory and simple applications to magnetic and conduction problems. *Journal of the Physical Society of Japan*, 12(6), 1957.

[127] L. Lamata, M. A. Martin-Delgado, and E. Solano. Relativity and lorentz invariance of entanglement distillability. *Physical Review Letters*, 97(25), 2006.

[128] G. Lambiase, M. Sakellariadou, and A. Stabile. Constraints on extended gravity models through gravitational wave emission. *Journal of Cosmology and Astroparticle Physics*, 2021(3), 2021.

[129] M. Lanzagorta. Effect of gravitational frame dragging on orbiting qubits. *arXiv e-prints*, 2012.

[130] T. D. Lee and C. N. Yang. Low-temperature behavior of a dilute Bose system of hard spheres. II. nonequilibrium properties. *Physical Review, Series II*, 113(6), 1959.

[131] J.-Q. Liao and C. K. Law. Parametric generation of quadrature squeezing of mirrors in cavity optomechanics. *Physical Review A*, 83(3), 2011.

[132] G. Lifschytz and M. Ortiz. Scalar field quantization on the (2+1)-dimensional black hole background. *Physical Review D*, 49(4), 1994.

[133] LIGO Scientific Collaboration and Virgo Collaboration. GWTC-1: A gravitational-wave transient catalog of compact binary mergers observed by LIGO and Virgo during the first and second observing runs. *Physical Review X*, 9(3), 2019.

[134] T. B. Littenberg et al. Astro2020 decadal science white paper: Gravitational wave survey of galactic ultra compact binaries. *arXiv e-prints*, 2019.

[135] M. P. E. Lock and I. Fuentes. Quantum and classical effects in a light-clock falling in Schwarzschild geometry. *Classical and Quantum Gravity*, 36(17), 2019.

[136] L. Lombriser et al. Constraints on f(R) gravity from probing the large-scale structure. *Physical Review D*, 85(12), 2012.

[137] J. Louko. Thermality from a Rindler quench. *Classical and Quantum Gravity*, 35(20), 2018.

[138] A. I. Lvovsky. Squeezed Light. *arXiv: 1401.4118*, 2014.

[139] M. Maggiore. *Gravitational Waves: Volume 1: Theory and Experiments*. Gravitational Waves. OUP Oxford, 2008.

[140] M. Maggiore et al. Science case for the Einstein Telescope. *Journal of Cosmology and Astroparticle Physics*, 2020(3), 2020.

[141] R. B. Mann. *Black Holes: Thermodynamics, Information, and Firewalls*. SpringerBriefs in Physics. Springer, 2015.

[142] R. B. Mann and S. N. Solodukhin. Quantum scalar field on three-dimensional (BTZ) black hole instanton: Heat kernel, effective action and thermodynamics. *Physical Review D*, 55, 1997.

[143] P. Marian and T. A. Marian. Uhlmann fidelity between two-mode Gaussian states. *Physical Review A*, 86(2), 2012.

[144] P. C. Martin and J. Schwinger. Theory of many-particle systems. I. *Physical Review, Series II*, 115(6), 1959.

[145] E. Martín-Martínez. Causality issues of particle detector models in QFT and quantum optics. *Physical Review D*, 92(10), 2015.

[146] E. Martín-Martínez, M. Montero, and M. del Rey. Wavepacket detection with the Unruh-DeWitt model. *Physical Review D*, 87(6), 2013.

[147] E. Martín-Martínez, A. R. H. Smith, and D. R. Terno. Spacetime structure and vacuum entanglement. *Physical Review D*, 93(4), 2016.

[148] C. Martínez, C. Teitelboim, and J. Zanelli. Charged rotating black hole in three spacetime dimensions. *Physical Review D*, 61(10), 2000.

[149] D. V. Martynov et al. Sensitivity of the Advanced LIGO detectors at the beginning of gravitational wave astronomy. *Physical Review D*, 93(11), 2016.

[150] A. Maselli et al. Constraining modified theories of gravity with gravitational-wave stochastic backgrounds. *Physical Review Letters*, 117(9), 2016.

[151] S. D. Mathur. The Information paradox: A Pedagogical introduction. *Classical and Quantum Gravity*, 26, 2009.

[152] I. A. Meitei et al. Quantum gravity effects on scalar particle tunneling from rotating BTZ black hole. *International Journal of Modern Physics A*, 33(12), 2018.

[153] R. Meppelink, S. B. Koller, and P. van der Straten. Sound propagation in a Bose-Einstein condensate at finite temperatures. *Physical Review A*, 80(4), 2009.

[154] T. P. Meyrath, F. Schreck, J. L. Hanssen, C.-S. Chuu, and M. G. Raizen. Bose-einstein condensate in a box. *Physical Review A*, 71(4), 2005.

[155] P. Meystre and I. Murray. *Elements of Quantum Optics*. Springer Berlin Heidelberg, 1991.

[156] M. C. Miller and N. Yunes. The new frontier of gravitational waves. *Nature*, 568(7753), 2019.

[157] O. Misochko, M. Hase, K. Ishioka, and M. Kitajima. Transient Bose-Einstein condensation of phonons. *Physics Letters A*, 321(5), 2004.

[158] C. J. Moore, R. H. Cole, and C. P. L. Berry. Gravitational-wave sensitivity curves. *Classical and Quantum Gravity*, 32(1), 2015.

[159] C. J. Moore, R. H. Cole, and C. P. L. Berry. Gravitational wave detectors and sources. *http://gwplotter.com/*, 2016.

[160] P.-A. Moreau et al. Imaging Bell-type nonlocal behavior. *Science Advances*, 5(7), 2019.

[161] P. Morse and H. Feshbach. *Methods of Theoretical Physics*. International series in pure and applied physics. McGraw-Hill, 1953.

[162] G. Nelemans, L. R. Yungelson, and S. F. Portegies Zwart. The gravitational wave signal from the Galactic disk population of binaries containing two compact objects. *Astronomy & Astrophysics*, 375, 2001.

[163] K. K. Ng et al. Unruh-dewitt detector response along static and circular-geodesic trajectories for schwarzschild–anti-de sitter black holes. *Physical Review D*, 90(6), 2014.

[164] K. K. Ng, R. B. Mann, and E. Martín-Martínez. Over the horizon: Distinguishing the Schwarzschild spacetime and the $\mathbb{RP}^3$ spacetime using an Unruh-DeWitt detector. *Physical Review D*, 96(8), 2017.

[165] K. K. Ng, R. B. Mann, and E. Martín-Martínez. New techniques for entanglement harvesting in flat and curved spacetimes. *Physical Review D*, 97(12), 2018.

[166] K. K. Ng, R. B. Mann, and E. Martín-Martínez. Unruh-DeWitt detectors and entanglement: The anti–de Sitter space. *Physical Review D*, 98(12), 2018.

[167] A. Nicolis, R. Penco, and R. A. Rosen. Relativistic fluids, superfluids, solids, and supersolids from a coset construction. *Physical Review D*, 89(4), 2014.

[168] M. Nielsen and I. Chuang. *Quantum Computation and Quantum Information: 10th Anniversary Edition*. Cambridge University Press, 2010.

[169] T. Nikuni et al. Bose-Einstein condensation of dilute magnons in $TlCuCl_3$. *Physical Review Letters*, 84(25), 2000.

[170] S. Olivares. Quantum optics in the phase space. *The European Physical Journal Special Topics*, 203(1), 2012.

[171] D. C. M. Ostapchuk et al. Entanglement dynamics between inertial and non-uniformly accelerated detectors. *Journal of High Energy Physics*, 07, 2012.

[172] A. C. Ottewill and E. Winstanley. Divergence of a quantum thermal state on Kerr space-time. *Physics Letters A*, 273, 2000.

[173] D. N. Page. Hawking radiation and black hole thermodynamics. *New Journal of Physics*, 7(1), 2005.

[174] K. Pardo et al. Limits on the number of spacetime dimensions from GW170817. *Journal of Cosmology and Astroparticle Physics*, 2018(7), 2018.

[175] M. Parikh, F. Wilczek, and G. Zahariade. Quantum mechanics of gravitational waves. *arXiv e-prints*, 2020.

[176] M. Parikh, F. Wilczek, and G. Zahariade. Signatures of the quantization of gravity at gravitational wave detectors. *arXiv e-prints*, 2020.

[177] M. Parikh, F. Wilczek, and G. Zahariade. The noise of gravitons. *International Journal of Modern Physics D*, 29(14), 2020.

[178] P. B. Patel et al. Universal sound diffusion in a strongly interacting fermi gas. *arXiv e-prints*, 2019.

[179] S. Patrick and S. Weinfurtner. Superradiance in dispersive black hole analogues. *Physical Review D*, 102(8), 2020.

[180] U. Percoco and V. M. Villalba. Particle creation in an asymptotically uniformly accelerated frame. *Classical and Quantum Gravity*, 9, 1992.

[181] A. Peres and D. R. Terno. Quantum information and relativity theory. *Reviews of Modern Physics*, 76(1), 2004.

[182] E. S. Perlman et al. New constraints on quantum gravity from X-ray and gamma-ray observations. *American Physics Journal*, 805(1), 2015.

[183] C. J. Pethick and H. Smith. *Bose-Einstein Condensation in Dilute Gases*. Cambridge University Press, second edition, 2008.

[184] A. Pozas-Kerstjens and E. Martín-Martínez. Entanglement harvesting from the electromagnetic vacuum with hydrogenlike atoms. *Physical Review D*, 94(6), 2016.

[185] J. Preskill. Do black holes destroy information? In *International Symposium on Black holes, Membranes, Wormholes and Superstrings Woodlands, Texas, January 16-18, 1992*, 1992.

[186] N. Proukakis, D. Snoke, and P. Littlewood. *Universal Themes of Bose-Einstein Condensation*. Cambridge University Press, 2017.

[187] T. C. Ralph, G. J. Milburn, and T. Downes. Quantum connectivity of space-time and gravitationally induced decorrelation of entanglement. *Physical Review A*, 79(2), 2009.

[188] R. H. Rand. Lecture notes on nonlinear vibrations. https://ecommons.cornell.edu/handle/1813/28989, 2012.

[189] D. Rätzel et al. Dynamical response of bose–einstein condensates to oscillating gravitational fields. *New Journal of Physics*, 20(7), 2018.

[190] D. Rätzel and R. Schützhold. Decay of quantum sensitivity due to three-body loss in Bose-Einstein condensates. *arXiv e-prints*, 2021.

[191] C. A. Regal, M. Greiner, and D. S. Jin. Observation of resonance condensation of fermionic atom pairs. *Physical Review Letters*, 92(4), 2004.

[192] D. Reitze et al. Cosmic Explorer: The U.S. contribution to gravitational-wave astronomy beyond LIGO. In *Bulletin of the American Astronomical Society*, volume 51, 2019.

[193] B. Reznik. Entanglement from the vacuum. *Foundations of Physics*, 33(1), 2003.

[194] B. Reznik, A. Retzker, and J. Silman. Violating Bell's inequalities in vacuum. *Physical Review A*, 71(4), 2005.

[195] K. Riles. Recent searches for continuous gravitational waves. *Modern Physics Letters A*, 32(39), 2017.

[196] M. P. G. Robbins, N. Afshordi, and R. B. Mann. Bose-Einstein condensates as gravitational wave detectors. *Journal of Cosmology and Astroparticle Physics*, 2019(7), 2019.

[197] M. P. G. Robbins, L. J. Henderson, and R. B. Mann. Entanglement amplification from rotating black holes. *Classical and Quantum Gravity*, 2021.

[198] S. Ryu and T. Takayanagi. Holographic derivation of entanglement entropy from AdS/CFT. *Physical Review Letters*, 96, 2006.

[199] C. Sabín et al. Phonon creation by gravitational waves. *New Journal of Physics*, 16(8), 2014.

[200] C. Sabín et al. Thermal noise in BEC-phononic gravitational wave detectors. *EPJ Quantum Technology*, 3(1), 2016.

[201] G. Salton, R. B. Mann, and N. C. Menicucci. Acceleration-assisted entanglement harvesting and rangefinding. *New Journal of Physics*, 17(3), 2015.

[202] B. Sathyaprakash et al. Scientific objectives of Einstein Telescope. *Classical and Quantum Gravity*, 29(12), 2012.

[203] P. Saulson. *Fundamentals Of Interferometric Gravitational Wave Detectors (Second Edition)*. World Scientific Publishing Company, 2017.

[204] D. Schroeder. *An Introduction to Thermal Physics*. Addison Wesley, 2000.

[205] R. Schützhold. *Effective Horizons in the Laboratory*. Spring Science+Business Media, LLC, 2007.

[206] R. Schützhold. Interaction of a Bose-Einstein condensate with a gravitational wave. *ArXiv e-prints*, 2018.

[207] R. Schützhold. Reply to comment on "Interaction of a BEC with a gravitational wave". *arXiv e-prints*, 2019.

[208] M. O. Scully and M. S. Zubairy. *Quantum Optics*. Cambridge University Press, 1997.

[209] H. Senf et al. Analysis of experimental and numerical investigations with rigid projectiles impacting glass targets of differing physical quality. *Journal de Physique Colloques*, 49(C3), 1988.

[210] N. Sennett et al. Gravitational-wave constraints on an effective-field-theory extension of general relativity. *Physical Review D*, 102(4), 2020.

[211] A. Serafini et al. Quantifying decoherence in continuous variable systems. *Journal of Optics B: Quantum and Semiclassical Optics*, 7(4), 2005.

[212] A. Serafini, A. Retzker, and M. B. Plenio. Manipulating the quantum information of the radial modes of trapped ions: linear phononics, entanglement generation, quantum state transmission and non-locality tests. *New Journal of Physics*, 11(2), 2009.

[213] G. L. Sewell. Quantum fields on manifolds: Pct and gravitationally induced thermal states. *Annals of Physics*, 141(2), 1982.

[214] I. Shammass et al. Phonon dispersion relation of an atomic Bose-Einstein condensate. *Physical Review Letters*, 109(19), 2012.

[215] P. Simidzija and E. Martín-Martínez. Harvesting correlations from thermal and squeezed coherent states. *Physical Review D*, 98(8), 2018.

[216] D. V. Singh and S. Siwach. Scalar Fields in BTZ Black Hole Spacetime and Entanglement Entropy. *Classical and Quantum Gravity*, 30, 2013.

[217] S. Singh, L. A. De Lorenzo, I. Pikovski, and K. C. Schwab. Detecting continuous gravitational waves with superfluid ^{4}He. *New Journal of Physics*, 19(7), 2017.

[218] A. R. H. Smith and M. Ahmadi. Quantum clocks observe classical and quantum time dilation. *Nature Communications*, 11, 2020.

[219] A. R. H. Smith and R. B. Mann. Looking inside a black hole. *Classical and Quantum Gravity*, 31(8), 2014.

[220] A. R. Smith. *Detectors, Reference Frames, and Time*. PhD thesis, U. Waterloo (main), 2017.

[221] S. N. Solodukhin. Entanglement entropy of black holes. *Living Reviews in Relativity*, 14(1), 2011.

[222] D. T. Son. Low-energy quantum effective action for relativistic superfluids. *arXiv e-prints*, 2002.

[223] P. K. Sørensen. Three-Body Recombination in Cold Atomic Gases. *arXiv e-prints*, 2013.

[224] V. Srivastava et al. Detection prospects of core-collapse supernovae with supernova-optimized third-generation gravitational-wave detectors. *Physical Review D*, 100(4), 2019.

[225] G. V. Steeg and N. C. Menicucci. Entangling power of an expanding universe. *Physical Review D*, 79(4), 2009.

[226] L. Stella et al. Gravitational radiation from newborn magnetars in the Virgo Cluster. *The Astrophysical Journal Letters*, 634(2), 2005.

[227] J. Stenger et al. Bragg spectroscopy of a Bose-Einstein condensate. *Physical Review Letters*, 82(23), 1999.

[228] H. Stolz and Rothers. Condensation of excitons in Cu_2O at ultracold temperatures: experiment and theory. *New Journal of Physics*, 14(10), 2012.

[229] E. W. Streed et al. Large atom number Bose-Einstein condensate machines. *Review of Scientific Instruments*, 77(2), 2006.

[230] S. J. Summers and R. Werner. The vacuum violates Bell's inequalities. *Physics Letters A*, 110(5), 1985.

[231] S. J. Summers and R. Werner. Bell's inequalities and quantum field theory. II. bell's inequalities are maximally violated in the vacuum. *Journal of Mathematical Physics*, 28(10), 1987.

[232] T. G. Tiecke et al. High-flux two-dimensional magneto-optical-trap source for cold lithium atoms. *Physical Review A*, 80(1), 2009.

[233] G. M. Tino. Testing gravity with cold atom interferometry: results and prospects. *Quantum Science and Technology*, 6(2), 2021.

[234] E. Tjoa and R. B. Mann. Harvesting correlations in Schwarzschild and collapsing shell spacetimes. *Journal of High Energy Physics*, 2020(8), 2020.

[235] T. Torres et al. Rotational superradiant scattering in a vortex flow. *Nature Physics*, 13(9), 2017.

[236] C. Tozzo and F. Dalfovo. Phonon evaporation in freely expanding bose-einstein condensates. *Physical Review A*, 69(5), 2004.

[237] M. Tse et al. Quantum-enhanced Advanced LIGO detectors in the era of gravitational-wave astronomy. *Physical Review Letters*, 123(23), 2019.

[238] C. Ufrecht et al. Atom-interferometric test of the universality of gravitational redshift and free fall. *Physical Review Research*, 2(4), 2020.

[239] A. Uhlmann. The "transition probability" in the state space of a *-algebra. *Reports on Mathematical Physics*, 9(2), 1976.

[240] W. G. Unruh. Notes on black-hole evaporation. *Physical Review D*, 14(4), 1976.

[241] V. Vadakkumbatt et al. Prototype Superfluid Gravitational Wave Detector. *arXiv e-prints*, 2021.

[242] E. C. Vagenas. Two-Dimensional Dilatonic Black Holes and Hawking Radiation. *Modern Physics Letters A*, 17(10), 2002.

[243] H. Vahlbruch et al. Detection of 15 dB squeezed states of light and their application for the absolute calibration of photoelectric quantum efficiency. *Physical Review Letters*, 117(11), 2016.

[244] A. Valentini. Non-local correlations in quantum electrodynamics. *Physics Letters A*, 153(6), 1991.

[245] M. Vengalattore et al. High-resolution magnetometry with a spinor Bose-Einstein condensate. *Physical Review Letters*, 98(20), 2007.

[246] J. P. W. Verbiest, S. Oslowski, and S. Burke-Spolaor. Pulsar Timing Array experiments. *arXiv e-prints*, 2021.

[247] G. Vidal and R. F. Werner. Computable measure of entanglement. *Physical Review A*, 65(3), 2002.

[248] V. M. Villalba and J. Mateu. Vacuum effects in an asymptotically uniformly accelerated frame with a constant magnetic field. *Physical Review D*, 61, 2000.

[249] K. Vogtmann, A. Weinstein, and V. I. Arnold. *Mathematical Methods of Classical Mechanics*. Graduate Texts in Mathematics. Springer New York, 1989.

[250] B. Watterson. Calvin and Hobbes. *It's a Magical World: A Calvin and Hobbes Collection*, December 31, 1995.

[251] J. M. Weisberg, D. J. Nice, and J. H. Taylor. Timing measurements of the relativistic binary pulsar psr b1913+16. *The Astrophysical Journal*, 722(2), 2010.

[252] J. M. Weisberg, J. H. Taylor, and L. A. Fowler. Gravitational waves from an orbiting pulsar. *Scientific American*, 245, 1981.

[253] E. Winstanley. Classical super-radiance in kerr-newman-anti-de sitter black holes. *Physical Review D*, 64(10), 2001.

[254] W. K. Wootters. Entanglement of formation of an arbitrary state of two qubits. *Physical Review Letters*, 80(10), 1998.

[255] Q. Xu, S. Ali Ahmad, and A. R. H. Smith. Gravitational waves affect vacuum entanglement. *Physical Review D*, 102(6), 2020.

[256] M. Yan et al. Controlling condensate collapse and expansion with an optical feshbach resonance. *Physical Review Letters*, 110(12), 2013.

[257] M. Zaccanti et al. Observation of an Efimov spectrum in an atomic system. *Nature Physics*, 5(8), 2009.

[258] S. J. Zhu et al. Characterizing the continuous gravitational-wave signal from boson clouds around galactic isolated black holes. *Physical Review D*, 102(6), 2020.

APPENDICES

Appendix A

Derivation and Solution to Equation (4.12)

Equations (4.9) and (4.10) give the form of our solution for π and $\dot{\pi}$ to equation (4.8):

$$\pi = \alpha(t)\frac{e^{-i\int\omega_1(t')dt'}}{\sqrt{2\omega_1(t)}} + \beta(t)\frac{e^{i\int\omega_1(t')dt'}}{\sqrt{2\omega_1(t)}}\,, \tag{A.1}$$

$$\dot{\pi} = -i\alpha(t)\sqrt{\frac{\omega_1(t)}{2}}e^{-i\int\omega_1(t')dt'} + i\beta(t)\sqrt{\frac{\omega_1(t)}{2}}e^{i\int\omega_1(t')dt'}\,, \tag{A.2}$$

We can obtain a pair of coupled differential equations between the time-dependent Bogoliubov coefficients $\alpha(t)$ and $\beta(t)$:

$$\dot{\alpha} = \frac{\dot{\omega}_1}{2\omega_1}e^{2i\int\omega_1(t')dt'}\beta(t) \qquad \dot{\beta} = \frac{\dot{\omega}_1}{2\omega_1}e^{-2i\int\omega_1(t')dt'}\alpha(t) \tag{A.3}$$

Let $\delta\omega = \omega - \bar{\omega}$ and let

$$\hat{\alpha} = e^{-\bar{\omega}t}\alpha\,, \tag{A.4}$$

$$\hat{\beta} = e^{\bar{\omega}t}\beta\,. \tag{A.5}$$

Differentiating with respect to time and using (A.3), we obtain

$$i\omega\hat{\alpha} + \frac{d\hat{\alpha}}{dt} = \frac{\dot{\omega}}{2\omega}\exp\left[2i\int\delta\omega(\tau)d\tau\right]\hat{\beta}\,, \tag{A.6}$$

$$-i\bar{\omega}\hat{\beta} + \frac{d\beta}{dt} = \frac{\dot{\omega}}{2\omega}\exp\left[-2i\int\delta\omega(\tau)d\tau\right]\hat{\alpha}\,. \tag{A.7}$$

We note that we can recast these equations in the form of a matrix:

$$\frac{d}{dt}\begin{pmatrix}\hat{\alpha}\\ \hat{\beta}\end{pmatrix} = \begin{pmatrix}-i\bar{\omega} & \frac{\dot{\omega}}{2\omega}\exp\left[2i\int\delta\omega(\tau)d\tau\right]\\ \frac{\dot{\omega}}{2\omega}\exp\left[-2i\int\delta\omega(\tau)d\tau\right] & i\bar{\omega}\end{pmatrix} \tag{A.8}$$

To first-order, let $\hat{\alpha} = \hat{\alpha}_+ b\hat{\alpha}_1$ and $\hat{\beta} = \hat{\beta}_0 + b\hat{\beta}_1$, where $b \ll 1$. We find

$$\frac{d\hat{\alpha}_0}{dt} = -i\bar{\omega}\hat{\alpha}_0 \tag{A.9}$$

$$\frac{d\hat{\beta}_0}{dt} = i\bar{\omega}\hat{\beta}_0 \tag{A.10}$$

$$\frac{d\alpha_1}{dt} = -i\bar{\omega}\hat{\alpha}_1 + \frac{\bar{\omega}}{2\omega}\exp\left[2i\int \delta\omega(\tau)d\tau\right]\hat{\beta}_0 \tag{A.11}$$

$$\frac{d\beta_1}{dt} = i\bar{\omega}\hat{\beta}_1 + \frac{\bar{\omega}}{2\omega}\exp\left[-2i\int \delta\omega(\tau)d\tau\right]\hat{\alpha}_0 \tag{A.12}$$

These equations can be solved immediately by noting that $\hat{\alpha}_0 = e^{-i\bar{\omega}t}\hat{\alpha}(0)$, $\hat{\beta}_0 = e^{i\bar{\omega}t}\hat{\beta}(0)$, and $\frac{df}{dt} = iaf + h(t)b$ is solved with

$$f(t) = be^{iat}\left(\int h(t)e^{-iat}dt\right) + Ce^{iat}\,, \tag{A.13}$$

where C is a constant. Therefore,

$$\hat{\alpha}_1 = \hat{\beta}(0)e^{-i\bar{\omega}t}\left(\frac{\dot{\omega}}{2\omega}\left[2i\int_0^t \delta\omega(\tau)d\tau\right]\right) + C_1 e^{-i\bar{\omega}t}\,, \tag{A.14}$$

$$\hat{\beta}_1 = \hat{\alpha}(0)e^{i\bar{\omega}t}\left(\frac{\dot{\omega}}{2\omega}\left[-2i\int_0^t \delta\omega(\tau)d\tau\right]\right) + C_2 e^{i\bar{\omega}t}\,. \tag{A.15}$$

At $t = 0$, we have $\beta(0) = 0$ and $\alpha(0) = 1$. Therefore, $\hat{\beta}(0) = 0$ and $\hat{\alpha}(0) = 1$. From the initial conditions, we also have $C_1 = C_2 = 0$.

We can do similar calculations to obtain the second-order corrections to $\hat{\alpha}_0$ and $\hat{\beta}_0$. Using Mathematica, we obtain

$$\begin{pmatrix}\hat{\alpha}(T)\\ \hat{\beta}(T)\end{pmatrix} = M\begin{pmatrix}\hat{\alpha}(0)\\ \hat{\beta}(0)\end{pmatrix} = \begin{pmatrix}M_{11} & M_{12}\\ M_{12}^* & M_{22}\end{pmatrix}\begin{pmatrix}\hat{\alpha}(0)\\ \hat{\beta}(0)\end{pmatrix}\,, \tag{A.16}$$

where after a a period $T = 2\pi/\Omega$, we have

$$M_{11} = \frac{e^{-2i\pi q}\left(4 + q^2\left(b^2\left(-\left(-8i\pi q^3 + 2i\pi q + e^{4i\pi q} - 1\right)\right) + 64q^2 - 32\right)\right)}{4\left(1 - 4q^2\right)^2}\,, \tag{A.17}$$

$$M_{12} = \frac{bq\left(-3ibq + 4q^2 - 4\right)\sin(2\pi q)}{4\left(4q^4 - 5q^2 + 1\right)}\,, \tag{A.18}$$

$$M_{22} = \frac{e^{-2i\pi q}\left(-b^2q^2 + e^{4i\pi q}\left(4 + q^2\left(b^2\left(-8i\pi q^3 + 2i\pi q + 1\right) + 64q^2 - 32\right)\right)\right)}{4\left(1 - 4q^2\right)^2}\,, \tag{A.19}$$

where $q = \frac{\omega}{\Omega}$.

Appendix B

Calculation of Squeezing Expectation Values

We have

$$S_0^\dagger a S_0 = a\cosh r_0 - a^\dagger e^{i\phi_0}\sinh r_0 \tag{B.1}$$

$$S_0^\dagger a^\dagger S_0 = a^\dagger\cosh r_0 - a e^{-i\phi_0}\sinh r_0\,. \tag{B.2}$$

Therefore,

$$\begin{aligned} S_0^\dagger a^{\dagger 2} S_0 &= S_0^\dagger a^\dagger S_0 S_0^\dagger a^\dagger S_0 \\ &= a^{\dagger 2}\cosh^2 r_0 - a^\dagger a e^{-i\phi_0}\cosh r_0\sinh r - a^\dagger a e^{-i\phi_0}\cosh r_0\sinh r_0 + a^2 e^{-2i\phi_0}\sinh^2 r_0 \end{aligned} \tag{B.3}$$

Noting that $\langle 0|a^\dagger a|0\rangle = 0$ and $\langle 0|aa^\dagger|0\rangle = 1$, we find that

$$\langle 0|S_0^\dagger a^{\dagger 2} S_0|0\rangle = -e^{-i\phi_0}\cosh r_0\sinh r_0\,. \tag{B.4}$$

As $(S_0^\dagger a^2 S_0)^\dagger = S_0^\dagger a^{\dagger 2} S_0$, we also have

$$\langle 0|S_0^\dagger a^{\dagger 2} S_0|0\rangle = -e^{i\phi_0}\cosh r_0\sinh r_0\,. \tag{B.5}$$

We can also calculate

$$\begin{aligned} \langle 0|S_0^\dagger a^{\dagger 4} S_0|0\rangle = \langle 0|\,&\left(a^{\dagger 2}\cosh^2 r_0 - aa^\dagger\cosh r_0\sinh r e^{-i\phi_0} - aa^\dagger e^{-i\phi_0}\cosh r_0\sinh r + a^2 e^{-2i\phi_0}\sinh^2 r_0\right) \\ &\times\left(a^{\dagger 2}\cosh^2 r_0 - aa^\dagger\cosh r_0\sinh r e^{-i\phi_0} - aa^\dagger e^{-i\phi_0}\cosh r_0\sinh r + a^2 e^{-2i\phi_0}\sinh^2 r_0\right)|0\rangle\,. \end{aligned} \tag{B.6}$$

We see that the only non-vanishing terms are

$$\langle 0|S_0^\dagger a^{\dagger 4} S_0|0\rangle = \langle 0|aa^\dagger aa^{\dagger 0} e^{-2i\phi_0}\cosh^2 r_0\sinh^2 r_0 + a^2 a^{\dagger 2} e^{-2i\phi_0}\cosh^2 r_0\sinh^2 r_0|0\rangle\,. \tag{B.7}$$

Noting that $\langle 0|aa^\dagger aa^\dagger|0\rangle = 1$ and $\langle 0|a^2 a^{\dagger 2}|0\rangle = 2$, we see that

$$\langle 0|S_0^\dagger a^{\dagger 4} S_0|0\rangle = 3e^{-2i\phi}\cosh^2 r_0\sinh^2 r_0 \tag{B.8}$$

and

$$\langle 0|S_0^\dagger a^4 S_0|0\rangle = 3e^{2i\phi_0}\cosh^2 r_0\sinh^2 r_0\,. \tag{B.9}$$

Repeating the same steps, we calculate

$$\begin{aligned} S_0^\dagger a^{\dagger 2} a^2 S_0 = &\left(a^{\dagger 2}\cosh^2 r_0 - a^\dagger a e^{-i\phi_0}\cosh r_0 \sinh r_0 - a a^\dagger e^{-i\phi_0}\cosh r_0 \sinh r_0 + a^2 2^{-2i\phi_0}\sinh^2 r_0\right) \\ &\times \left(a^2\cosh^2 r_0 - a a^\dagger e^{i\phi_0}\cosh r_0 \sinh r_0 - a^\dagger a e^{i\phi_0}\cosh r_0 \sinh r_0 + a^{\dagger 2} 2^{2i\phi_0}\sinh^2 r_0\right) \end{aligned} \tag{B.10}$$

so that

$$\langle 0|S_0^\dagger a^{\dagger 2} a^2 S_0|0\rangle = \langle a^2 a^{\dagger 2}\sinh^4 r_0 + a a^\dagger a a^\dagger \cosh^2 r_0 \sinh^2 r_0\rangle = 2\sinh^4 r_0 + \cosh^2 r_0 \sinh^2 r_0\,. \tag{B.11}$$

Similarly,

$$\langle 0|S_0 a^2 a^{\dagger 2} S_0|0\rangle = \langle a^2 a^{\dagger 2}\cosh^4 r_0 + a a^\dagger a a^\dagger \cosh^2 r_0 \sinh^2 r_0\rangle = 2\cosh^4 r_0 + \cosh^2 r_0 \sinh^2 r_0\,. \tag{B.12}$$

Appendix C

Calculating the Matrix Elements of Equation (5.11)

C.1 Detector Transition Probability

We will now calculate

$$P_D = \lambda^2 \int d\tau_D d\tau'_D \chi_D(\tau_D)\chi_D(\tau'_D) e^{-i\Omega_D(\tau_D-\tau'_D)} W(x_D(\tau_D), x_D(\tau'_D)) \ . \tag{C.1}$$

Using equations (5.30) and (5.26), we find

$$\sigma(x, \Gamma^n x') = -1 + \alpha(r)\cosh\left[G_P\right] - (\alpha(r)-1)\cosh\left[H_P\right] \tag{C.2}$$

where

$$G_P = \frac{r_+}{\ell}\left\{\frac{r_-}{\sqrt{r^2-r_+^2}\sqrt{r_+^2-r_-^2}}(\tau-\tau') - 2\pi n\right\} - \frac{r_-}{\ell^2}\frac{\ell r_+}{\sqrt{r^2-r_+^2}\sqrt{r_+^2-r_-^2}}(\tau-\tau') \tag{C.3}$$

$$H_P = \frac{r_+}{\ell^2}\frac{r_+\ell}{\sqrt{r^2-r_+^2}\sqrt{r_+^2-r_-^2}}(\tau-\tau') - \frac{r_-}{\ell}\left\{\frac{r_-}{\sqrt{r^2-r_+^2}\sqrt{r_+^2-r_-^2}}(\tau-\tau') - 2\pi n\right\} , \tag{C.4}$$

Subtract an $i\epsilon$ regulator[1] and define

$$(\rho_n^{\pm}(\tau-\tau'))^2 = \pm 1 + \alpha(r)\cosh\left[G_P - i\epsilon\right] - (\alpha(r)-1)\cosh\left[H_P - i\epsilon\right] \ , \tag{C.5}$$

so that simplifying yields

$$\begin{aligned}(\rho_n^{\pm}(\tau-\tau'))^2 = (\alpha(r)-1)\Bigg\{&\frac{1}{\alpha(r)-1}\left(\pm 1 + \alpha(r)\cosh\left[2\pi n\frac{r_+}{\ell}\right]\right) \\ &- \cosh\left[(\tau-\tau')\left(\frac{r_+^2-r_-^2}{R^3} + 2\pi n\frac{r_-}{\ell} - i\epsilon\right)\right]\Bigg\}\end{aligned} \tag{C.6}$$

[1] In general, a regulator is required to prevent divergences. However, for our case, a regulator turns out not to be necessary, though we keep the $i\epsilon$ until the end for the sake of completeness.

where

$$R^3 = \ell\sqrt{r^2 - r_+^2}\sqrt{r_+^2 - r_-^2}\,. \tag{C.7}$$

Define $\cosh(\alpha_n^\pm) = \frac{1}{\alpha(r)-1}\left[\pm 1 + \alpha(r)\cosh\left(2\pi n\frac{r_+}{\ell}\right)\right]$. Then,

$$\rho_n^\pm(\tau-\tau') = \sqrt{(\alpha(r)-1)\left(\cosh(\alpha_n^\pm) - \cosh\left[(\tau-\tau')\left(\frac{r_+^2-r_-^2}{R^3}\right) + 2\pi n\frac{r_-}{\ell} - i\epsilon\right]\right)}\,. \tag{C.8}$$

We can rewrite the detector transition probabilities in the form $P_D = \sum_{n=-\infty}^{\infty}\eta^n\left\{I_n^- - \zeta I_n^+\right\}$ where we are using Gaussian switching, $\chi(\tau_D) = e^{-\tau_D^2/2\sigma_D^2}$, such that

$$I_n^\pm = \frac{\lambda^2}{4\sqrt{2}\pi\ell}\int_{-\infty}^{\infty}d\tau\int_{-\infty}^{\infty}d\tau'\frac{e^{-\tau^2/2\sigma_D^2}e^{-\tau'^2/2\sigma_D^2}e^{-i\Omega_D(\tau-\tau')}}{\rho_n^\pm(\tau-\tau')}\,. \tag{C.9}$$

Letting $\tau = \frac{u+v}{2}$ and $\tau' = \frac{v-u}{2}$, we have

$$I_n^\pm = \frac{\lambda^2\sigma_D}{4\sqrt{2}\pi\ell}(\alpha(r)-1)^{-1/2}\int_{-\infty}^{\infty}du\frac{e^{-\frac{u^2}{4\sigma_D^2}}e^{-i\Omega_D u}}{\sqrt{\left(\cosh(\alpha_n^\pm) - \cosh\left[u\left(\frac{r_+^2-r_-^2}{R^3}\right) + 2\pi n\frac{r_-}{\ell} - i\epsilon\right]\right)}}\,. \tag{C.10}$$

Let $y = \frac{r_+^2-r_-^2}{R^3}u$. Thus, $dy = \frac{r_+^2-r_-^2}{R^3}du$. Therefore,

$$I_n^\pm = \frac{\lambda^2\sigma_D}{4\sqrt{2}\pi\ell}(\alpha(r)-1)^{-1/2}\left(\frac{r_+^2-r_-^2}{R^3}\right)^{-1}\int_{-\infty}^{\infty}dy\frac{e^{-\frac{\left(\frac{R^3}{r_+^2-r_-^2}\right)^2y^2}{4\sigma_D^2}}e^{-\frac{i\Omega_D R^3 y}{r_+^2-r_-^2}}}{\sqrt{\left(\cosh(\alpha_n^\pm) - \cosh\left[y + 2\pi n\frac{r_-}{\ell} - i\epsilon\right]\right)}}\,. \tag{C.11}$$

Let $z = y + \frac{2\pi n r_-}{\ell}$, so $dz = dy$. Then,

$$I_n^\pm = \frac{\lambda^2\sigma_D}{4\sqrt{2}\pi\ell}(\alpha(r)-1)^{-1/2}\left(\frac{r_+^2-r_-^2}{R^3}\right)^{-1}\int_{-\infty}^{\infty}dz\frac{e^{-\frac{1}{4\sigma_D^2}\left(\frac{R^3}{r_+^2-r_-^2}\right)^2\left(z-\frac{2\pi n r_-}{\ell}\right)^2}e^{-\frac{i\Omega_D R^3}{r_+^2-r_-^2}\left(z-\frac{2\pi n r_-}{\ell}\right)}}{\sqrt{(\cosh(\alpha_n^\pm) - \cosh\left[z - i\epsilon\right])}}\,. \tag{C.12}$$

As expanding as a Laurent series shows that the singularity is not a pole, so the regulator can be dropped. Therefore, we obtain an expression for the detector transition probabilities,

$$I_n^\pm = K_P\int_{-\infty}^{\infty}dz\frac{e^{-a\left(z-\frac{2\pi n r_-}{\ell}\right)^2}e^{-i\beta\left(z-\frac{2\pi n r_-}{\ell}\right)}}{\sqrt{(\cosh(\alpha_n^\pm) - \cosh(z))}}\,, \tag{C.13}$$

and

$$K_P = \frac{\lambda^2 \sigma_D}{4\sqrt{2\pi}} \tag{C.14}$$

$$a = \frac{R_D^2 - r_+^2}{r_+^2 - r_-^2} \frac{\ell^2}{4\sigma_D^2} \tag{C.15}$$

$$\beta = \Omega_D \ell \sqrt{\frac{R_D^2 - r_+^2}{r_+^2 - r_-^2}} \tag{C.16}$$

$$\cosh(\alpha_n^{\pm}) = \frac{1}{\alpha(R_D) - 1} \left[\pm 1 + \alpha(R_D) \cosh\left(2\pi n \frac{r_+}{\ell}\right) \right] . \tag{C.17}$$

C.2 Detector Non-localities

We will now calculate

$$\begin{aligned} X = -\lambda^2 \int d\tau_A d\tau_B \chi(\tau_A)\chi(\tau_B) e^{-i(\Omega_A \tau_A + \Omega_B \tau_B)} \Big\{ & \Theta[t' - t] W(x_A(t'), x_B(t)) \\ & + \Theta[t' - t] W(x_B(t), x_A(t')) \Big\} \end{aligned} \tag{C.18}$$

where the Wightman function is defined in equation (5.29) and the co-rotating frame is in equation (5.26). Let the trajectories of the detectors be

$$x_A(\tau_A) := \left\{ t' = \frac{\ell r_+ \tau_A}{\sqrt{r^2 - r_+^2}\sqrt{r_+^2 - r_-^2}}, r = R_A, \phi_A = \frac{r_- \tau_A}{\sqrt{r^2 - r_+^2}\sqrt{r_+^2 - r_-^2}} \right\} , \tag{C.19}$$

$$x_B(\tau_B) := \left\{ t = \frac{\ell r_+ \tau_B}{\sqrt{r^2 - r_+^2}\sqrt{r_+^2 - r_-^2}}, r = R_B, \phi_B = \frac{r_- \tau_B}{\sqrt{r^2 - r_+^2}\sqrt{r_+^2 - r_-^2}} \right\} . \tag{C.20}$$

Therefore,

$$\sigma_\epsilon(x_A, \Gamma^n x_B)^2 = -1 + \sqrt{\alpha(R_A)\alpha(R_B)} \cosh[G_X] - \sqrt{\alpha(R_A) - 1}\sqrt{\alpha(R_B) - 1} \cosh[H_X] . \tag{C.21}$$

where

$$G_X = \frac{r_+}{\ell} \left\{ \frac{r_- \left(\frac{\tau_A}{\sqrt{R_A^2 - r_+^2}} - \frac{\tau_B}{\sqrt{R_B^2 - r_+^2}} \right)}{\sqrt{r_+^2 - r_-^2}} - 2\pi n \right\} - \frac{r_+ r_- \ell \left(\frac{\tau_A}{\sqrt{R_A^2 - r_+^2}} - \frac{\tau_B}{\sqrt{R_B^2 - r_+^2}} \right)}{\ell^2 \sqrt{r_+^2 - r_-^2}} , \tag{C.22}$$

$$H_X = \frac{r_+ r_+ \ell \left(\frac{\tau_A}{\sqrt{R_A^2 - r_+^2}} - \frac{\tau_B}{\sqrt{R_B^2 - r_+^2}} \right)}{\ell^2 \sqrt{r_+^2 - r_-^2}} - \frac{r_-}{\ell} \left\{ \frac{r_- \left(\frac{\tau_A}{\sqrt{R_A^2 - r_+^2}} - \frac{\tau_B}{\sqrt{R_B^2 - r_+^2}} \right)}{\sqrt{r_+^2 - r_-^2}} - 2\pi n \right\} . \tag{C.23}$$

Define

$$(\rho_n(t'-t)^{\pm})^2 = \pm 1 + \sqrt{\alpha(R_A)\alpha(R_B)}\cosh\left(\frac{2\pi n r_+}{\ell}\right) - \sqrt{\alpha(R_A)-1}\sqrt{\alpha(R_B)-1}\cosh\left[\frac{r_+^2-r_-^2}{\ell^2 r_+}(t-t') + \frac{2\pi n r_-}{\ell} - i\epsilon\right] = \sqrt{\alpha(R_A)-1}\sqrt{\alpha(R_B)-1}\cosh(\alpha_n^{\pm}) - \cosh\left[\frac{r_+^2-r_-^2}{\ell^2 r_+}(t-t') + \frac{2\pi n r_-}{\ell} - i\epsilon\right] \tag{C.24}$$

where $t'-t = \frac{\left(\frac{\tau_A}{\sqrt{R_A^2-r_+^2}} - \frac{\tau_B}{\sqrt{R_B^2-r_+^2}}\right)}{\sqrt{r_+^2-r_-^2}}$ and $\cosh(\alpha_n^{\pm}) = \frac{\pm 1 + \sqrt{\alpha(R_A)}\sqrt{\alpha(R_B)}\cosh(2\pi n r_+/\ell)}{\sqrt{\alpha(R_A)-1}\sqrt{\alpha(R_B)-1}}$.

Then,

$$X = -\lambda^2 \int_{t>t'} \left[\eta_B(t)\eta_A(t') e^{-i[\Omega_B\tau_B(t)+\Omega_A\tau_A(t')]} W(x_A(t'), x_B(t)) + A \leftrightarrow B\right] . \tag{C.25}$$

where

$$\eta_A(t) = \frac{d\tau_A}{dt}\chi_A(\tau_A) = \gamma_A\, , e^{-\tau_A^2/2\sigma_A^2} \tag{C.26}$$

$$\eta_B(t) = \frac{d\tau_B}{dt}\chi_B(\tau_B) = \gamma_B\, , e^{-\tau_B^2/2\sigma_B^2} \tag{C.27}$$

$$\gamma_A = \frac{\sqrt{R_A^2-r_+^2}\sqrt{r_+^2-r_-^2}}{\ell r_+}\, , \tag{C.28}$$

$$\gamma_B = \frac{\sqrt{R_B^2-r_+^2}\sqrt{r_+^2-r_-^2}}{\ell r_+}\, . \tag{C.29}$$

Let us write

$$\eta_A(t) = \gamma_A e^{-\gamma_A^2 t^2/2\sigma_A^2} = \gamma_A e^{-t^2/2\bar{\sigma}_A^2}\, , \tag{C.30}$$

$$\eta_B(t) = \gamma_B e^{-\gamma_B^2 t^2/2\sigma_B^2} = \gamma_B e^{-t^2/2\bar{\sigma}_B^2}\, , \tag{C.31}$$

and

$$\bar{\sigma}_A = \sigma_A/\gamma_A\, , \tag{C.32}$$

$$\bar{\sigma}_B = \sigma_B/\gamma_B\, , \tag{C.33}$$

$$\Omega_A\tau_A = \Omega_A\gamma_A t := \bar{\Omega}_A t\, , \tag{C.34}$$

$$\Omega_B\tau_B = \Omega_B\gamma_B t := \bar{\Omega}_B t\, . \tag{C.35}$$

Therefore, $X = \sum_{n=-\infty}^{\infty}\eta^n\{I_{AB,n}^- - \zeta I_{AB,n}^+ + A \leftrightarrow B\}$, where

$$I_{AB,n}^{\pm} = -\frac{\lambda^2\gamma_A\gamma_B}{4\sqrt{2}\pi\ell}\int_{-\infty}^{\infty} dt \int_{-\infty}^{t} dt' \frac{e^{-t^2/2\bar{\sigma}_B^2} e^{-t'^2/2\bar{\sigma}_A^2} e^{-i[\bar{\Omega}_B t + \bar{\Omega}_A t']}}{\rho_n^{\pm}(t-t')}\, . \tag{C.36}$$

Let $t = \frac{v+u}{2}$ and $t' = \frac{v-u}{2}$. Then,

$$I_{AB,n}^{\pm} = -\frac{\lambda^2}{4\sqrt{\pi}\ell}\frac{\bar{\sigma}_A\bar{\sigma}_B}{\sqrt{\sigma_A^2+\sigma_B^2}}\frac{\gamma_A\gamma_B}{\sqrt{\sqrt{\alpha(R_A)-1}\sqrt{\alpha(R_B)-1}}} e^{-\frac{\bar{\sigma}_A^2\bar{\sigma}_B^2(\bar{\Omega}_A^2+\bar{\Omega}_B^2)}{2(\bar{\sigma}_A^2+\bar{\sigma}_B^2)}} \times \int_0^{\infty} du e^{-\frac{u^2}{2(\bar{\sigma}_A^2+\bar{\sigma}_B^2)}} e^{-i\frac{(\bar{\sigma}_B^2\bar{\Omega}_B - \bar{\sigma}_A^2\bar{\Omega}_A}{\bar{\sigma}_A^2+\bar{\sigma}_B^2}u} \frac{1}{\sqrt{\cosh(\alpha_n^{\pm}) - \cosh\left[\frac{r_+^2-r_-^2}{\ell^2 r_+}u + \frac{2\pi n r_-}{\ell} - i\epsilon\right]}}\, . \tag{C.37}$$

Let $z = \frac{r_+^2 - r_-^2}{\ell^2 r_+} u + 2\pi n r_-/\ell$. Then, $u = \frac{\ell^2 r_+}{r_+^2 - r_-^2}(z - 2\pi n r_-/\ell)$. Similarly calculations as P_D shows $X = \sum_{n=-\infty}^{\infty} \eta^n \left[\left(I^-_{AB,n} + I^-_{BA,-n} \right) - \zeta \left(I^+_{AB,n} + I^+_{BA,-n} \right) \right]$, which describes the non-local correlations, where

$$I^{\pm}_{AB,n} + I^{\pm}_{BA,-n} = \frac{K_X}{2} \int_0^{\infty} dz \left[\frac{e^{-a_X \left(z - \frac{2\pi n r_-}{\ell} \right)^2} e^{-i\beta_X \left(z - \frac{2\pi n r_-}{\ell} \right)} + e^{-a_X \left(z + \frac{2\pi n r_-}{\ell} \right)^2} e^{i\beta_X \left(z + \frac{2\pi n r_-}{\ell} \right)}}{\sqrt{\cosh(\alpha^{\pm}_{X,n}) - \cosh(z)}} \right], \tag{C.38}$$

with

$$K_X = -\frac{\lambda^2 \sigma_A \sigma_B \sqrt[4]{(R_A^2 - r_+^2)(R_B^2 - r_+^2)} \exp\left(-\frac{\sigma_A^2 \sigma_B^2 \left(\Omega_A \sqrt{R_A^2 - r_+^2} + \Omega_B \sqrt{R_B^2 - r_+^2} \right)^2}{2\left(\sigma_A^2 \left(R_B^2 - r_+^2 \right) + \sigma_B^2 \left(R_A^2 - r_+^2 \right) \right)} \right)}{2\sqrt{\pi} \sqrt{\sigma_A^2 (R_B^2 - r_+^2) + \sigma_B^2 (R_A^2 - r_+^2)}}, \tag{C.39}$$

$$a_X = \frac{1}{2(\bar{\sigma}_A^2 + \bar{\sigma}_B^2)} \left(\frac{\ell^2 r_+}{r_+^2 - r_-^2} \right)^2, \tag{C.40}$$

$$\beta_X = \frac{(\bar{\sigma}_B^2 \bar{\Omega}_B - \bar{\sigma}_A^2 \bar{\Omega}_A)}{\bar{\sigma}_A^2 + \bar{\sigma}_B^2} \left(\frac{\ell^2 r_+}{r_+^2 - r_-^2} \right), \tag{C.41}$$

$$\cosh(\alpha^{\pm}_{X,n}) = \frac{1}{\sqrt{\alpha(R_A) - 1} \sqrt{\alpha(R_B) - 1}} \left[\pm 1 + \sqrt{\alpha(R_A)} \sqrt{\alpha(R_B)} \cosh\left(2\pi n \frac{r_+}{\ell} \right) \right]. \tag{C.42}$$

C.3 Total Correlations

Our final task is to calculate the total correlation, which is given by

$$L_{AB} = \lambda^2 \int dt dt' \eta_B(t') \eta_A(t) e^{-i[\Omega_B \tau_B(t') - \Omega_A \tau_A(t)]} W(x_A(t), x_B(t')) \,, \tag{C.43}$$

where $\eta_D(t) = \frac{d\tau_D}{dt} \chi(\tau_D) = \gamma_D e^{-\tau_D^2 / 2\sigma_D^2}$.

Working in the co-rotating frame, we can do similar calculations as P_D and X to write the total correlations as $L_{AB} = \sum_{n=-\infty}^{\infty} (I_n^- - \zeta I_n^+)$ where

$$I_n^{\pm} = K_L \int_{-\infty}^{\infty} dz \frac{e^{-a_X \left(z - \frac{2\pi n r_-}{\ell} \right)^2} e^{-i\beta_X \left(z - \frac{2\pi n r_-}{\ell} \right)}}{\sqrt{\cosh(\alpha^{\pm}_{X,n}) - \cosh(z)}}, \tag{C.44}$$

with

$$K_L = \frac{1}{\sqrt{\sqrt{\alpha(R_A) - 1} \sqrt{\alpha(R_B) - 1}}} \frac{\lambda^2}{8\pi\sqrt{2}\ell} \gamma_B \gamma_A \left(\frac{2\sqrt{2\pi} \bar{\sigma}_A \bar{\sigma}_B}{\sqrt{\bar{\sigma}_A^2 + \bar{\sigma}_B^2}} \right) e^{-\frac{\bar{\sigma}_A^2 \bar{\sigma}_B^2 (\bar{\Omega}_A - \bar{\Omega}_B)^2}{2(\bar{\sigma}_A^2 + \bar{\sigma}_B^2)}} \frac{\ell^2 r_+}{r_+^2 - r_-^2}. \tag{C.45}$$